Glacier response to climate variability and climate change across the Southern Andes

Kumulative Dissertation zur Erlangung des akademischen Grades
doctor rerum naturalium (Dr. rer. nat.) im Fach Geographie
eingereicht an der Mathematisch-Naturwissenschaftlichen Fakultät der
Humboldt-Universität zu Berlin

M.Sc. Stephanie Suzanne Weidemann, geb. Reinartz

Präsidentin der Humboldt-Universität zu Berlin: Prof. Dr.-Ing. Dr. Sabine Kunst
Dekan der Mathematisch-Naturwissenschaftlichen Fakultät: Prof. Dr. Elmar Kulke

Gutachter/in:

1. Prof. Dr. Christoph Schneider
2. Prof. Dr. Julia Boike
3. Prof. Dr. Matthias Braun

Tag der mündlichen Prüfung: 17.05.2021

Contents

Abstract

Glacier mass loss of the Southern Andes contributes largely to sea-level rise during recent decades and also affects the regional water availability. Despite the overall glacier retreat of most glaciers in Patagonia and Tierra del Fuego, a recent increase in mass loss of individual glaciers has been observed. Within the framework of the German-Chilean project 'Responses of **Gla**ciers, **B**iosphere and H**y**drology to Climate **Va**riability and Climate Change across the **S**outhern **A**ndes' (GABY-VASA) funded by the Comisión Nacional de Investigación Científica y Tecnológica (CONICYT) and by the Bundesministerium für Bildung und Forschung (BMBF), the recent variability of climate and climatic mass balance for selected glaciated study sites in Patagonia and Tierra del Fuego are investigated in this thesis. Improving our understanding on the spatial and temporal variations of climatic mass balance processes, its atmospheric drivers, and their impact on the recently observed individual glacier behavior are further important aims. With respect to these, the main objectives of this thesis were to find cost-effective and suitable statistical and numerical approaches and to collect measured data at the study sites in order to make robust estimates of recent climate variability and changes in climatic mass balance of glaciers on Fuego-Patagonia.

Since climate variability is the key driver of local changes in the cryosphere in the Southern Andes, a unique record of meteorological observations across the Gran Campo Nevado Ice Cap in Southernmost Patagonia was analyzed with regard to main climate features and the relationship between the in-situ observations, large-scale climate modes and mesoscale weather patterns. Synoptic weather types with westerly and southwesterly airflow prevail during the year, leading to maritime climate conditions at the Gran Campo Nevado Ice Cap with a sharp gradient in precipitation between the west and east-side of the mountain range, and the spatial pattern of air temperature reflecting the proximity to the Pacific Ocean.

Furthermore, recent climatic mass balance variability was simulated for selected glaciers in Southern Patagonia and Tierra del Fuego by implementing the 'COupled Snow and Ice energy and MAss balance model' COSIMA, and its follow-up Python-based version

COSIPY. Contrasting patterns of positive simulated glacier-wide mean annual climatic mass balance and clearly negative geodetic mass balance were found for the two neighboring glaciers Grey and Tyndall located at the Southern Patagonia Icefield between 2000 and 2014. This highlights the importance of understanding of both, the climatic mass balance, and the ice-dynamical processes. A continuous negative annual climatic mass balance during the past two decades was modeled for Schiaparelli Glacier in Tierra del Fuego. The comparison of the different study sites in Southern Patagonia and Tierra del Fuego underlines the individual impact of climatic mass balance processes on the overall observed glacier mass loss, also depending on atmospheric drivers. Climatic mass balance simulations were further used to derive glacier steady-state conditions for recent (2000-2010) and past (Little Ice Age) glacier extents of Schiaparelli Glacier, aiming for a model-based approximation of climate conditions during the Little Ice Age.

Kurzfassung

Die Gletscherschmelze in den südlichen Anden trägt maßgeblich zum Anstieg des Meeresspiegels der letzten Jahrzehnte bei und beeinflusst regional die saisonale Wasserverfügbarkeit. In jüngster Zeit wurde eine rapide Zunahme der Massenverluste insbesondere einzelner großer Auslassgletscher des Nördlichen und Südlichen Patagonisches Eisfeldes beobachtet. Im Rahmen des deutsch-chilenischen Projekts 'Responses of **G**l**a**ciers, **B**iosphere und H**y**drology to Climate **Va**riability and Climate Change across the **S**outhern **A**ndes' (GABY-VASA), gefördert durch die Comisión Nacional de Investigación Científica y Tecnológica (CONICYT) und durch das Bundesministerium für Bildung und Forschung (BMBF), wurde die rezente Variabilität des Klimas und der klimatischen Massenbilanz für ausgewählte vergletscherte Gebiete in Patagonien und Feuerland untersucht. Die Verbesserung unseres Verständnisses über räumliche und zeitliche Muster der klimatischen Massenbilanz, ihrer atmosphärischen Antriebsfaktoren und ihres Einflusses auf das in jüngster Vergangenheit beobachtete individuelle Gletscherverhalten, sind weitere wichtige Ziele. Im Hinblick darauf bestanden die Hauptziele dieser Arbeit zum Einen in der Auswahl effizienter und geeigneter statistischer und numerischer Ansätze und zum Anderen in der Erhebung von Messdaten in den Untersuchungsgebieten, um robuste Schätzungen zur jüngsten Klimavariabilität und zu den Veränderungen der klimatischen Massenbilanz der Gletscher in Patagonien und Feuerland vornehmen zu können.

Da die Klimavariabilität die Hauptursache für lokale Veränderungen in der Kryosphäre der südlichen Anden ist, wurden langjährige meteorologische Beobachtungen im Gebiet der Gran Campo Nevado-Eiskappe im südlichsten Patagonien im Hinblick auf räumliche und zeitliche Variabilität und Trends untersucht. Zudem wurde der Einfluss mesoskaliger Wettermuster und Modi atmosphärischer Oszillationen auf die Ausprägung des Klimas analysiert. Synoptische Wettertypen mit westlicher und südwestlicher Luftanströmung herrschen während des Jahres vor, was zu maritimen Klimabedingungen im Gebiet der Gran Campo Nevado Eiskappe führt. Orographische Effekte führen zu einem starken Niederschlagsgradienten zwischen der West- und der Ostseite der Gebirgskette, während das räumliche Muster der Lufttemperatur weitestgehend durch die Nähe zum Pazifischen

Ozean bestimmt wird.

Darüber hinaus wurde die rezente Variabilität der klimatischen Massenbilanz für ausgewählte Gletscher in Südpatagonien und Feuerland durch die Implementierung des Energie- und Massenbilanzmodells COSIMA und der neueren Python-basierten Version COSIPY simuliert. Für die beiden benachbarten Gletscher Grey und Tyndall des Südlichen Patagonischen Eisfeldes wurden zum Einen eine positive mittlere jährliche klimatische Massenbilanz und zum Anderen eine deutlich negative geodätische Massenbilanz zwischen 2000 und 2014 ermittelt. Die unterschiedliche Ausprägung dieser beiden Massenbilanzen unterstreicht wie wichtig ein besseres Verständnis über die Prozesse der klimatischen Massenbilanz und Eisdynamik ist.

Eine kontinuierlich negative jährliche klimatische Massenbilanz wurde hingegen für den Gletscher Schiaparelli im Monte Sarmiento Massiv auf Feuerland während der letzten zwei Jahrzehnte modelliert. Der Vergleich der verschiedenen Untersuchungsgebiete in Südpatagonien und Feuerland unterstreicht den individuellen Einfluss der Prozesse der klimatischen Massenbilanz auf den insgesamt beobachteten Gletschermassenverlust, insbesondere auch in Abhängigkeit von atmosphärischen Faktoren. Des Weiteren wurden Simulationen der klimatischen Massenbilanz eingesetzt, um eine ausgeglichene Massenbilanz für rezente (2000-2010) und vergangene (Kleine Eiszeit) Ausdehnungen des Gletschers Schiaparelli abzuleiten. Ziel war es, eine modellgestützte Annäherung an die klimatischen Bedingungen während der Kleinen Eiszeit zu simulieren.

List of Publications

This thesis is presented in cumulative form and is based on the following three peer-reviewed papers. The papers are summarized in Chapter 3, Chapter 4, and Chapter 5, while they are reproduced in their original journal formats in the Appendices A.1, A.2, A.3.

Weidemann, S., T. Sauter, R. Kilian, D. Steger, N. Butorovic, and C. Schneider (2018). 'A 17-year Record of Meteorological Observations Across the Gran Campo Nevado Ice Cap in Southern Patagonia, Chile, Related to Synoptic Weather Types and Climate Modes'. In: *Frontiers in Earth Science* 6, p. 53. ISSN: 2296-6463. DOI: 10.3389/feart.2018.00053. URL: https://www.frontiersin.org/article/10.3389/feart.2018.00053.

Weidemann, S., T. Sauter, P. Malz, R. Jaña, J. Arigony-Neto, G. Casassa, and C. Schneider (2018). 'Glacier Mass Changes of Lake-Terminating Grey and Tyndall Glaciers at the Southern Patagonia Icefield Derived From Geodetic Observations and Energy and Mass Balance Modeling'. In: *Frontiers in Earth Science* 6, p. 81. ISSN: 2296-6463. DOI: 10.3389/feart.2018.00081. URL: https://www.frontiersin.org/article/10.3389/feart.2018.00081.

Weidemann, S., J. Arigony-Neto, R. Jaña, G. Netto, I. Gonzalez, G. Casassa, and C. Schneider (2020). 'Recent Climatic Mass Balance of the Schiaparelli Glacier at the Monte Sarmiento Massif and Reconstruction of Little Ice Age Climate by Simulating Steady-State Glacier Conditions.' In: *Geosciences* 10, p. 272. DOI: 10.3390/geosciences10070272. URL: https://doi.org/10.3390/geosciences10070272.

List of Figures

List of Tables

List of abbreviations

AAO	Antarctic Oscillation
AAOI	Antarctic Oscillation Index
AWS	Automatic Weather Station
BMBF	Bundesministerium für Bildung und Forschung
CD	Cordillera Darwin
CDI	Cordillera Darwin Icefield
CMB	Climatic Mass Balance
COND	Condensation
CONICYT	Comisión Nacional de Investigación Científica y Tecnológica
COSIPY	Coupled Snowpack and Ice surface energy and mass balance model in Python
COSIMA	Coupled Snowpack and Ice surface energy and Mass balance model
DEM	Digital Elevation Model
DGPS	Differential Global Positioning System
ELA	Equilibrium Line Altitude
ENSO	El Niño-Southern Oscillation
EVAPO	Evaporation
GABY-VASA	Responses of Glaciers, Biosphere and Hydrology to Climate Variability and Climate Change across the Southern Andes
GCN	Gran Campo Nevado
LIA	Little Ice Age
LW_{NET}	Net Longwave Radiation
m a.s.l.	Meter above sea level
MK	Mann-Kendall
MODIS	Moderate Resolution Imaging Spectroradiometer
MSM	Monte Sarmiento Massif
M_{SUB}	Subsurface Melt
M_{SURF}	Surface Melt

m w.e.	Meter Water Equivalent
NPI	Northern Patagonia Icefield
ONI	Oceanic Niño Index
OPM	Orographic Precipitation Model
PO	Precipitation Offset
P_{SOLID}	Solid Precipitation
Q_G	Ground heat Flux
Q_{LAT}	Latent Heat Flux
Q_{MELT}	Surface Melt
Q_{SENS}	Sensible Heat Flux
SMB	Surface Mass Balance
SPI	Southern Patagonia Icefield
SSE	Sen Slope Estimator
SUBLIM	Sublimation
SW_{IN}	Incoming Shortwave Radiation
SW_{NET}	Net Shortwave Radiation
T_{2m}	Air Temperature
TO	Temperature Offset
WS	Weather Station

CHAPTER 1

Introduction

1.1 Scope and motivation

The glaciers in Patagonia and Tierra del Fuego have shown one of the largest retreats in the past decades worldwide, with the Northern Patagonia Icefield (NPI) and the Southern Patagonia Icefield (SPI) being the largest contributors to sea-level rise (Willis et al. 2012b; Willis et al. 2012a; Gardner et al. 2013; Braun et al. 2019). The mass loss of the large icefields seems to be mainly caused by long-term warming, but the dynamical adjustment of individual calving glaciers accelerates the mass loss during recent decades (Casassa et al. 1997; Koppes et al. 2011; Rivera et al. 2012; Willis et al. 2012b; Willis et al. 2012a; Sakakibara and Sugiyama 2014; Malz et al. 2018; Braun et al. 2019). In particular, calving glaciers have the potential to disproportionately contribute to sea level rise due to a possible rapid retreat (Benn et al. 2007). The accelerated glacier mass loss in the Southern Andes (Aniya 1999; Davies and Glasser 2012; Meier et al. 2018) affects the available water resources (Huss and Hock 2018; Dussaillant et al. 2019) and the risks of floods due to the growing of glacial lakes (Loriaux and Casassa 2013; Wilson et al. 2018).

The number of remote sensing studies, updating the glacier inventories of the Southernmost Andes, assessing glacier area changes for different time periods (Davies and Glasser 2012; Meier et al. 2018) and estimating the overall contribution to see level rise (Willis et al. 2012b; Willis et al. 2012a; Malz et al. 2018; Braun et al. 2019; Dussaillant et al. 2019), have increased in the past decade. However, to estimate future changes of glaciers, we need to improve our understanding of the individual spatial and temporal variation of glacier retreat for different glacier catchments and different sets of atmospheric drivers (Schneider et al. 2020a). Numerical simulations of surface mass balance processes and ice dynamical processes therefore need further to be extended to study the drivers of the nonuniform retreat of glaciers in Fuego-Patagonia. The key driver of local glacier changes in Fuego-Patagonia is climate variability (Möller et al. 2007; Davies and Glasser 2012). In this respect, the most challenging part of surface mass balance modelling studies is the estimation of accumulation amounts along the mountain ranges of the Southernmost

Andes due to the lack of observations. The remoteness of the glaciated areas and the harsh weather conditions limit the amount of in-situ observations to a few firn-core measurements such as reported by Godoi et al. (2002), Shiraiwa et al. (2002), Kohshima et al. (2007), and Schwikowski et al. (2013). The quality of surface mass balance modelling studies however heavily relies on an accurate estimate of climate forcing data. Recent surface mass balance modeling studies (Lenaerts et al. 2014; Schaefer et al. 2015; Mernild et al. 2016) estimate a significant positive surface mass balance for the NPI and SPI, suggesting a slight increase in precipitation and cooling of the upper-atmosphere during the last decade as being the main drivers. The contrasting pattern of observed glacier retreat and positive modeled surface mass balance (SMB) are assumed to be a result of increasing ice flow velocities associated with ice loss due to calving by these authors. However, ice loss due to increasing ice flow velocities has been observed only for a few tide-water glaciers undergoing a recent rapid retreat (Sakakibara et al. 2013). It is more likely that an unrealistic overestimation of annual accumulation amounts in particular in the vicinity of the icefields are responsible for the overall positive surface mass balance results (Sauter 2020). The SMB modelling studies (Lenaerts et al. 2014; Schaefer et al. 2015; Mernild et al. 2016; Weidemann et al. 2013) show how sensitive surface mass balance simulations react to atmospheric input data, in particular to estimated solid precipitation and air temperature. Therefore, advancing the comparison of modelling approaches for estimating high resolution atmospheric data and glacier surface energy and mass balance is still essential. Reliable long-term meteorological observations in the glaciated areas are still rare, but prerequisite to constrain numerical models, and to study the individual glacier response to climate variability and warming (Masiokas et al. 2020).

1.2 Research questions and objectives

Individual glacier-climate interactions and the influence of climatic mass balance processes controlling the specific glacier response to climate forcing are the main objectives of this thesis. Understanding those is a key to understand past glacier changes as well as to estimate future glacier responses. The investigations presented in this thesis have been carried out mainly as part of the German-Chilean project 'Responses of **G**l**a**ciers, **B**iosphere and H**y**drology to Climate **Va**riability and Climate Change across the **S**outhern **A**ndes' (GABY-VASA)[1] of the Universidad de Magallanes and the Instituto Antártico Chileno in Chile, and the Humboldt-Universität zu Berlin, the Friedrich-Alexander University Erlangen, and the RWTH Aachen University in Germany (Schneider et al. 2020a). The

1 https://www.geographie.hu-berlin.de/de/abteilungen/klimatologie/forschung/gaby-vasa

joint project was funded by the Comisión Nacional de Investigación Científica y Tecnológica (CONICYT) and by the Bundesministerium für Bildung und Forschung (BMBF). The following main research questions are addressed in three peer-reviewed publications:

RQ1 What has been the state of climate variability during the past two decades in glaciated areas of Southernmost Patagonia? Can annual and seasonal trends in air temperature and precipitation be identified? How are large-scale modes of climate variability linked to local variability of air temperature and precipitation? (Publication 1, A.1)

RQ2 How do glaciers in the Southernmost Andes behave under recent climate conditions? What are the main atmospheric drivers of the spatial and temporal variation in climatic mass balance patterns? How large is the contribution of climatic mass balance to the overall glacier mass balance? (Publication 2, A.2)

RQ3 How large is the impact of regional climatic conditions and the specific topographic setting on the climatic mass balance variability in Fuego-Patagonia? Can climate conditions be reconstructed for known past glacier extents? (Publication 3, A.3)

A unique 17-year record of meteorological observations of four automatic weather stations located in the proximity of the Gran Campo Nevado Ice Cap are analyzed to improve our understanding of climatic variability in the partially glaciated Southernmost Andes and of climate forcing on recent glacier change (RQ1). One aim of this study is to provide robust estimates of annual and seasonal means, anomalies, extremes and trends of meteorological observations from a region with sparse long-term measurements. Time series of air temperature and precipitation are described using selected indices of extremes, and analyzed regarding their anomalies and trends. The relationship between in-situ observations and large-scale climate modes and mesoscale weather patterns are also revisited. In this expected, that future modelling studies of glacier mass balance will benefit from such a network of long-term observations.

Addressing the research questions RQ2, the 'COupled Snowpack and Ice surface energy and MAss balance model' COSIMA is adapted to selected glaciers of the Southern Patagonia Icefield. Prior to mass balance modelling itself, suitable downscaling methods for each atmospheric variable had to be set up to overcome the gap in spatial resolution between the driving atmospheric reanalysis data and required input data for COSIMA. Extensive field work has been carried out to collect data records to ensure the validation of downscaled atmospheric data and climatic mass balance results. Quantifying the contribution of

climatic mass balance to the observed mass loss by combining modelling results and geodetic mass balance data, is the final objective of this study.

The methodological approaches used to answer RQ2, are extended to Schiaparelli Glacier at the Monte Sarmiento Massif in Tierra del Fuego to ensure model applicability for different regions in the Southernmost Andes and to compare the influence of climatic mass balance processes on the recent individual glacier response. In this case study COSIPY, the follow-up version of COSIMA programmed in Python, was employed. Furthermore, climatic mass balance simulations are utilized to reconstruct glacier steady-state conditions for recent and past glacier extents. This in turn provides constraint and indication on how climate conditions must have been during the formation of lateral moraines from this earlier period.

1.3 Structure of the thesis

This thesis is based on the content of three published, peer-reviewed journal papers, written in collaboration with several co-authors. Each paper forms one chapter (Chapter 3, Chapter 4, Chapter 5), each giving an overview of the used data, methodological approaches and the main outcomes. In the synthesis, the main outcomes of each paper are summarized and linked to the main objectives and research questions. Some overlap between the content of Chapter 2 and Chapter 6 and the content of the three publications is inevitable.

Chapter One - Introduction gives a brief overview of the motivation, the main research questions and objectives of this thesis.

Chapter Two - Regions of interest describes the main characteristics of climate and cryosphere of Fuego-Patagonia with special interest in the glaciated areas investigated in this thesis. The chapter further contains information on the devices and measurements, installed and carried out during several field campaigns as part of the GABY-VASA project.

Chapter Three - Climate variability across the Gran Campo Nevado Ice Cap provides the detailed analysis of long-term meteorological observations in the Southernmost Andes, including a statistical description of climate features, trend analysis, a classification of mesoscale weather patterns, and the investigation of the impact of El Niño Southern Oscillation and Antarctic Oscillation on regional climate variability.

Chapter Four - Recent glacier mass changes of Grey Glacier and Tyndall Glacier at the Southern Patagonia Icefield quantifies in detail the energy fluxes and climatic mass balance processes at the glacier surface of two glaciers based on high-resolution surface mass balance simulations, and the contribution of climatic mass balance to the observed glacier mass losses.

Chapter Five - Reconstruction of Little Ice Age climate at Schiaparelli Glacier, Monte Sarmiento Massif investigates the recent climatic mass balance and further outlines the reconstruction of climate conditions during past glacier steady-state conditions.

Chapter Six - Synthesis and perspectives summarizes the main outcomes of this thesis and addresses perspectives for future research.

The **Appendices** contain the three peer-reviewed papers in their specific journal style.

CHAPTER 2

Region of interest

All study sites addressed in this thesis are located in the glaciated areas of Patagonia and Tierra del Fuego, further referred to as Fuego-Patagonia. This chapter provides an non-exhausting overview of the recent understanding of climate, climate variability and glacier response in Southernmost South America as an introduction and supplement to the detailed investigations described in chapters 3, 4, and 5.

2.1 Recent climate and climate variability of Fuego-Patagonia

The climate of Southernmost South America is heavily influenced by prevailing Southern Hemisphere westerlies and the proximity to the Pacific Ocean. The impinging air masses are modified by the north-south stretching Southernmost Andes and the northwest-southeast running Cordillera Darwin mountain range leading to large-scale orographic lifting of these air masses which are accompanied by strong orographic precipitation events (Holmlund and Fuenzalida 1995; Schneider et al. 2003; Schneider et al. 2020b; Sauter 2020; Temme et al. 2020) and high drying ratios (Escobar et al. 1992; Carrasco et al. 2002; Lenaerts et al. 2014). Accumulation in the most elevated and glaciated regions of the Southernmost Andes can only be deduced from firn core measurements ranging from 3.4 to 14.7 $\mathrm{m\,w.e.\,a^{-1}}$ (Godoi et al. 2002; Shiraiwa et al. 2002; Kohshima et al. 2007; Schwikowski et al. 2013) or numerical simulations ranging from 5 to 10 $\mathrm{m\,w.e.\,a^{-1}}$ at the NPI and SPI with extreme values of up to 34 m per year (Mernild et al. 2016; Schaefer et al. 2013; Schaefer et al. 2015; Lenaerts et al. 2014; Sauter 2020). No significant trend in precipitation has been observed since 1950, but large inter-annual and decadal variations have been found (Carrasco et al. 2008; Aravena and Luckman 2009; Lenaerts et al. 2014). Reanalysis data from 1960 to 2000 however show a slight decrease in solid precipitation over the two largest icefields in the Southernmost Andes as a result of increasing air temperatures (Rasmussen et al. 2007). Changes in wind pattern have enhanced the precipitation gradient between the luv-side and lee-side of the Cordillera Darwin mountain range since the beginning of the 20th century (Holmlund and Fuenzalida 1995; Koppes et al. 2009).

Air temperatures are moderate in Fuego-Patagonia with small daily and seasonal temperature amplitudes. The distribution of temperature is influenced by both latitude and elevation. The mean annual temperature decreases between 40°S to 55°S from 12°C to 4°C. It increases from the west to the east of the Patagonian Andes which is due to foehn effects which are induced by the forced uplift of air masses across the mountain range (Temme et al. 2020).

The lee-side of the Southernmost Andes is characterized by strong evapotranspiration, higher temperatures, and the dilution of cloud formations (Schneider et al. 2003; Villalba et al. 2003; Garreaud et al. 2009). A mean annual temperature trend between +0.4°C and +2.1°C was determined for Patagonia between 1900 to 1990 (Rosenblüth et al. 1997), with a larger temperature increase further South.

The spatial and temporal patterns of precipitation and air temperature in Southernmost South America is influenced at inter-annual to decadal time scales by large-scale modes of climate variability, in particular the El Niño Southern Oscillation (Schneider and Gies 2004; Gillett et al. 2006; Garreaud et al. 2009; Aravena and Luckman 2009), the Antarctic Oscillation (Thompson and Solomon 2002; Garreaud et al. 2009; Aravena and Luckman 2009), and the Pacific Decadal Oscillation (Villalba et al. 2003).

2.2 Glacier change along the southernmost Andes

In 2016, more than 11200 glaciers covering an area of 22636±905 km^2 were identified for the Patagonian Andes and Tierra del Fuego (south of 45.5°S) (Meier et al. 2018). The NPI (3675±80 km^2) and SPI (12232±201 km^2) are the two largest icefields in South America. Their major outlet glaciers (larger than 5 km^2) comprise more than 80% of the total glaciated area of Fuego-Patagonia (Meier et al. 2018). Moderate summer air temperatures and high accumulation amounts enable the formation of glaciated areas south of the NPI and SPI. Larger continuous glaciated areas can be found at the Gran Campo Nevado (GCN) (189±5 km^2), at Isla Santa Inés (ISI) (168±5 km^2), at the Monte Sarmiento Massif (MSM), at Cordillera Darwin (CD) (main icefield, (CDI) 1760±51 km^2) and at Isla Hoste (IH) (203±6 km^2) (Meier et al. 2018). The mean glacier elevation declines from 1640 m a.s.l. at the leeside of the NPI to about 765 m a.s.l. on Isla Santa Inés (Bown et al. 2014; Meier et al. 2018). In general, numerous outlet glaciers of the larger ice-bodies reach down to sea level and therefore calve into proglacial lakes or fjord systems (Porter and Santana 2003; Warren and Aniya 1999; Davies and Glasser 2012; Barcaza et al. 2017; Meier et al. 2018). The orientation of the large outlet glaciers is in most cases determined by the topography of the mountain range, leading to west and east facing glaciers at the NPI and SPI, and to north and south facing glaciers at the CD.

Most glaciers in Fuego-Patagonia have been thinning and retreating at high rates during the past decades. Mass loss of the NPI and the SPI contributed to sea-level rise by $0.042\pm0.002\,\mathrm{mm\,a^{-1}}$ between 1964/1975 and 2000 (Rignot et al. 2003), increasing to $0.054\pm0.002\,\mathrm{mm\,a^{-1}}$ between 2000 and 2015 (Braun et al. 2019). The NPI experienced a mean areal thinning of $0.85\pm0.007\,\mathrm{m\,a^{-1}}$ between 2000 and 2015, while the mean annual thinning for the SPI is reported to $0.86\pm0.008\,\mathrm{m\,a^{-1}}$ (Braun et al. 2019).

A reduction in the glaciated area of Fuego-Patagonia has been calculated to 5455 ± 1269 $\mathrm{km^2}$ ($19.4\pm4.5\%$), with 783 ± 112 $\mathrm{km^2}$ being lost from NPI and 1976 ± 273 $\mathrm{km^2}$ from SPI between the LIA ($\sim$1870) and 2016 (Meier et al. 2018). The highest negative rates are determined at northerly, land-terminating glaciers of the NPI (Davies and Glasser 2012; Meier et al. 2018). In general the annual rates of ice loss have increased significantly after 2001/2005 for both, the NPI and SPI (Davies and Glasser 2012; Meier et al. 2018).

The dynamic behavior of numerous large outlet glaciers in Fuego-Patagonia seems to be at least partially decoupled from climate change since some glaciers' changes do not coincide with the regional trend of glacier retreat but show sustained advances, accelerated retreats or long-maintained stillstands (Warren and Aniya 1999; Aniya et al. 1996; Rivera and Casassa 1999; Rivera et al. 2007; Lopez et al. 2010; Davies and Glasser 2012; Sakakibara and Sugiyama 2014; Minowa et al. 2015; Malz et al. 2018; Braun et al. 2019; Holmlund and Fuenzalida 1995). Rapid frontal retreats of large calving glaciers, such as Upsala and Jorge Montt glaciers are associated with ice flow acceleration and ice dynamical thinning near the calving front (Naruse and Skvarca 2000; Rivera et al. 2012; Jaber et al. 2013; Muto and Furuya 2013; Sakakibara and Sugiyama 2014; Mouginot and Rignot 2015; Bown et al. 2014), and cause an acceleration of the total mass loss of the large icefields (Casassa et al. 1997; Koppes et al. 2011; Rivera et al. 2012; Willis et al. 2012b; Willis et al. 2012a; Sakakibara and Sugiyama 2014; Braun et al. 2019). However, the total number of outlet glaciers showing an extraordinary retreat including a recent increment of ice velocity between 2000 and 2011 is small. The mean ice speed of the NPI and SPI even decreased between 2000 and 2011 compared to the time period from 1984 to 2000 (Sakakibara and Sugiyama 2014).

Mass loss of the CDI contributed to sea level rise by $0.01\pm0.004\,\mathrm{mm\,a^{-1}}$ between 2000 and 2011 with a thinning rate of $1.5\pm0.6\,\mathrm{m\ w.e.\,a^{-1}}$ (Melkonian et al. 2013). With a few exceptions (e.g. Glaciar Marinelli (Porter and Santana 2003)), glaciers at the southern slope of the Darwin Cordillera, in turn, are in remarkable stable state which has been related to higher orographic precipitation rates on its southern slope (Holmlund and Fuenzalida 1995; Davies and Glasser 2012). Land- and lake-terminating glaciers on the north-eastern side of the CD are on the other hand subject to considerable retreat within recent decades (Davies and Glasser 2012; Meier et al. 2018).

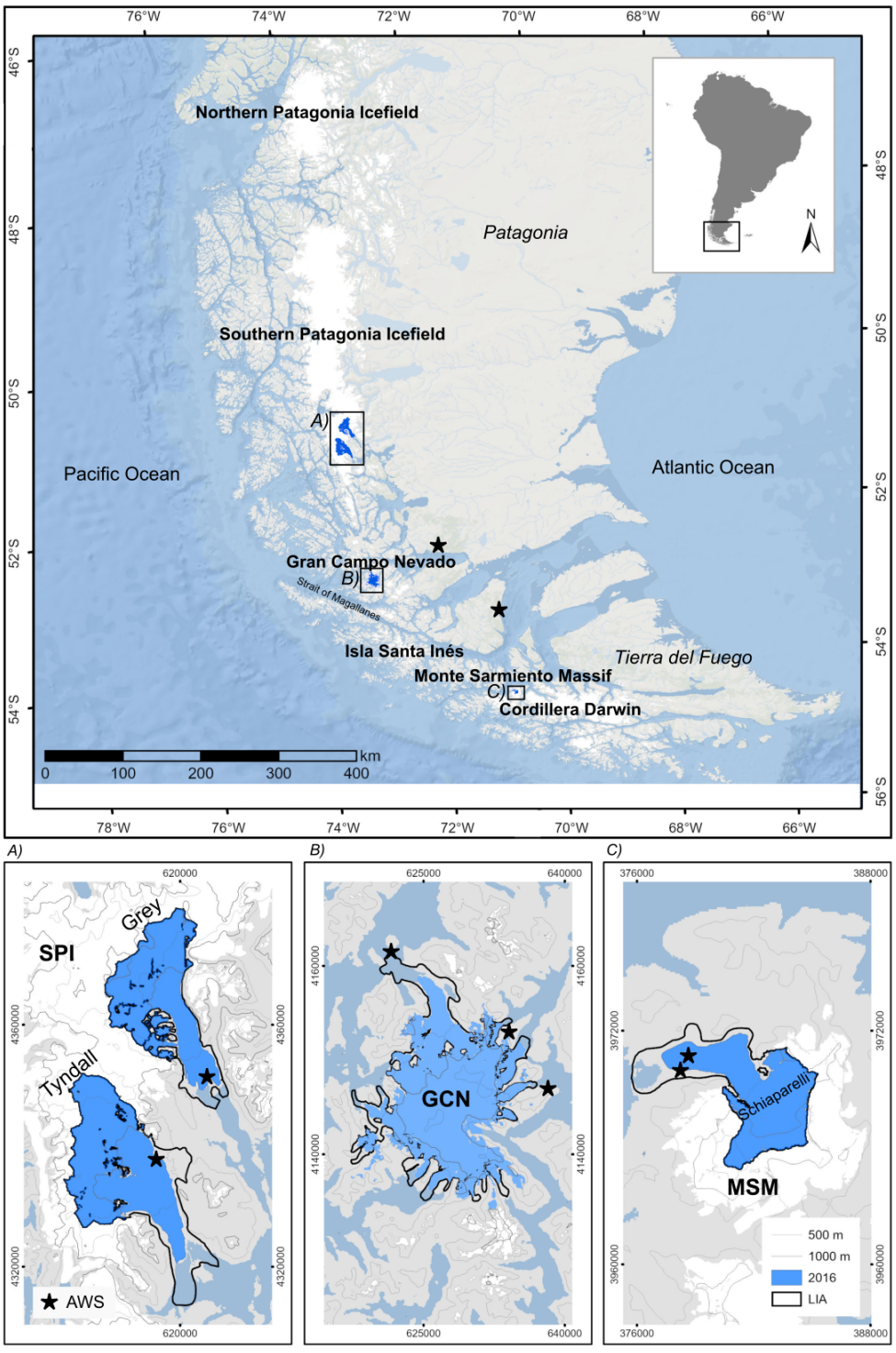

Figure 2.1: Location of the glaciated areas in Southernmost South America in 2016. Detailed investigations described in this thesis have been carried out at Grey Glacier and Tyndall Glacier (A) at the Southern Patagonia Icefield (SPI), Gran Campo Nevado (GCN) Ice Cap (B), and Schiaparelli Glacier (C) at the Monte Sarmiento Massif (MSM). Glacier outlines are visualized for 2016 and Little Ice Age (LIA) (Meier et al. 2018). The coordinates are in UTM zone 18S (A,B) and in UTM zone 19S in meters (C).

2.3 Study sites in Fuego-Patagonia

Detailed investigations have been carried out at the following three study sites:

- Grey Glacier and Tyndall Glacier at the SPI,
- Gran Campo Nevado Ice Cap,
- Schiaparelli Glacier at the Monte Sarmiento Massif, Tierra del Fuego.

The study sites of Grey Glacier and Tyndall Glacier are two of the major outlet glaciers of the SPI, located at its southeastern part (50.7°S to 51.3°S, 73.5°W to 73.1°W) (Figure 2.1, A). In 2016, glacier areas were estimated to 239.0 and 301.4 km^2, respectively (Meier et al. 2018). The Equilibrium Line Altitude (ELA) is estimated to be 970±50 m a.s.l. for Grey Glacier (De Angelis 2014; Schaefer et al. 2015) and 925±25 m a.s.l. for Tyndall Glacier (Nishida et al. 1995; De Angelis 2014). Grey Glacier calves into a proglacial lake divided into three glacier termini which have shown different retreat and thinning rates over the last decades. According to Davies and Glasser (2012), both glaciers showed similar annual shrinkage of about -0.10% to -0.15% (1970 to 2011), with the period of fastest loss of glacier area spanning from 1986 to 2001.

The Gran Campo Nevado Ice Cap is located in the south of the Muñoz Gamero Peninsula at about 53°S (Figure 2.1, B). The GCN Ice Cap is made up of the main glacier plateau with highest elevations of 1630 m a.s.l. and several individual outlet glaciers, some reaching sea level. Glacier area has changed from 263.2 km^2 in 1870 to 236.9 km^2 in 2011 (Davies and Glasser 2012). In 2016, the glaciated area of GCN Ice Cap was estimated to about 190 km^2 (Meier et al. 2018). The maximum annual precipitation amount was estimated to about 10000 mm at the highest elevations (Schneider et al. 2003) causing a high mass turnover with steep specific mass-balance gradients of the GCN outlet glaciers (Weidemann et al. 2013; Möller et al. 2007).

Schiaparelli Glacier descends north-west from Monte Sarmiento (54.39° S to 54.45° S, 70.90° W to 70.77° W), at the southwestern tip of Isla Grande de Tierra del Fuego (Figure 2.1, C). The glaciated parts of the Monte Sarmiento Massif have shrunk from 199.3 km^2 in 1870 to 183.1 km^2 in 2011 (Davies and Glasser 2012), in particular, due to the shrinkage of the land-terminating glaciers. The Schiaparelli Glacier lost an area of about 24% from 31.8 km^2 in ∼1870 to 24.3 km^2 in 2016 (Meier et al. 2018). The glacier calves into a moraine-dammed proglacial lake which formed after glacier recession in the 1940s (Meier et al. 2019). The existence of three terminal moraine ridges at Schiaparelli Glacier implies a glacial recession without distinct readvances since 1749±5 CE (Meier et al. 2019).

2.4 Field work

Field work was carried out tree times between 2015 and 2016 at both study sites Grey Glacier and Schiaparelli Glacier in cooperation with all partners of the GABY-VASA project to install and maintain devices as well as to collect meteorological, glaciological, dendrochronological, and hydrological data (Table 2.1).

Table 2.1: Field work at Grey Glacier and Schiaparelli Glacier as part of the GABY-VASA project at which the author of this thesis has participated.

Study site	Date	Work
Grey	March 2015	Installation of one AWS close to the glacier margin
		Installation of one basic AWS (Minikin sensor) on the glacier
		Installation of one time lapse camera near the calving front
		DGPS point measurements within the camera field of view
		Installation of ablation stakes
	September 2015	Data collection and maintenance of the AWS
		Data collection and maintenance of the time lapse camera
		Reading and re-installation of ablation stakes
		Assistance at tree sampling close to the Campamento Paso
		Removing the basic AWS located on the glacier
		Installation of one basic AWS close to the Campamento Paso
	October 2016	Data collection and maintenance of the AWS
		Data collection and maintenance of the time lapse camera
		Reading and re-installation of ablation stakes
		Removing the basic AWS close to the Campamento Paso
Schiaparelli	September 2015	Installation of one AWS close to the glacier margin
		Installation of two basic AWSs (Minikin sensor)
		Installation of new ablation stakes
		Installation of two time lapse cameras
		Assistance at ice thickness measurements
		Moss sampling
	April 2016	Maintenance and data collection of the AWS and basic AWSs
		Reading and re-installation of ablation stakes
		Installation of one water level sensor at the outflow of the glacier lake
		DGPS point measurements within the field of view of both cameras
		Data collection and maintenance of the time lapse cameras
		Removing the time lapse camera at the glacier margin
		Sampling of wood from tree trunks buried in moraine deposits
	October 2016	Maintenance and data collection of the AWS and the basic AWS uphill
		Removing the basic AWS at the beach site
		Reading and re-installation of ablation stakes
		Sampling of wood from tree trunks buried in moraine deposits

The data of the AWSs, ablation stake readings, and lake water level measurements are used as calibration and validation datasets in this thesis. The ice thickness measurements and the samples of wood from tree trunks buried in moraine deposits were used in further research studies of the GABY-VASA project (Gacitúa et al. 2020; Meier et al. 2019).

At Grey Glacier, one AWS manufactured by Campbell Scientific Ltd. (United Kingdom) was installed close to the glacier margin at 50.98°S, 73.22°W at 229 m a.s.l. (Figure 2.2, A) during the field campaign in March 2015. Since then, the AWS measures hourly incoming solar radiation, air temperature, relative humidity, precipitation, wind speed and wind direction (Table 2.2).

One basic AWS (Minikin sensor) manufactured by EMS Brno measured incoming solar radiation, air temperature, and relative humidity between March 2015 and September 2015 on the eastern ablation area of Grey Glacier (50.97°S, 73.22°W) (Figure 2.2, B). A second Minikin sensor was running between September 2015 and October 2016 close to the trekking path east of Grey Glacier at 50.96°S, 73.20°W at about 430 m a.s.l..

A self-constructed time lapse camera was placed on the Nunatak, taking pictures of the middle calving front of Grey Glacier every two hours since March 2015 (Figure 2.2, C). Main components of the self-constructed time lapse cameras are a Canon EOS 1200 D camera with standard lens, a timer, a Lithium battery pack ($\sim$ 12000 mAh, 7.4 V), and a modified Pelicase 1300 enclosure (Figure 2.2, D). Time series of the time lapse camera are arranged to short movies which can be viewed online [1].

The network of ablation stake measurements at Grey Glacier was renewed and extended during the GABY-VASA project. Three ablation stakes were installed on the western front of Grey Glacier considering different surface textures (Figure 2.2, E). Ablation stakes at both Grey and Schiaparelli Glacier consisted of 8 connected plastic tubes, each 1.5 meter long. They were placed in vertical boreholes drilled using a steam-driven Heucke Ice Drill (Heucke 2003). During the following field campaign, changes in glacier surface height relative to stake length are measured. The surface height changes are then calculated into ablation (m w.e.) by considering an ice density of 917 kg m^{-3}.

Table 2.2: Sensor information on the automatic weather station (Figure 2.2, A) installed in March 2015 at Grey Glacier as part of the GABY-VASA project.

Parameter	Sensor type	Accuracy	Sensor height
Incoming solar radiation	Campbell CS300	5% daily total	127 cm
Air temperature	Campbell CS215	0.4	180 cm
Rel. Humidity	Campbell CS215	2%	180 cm
Wind speed and direction	Young wind monitor 05103	0.3 m s^{-1}	224 cm
Precipitation	Young RM52203 (unheated)	3% up to 50 mm hr^{-1}	105 cm

1 https://www.geographie.hu-berlin.de/de/abteilungen/klimatologie/forschung/gaby-vasa-fortsetzung

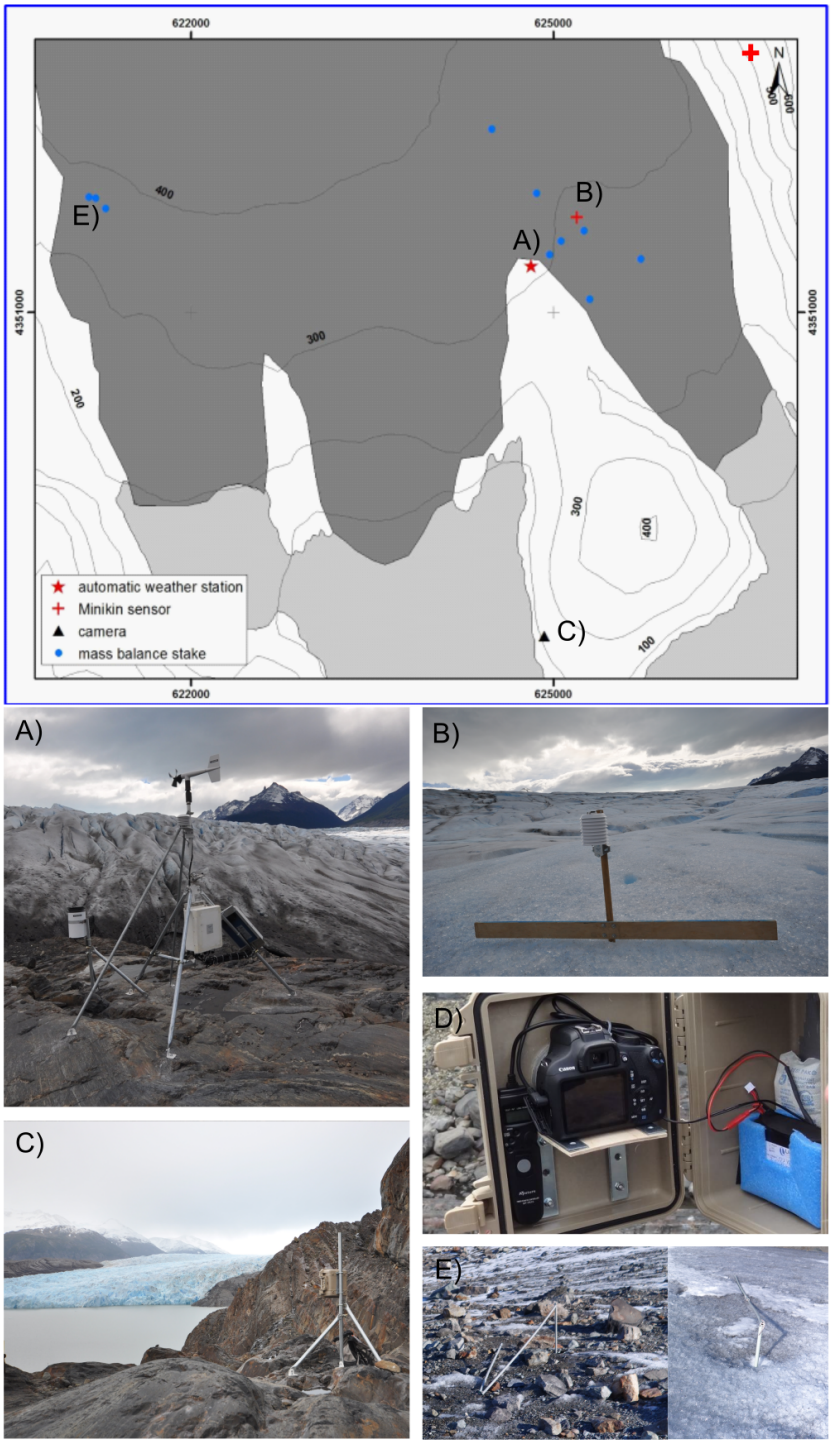

Figure 2.2: Locations and pictures of installed devices at Grey Glacier as part of the GABY-VASA project. A) Automatic weather station, B) Minikin Sensor, C) self-constructed time lapse camera, D) components of the time lapse camera (picture is provided by Christoph Schneider), and E) installed ablations stakes. Coordinates are given in UTM 18S in meters. Contour lines are visualized every 100 m.

Field work at Schiaparelli Glacier was carried out three times between 2015 and 2016 as part of the GABY-VASA project in particular to install and maintain one AWS close to the glacier margin, two basic AWSs in the surrounding of the glacier, two time lapse cameras, and one water level sensor.

The AWS was placed on the southern side of the glacier close to the glacier margin at 54.4°S, 70.87°W at 92 m a.s.l. (Figure 2.3, A), measuring hourly air temperature, relative humidity, incoming solar radiation, precipitation, wind speed, and wind direction since September 2015.

Two basic AWSs (Minikin sensor) were located in the surrounding of the glacier, one at the beach of the fjord close to the river mouth of the river that drains the proglacial lake of Schiaparelli Glacier at 54.42°S, 70.92°W at 4 m a.s.l., and one close to the tree line at 54.41°S, 70.88°W at 243 m a.s.l..

Two self-constructed time lapse cameras were installed at Schiaparelli Glacier during the field campaign in September 2015 (Figure 2.4). One time lapse camera was used to take pictures of the calving front every two hours, similar to the time lapse camera at Grey Glacier[2]. Differential Global Positioning System (DGPS) points were also measured within the camera field of view and along the glacier margin combined with photos in order to create georeferenced time lapse pictures. A second time lapse camera was placed south of the glacier margin in order to take pictures of the glacier area where two ablation stakes were installed (Figure 2.4, D-F). The stakes were marked every 0.5 m. The resulting image time series provided a higher temporal resolution of glacier melt compared to the manual semi-annual readings of ablation stakes.

Between April 2016 and March 2017 a HOBO water-level pressure sensor (Hydro sensor, Figure 2.3) was installed close to the outflow from the proglacial lake Lago Azul. The sensor recorded the water level and temperature of the lake at hourly resolution.

Table 2.3: Sensor information on the automatic weather station (Figure 2.3, A) installed in September 2015 at Schiaparelli Glacier as part of the GABY-VASA project.

Parameter	Sensor type	Accuracy	Sensor height
Incoming solar radiation	Campbell CS300	5% daily total	194 cm
Air temperature	Campbell CS215	0.4	193 cm
Rel. Humidity	Campbell CS215	2%	193 cm
Wind speed and direction	Young wind monitor 05103	0.3 m s^{-1}	234 cm
Precipitation	Young RM52203 (unheated)	3% up to 50 mm hr^{-1}	128 cm

2 https://www.geographie.hu-berlin.de/de/abteilungen/klimatologie/forschung/gaby-vasa-fortsetzung

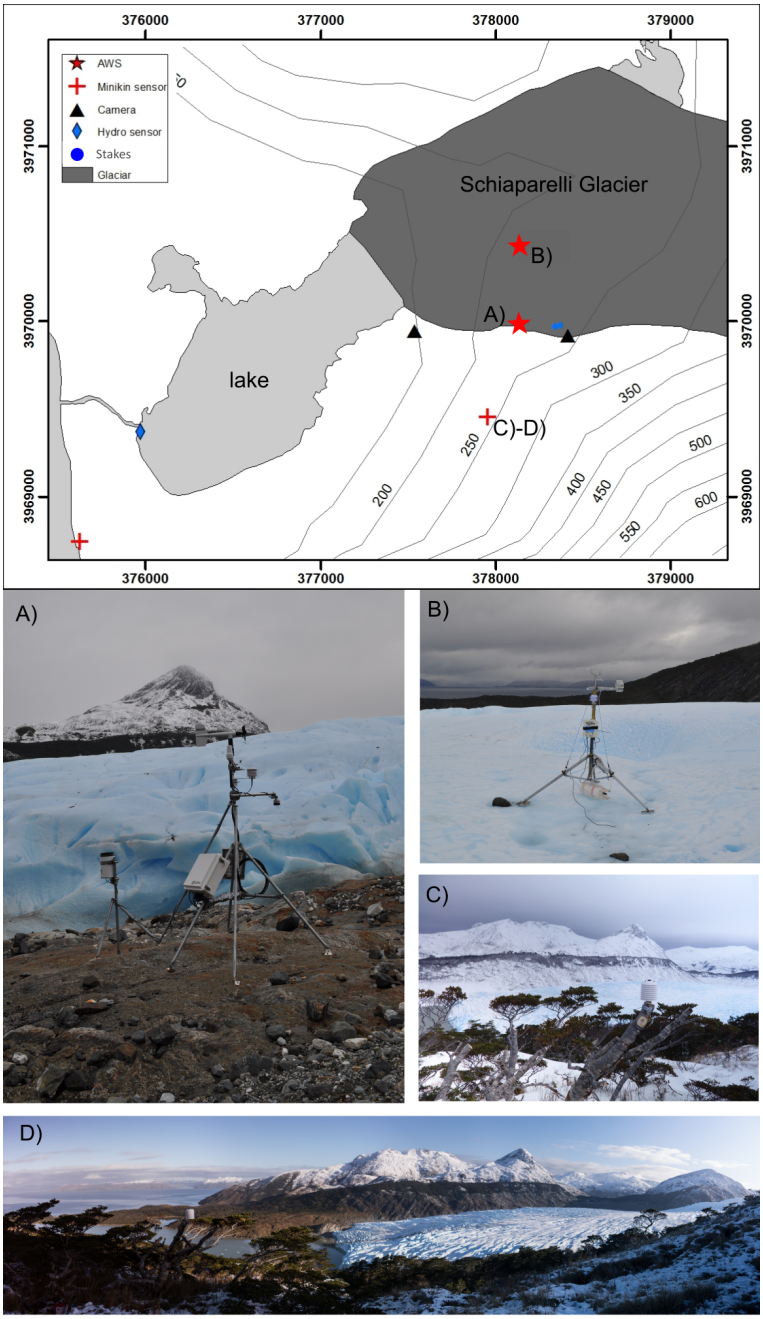

Figure 2.3: Locations and pictures of installed devices at Schiaparelli Glacier used in this thesis. A) Automatic weather station installed on rock, B) automatic weather station installed on the glacier by Universidade Federal do Rio Grande, C) and D) basic AWS (Minikin sensor) close to the tree line. Coordinates are given in UTM 19S in meters. Contour lines are visualized every 50 m.

Figure 2.4: Pictures related to the installed time lapse cameras at Schiaparelli Glacier during field work as part of the GABY-VASA project. The locations of devices are provided in Figure 2.3. A) Self-constructed time lapse camera located at the calving front, B) components of the time lapse camera (picture is provided by Christoph Schneider), C) self-constructed time lapse camera located at the southern glacier margin, D) DGPS measurements combined with pictures within the camera field of view (picture is provided by Christoph Schneider) E) picture taken by the time lapse camera with ablations stakes marked in red, and F) installation of one of the ablation stakes installed in the camera field of view of the camera shown in D using a steam drill.

CHAPTER 3

Recent climate variability across the Gran Campo Nevado Ice Cap

The scope of this chapter is the analysis of a 17-year record of meteorological observation across the Gran Campo Nevado Ice Cap. After a statistical analysis of the time-series focusing on means, trends and extremes, the relationships between the in-situ observations and meso-scale weather patterns and large-scale climate modes have been investigated.

My contribution to this paper (Publication 1, A.1) are the design of the study (with co-authors), compilation and processing of weather station data, the statistical analysis of meteorological time series, the definition of methods to detect trends and extremes in meteorological time series, link climate features to meso-scale weather patterns and large-scale indices, interpretation of the results (with co-authors), the visualization of the results in figures (except Fig. 7) and tables, writing the first draft of the manuscript (except 3.2), and incorporating the corrections by co-authors and reviewers.

3.1 Data collection and processing

The time series of four AWSs located at the GCN Ice Cap and one conventional weather station (WS) at Punta Arenas (Figure 3.1) in Chile have been processed and statistically analyzed. The similarly equipped stations measure air temperature, air humidity, precipitation, solar radiation, wind speed and wind direction. Data had to be pre-processed due to substantial data gaps caused by failures of power supply or sensors. The harsh weather conditions including strong winds also cause additional uncertainty in the precipitation measurements using tipping buckets. Values of precipitation amounts therefore need to be interpreted with caution. The quality of the time series was further assured by performing basic quality integrity and outlier checks (Durre et al. 2010).

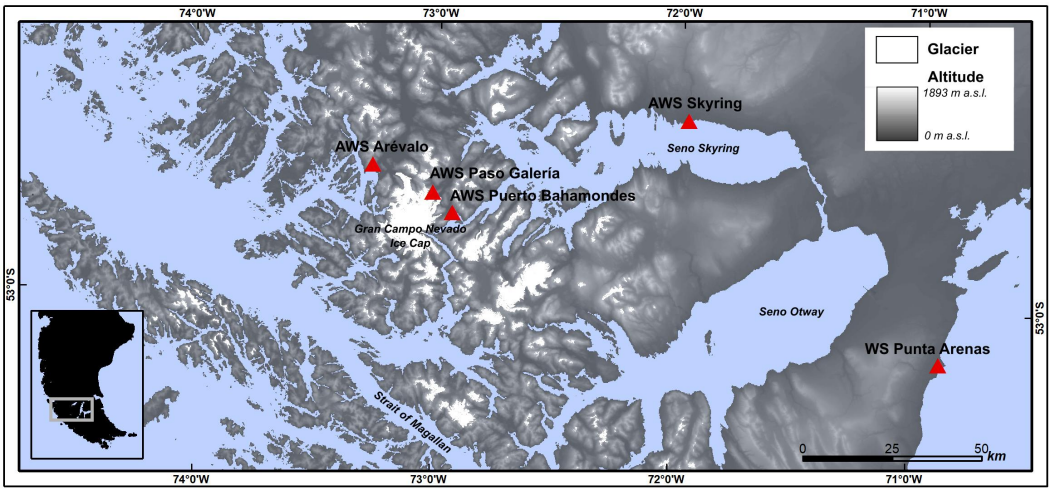

Figure 3.1: Location of four automatic weather stations (AWS) at the Gran Campo Nevado Ice Cap and the weather station (WS) at Punta Arenas. Glacier outlines are based on the Randolph Glacier Inventory 6.0 (RGI-Consortium 2017). Figure adapted from Publication 1 (A.1).

3.2 Spatial variability of climate features

The statistical analysis of the time series show spatial differences in air temperature, precipitation, and wind characteristics with increasing distance to the GCN Ice Cap and the Pacific Ocean. The influence of the Pacific Ocean leads to maritime climate conditions with lower amplitudes of the annual temperature cycle and less days with frost and ice at AWS Arévalo and AWS Puerto Bahamondes compared to stations AWS Skyring and WS Punta Arenas, with the latter two located further inland. Towards the east the mean annual air temperature increases to 6.6°C (Table 3.1). The coldest temperature regime with the lowest mean of daily maximum temperatures of +5.2°C and minimum temperatures of +2.4°C is found at AWS Paso Galería because of the highest altitude and its proximity to the ice cap. The influence on the air temperature distribution across the GCN mountain range due to orographic effects can also be detected in the spatial distribution of mean daily maximum and minimum air temperatures and air temperature range. The absolute extremes of daily air temperature range increases on the lee-side of the GCN Ice Cap from -8.9°C and +20.4°C at AWS Paso Galería to -11.3°C and +25.8°C at AWS Skyring during the observation period 2000 to 2016.

Within only tens of kilometers, precipitation amounts across the GCN Ice Cap differ strongly. From the westside to the eastside of GCN Ice Cap, mean annual precipitation (2008 to 2016) increases from ~3800 mm (AWS Arévalo) to ~6100 mm (AWS Paso Galería), while it decreases on the lee-side to ~4000 mm (AWS Puerto Bahamondes). Within a

Table 3.1: Pertinent data of the weather station and automatic weather stations used in this study. Annual means of daily mean (T), maximum (TX) and minimum (TN) air temperature, precipitation (P), wind speed (v), and wind direction (dir). Mean values are calculated based on the available observation period between 2000 and 2016. Table adapted and extended from Publication 1 (A.1).

Name	Latitude/Longitude	Altitude	T	TX	TN	P	v	dir
Arévalo	52°41'S/73°16'W	58 m	5.8	7.1	4.4	3813	4.7	158
Paso Galería	52°45'S/73°01'W	383 m	3.8	5.2	2.4	7513	5.1	245
Puerto Bahamondes	52°48'S/72°56'W	26 m	6.0	8.8	3.9	4057	3.1	255
Skyring	52°33'S/71°58'W	8 m	6.6	9.7	3.2	803	3.7	268
Punta Arenas (J.S.)	53°08'S/70°53'W	6 m	6.6	10.5	2.9	565	4.5	270

distance of about 80 km, precipitation sharply drops to ~790 mm at AWS Skyring and ~570 mm at WS Punta Arenas. The large number of days with precipitation amounts larger than 20 mm (160 in 2003 at AWS Paso Galería) and the maximum length of wet spells (61 consecutive days in 2006 at AWS Paso Galería), underscore the year-around wet conditions at the GCN Ice Cap. At AWS Skyring and WS Punta Arenas, the lengths of wet spells are substantially smaller while the lengths of dry spells are much longer compared to the three AWSs at the GCN Ice Cap.

Westerlies prevail year-around at the GCN Ice Cap with mean annual wind speeds ranging from 3.1 m s^{-1} (AWS Puerto Bahamondes) to 5.1 m s^{-1} (AWS Paso Galería). Prevailing north-west winds cause the highest mean of daily mean and maximum wind speeds of 5.1 m s^{-1} and 13.4 m s^{-1} at AWS Paso Galería. During winter wind speeds decrease at all stations but AWS Arévalo which is located closest to the Pacific Ocean.

3.3 Trend detection in air temperature records

Annual and seasonal trends in annual mean, minimum and maximum air temperature are detected using the non-parametric Mann-Kendall (MK) and Sen slope estimator (SSE) trend test. The combined MK and SSE test has been frequently used to quantify the significance and magnitude of trends in climatic and hydrological time series (Onyutha et al. 2016; Kisi and Ay 2014; Gocic and Trajkovic 2013; Hamed 2008).

Time series of annual mean air temperature at AWS Paso Galería and AWS Puerto Bahamondes show a significant trend of +0.05°C a^{-1} and +0.02°C a^{-1} at the 90% level. Positive trends of seasonal mean air temperature are apparent during the winter months at AWS Puerto Bahamondes and WS Punta Arenas. At AWS Paso Galería, we detected an increase of +0.31°C a^{-1} in annual minimum air temperature between 2000 and 2016 which in particular occurs during spring, winter and fall. Upward trends of the annual minimum air temperature during spring and fall can also be observed at the AWSs located at the

GCN Ice Cap. A downward trend in the annual maximum air temperature is detected for all investigated AWSs, with the largest trend of -0.24°C a^{-1} (2000 and 2016) occurring at AWS Paso Galería.

3.4 Link between climate features and mesoscale weather patterns

Ten major types of synoptic weather patterns - later arranged into 5 classes - have been classified for Southernmost Patagonia based on the automated classification map-pattern scheme by Lund (1963) using the ERA-Interim daily mean sea level pressure reanalysis data for the period 1979-2016 as input.

Southwesterly, northwesterly or westerly airflow prevail on 68% of all days in Southernmost Patagonia. These wind patterns form during synoptic weather types with distinct low-pressure cells in the Weddell Sea (type 2 and type 5) or Bellingshausen Sea (type 1, type 3, and type 9). High pressure cells over the southern Pacific Ocean (type 4, type 7, and type 10) or southern Atlantic Ocean (type 6 and type 8) determine the weather patterns during the rest of the year. Anticyclonic circulation patterns account for more than 40% of all days during the austral winter, leading to reduced wind speeds and lower daily air temperatures at the GCN Ice Cap compared to cyclonic weather types in the same season. Strong zonal westerly air flow and large positive air temperature anomalies, which come along with synoptic weather type 1, occur 30% of the year. The impact of strong westerlies on air temperature anomalies is largest during the austral fall. Air temperatures tend to drop at the stations located close to GCN Ice Cap on days with southwesterly airflow (class 2 & 5), while air temperatures rise during northwesterly airflow (class 3 & 9).

Table 3.2: Mean annual and seasonal frequency of synoptic weather types and classes (%) between 1979 to 2016 and between 2000 to 2016. Table is adapted and modified from Publication 1 (A.1).

	Frequency of synoptic types (%)										**Frequency of synoptic classes (%)**					
1979-2016	*1*	*2*	*3*	*4*	*5*	*6*	*7*	*8*	*9*	*10*	*1*	*2&5*	*3&9*	*4&7*	*6&8*	*10*
Mean	30	13	11	9	9	7	7	5	4	4	30	22	16	16	12	4
summer	38	15	8	7	11	3	10	1	4	2	38	26	12	17	4	2
fall	26	12	14	7	10	9	7	5	6	5	26	22	19	14	14	5
winter	20	12	13	10	9	8	5	9	5	8	20	21	19	15	17	8
spring	34	14	10	12	6	9	6	4	3	3	34	20	13	18	12	3
2000-2016	*1*	*2*	*3*	*4*	*5*	*6*	*7*	*8*	*9*	*10*	*1*	*2&5*	*3&9*	*4&7*	*6&8*	*10*
Mean	31	13	11	9	9	7	7	4	4	4	31	23	15	16	12	4
summer	40	16	6	8	11	4	10	1	2	2	40	27	8	18	5	2
fall	27	11	15	7	12	9	7	4	5	4	27	23	19	14	13	4
winter	21	12	14	10	9	8	6	8	6	7	21	20	21	15	16	7
spring	34	15	9	11	6	9	5	4	3	3	34	21	12	17	13	3

The orographic induced uplift of the humid air masses from west and southwest is enhanced during synoptic weather types 1, 2, and 5, leading to year-around positive precipitation anomalies at GCN Ice Cap. More than 80% of daily precipitation occurs during westerly airflow, while precipitation amounts decrease significantly during high-pressure influence. During west and southwesterly airflow, foehn-type weather conditions with cloud dispersal often occur due to the subsidence of air masses on the lee-side of the Cordillera. With increasing distance to the Pacific Ocean, the precipitation amount is less influenced by synoptic weather types with west and south-westerly wind patterns.

3.5 Teleconnection to El Niño Southern Oscillation and Antarctic Oscillation

The Oceanic Niño Index (ONI) and the Antarctic Oscillation Index (AAOI) provided by the National Oceanic and Atmospheric Administration are chosen to link in-situ observations to the large-scale climate modes El Niño Southern Oscillation (ENSO) and Antartctic Oscillation (AAO). The ONI identifies El Niño and La Niña events in the tropical Pacific which affects the sea surface temperature along the west coast of the Southern Andes. Positive or negative phases of the AAO come along with strengthening or weakening of the westerlies which again affect the regional climate variability.

The strengthening of the westerlies during positive AAO phases causes an increase of mean monthly air temperatures by up to +20% (+0.6°C) at the GCN Ice Cap and by up to +13% (+0.9°C) at WS Punta Arenas compared to the monthly average (2000 - 2016) (Table 3.3). Positive precipitation and wind speed anomalies can also be detected at all stations located at the GCN Ice Cap. During negative phases of AAO high-pressure influence (class 10) is intensified, leading to colder conditions with up to 23% (-1.0°C) below the average (AWS Paso Galería) in Southernmost Patagonia. Monthly precipitation range from -16% to +8% at AWS Paso Galería, -9% to +10% at AWS Puerto Bahamondes and -6% to +10% at AWS Seno Skyring between negative and positive AAO phases (Table 3.3).

The impact of ENSO on air temperature and precipitation anomalies as well as on the variability of synoptic weather patterns are in general weak, which is consistent with previous studies (Schneider and Gies 2004; Garreaud et al. 2009). Only one significant negative correlation of -0.26 at AWS Puerto Bahamondes can be identified in case of precipitation anomalies. Monthly precipitation decreases by -9% during El Niño events at AWS Puerto Bahamondes compared to the monthly mean (2000 - 2016) while it increases by +9% during La Niña events (Table 3.3). An intensified low-pressure cell over the Weddell Sea causing southwesterly air flow (class 2 & 5) is enhanced during stronger El Niño events, while northwesterly airflow (class 3 & 9) occurs less frequently. During La

Table 3.3: Deviations (%) of monthly mean air temperature (T), precipitation (P) and wind speed (v) from the monthly means (2000-2016) during positive (ONI $\geq$ 0.5) and negative (ONI $\leq$ -0.5) ENSO (O+,O-) and AAO (A+,A-) phases. Results are listed for different time lags (T0, no lag up to T+3, 3 months of lag) for AWS Paso Galería (PG), AWS Puerto Bahamondes (BH), AWS Skyring (SR), and WS Punta Arenas (PA). Table adapted and modified from Publication 1 (A.1).

		PG		**BH**		**SR**		**PA**		**PG**		**BH**		**SR**		**PA**	
		O+	*O-*	*O+*	*O-*	*O+*	*O-*	*O+*	*O-*	*A+*	*A-*	*A+*	*A-*	*A+*	*A-*	*A+*	*A-*
T	*T0*	-4	8	12	2	10	11	7	13	20	-23	16	-17	14	-13	13	-10
	T+1	4	6	20	5	21	12	14	13	6	10	7	-2	9	-1	5	2
	T+2	5	1	22	5	26	9	15	9	3	15	4	1	7	1	1	9
	T+3	4	-6	18	-1	24	1	11	3	-1	13	3	3	3	2	-2	10
P	*T0*	7	-13	-9	9	-6	-10	-4	-9	8	-16	10	-9	10	-6	-8	1
	T+1	11	-5	-5	15	-4	-11	-4	-9	-7	18	-1	8	0	0	-2	-7
	T+2	14	0	1	21	-2	4	-2	2	-6	3	9	0	9	-4	5	-11
	T+3	8	-1	1	14	0	6	8	1	-22	14	-4	-5	-1	-3	-2	-8
v	*T0*	-3	0	2	3	4	4	7	-5	11	-13	11	-10	3	-1	3	-1
	T+1	0	0	3	4	4	6	5	-3	6	-1	4	-3	1	2	5	2
	T+2	3	1	3	5	4	6	3	-2	9	-7	3	-1	2	-1	5	5
	T+3	2	0	1	4	1	4	1	-4	3	-2	-2	3	-2	3	2	7

Niña events, the frequency of north-westerly advection of humid air masses (class 3 & 9) rises, while synoptic weather types with high-pressure influence tend to decrease (classes 6 & 8 and 10). Intensified westerlies (+27%) and higher precipitation amounts at the GCN Ice Cap can be associated with strong La Niña events.

CHAPTER 4

Recent glacier mass changes of Grey Glacier and Tyndall Glacier at the Southern Patagonia Icefield

This chapter deals with the contrasting pattern of observed glacier retreat and positive modeled climatic mass balance of two neighboring glaciers Grey and Tyndall at the SPI. The main focus lies on the discussion and explanation of the chosen modelling approaches to simulate glacier surface energy fluxes and climatic mass balance processes and to derive atmospheric forcing data, and their impacts on the simulation results, and on the contribution of climatic mass balance variability to the overall glacier mass loss.

My contribution to this paper (Publication 2, A.2) are the design of the study (with co-authors), the collection of meteorological and glaciological data (with co-authors), statistical downscaling of ERA-Interim Reanalysis data, processing of MODIS cloud cover data, simulation of climatic mass balance using COSIMA including uncertainty estimations, calculation of frontal ablation amounts, analysis and interpretation of the results (with co-authors), creating figures and tables, writing the first draft of the manuscript, and incorporating the corrections by co-authors and reviewers.

4.1 Data and methods

Modelling of glacier accumulation and ablation in mass balance models mostly employs statistical downscaling methods to overcome the gap in spatial resolution between coarse-resolution atmospheric data and the requirements for local glaciological impact studies. In southern Patagonia where orographic precipitation influences spatial patterns of mass balance, the application of orographic precipitation models seems to be a promising approach to estimate accumulation fields (Weidemann et al. 2013). The linear model of orographic precipitation (OPM) of Smith and Barstad (2004) estimates precipitation resulting from forced orographic uplift of air masses over a mountain assuming stable and saturated atmospheric conditions. The model estimates the condensation rate by the terrain-induced vertical air velocity, the horizontal wind speed and advection of water vapor, and includes effects of airflow dynamics and downslope evaporation as well. Spatial patterns of surface

air temperature are determined by using vertical gradients. Incoming shortwave radiation is derived from a radiation model after Kumar et al. (1997) that computes clear-sky direct and diffuse shortwave radiation and considers cloud cover effects by means of observations of incoming solar radiation at an AWS (Figure 4.1), and the MODIS/Terra Snow Cover Daily L3 Global 500m Grid (MOD10A1) cloud cover dataset (Hall and Riggs 2016). At both Grey Glacier and Tyndall Glacier, similarly equipped AWSs are installed (Figure 2.1, Figure 4.1). In-situ observations are used to downscale ERA-Interim reanalysis data (Dee et al. 2011) of air temperature and incoming solar radiation using quantile mapping before simulating spatial fields. Observed and downscaled time series of air temperature and solar radiation show strong correlations (r^2=0.8) for both stations. Precipitation measurements at Grey Glacier are used to calibrate and validate the simulated precipitation amounts by the OPM. Observed and simulated precipitation amounts correlate strongly (r^2=0.7). Modeled orographic precipitation by the OPM accounts for about 41% of the total precipitation amount at AWS Grey which is located on the lee-side of the SPI.

4.2 Surface energy and climatic mass balance model

Surface energy and climatic mass balance is simulated by implementing the open-source 'COupled Snowpack and Ice surface energy and MAss balance model' COSIMA (Huintjes et al. 2015), in which the energy balance at the glacier surface is coupled with glacier subsurface processes. The model was designed and validated by Huintjes et al. (2015) and further updated and published as the 'COupled Snowpack and Ice surface energy and mass balance model in PYthon' COSIPY by Sauter et al. (2020). The following energy fluxes and parameters that contribute to the surface energy budget or impact the energy available for surface melting Q_{melt} are considered in the energy balance model of COSIMA: the shortwave incoming radiation SW_{in}, the albedo α, the incoming LW_{in} and outgoing longwave radiation LW_{out}, the sensible Q_{sens} and the latent heat flux Q_{lat} and, the ground heat flux Q_g. In this study the energy balance model is extended by the heat flux of liquid precipitation Q_{liq} due to the significant amount of liquid precipitation in the ablation area of Patagonian glaciers. Ablation occurs due to sublimation, evaporation, subsurface melt, and surface melt. Turbulent heat fluxes are calculated based on the the bulk aerodynamic method (Oerlemans 2001) between the surface and two meters above ground by means of air temperature, relative humidity and wind speed. The subsurface model part consists of a defined number of layers, where each is characterized by a temperature, density and liquid water content.

During the calibration, COSIMA was driven by varying parameters like model domain depth, layer depth, initial temperature profile, and albedo values to achieve the best model

results at the locations of measured mass balance at each glacier (Figure 4.1). The RMSE between best model fit and observed values is ±0.53 m w.e. for Grey Glacier and ±0.64 m w.e. for Tyndall Glacier. The uncertainties in COSIMA are estimated by considering uncertainties in the spatial distribution of air temperature and solid precipitation, which are mainly due to the lack of observations in the accumulation areas of the glaciers. The uncertainty assessment of glacier-wide climatic mass balance (CMB) results in a standard deviation of ±0.52 m w.e. a^{-1} for Grey Glacier and ±0.54 m w.e. a^{-1} for Tyndall Glacier.

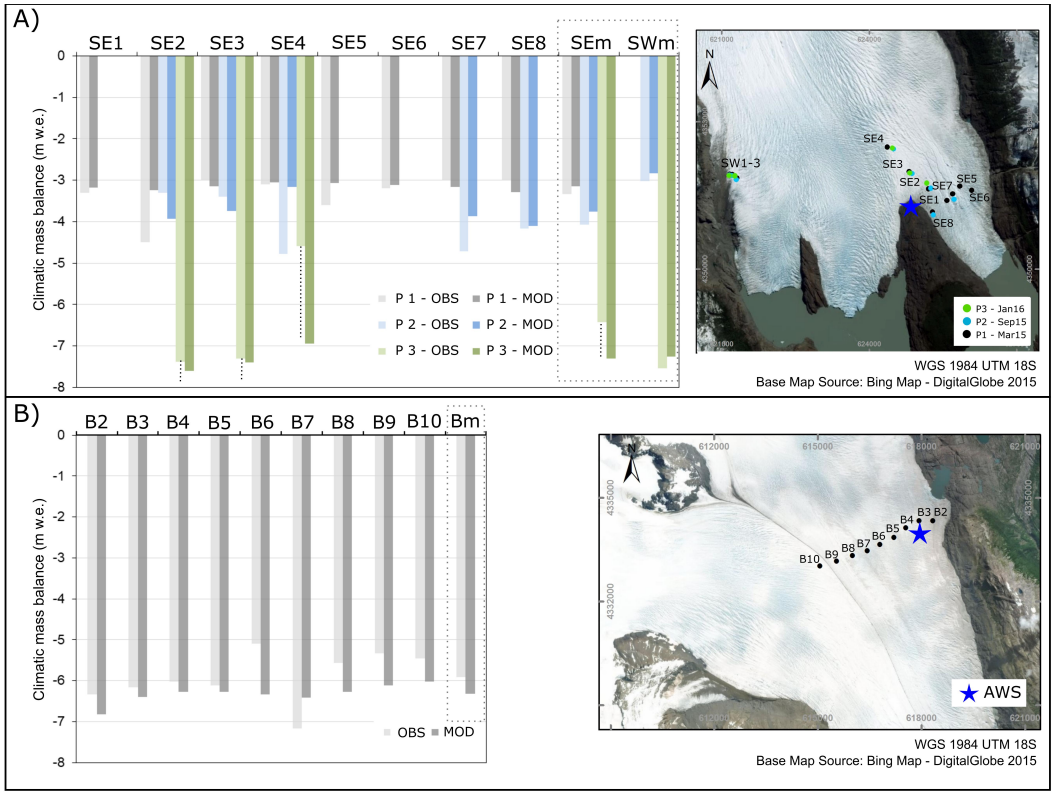

Figure 4.1: Comparison of modeled and observed climatic mass balance at Grey Glacier and Tyndall Glacier by means of ablation stake data. A) Measurements at Grey Glacier were carried out three times: from January 2015 to March 2015 (P1), March 2015 to September 2015 (P2), and September 2015 to January 2016 (P3). Observations of ablation are separately averaged at the western SWm and the eastern glacier tongue SEm. The black dashed lines indicate that the observed surface mass balance values represent only minimum values since these stakes completely melted out over the austral summer 2015/16. B) Surface mass balance observations at Tyndall Glacier are available along a transect (B2-B10) from November 2012 to May 2013 (Geoestudios 2013). Bm is the mean of measured ablation. The coordinates of the subset maps are in UTM zone 18S in meters. Figure and description adapted from Publication 2 (A.2).

4.3 Characteristics of the glacier climatic mass balance between 2000 and 2016

The glacier-wide mean annual CMB is positive for both Grey Glacier and Tyndall Glacier, with +0.86±0.52m w.e. a^{-1} and +0.41±0.54m w.e. a^{-1} between 2000 and 2016. The simulated inter-annual variations of CMB are high, ranging from -2.6±0.54m w.e. a^{-1} to +3.6±0.54m w.e. a^{-1} at Tyndall Glacier and from -1.3±0.52m w.e. a^{-1} to +2.9±0.52m w.e. a^{-1} at Grey Glacier (Figure 4.2). The CMB of Tyndall Glacier is negative in 7 out of 16 mass balance years as a result of above average air temperature and incoming solar radiation anomalies combined with low amounts of solid precipitation (Figure 4.2). Surface melt and the amount of solid precipitation mainly control the climatic mass balance. Main sources of melt energy at the glacier surface are incoming solar radiation and the sensible heat flux.

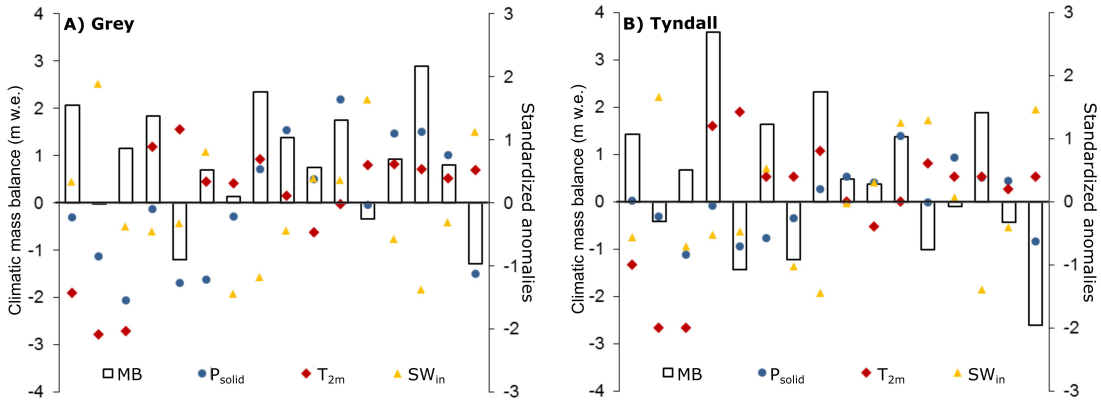

Figure 4.2: Modeled annual climatic mass balance (MB) based on COSIMA simulations and standardized anomalies of solid precipitation P_{solid}, air temperature at 2 m T_{2m}, incoming solar radiation SW_{in} from the mean between April 2000 and March 2016 for A) Grey Glacier and B) Tyndall Glacier. Figure and description adapted from Publication 2 (A.2).

At Grey Glacier, 4 out of 16 mass balance years show a negative CMB. In the lowest parts of the glaciers, the glacier-wide mean CMB was simulated to -11.9±2.1m w.e. a^{-1} at Grey Glacier and to -10.9±3.2m w.e. a^{-1} at Tyndall Glacier between 2000 and 2016 (Figure 4.3). In the most elevated part of the glaciers, the modeled CMB reaches values of up to +14.7 m w.e. (Tyndall Glacier) in single mass balance years. The modeled mean ELA of 960± 70 m a.s.l. at Grey Glacier and 920± 60 m a.s.l. at Tyndall Glacier are similar.

Previous surface mass balance studies simulated larger positive CMB of Grey Glacier and Tyndall Glacier due to the assumed amount of solid precipitation which is significantly

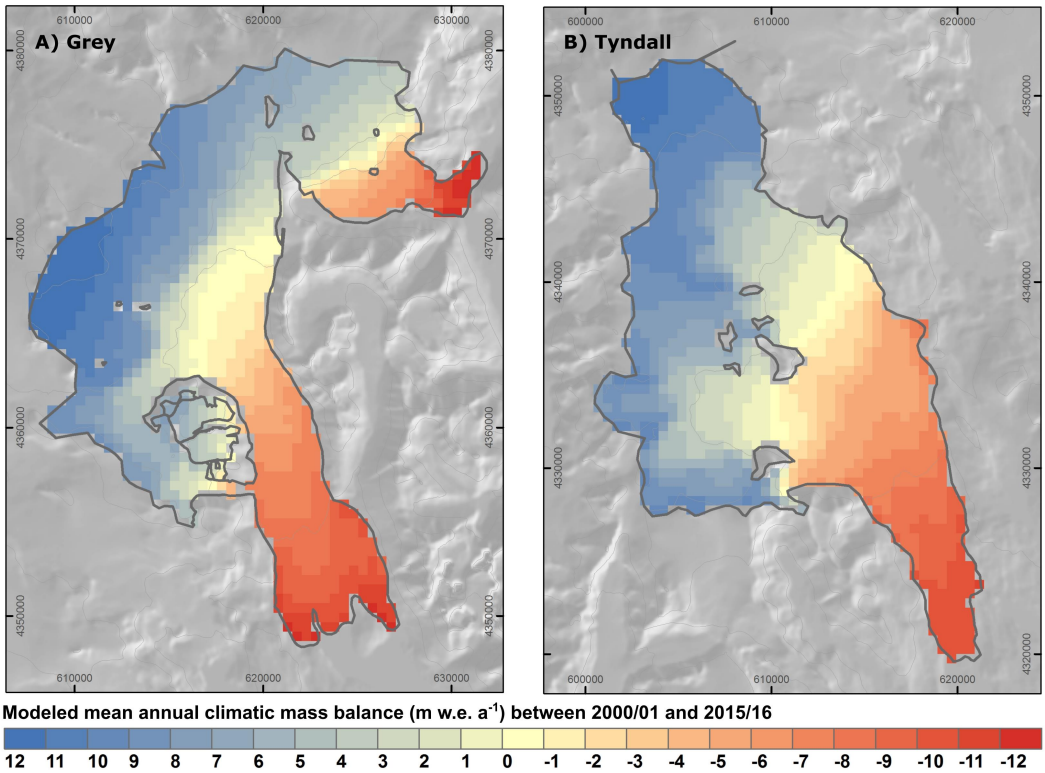

Figure 4.3: Modeled mean annual climatic mass balance in m w.e. a^{-1} based on COSIMA simulations for the study period April 2000 to March 2016 for A) Grey Glacier and B) Tyndall Glacier. The coordinates are in UTM zone 18S in meters. Figure and description adapted from Publication 2 (A.2).

higher in previous studies (Schaefer et al. 2015; Lenaerts et al. 2014; Mernild et al. 2016). Sauter (2020) however indicates that the modeled solid precipitation amount in particular in the most elevated parts of the icefields were overestimated in these studies. Due to the lack of observations across the icefields a final validation still cannot be provided.

4.4 Glacier mass change between 2000 and 2014

The contribution of CMB processes to the observed mass balance of both glaciers, is estimated using COSIMA CMB simulations and geodetic mass balance derived from TanDEM-X/SRTM between 2000 and 2014.

Comparing COSIMA simulations with TanDEM-X/SRTM data, large differences in surface height changes can be detected. COSIMA simulates an overall increase of $+2.34\pm0.65\,\mathrm{m\,a^{-1}}$ for Grey Glacier and $+1.93\pm0.67\,\mathrm{m\,a^{-1}}$ Tyndall Glacier, while ice thinning of $-1.23\pm0.19\,\mathrm{m\,a^{-1}}$ and $-3.04\pm0.24\,\mathrm{m\,a^{-1}}$ is observed for Grey and Tyndall glaciers

based on TanDEM-X/SRTM data. The spatial pattern in surface height differences between CMB and geodetic mass balance derived changes at the different glacier fronts of Grey Glacier result from different ice dynamical effects at each glacier tongue (Figure 4.4). Large differences at the middle part of the glacier indicate a constant ice flow over a longer period from the upper parts to the front to compensate for surface lowering by surface melt processes. In contrast, the outer fronts of the glacier seem to be mainly decoupled from the main ice flow so that surface mass balance processes dominate the overall mass balance. Mass loss due to frontal ablation is estimated as the differences between modeled CMB and the geodetic mass balance which results in -2.07±0.70 m w.e. a^{-1} for Grey Glacier and -3.26±0.82 m w.e. a^{-1} for Tyndall Glacier. These results underline a significantly different contribution of CMB processes to the recent mass loss between both glaciers.

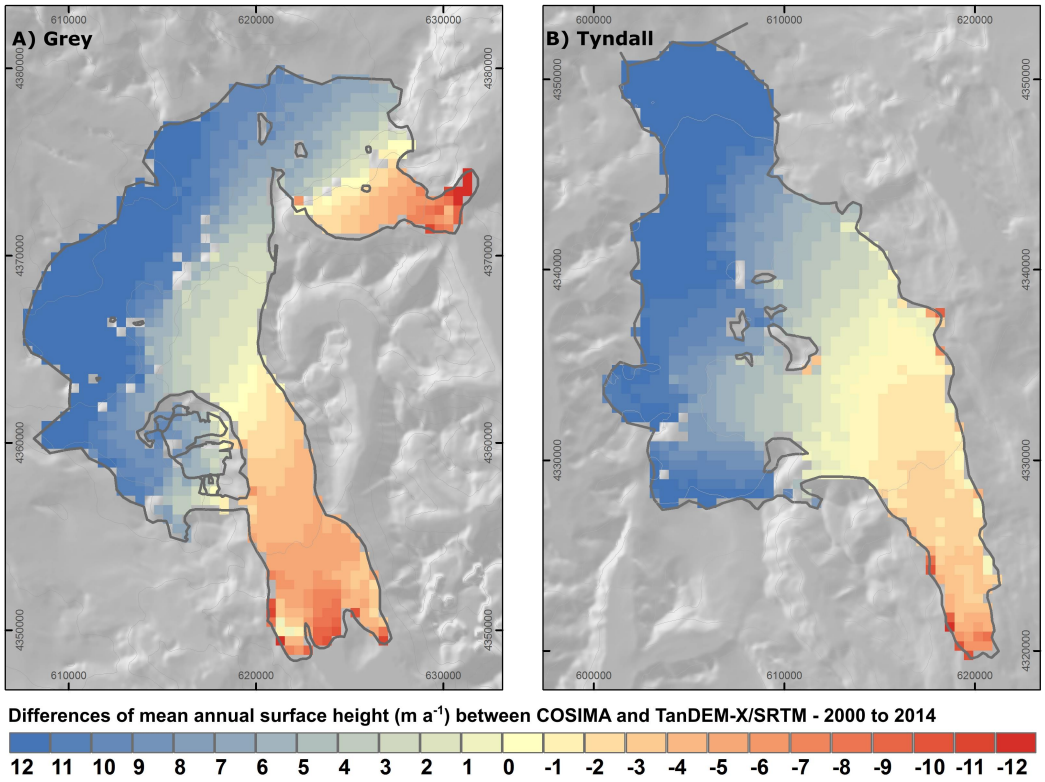

Figure 4.4: Differences between mean annual surface height changes (m) based on COSIMA as the result of climatic mass balance and mean annual surface height changes (m) based on TanDEM-X/SRTM, interpolated to a horizontal resolution of 500 m, between 2000 and 2014 for A) Grey Glacier and B) Tyndall Glacier. The coordinates are in UTM zone 18S in meters. Figure and description adapted from Publication 2 (A.2).

CHAPTER 5

Reconstruction of Little Ice Age climate at Schiaparelli Glacier, Monte Sarmiento Massif

This chapter deals with the detailed investigation of climatic mass balance (CMB) processes of Schiaparelli Glacier at the Monte Sarmiento Massif in Tierra del Fuego for recent and past glacier extents. Simulated energy and CMB components are validated by observations and compared to previous modelling results of Grey Glacier and Tyndall Glacier (Chapter 4) located at the SPI. Meteorological observations and CMB results are further linked to measured lake level changes. Efforts are taken to reconstruct climate during the LIA by simulating steady-state glacier conditions based on the LIA glacier extent.

My contributions to this paper (Publication 3, A.3) are the design of the study (with co-authors), the collection of meteorological and glaciological data (with co-authors), statistical downscaling of ERA-Interim Reanalysis data, the simulation of climatic mass balance using COSIPY, the calculation of LIA glacier heights, the simulation of LIA climate conditions, the analysis and interpretation of the results (with co-authors), visualization of results, writing the first draft of the manuscript, and incorporating the corrections by co-authors and reviewers.

5.1 Data and methods

Two AWSs are installed within the study area of Schiaparelli Glacier (Figure 2.1, C). One AWS is located on the glacier operated by the Universidad Federal do Rio Grande, Brazil since March 2013. Another AWS has been installed in September 2015 as part of the GABY-VASA project at the glacier margin on solid ground. The purpose of the second AWS was to get a more reliable record of meteorological observations in particular of precipitation and solar radiation. Hourly data of observed air temperature, relative humidity, surface pressure, incoming solar radiation and precipitation are used to downscale the latest large-scale ERA-Interim reanalysis data supplied by the European Centre for Medium-Range Weather Forecasts (Dee et al. 2011) which is needed as forcing data for the CMB simulations. The same downscaling methods are chosen as described in Chapter

4. The updated version of COSIMA, COSIPY (Sauter 2020) is implemented to simulate CMB of Schiaparelli Glacier. The chosen parameter setting of the model and the method of uncertainty assessment are identical to Chapter 4 in order to compare simulation results from the different study sites.

The reconstruction of LIA climate is based on the simulation of steady-state conditions for the recent (2016) and past (~1870, LIA) glacier extents (Meier 2018) of Schiaparelli Glacier. We assume that the glacier has been in equilibrium over a short period of time during the formation of the associated terminal moraine when the shift of climate started from cooler or wetter LIA to warmer or drier present-day conditions, similar to the approach followed in Huintjes et al. (2016). Precipitation and air temperature offsets to the present-day climate are used as COSIPY forcing to derive an average CMB in equilibrium for the recent time period (simulation period 2000-2010). LIA climate is then reconstructed, using additional precipitation and air temperature offsets to the simulated present-day steady-state climate conditions along with the LIA glacier extent (Meier 2018) and adapted glacier height by means of SRTM data and moraine system information.

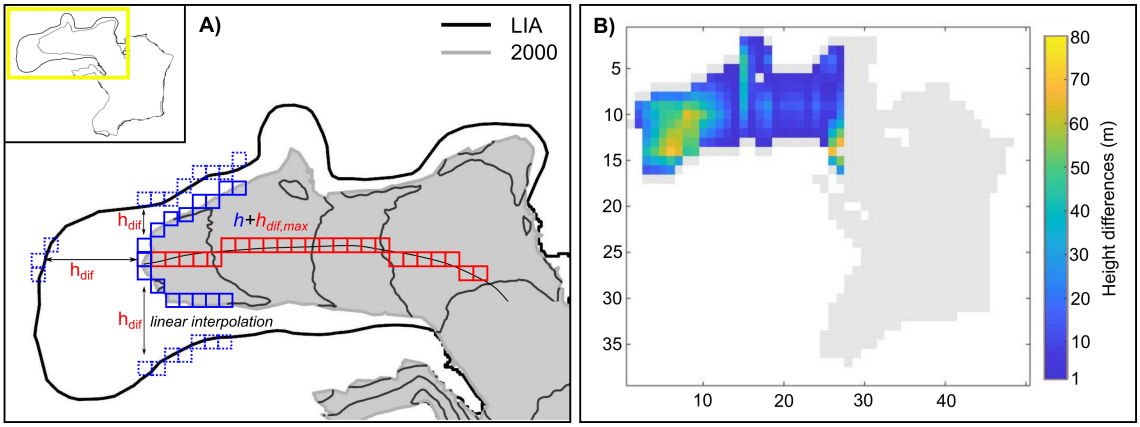

Figure 5.1: Schematic illustration of LIA glacier height calculations using SRTM data and glacier outlines from 1870 (LIA) (Meier et al. 2018) and 2000 (RGI-Consortium 2017) (A), and calculated height differences between the DEM adapted to LIA conditions and the initial SRTM dervied DEM (B). Figure adapted from Publication 3 (A.3).

The recent glacier heights based on SRTM data from 2000 and glacier outline information from 2000 and LIA are used to reproduce glacier heights of Schiaparelli Glacier during LIA (Figure 5.1). In a first step, height differences (h_{dif}) are calculated for each pixel between the glacier outline of 2000 and LIA (Figure 5.1, A). The maximum height difference along the LIA outlines ($h_{dif,max}$) perpendicular to any position along the flowline are added to the height (h) of the pixel at this position of the flowline. The heights between the glacier's

LIA outlines and the height adjusted flowline are linearly interpolated. This procedure is limited to the part of the glacier where the LIA glacier outline extends further than the glacier outline in 2000 (Figure 5.1A, inset).

5.2 Variability of climatic mass balance between 2000 to 2017

The modeled glacier-wide mean annual CMB of Schiaparelli Glacier between April 2000 and March 2017 is simulated to -1.8±0.36 m w.e. a^{-1}. The modeled annual CMB ranges between -2.7±0.36 m w.e. a^{-1} (2016/17) and -0.7±0.36 m w.e. a^{-1} (2009/10). Positive anomalies of mean annual glacier-wide air temperature cause high negative CMB values. Positive solid precipitation or negative solar radiation anomalies cannot fully compensate positive air temperature anomalies as observed in the mass balance years 2007/08 and 2008/09. In general, the modeled CMB is dominated by surface melt (60%) and solid precipitation (37%). Sublimation, deposition, refreezing, and evaporation have only a small impact (Figure 5.2, B). These findings are reflected by strong correlations between CMB and air temperature (r=-0.77) and CMB and solid precipitation (r=0.80). Modeled annual ELA ranges from 650±50 m a.s.l. to 800±50 m a.s.l. with a mean of 730±50 m a.s.l. which are values similar to those mentioned in Strelin et al. (2008).

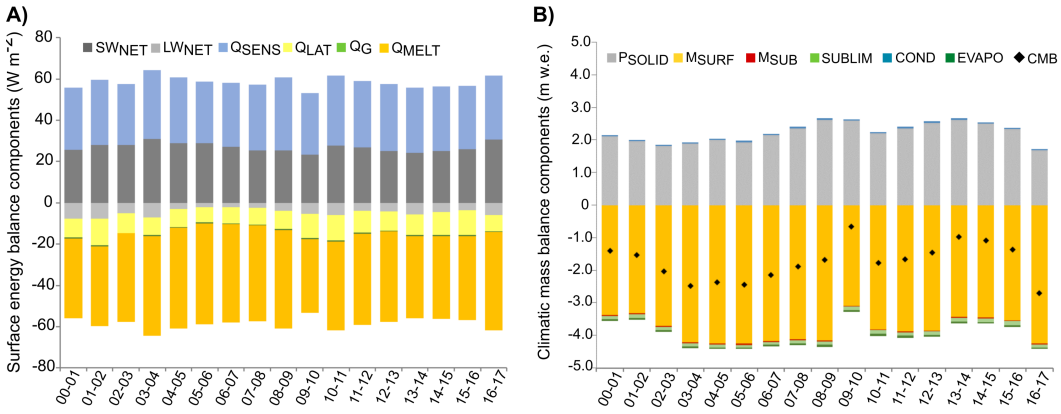

Figure 5.2: Annual surface energy balance components (A) and climatic mass balance components (B) averaged on an annual basis between April 2000 and March 2017. SW_{NET}: net shortwave radiation, LW_{NET}: net longwave radiation, Q_{SENS}: sensible heat flux, Q_{LAT}: latent heat flux, Q_G: ground heat flux, Q_{MELT}: surface melt, P_{SOLID}: solid precipitation, M_{SURF}: surface melt, , M_{SUB}: subsurface melt, $SUBLIM$: sublimation, $COND$: condensation, $EVAPO$: evaporation, CMB: climatic mass balance. Figure adapted from Publication 3 (A.3).

The recent glacier response to climate differs significantly between Schiaparelli Glacier at the Monte Sarmiento Massif and Grey and Tyndall glaciers located at the SPI (Chapter 4).

Climate conditions at Grey Glacier and Tyndall Glacier are wetter and colder compared to Schiaparelli Glacier due to higher mean glacier elevations and stronger orographic effects. Analyzing the energy balance components in detail, shortwave net radiation is much lower at Schiaparelli Glacier than at the SPI while the sensible heat flux is more important as a source of energy input at the glacier surface. Nevertheless, all three glaciers underwent a massive retreat in the past decades. Climatic mass balance simulations however are positive with a glacier-wide mean annual value of +0.86±0.52 m w.e. a^{-1} for Grey Glacier and +0.41±0.54 m w.e. a^{-1} for Tyndall Glacier between 2000 and 2016 while the CMB of Schiaparelli Glacier is clearly negative with -1.69±0.36 m w.e. a^{-1} during the same period. The positive CMB of Grey Glacier and Tyndall Glacier cannot compensate the mass loss which is caused by ice dynamical processes, leading to overall negative mass balances. Extensive glacier thinning due to dynamical adjustment has not been observed at Schiaparelli Glacier (Melkonian et al. 2013; Braun et al. 2019). Mass loss due to a negative CMB seems to be the main reason for the recent areal changes of Schiaparelli Glacier. In general, the recent glacier mass losses at the CDI and Monte Sarmiento Massif are rather driven by atmospheric warming than by ice dynamical processes (Koppes et al. 2009; Bown et al. 2014) which is accordance with the findings of this study.

5.3 Reconstruction of Little Ice Age climate

Steady-state conditions for the recent glacier extent of Schiaparelli Glacier is simulated using several temperature (TO) and precipitation offset (PO) combinations between 2000 and 2010 (Table 5.1). Negative air temperature offsets between -0.5°C and -0.9°C in combination with an increase of precipitation amounts of up to 30% are needed to simulate a glacier in equilibrium. A nearly zero CMB under actual climate conditions (2000-2010) would imply a glacier length reduction of about 3.8 km back from the glacier front in 2016.

The TO/PO combination TO=-0.6°C and PO=20% is chosen to represent the recent steady-state climate conditions and as starting point for LIA climate reconstruction. Forcing COSIPY with the recent steady-state climate conditions results in a negative CMB of -1.64±0.48 m w.e. a^{-1} for the glacier extent in 1870. A nearly zero CMB is simulated by forcing the model with air temperature offsets between additional -0.4 to -0.8°C in combination with an increase in precipitation of up to 30% to the artificial steady-state of 2000-2010 (Table 5.2). Summing up the air temperature and precipitation offset to derive steady-state conditions for recent and past glacier extents, a lowering of air temperature between -0.9°C and -1.7°C and a precipitation increase of up to +60% with respect to the actual climate conditions between 2000 and 2010 were achieved. These findings are similar to previous Holocene climate reconstructions in Southern Patagonia (Kilian et al. 2007;

Villalba 1990; Haberzettl et al. 2007) which also indicate colder and wetter conditions during the LIA. The mean air temperature was simulated to be below the 1900-1990 means by 0.86°C in the southern parts of Southern Andes (Strelin et al. 2008).

Table 5.1: Precipitation (PO) and air temperature offsets (TO) are combined to simulate steady-state conditions (m w.e. a^{-1}) for the recent extent of Schiaparelli Glacier; Table adapted from Publication 3 (A.3).

TO/PO	**-10%**	**-5%**	**0%**	**5%**	**10%**	**15%**	**20%**	**25%**	**30%**
0.0°C			-1.81						
-0.4°C								-0.29	-0.17
-0.5°C							-0.22	-0.08	0.05
-0.6°C						-0.14	-0.01	0.13	
-0.7°C					-0.07	0.06	0.20		
-0.8°C			-0.16	-0.02	0.12				
-0.9°C		-0.13	0.02						
-1.0°C	-0.10	0.05	0.19						

Table 5.2: Precipitation (PO) and air temperature offsets (TO) are combined to simulate steady-state conditions (m w.e. a^{-1}) for the LIA extent of Schiaparelli Glacier based on the adapted SRTM heights as offsets from the 'artificial' steady-state climate for a glacier in equilibrium with its current area and volume. Table adapted from Publication 3 (A.3).

TO/PO	**-10%**	**-5%**	**0%**	**5%**	**10%**	**15%**	**20%**	**25%**	**30%**
0.0°C			-1.64						
-0.4°C							-0.23	-0.09	0.05
-0.5°C						-0.17	-0.02	0.12	
-0.6°C					-0.13	0.03			
-0.7°C				-0.08	0.07				
-0.8°C			-0.03	0.12					
-0.9°C	-0.13	0.01	0.17						
-1.0°C	0.05	0.19	0.34						

CHAPTER 6

Synthesis and perspectives

The recent variability of climate and glacier climatic mass balance of selected glaciated study sites in Patagonia and Tierra del Fuego were addressed in this thesis, aiming to improve our understanding of the individual glacier response to climate variability during recent decades.

Meteorological time series of four AWSs across the Gran Campo Nevado Ice Cap have been analyzed statistically regarding their means, trends, and extremes during the past two decades to answer RQ1. A sharp gradient of precipitation was found between the luv-side and lee-side of the GCN mountain range. Annual precipitation amounts published in Schneider et al. (2003) were revisited. Close to the vicinity of the GCN Ice Cap, a mean annual amount of up to 7500 mm was determined in this thesis which overall is consistent with the estimates provided in Schneider et al. (2003). With increasing distance to the GCN Ice Cap, the influence of the Pacific Ocean on climate conditions diminishes, leading to larger amplitudes of daily and annual air temperature and lower amounts of annual precipitation. A positive trend in mean air temperature between $+0.02$°C a^{-1} and $+0.05$°C a^{-1} was detected at the GCN Ice Cap during the past two decades.

Publication 1 (A.1) further highlighted the year-around persistence of synoptic weather types with humid westerly and southwesterly airflow causing strong orographic induced effects on the spatial variability of climate patterns. Positive and negative phases of the Antarctic Oscillation influence strongly the prevailing synoptic weather types along with intra-annual precipitation and air temperature variations.

During the processing step of the meteorological time series, it became obvious how important similar standards of measurements are in order to achieve reliable comparisons between observations. Measurement uncertainties in particular of precipitation which occur over time due to the harsh weather conditions in the study region are difficult to avoid completely but also notoriously difficult to quantify afterwards. Each data record had to be processed thoroughly before further analysis could be carried out. Large efforts must be taken to maintain meteorological networks like the one at the GCN Ice Cap.

Long-term records of in-situ observations as outcome however are immensely useful for climatic, dendrochronological, glaciological, and hydrological studies in the Southern Andes. Keeping a net of AWSs running in a remote region such as the Peninsula Muñoz Gamero with its ice cap Gran Campo Nevado over almost two decades, as has been achieved by Rolf Kilian, Christoph Schneider, and Tobias Sauter without any continued institutional funds in this respect was both a tremendous scientific effort and achievement (Schneider et al. 2003).

In Publication 2 (A.2), geodetic mass balance based on remote sensing data and simulated climatic mass balance were combined to derive mass loss due to frontal ablation for the two neighboring glaciers Grey and Tyndall at the SPI. Recent climatic mass balance was determined by implementing the surface energy and mass balance model COSIMA. Downscaled ERA-Interim Reanalysis and MODIS cloud cover data were used as atmospheric forcing data of COSIMA.

The positive simulated glacier-wide climatic mass balances of $+1.02\pm0.52$ m w.e. a^{-1} for Grey Glacier and of $+0.68\pm0.54$ m w.e. a^{-1} for Tyndall Glacier between 2000 and 2014 were in contrast with the observed negative geodetic mass balance. Ice losses due to frontal ablation as the resulting compensating mass flux were calculated to 2.07 ± 0.70 m w.e. a^{-1} for Grey Glacier and 3.26 ± 0.82 m w.e. a^{-1} for Tyndall Glacier for the study period. The contrasting pattern between positive climatic mass balance and observed glacier retreat highlights the important role of ice dynamical effects and ice loss at calving fronts on the individual glacier response to climate variability in recent decades.

Climatic mass balance is mainly controlled by the amount of solid precipitation and surface melt which is driven by incoming solar radiation and the sensible heat flux. Accumulation estimates result in the largest uncertainties in the system due to the lack of observations in the accumulation areas of the SPI. In fact, climatic mass balance results of this thesis and previous studies (Schaefer et al. 2015; Lenaerts et al. 2014; Mernild et al. 2016) differ mainly because of the application of different precipitation modelling schemes. Therefore, future research should aim at more reliable and more extensive direct field and remote sensing observations of accumulation, snowdrift, and sublimation in the accumulation areas of glaciers and icefields in Fuego-Patagonia.

In Publication 3 (A.3), special attention was given to the comparison of climatic mass balance simulations between the different study sites at the SPI and the Cordillera Darwin on Tierra del Fuego. Contrary to the SPI, a continuous negative annual climatic mass balance between 2000 and 2017 was modeled for Schiaparelli Glacier in Tierra del Fuego. Climatic conditions and glacier-relevant processes differ largely between both study areas. In case of Schiaparelli Glacier, climatic mass balance processes seem to be the main driver

of mass loss rather than any dynamical adjustment of the glacier or relevant calving.

The two time lapse camera installations covering ice movement, frontal ablation, and calving events at Grey Glacier and Schiaparelli Glacier over periods of many months at each site provide substantial datasets in this regard. These data stem from the empirical work of the GABY-VASA project. The data may provide the basis for future investigations to better constrain the importance of the processes at the calving fronts of such lake-terminating glaciers in Fuego-Patagonia as compared to ice-dynamical response and CMB.

COSIPY simulations were further extended to derive steady-state glacier conditions during the Little Ice Age using information of moraine systems and glacier areal extent. To finally reconstruct climate conditions during LIA, precipitation and air temperature offsets to present-day climate were implemented in the model runs. An air temperature decrease between -0.9 °C and -1.7 °C in combination with a precipitation offset of up to $+60\%$ to recent (2000-2010) climate conditions would be necessary to simulate steady-state conditions for Schiaparelli Glacier during LIA.

The outcomes of Publication 2 (A.2) and Publication 3 (A.3) confirm that the chosen methodological approaches to assess surface energy-fluxes and climatic mass balance provide reliable results and are suitable to be applied to different glaciated regions in Fuego-Patagonia. However, networks of meteorological and glaciological observations in the glaciated areas still need to be extended. Without reliable validation datasets, the uncertainties of numerical simulations are large and results of different studies can hardly be compared and evaluated. The research question on how individual glacier processes are responsible for the non-uniform pattern of glacier mass loss in Fuego-Patagonia still needs to be further investigated in future studies. By knowing this, more reliable estimates of the future contribution of glacier mass loss in the Southern Andes to sea-level rise can be provided.

Combined approaches of numerical simulations and remote sensing data are very useful to get faithful information of specific glacier processes despite the limited amount of in-situ observations (Schaefer et al. 2015; Nuth et al. 2012; Masiokas et al. 2020; Davies et al. 2020). Nevertheless, the scarcity of information about the bedrock topography or ice thickness (Gacitúa et al. 2020) limit the applicability of high resolution ice dynamical models up to now. To fully quantify ice dynamical processes and their impact on the overall mass change, the use of ice dynamical models would be a crucial advancement in future investigations. Studies of future glacier mass loss would benefit tremendously if reliable and realistic estimates of both, the climatic mass balance and the ice dynamical processes of individual glacier catchments, in particular of the major outlet glaciers in Southern Patagonian and Tierra del Fuego, exist.

Bibliography

Aniya, M. (1999). 'Recent Glacier Variations of the Hielos Patagnicos, South America, and Their Contribution to Sea-Level Change'. In: *Arctic, Antarctic, and Alpine Research* 31.2, pp. 165–173.

Aniya, M., H. Sato, R. Naruse, P. Skvarca, and G. Casassa (1996). 'The use of satellite and airborne imagery to inventory outlet glaciers of the southern Patagonia Icefield, South America'. In: *Photogramm. Eng. Remote Sens* 62, pp. 1361–1369.

Aravena, J.-C. and B. H. Luckman (2009). 'Spatio-temporal rainfall patterns in Southern South America'. In: *International Journal of Climatology* 29.14, pp. 2106–2120. ISSN: 1097-0088. DOI: 10.1002/joc.1761. URL: http://dx.doi.org/10.1002/joc.1761.

Barcaza, G., S. Nussbaumer, G. Tapia, J. Valdés, J. García, Y. Videla, A. Albornoz, and V. Arias (2017). 'Glacier inventory and recent glacier variations in the Andes of Chile, South America'. In: *Annals of Glaciology* 58.75pt2, pp. 166–180. DOI: 10.1017/aog.2017.28.

Benn, D., C. Warren, and R. Mottram (June 2007). 'Calving processes and the dynamics of calving glaciers'. In: *Earth-Science Reviews* 82, pp. 143–179. DOI: 10.1016/j.earscirev.2007.02.002.

Bown, F., A. Rivera, P. Zenteno, C. Bravo, and F. Cawkwell (2014). 'First Glacier Inventory and Recent Glacier Variation on Isla Grande de Tierra Del Fuego and Adjacent Islands in Southern Chile'. In: *Global Land Ice Measurements from Space*. Ed. by J. S. Kargel, G. J. Leonard, M. P. Bishop, A. Kääb, and B. H. Raup. Berlin, Heidelberg: Springer Berlin Heidelberg, pp. 661–674. ISBN: 978-3-540-79818-7. DOI: 10.1007/978-3-540-79818-7_28. URL: https://doi.org/10.1007/978-3-540-79818-7_28.

Braun, M., P. Malz, C. Sommerand, D. Farías-Barahona, T. Sauter, G. Casassa, A. Soruco, P. Skvarca, and T. Seehaus (2019). 'Constraining glacier elevation and mass changes in South America'. In: *Nature Climate Change* 9, pp. 130–136. DOI: 10.1038/s41558-018-0375-7.

Carrasco, J., G. Casassa, and A. Rivera (2002). 'Meteorological and climatological aspect of the southern Patagonia Icefield.' In: *The Patagonia Icefields*. Ed. by C. G., S. F., and S. R. New York: Kluwer-Plenum, pp. 29–41.

Carrasco, J., R. Osorio, and G. Casassa (2008). 'Secular trend of the equilibrium-line altitude on the western side of the southern Andes, derived from radiosonde and surface observations'. In: *Journal of Glaciology* 54.186, pp. 538–550. DOI: 10.3189/002214308785837002.

Casassa, G., H. Brecher, A. Rivera, and M. Aniya (1997). 'A century-long recession record of Glacier O'Higgins, Chilean Patagonia'. In: *Annals of Glaciology* 24, pp. 106–110. DOI: 10.1017/S0260305500012015.

Davies, B. and N. Glasser (2012). 'Accelerating shrinkage of Patagonian glaciers from the Little Ice Age (AD 1870) to 2011'. In: *Journal of Glaciology* 58.212, pp. 1063–1084. DOI: doi:10.3189/2012JoG12J026.

Davies, B. et al. (2020). 'The evolution of the Patagonian Ice Sheet from 35 ka to the present day (PATICE)'. In: *Earth-Science Reviews* 204, p. 103152. ISSN: 0012-8252. DOI: https://doi.org/10.1016/j.earscirev.2020.103152.

De Angelis, H. (2014). 'Hypsometry and sensitivity of the mass balance to changes in equilibrium-line altitude: the case of the Southern Patagonia Icefield'. In: *Journal of Glaciology* 60.219, pp. 14–28. DOI: 10.3189/2014JoG13J127.

Dee, D. et al. (2011). 'The ERA-Interim reanalysis: configuration and performance of the data assimilation system'. In: *Quarterly Journal of the Royal Meteorological Society* 137.656, pp. 553–597. DOI: 10.1002/qj.828.

Durre, I., M. J. Menne, B. E. Gleason, T. G. Houston, and R. S. Vose (2010). 'Comprehensive Automated Quality Assurance of Daily Surface Observations'. In: *Journal of Applied Meteorology and Climatology* 49.8, pp. 1615–1633. DOI: 10.1175/2010JAMC2375.1.

Dussaillant, I., E. Berthier, F. Brun, M. Masiokas, R. Hugonnet, V. Favier, A. Rabatel, P. Pitte, and L. Ruiz (2019). 'Two decades of glacier mass loss along the Andes.' In: *Nature Geoscience* 12, pp. 802–808. DOI: https://doi.org/10.1038/s41561-019-0432-5.

Escobar, F., F. Vidal, and C. Garin (1992). 'Water Balance in the Patagonia Icefield.' In: *Glaciological Researches in Patagonia*. Ed. by R. Natuse. Japanese Society of Snow and Ice, pp. 109–119.

Gacitúa, G., C. Schneider, J. Arigony, I. González, R. Jaña, and G. Casassa (2020). 'First ice thickness measurements in Tierra del Fuego at Glacier Schiaparelli, Chile'. In: *Earth System Science Data Discussions* 2020, pp. 1–8. DOI: 10.5194/essd-2020-111. URL: https://essd.copernicus.org/preprints/essd-2020-111/.

Gardner, A. S. et al. (2013). 'A Reconciled Estimate of Glacier Contributions to Sea Level Rise: 2003 to 2009'. In: *Science* 340.6134, pp. 852–857. DOI: 10.1126/science.1234532.

Garreaud, R. D., M. Vuille, R. Compagnucci, and J. Marengo (2009). 'Present-day South American climate'. In: *Palaeogeography, Palaeoclimatology, Palaeoecology* 281.3–4, pp. 180–195. DOI: https://doi.org/10.1016/j.palaeo.2007.10.032.

Geoestudios (2013). 'Implementación Nivel 2 Estrategia Nacional De Glaciares: Mediciones Glaciológicas Terrestres En Chile Central, Zona Sur Y Patagonia'. In: *Report Dirección General de Aguas, Santiago, Chile* SIT 327, pp. 1–475.

Gillett, N. P., T. D. Kell, and P. D. Jones (2006). 'Regional climate impacts of the Southern Annular Mode'. In: *Geophysical Research Letters* 33.23, n/a–n/a. ISSN: 1944-8007. DOI: 10.1029/2006GL027721. URL: http://dx.doi.org/10.1029/2006GL027721.

Gocic, M. and S. Trajkovic (2013). 'Analysis of changes in meteorological variables using Mann-Kendall and Sen's slope estimator statistical tests in Serbia'. In: *Global and Planetary Change* 100.Supplement C, pp. 172–182. ISSN: 0921-8181. DOI: https://doi.org/10.1016/j.gloplacha.2012.10.014. URL: http://www.sciencedirect.com/science/article/pii/S0921818112002032.

Godoi, M. A., T. Shiraiwa, S. Kohshima, and K. Kubota (2002). 'Firn-Core Drilling Operation at Tyndall Glacier, Southern Patagonia Icefield'. In: *The Patagonian Icefields: A Unique Natural Laboratory for Environmental and Climate Change Studies*. Ed. by G. Casassa, F. V. Sepúlveda, and R. M. Sinclair. Boston, MA: Springer US, pp. 149–156. ISBN: 978-1-4615-0645-4. DOI: 10.1007/978-1-4615-0645-4_14.

Haberzettl, T. et al. (2007). 'Lateglacial and Holocene wet—dry cycles in southern Patagonia: chronology, sedimentology and geochemistry of a lacustrine record from Laguna Potrok Aike, Argentina'. In: *The Holocene* 17.3, pp. 297–310. DOI: 10.1177/0959683607076437. eprint: https://doi.org/10.1177/0959683607076437. URL: https://doi.org/10.1177/0959683607076437.

Hall, D. K. and G. A. Riggs (2016). 'MODIS/Terra Snow Cover Daily L3 Global 500m Grid V005, 2000 to 2016'. In: *Boulder, Colorado USA. NASA National Snow and Ice Data Center Distributed Active Archive Center*. DOI: http://dx.doi.org/10.5067/MODIS/MOD10A1.006..

Hamed, K. H. (2008). 'Trend detection in hydrologic data: The Mann–Kendall trend test under the scaling hypothesis'. In: *Journal of Hydrology* 349.3, pp. 350–363. ISSN: 0022-1694. DOI: https://doi.org/10.1016/j.jhydrol.2007.11.009. URL: http://www.sciencedirect.com/science/article/pii/S0022169407006865.

Heucke, E. (2003). 'A Light Portable Steam-driven Ice Drill Suitable for Drilling Holes in Ice and Firn'. In: *Geografiska Annaler: Series A, Physical Geography* 81, pp. 603–609. DOI: 10.1111/1468-0459.00088.

Holmlund, P. and H. Fuenzalida (1995). 'Anomalous glacier responses to 20th century climatic changes in Darwin Cordillera, southern Chile'. In: *Journal of Glaciology* 41.139, pp. 465–473. DOI: 10.3189/S0022143000034808.

Huintjes, E., D. Loibl, F. Lehmkuhl, and C. Schneider (2016). 'A modelling approach to reconstruct Little Ice Age climate from remote-sensing glacier observations in southeastern Tibet'. In: *Annals of Glaciology* 57.71, pp. 359–370. DOI: 10.3189/2016AoG71A025.

Huintjes, E., T. Sauter, B. Schröter, F. Maussion, W. Yang, J. Kropáček, M. Buchroithner, D. Scherer, S. Kang, and C. Schneider (2015). 'Evaluation of a Coupled Snow and Energy Balance Model for Zhadang Glacier, Tibetan Plateau, Using Glaciological Measurements and Time-Lapse Photography'. In: *Arctic, Antarctic, and Alpine Research* 47.3, pp. 573–590. DOI: 10.1657/AAAR0014-073.

Huss, M. and R. Hock (2018). 'Global-scale hydrological response to future glacier mass loss'. In: *Nature Climate Change* 8, pp. 135–140. DOI: 10.1038/s41558-017-0049-x.

Jaber, W. A., D. Floricioiu, H. Rott, and M. Eineder (2013). 'Surface elevation changes of glaciers derived from SRTM and TanDEM-X DEM differences'. In: *IGARSS 2013*. IEEE Xplore, pp. 1893–1896.

Kilian, R., C. Schneider, J. Koch, M. Fesq-Martin, H. Biester, C. Casassa, M. Arévalo, G. Wendt, O. Baeza, and J. Behrmann (2007). 'Palaeoecological constraints on Late Glacial and Holocene ice retreat in the Southern Andes (53°S).' In: *Global and Planetary Change* 59.1-4, pp. 49–66. DOI: 10.1016/j.gloplacha.2006.11.034.

Kisi, O. and M. Ay (2014). 'Comparison of Mann–Kendall and innovative trend method for water quality parameters of the Kizilirmak River, Turkey'. In: *Journal of Hydrology* 513.Supplement C, pp. 362–375. ISSN: 0022-1694. DOI: https://doi.org/10.1016/j.jhydrol.2014.03.005. URL: http://www.sciencedirect.com/science/article/pii/S0022169414001796.

Kohshima, S., N. Takeuchi, J. Uetake, T. Shiraiwa, R. Uemura, N. Yoshida, S. Matoba, and M. A. Godoi (2007). 'Estimation of net accumulation rate at a Patagonian glacier by ice core analyses using snow algae'. In: *Global and Planetary Change* 59.1–4, pp. 236–244. DOI: 10.1016/j.gloplacha.2006.11.014.

Koppes, M., H. Conway, L. A. Rasmussen, and M. Chernos (2011). 'Deriving mass balance and calving variations from reanalysis data and sparse observations, Glaciar San Rafael, northern Patagonia, 1950–2005'. In: *The Cryosphere* 5.3, pp. 791–808. DOI: 10.5194/tc-5-791-2011.

Koppes, M., B. Hallet, and J. Anderson (2009). 'Synchronous acceleration of ice loss and glacial erosion, Glaciar Marinelli, Chilean Tierra del Fuego'. In: *Journal of Glaciology* 55.190, pp. 207–220. DOI: 10.3189/002214309788608796.

Kumar, L., A. K. Skidmore, and E. Knowles (1997). 'Modelling topographic variation in solar radiation in a GIS environment'. In: *International Journal of Geographical Information Science* 11.5, pp. 475–497. DOI: 10.1080/136588197242266.

Lenaerts, J. T. M., M. R. van den Broeke, J. M. van Wessem, W. J. van de Berg, E. van Meijgaard, L. H. van Ulft, and M. Schaefer (2014). 'Extreme Precipitation and Climate Gradients in Patagonia Revealed by High-Resolution Regional Atmospheric Climate Modeling'. In: *Journal of Climate* 27.12, pp. 4607–4621. DOI: 10.1175/JCLI-D-13-00579.1.

Lopez, P., P. Chevallier, V. Favier, B. Pouyaud, F. Ordenes, and J. Oerlemans (2010). 'A regional view of fluctuations in glacier length in southern South America'. In: *Global and Planetary Change* 71.1–2, pp. 85–108. ISSN: 0921-8181. DOI: 10.1016/j.gloplacha.2009.12.009.

Loriaux, T. and G. Casassa (2013). 'Evolution of glacial lakes from the Northern Patagonia Icefield and terrestrial water storage in a sea-level rise context'. In: *Global and Planetary Change* 102, pp. 33–40. ISSN: 0921-8181. DOI: https://doi.org/10.1016/j.gloplacha.2012.12.012. URL: http://www.sciencedirect.com/science/article/pii/S0921818112002408.

Lund, I. (1963). 'Map-pattern classification by statistical methods'. In: *Journal of Applied Meteorology* 2, pp. 56–65.

Malz, P., W. Meier, G. Casassa, R. Jaña, P. Skvarca, and M. Braun (2018). 'Elevation and Mass Changes of the Southern Patagonia Icefield Derived from TanDEM-X and SRTM Data'. In: *Remote Sensing* 10.188. ISSN: 2072-4292. DOI: 10.3390/rs10020188.

Masiokas, M. H. et al. (2020). 'A Review of the Current State and Recent Changes of the Andean Cryosphere'. In: *Frontiers in Earth Science* 8, p. 99. ISSN: 2296-6463. DOI: 10.3389/feart.2020.00099. URL: https://www.frontiersin.org/articles/10.3389/feart.2020.00099.

Meier, W. J.-H., J. Grießinger, P. Hochreuther, and M. H. Braun (2018). 'An Updated Multi-Temporal Glacier Inventory for the Patagonian Andes With Changes Between the Little Ice Age and 2016'. In: *Frontiers in Earth Science* 6, p. 62. DOI: 10.3389/feart.2018.00062. URL: https://www.frontiersin.org/article/10.3389/feart.2018.00062.

Meier, W. J.-H. (2018). *Glacier inventory for the Patagonian Andes, link to shape files.* data set. Supplement to: Meier, Wolfgang Jens-Henrik; Grießinger, Jussi; Hochreuther, Philipp; Braun, Matthias Holger (2018): An Updated Multi-Temporal Glacier Inventory for the Patagonian Andes With Changes Between the Little Ice Age and 2016. Frontiers in Earth Science, 6, 62 pp, https://doi.org/10.3389/feart.2018.00062. DOI: 10.1594/PANGAEA.891211. URL: https://doi.org/10.1594/PANGAEA.891211.

Meier, W. J.-H., J.-C. Aravena, J. Grießinger, P. Hochreuther, P. Soto-Rogel, H. Zhu, R. D. Pol-Holz, C. Schneider, and M. H. Braun (2019). 'Late Holocene Glacial Fluctuations of Schiaparelli Glacier at Monte Sarmiento Massif, Tierra del Fuego (54°24'S)'. In: *Geosciences* 9.8. ISSN: 2076-3263. DOI: 10.3390/geosciences9080340. URL: https://www.mdpi.com/2076-3263/9/8/340.

Melkonian, A. K., M. J. Willis, M. E. Pritchard, A. Rivera, F. Bown, and S. A. Bernstein (2013). 'Satellite-derived volume loss rates and glacier speeds for the Cordillera Darwin Icefield, Chile'. In: *The Cryosphere* 7.3, pp. 823–839. DOI: 10.5194/tc-7-823-2013. URL: https://www.the-cryosphere.net/7/823/2013/.

Mernild, S. H., G. E. Liston, C. Hiemstra, and R. Wilson (2016). 'The Andes Cordillera. Part III: glacier surface mass balance and contribution to sea level rise (1979–2014)'. In: *International Journal of Climatology*. DOI: 10.1002/joc.4907.

Minowa, M., S. Sugiyama, D. Sakakibara, and T. Sawagaki (2015). 'Contrasting glacier variations of Glaciar Perito Moreno and Glaciar Ameghino, Southern Patagonia Icefield'. In: *Annals of Glaciology* 56.70, pp. 26–32. DOI: doi:10.3189/2015AoG70A020.

Möller, M., C. Schneider, and R. Kilian (2007). 'Glacier change and climate forcing in recent decades at Gran Campo Nevado, southernmost Patagonia'. In: *Annals of Glaciology* 46.1, pp. 136–144. DOI: doi:10.3189/172756407782871530.

Mouginot, J. and E. Rignot (2015). 'Ice motion of the Patagonian Icefields of South America: 1984–2014'. In: *Geophysical Research Letters* 42.5, pp. 1441–1449. DOI: 10.1002/2014GL062661.

Muto, M. and M. Furuya (2013). 'Surface velocities and ice-front positions of eight major glaciers in the Southern Patagonian Ice Field, South America, from 2002 to 2011'. In: *Remote Sensing of Environment* 139, pp. 50–59. DOI: 10.1016/j.rse.2013.07.034.

Naruse, R. and P. Skvarca (2000). 'Dynamic Features of Thinning and Retreating Glaciar Upsala, a Lacustrine Calving Glacier in Southern Patagonia'. In: *Arctic, Antarctic, and Alpine Research* 32.4, pp. 485–491.

Nishida, K., K. Satow, M. Aniya, G. Casassa, and T. Kadota (1995). 'Thickness change and flow of Glaciar Tyndall, Patagonia'. In: *Bull. Glacier Res* 13, pp. 29–34.

Nuth, C., T. V. Schuler, J. Kohler, B. Altena, and J. O. Hagen (2012). 'Estimating the long-term calving flux of Kronebreen, Svalbard, from geodetic elevation changes and mass-balance modeling'. In: *Journal of Glaciology* 58.207, pp. 119–133. DOI: 10.3189/2012JoG11J036.

Oerlemans, J. (2001). *Glaciers and Climate Change*. Lisse: Taylor Francis. ISBN: 9789026518133.

Onyutha, C., H. Tabari, M. T. Taye, G. N. Nyandwaro, and P. Willems (2016). 'Analyses of rainfall trends in the Nile River Basin'. In: *Journal of Hydro-environment Research*

13.Supplement C, pp. 36–51. ISSN: 1570-6443. DOI: https://doi.org/10.1016/j.jher.2015.09.002. URL: http://www.sciencedirect.com/science/article/pii/S1570644315000635.

Porter, C. and A. Santana (Jan. 2003). 'Rapid 20th century retreat of Ventisquero Marinelli in the Cordillera Darwin Icefield'. In: *An. Inst. Patagonia* 31, pp. 17–26.

Rasmussen, L., H. Conway, and C. Raymond (2007). 'Influence of upper air conditions on the Patagonia icefields'. In: *Global and Planetary Change* 59, pp. 203–216.

RGI-Consortium (2017). 'Randolph Glacier Inventory – A Dataset of Global Glacier Outlines: Version 6.0.: Technical Report'. In: *Global Land Ice Measurements from Space, Colorado, USA. Digital Media.* DOI: https://doi.org/10.7265/N5-RGI-60.

Rignot, E., A. Rivera, and G. Casassa (2003). 'Contribution of the Patagonia Icefields of South America to Sea Level Rise'. In: *Science* 302.5644, pp. 434–437. DOI: 10.1126/science.1087393.

Rivera, A., M. Koppes, C. Bravo, and J. C. Aravena (2012). 'Little Ice Age advance and retreat of Glaciar Jorge Montt, Chilean Patagonia'. In: *Climate of the Past* 8.2, pp. 403–414. DOI: 10.5194/cp-8-403-2012.

Rivera, A., T. Benham, G. Casassa, J. Bamber, and J. A. Dowdeswell (2007). 'Ice elevation and areal changes of glaciers from the Northern Patagonia Icefield, Chile'. In: *Global and Planetary Change* 59.1–4, pp. 126–137. DOI: 10.1016/j.gloplacha.2006.11.037.

Rivera, A. and G. Casassa (1999). 'Volume changes on Pío XI glacier, Patagonia: 1975-1995'. In: *Global and Planetary Change* 22, pp. 233–244.

Rosenblüth, B., H. A. Fuenzalida, and P. Aceituno (1997). 'Recent temperature variations in southern South America'. In: *International Journal of Climatology* 17.1, pp. 67–85. DOI: 10.1002/(SICI)1097-0088(199701)17:1<67::AID-JOC120>3.0.CO;2-G.

Sakakibara, D. and S. Sugiyama (2014). 'Ice-front variations and speed changes of calving glaciers in the Southern Patagonia Icefield from 1984 to 2011'. In: *Journal of Geophysical Research: Earth Surface* 119.11, pp. 2541–2554. DOI: 10.1002/2014JF003148.

Sakakibara, D., S. Sugiyama, T. Sawagaki, S. Marinsek, and P. Skvarca (2013). 'Rapid retreat, acceleration and thinning of Glaciar Upsala, Southern Patagonia Icefield, initiated in 2008'. In: *Annals of Glaciology* 54.63, pp. 131–138. DOI: doi:10.3189/2013AoG63A236.

Sauter, T. (2020). 'Revisiting extreme precipitation amounts over southern South America and implications for the Patagonian Icefields'. In: *Hydrology and Earth System Sciences* 24.4, pp. 2003–2016. DOI: 10.5194/hess-24-2003-2020. URL: https://www.hydrol-earth-syst-sci.net/24/2003/2020/.

Sauter, T., A. Arndt, and C. Schneider (2020). 'COSIPY v1.2 – An open-source coupled snowpack and ice surface energy and mass balance model'. In: *Geoscientific Model*

Development Discussions 2020, pp. 1–25. DOI: 10.5194/gmd-2020-21. URL: https://www.geosci-model-dev-discuss.net/gmd-2020-21/.

Schaefer, M., H. Machguth, M. Falvey, and G. Casassa (2013). 'Modeling past and future surface mass balance of the Northern Patagonia Icefield'. In: *Journal of Geophysical Research: Earth Surface* 118.2, pp. 571–588. ISSN: 2169-9011. DOI: 10.1002/jgrf.20038. URL: http://dx.doi.org/10.1002/jgrf.20038.

Schaefer, M., H. Machguth, M. Falvey, G. Casassa, and E. Rignot (2015). 'Quantifying mass balance processes on the Southern Patagonia Icefield'. In: *The Cryosphere* 9.1, pp. 25–35. DOI: 10.5194/tc-9-25-2015.

Schneider, C., M. H. Braun, M. Schaefer, J. Grießinger, and G. Casassa (2020a). 'Climate Impacts on Glaciers and Biosphere in Fuego-Patagonia.' In: *Lausanne: Frontiers Media SA*. DOI: doi:10.3389/978-2-88963-758-4.

Schneider, C., M. Glaser, R. Kilian, A. Santana, N. Butorovic, and G. Casassa (2003). 'Weather Observations Across the Southern Andes at 53°S'. In: *Physical Geography* 24, pp. 97–119.

Schneider, C., M. H. Braun, M. Schaefer, J. Grießinger, and G. Casassa (2020b). 'Editorial: Climate Impacts on Glaciers and Biosphere in Fuego-Patagonia'. In: *Frontiers in Earth Science* 8, p. 91. ISSN: 2296-6463. DOI: 10.3389/feart.2020.00091. URL: https://www.frontiersin.org/article/10.3389/feart.2020.00091.

Schneider, C. and D. Gies (2004). 'Effects of El Niño–southern oscillation on southernmost South America precipitation at 53°S revealed from NCEP–NCAR reanalyses and weather station data'. In: *International Journal of Climatology* 24.9, pp. 1057–1076. ISSN: 1097-0088. DOI: 10.1002/joc.1057. URL: http://dx.doi.org/10.1002/joc.1057.

Schwikowski, M., M. Schläppi, P. Santibañez, A. Rivera, and G. Casassa (2013). 'Net accumulation rates derived from ice core stable isotope records of Pío XI glacier, Southern Patagonia Icefield'. In: *The Cryosphere* 7.5, pp. 1635–1644. DOI: 10.5194/tc-7-1635-2013.

Shiraiwa, T., S. Kohshima, R. Uemura, N. Yoshida, S. Matoba, J. Uetake, and M. Godoi (2002). 'High net accumulation rates at the Campo de Hielo Patagonico Sur, South America, revealed by analyses of a 45.97m long ice core.' In: *Annals of Glaciology* 35, pp. 84–90.

Smith, R. B. and I. Barstad (2004). 'A Linear Theory of Orographic Precipitation'. In: *Journal of the Atmospheric Sciences* 61.12, pp. 1377–1391.

Strelin, J., G. Casassa, G. Rosqvist, and P. Holmlund (Apr. 2008). 'Holocene glaciations in the Ema Glacier Valley, Monte Sarmiento Massif, Tierra del Fuego'. In: 260, pp. 299–314.

Temme, F., J. Turton, T. Mölg, and T. Sauter (2020). 'Flow Regimes and Föhn Types Characterize the Local Climate of Southern Patagonia'. In: *Atmosphere* 11.9, p. 899. DOI: 10.3390/atmos11090899.

Thompson, D. W. J. and S. Solomon (2002). 'Interpretation of Recent Southern Hemisphere Climate Change'. In: *Science* 296.5569, pp. 895–899. ISSN: 0036-8075. DOI: 10.1126/science.1069270. eprint: http://science.sciencemag.org/content/296/5569/895.full.pdf. URL: http://science.sciencemag.org/content/296/5569/895.

Villalba, R. (1990). 'Climatic fluctuations in northern Patagonia during the last 1000 years as inferred from tree-ring records'. In: *Quaternary Research* 34.3, pp. 346–360. ISSN: 0033-5894. DOI: https://doi.org/10.1016/0033-5894(90)90046-N. URL: http://www.sciencedirect.com/science/article/pii/003358949090046N.

Villalba, R., A. Lara, J. A. Boninsegna, M. Masiokas, S. Delgado, J. C. Aravena, F. A. Roig, A. Schmelter, A. Wolodarsky, and A. Ripalta (2003). 'Large-Scale Temperature Changes Across the Southern Andes: 20th-Century Variations in the Context of the Past 400 Years'. In: *Climate Variability and Change in High Elevation Regions: Past, Present, Future*. Ed. by H. F. Diaz. Dordrecht: Springer Netherlands, pp. 177–232. DOI: 10.1007/978-94-015-1252-7_10.

Warren, C. R. and M. Aniya (1999). 'The calving glaciers of southern South America'. In: *Global and Planetary Change* 22, pp. 59–77.

Weidemann, S., T. Sauter, L. Schneider, and C. Schneider (2013). 'Impact of two conceptual precipitation downscaling schemes on mass-balance modeling of Gran Campo Nevado ice cap, Patagonia'. In: *Journal of Glaciology* 59.218, pp. 1106–1116. DOI: 10.3189/2013JoG13J046.

Willis, M., A. Melkonian, M. Pritchard, and J. Ramage (2012a). 'Ice loss rates at the Northern Patagonian Icefield derived using a decade of satellite remote sensing'. In: *Remote Sensing of Environment* 117, pp. 184–198. DOI: https://doi.org/10.1016/j.rse.2011.09.017.

Willis, M., A. Melkonian, M. Pritchard, and A. Rivera (2012b). 'Ice loss from the Southern Patagonian Ice Field, South America, between 2000 and 2012'. In: *Geophysical Research Letters* 39.17. DOI: 10.1029/2012GL053136.

Wilson, R., N. F. Glasser, J. M. Reynolds, S. Harrison, P. I. Anacona, M. Schaefer, and S. Shannon (2018). 'Glacial lakes of the Central and Patagonian Andes'. In: *Global and Planetary Change* 162, pp. 275–291. ISSN: 0921-8181. DOI: https://doi.org/10.1016/j.gloplacha.2018.01.004. URL: http://www.sciencedirect.com/science/article/pii/S0921818117306562.

A Appendices

A.1 Publication 1

A 17-year Record of Meteorological Observations Across the Gran Campo Nevado Ice Cap in Southern Patagonia, Chile, Related to Synoptic Weather Types and Climate Modes.

Weidemann S.S., Sauter T., Kilian R., Steger D., Butorovic N. and Schneider C. (2018): A 17-year Record of Meteorological Observations Across the Gran Campo Nevado Ice Cap in Southern Patagonia, Chile, Related to Synoptic Weather Types and Climate Modes. Front. Earth Sci. 6:53. doi: 10.3389/feart.2018.00053

Status: Published.

Own contribution:

- design of the study (with co-authors)
- compilation and processing of weather station data
- statistical analysis of meteorological time series (means, anomalies, extremes, trends)
- link climate features to mesoscale weather pattern and large-scale indices
- interpretation of the results (with co-authors)
- creating figures and tables (except Fig. 7)
- writing the first draft of the manuscript (except 3.2.)
- incorporating the remarks of the co-authors and reviewers

frontiers in Earth Science

ORIGINAL RESEARCH
published: 08 May 2018
doi: 10.3389/feart.2018.00053

A 17-year Record of Meteorological Observations Across the Gran Campo Nevado Ice Cap in Southern Patagonia, Chile, Related to Synoptic Weather Types and Climate Modes

Stephanie S. Weidemann[1,2]*, *Tobias Sauter*[3], *Rolf Kilian*[4,5], *David Steger*[1], *Nicolas Butorovic*[6] *and Christoph Schneider*[1]

[1] Geography Department, Humboldt University, Berlin, Germany, [2] Department of Geography, RWTH Aachen University, Aachen, Germany, [3] Department of Geography, Friedrich-Alexander University, Erlangen, Germany, [4] Department of Geology, University of Trier, Trier, Germany, [5] Departamento de Biologia Marina, Universidad de Magallanes, Punta Arenas, Chile, [6] Laboratorio de Climatologia, Instituto de la Patagonia, Universidad de Magallanes, Punta Arenas, Chile

OPEN ACCESS

Edited by:
John F. Burkhart,
University of Oslo, Norway

Reviewed by:
Zoe Courville,
US Army Corps of Engineers Cold Regions Research and Engineering Laboratory, United States
Guillermo Pablo Podesta,
University of Miami, United States
Joseph Michael Shea,
University of Northern British Columbia, Canada

***Correspondence:**
Stephanie S. Weidemann
s.weidemann@geo.rwth-aachen.de

Specialty section:
This article was submitted to Interdisciplinary Climate Studies, a section of the journal Frontiers in Earth Science

Received: 01 January 2018
Accepted: 18 April 2018
Published: 08 May 2018

Citation:
Weidemann SS, Sauter T, Kilian R, Steger D, Butorovic N and Schneider C (2018) A 17-year Record of Meteorological Observations Across the Gran Campo Nevado Ice Cap in Southern Patagonia, Chile, Related to Synoptic Weather Types and Climate Modes. Front. Earth Sci. 6:53. doi: 10.3389/feart.2018.00053

The network of long-term meteorological observations in Southernmost Patagonia is still sparse but crucial to improve our understanding of climatic variability, in particular in the more elevated and partially glaciated Southernmost Andes. Here we present a unique 17-year meteorological record (2000–2016) of four automatic weather stations (AWS) across the Gran Campo Nevado Ice Cap (53°S) in the Southernmost Andes (Chile) and the conventional weather station Jorge Schythe of the Instituto de la Patagonia in Punta Arenas for comparison. We revisit the relationship between *in situ* observations and large-scale climate models as well as mesoscale weather patterns. For this purpose, a 37-year record of ERA Interim Reanalysis data has been used to compute a weather type classification based on a hierarchical correlation-based leader algorithm. The orographic perturbation on the predominantly westerly airflow determines the hydroclimatic response across the mountain range, leading to significant west-east gradients of precipitation, air temperature and humidity. Annual precipitation sums heavily drop within only tens of kilometers from ~7,500 mm a^{-1} to less than 800 mm a^{-1}. The occurrence of high precipitation events of up to 620 mm in 5 days and wet spells of up to 61 consecutive days underscore the year-around wet conditions in the Southernmost Andes. Given the strong link between large-scale circulation and orographically controlled precipitation, the synoptic-scale weather conditions largely determine the precipitation and temperature variability on all time scales. Major synoptic weather types with distinct low-pressure cells in the Weddell Sea or Bellingshausen Sea, causing a prevailing southwesterly, northwesterly or westerly airflow, determine the weather conditions in Southernmost Patagonia during 68% of the year. At Gran Campo Nevado, more than 80% of extreme precipitation events occur during the persistence of these weather types. The evolution of the El Niño Southern Oscillation and Antarctic Oscillation

impose intra- and inter-annual precipitation and temperature variations. Positive Antarctic Oscillation phases on average are linked to an intensified westerly airflow and warmer conditions in Southernmost Patagonia. Circulation patterns with high-pressure influence leading to colder and dryer conditions in Southernmost Patagonia are more frequent during negative Antarctic Oscillation phases.

Keywords: Southern Patagonia, Chile, meteorological observations, Gran Campo Nevado Ice Cap, weather type classification, ENSO, Mann-Kendall trend test

1. INTRODUCTION

The climate of Southernmost Patagonia is dominated by impinging westerlies coming from the Pacific Ocean, which are strongly perturbed by the north-south striking Southern Andes. The strong orographic induced uplift results in hyperhumid conditions at the windward side of the Southernmost Andes while downslope subsidence leads to strong arid conditions within a belt of a few hundred kilometers on the eastern side (Carrasco et al., 2002; Schneider et al., 2003; Garreaud et al., 2013). Due to the prevailing westerlies and the vicinity of the Pacific Ocean, temperatures are moderate in Southernmost Patagonia with low daily and seasonal temperature amplitudes (Paruelo et al., 1998; Schneider et al., 2003; Villalba et al., 2003).

Moderate summer temperatures and high accumulation amounts constrain the equilibrium altitude line (ELA) at around 700 m elevation and thus enabled the formation of glaciated areas south of the Southern Patagonian Icefield. One of these is the Gran Campo Nevado (GCN) Ice Cap which extends to about 200 km^2 in the south of the Muñoz Gamero peninsula at about 53°S (**Figure 1**) (Schneider et al., 2007). The GCN Ice Cap is made up of the main glacier plateau with highest elevations of ~1,630 m a.s.l. and several individual outlet glaciers, some reaching sea level. The predominant westerlies cause overall strong winds and sharp local west-east gradients in precipitation and air temperature. Schneider et al. (2003) estimated the maximal annual precipitation amount of up to 10,000 mm a^{-1} at the highest elevations causing a high mass turnover with steep specific mass-balance gradients of the GCN outlet glaciers (Möller et al., 2007; Weidemann et al., 2013).

Large-scale modes of climate variability like the El Niño Southern Oscillation (ENSO) and Antarctic Oscillation (AAO), also known as the Southern Hemisphere Annular Mode (SAM), significantly influence precipitation and air temperature in southern South America (e.g., Thompson and Solomon, 2002; Marshall, 2003; Schneider and Gies, 2004; Fogt and Bromwich, 2006; Gillett et al., 2006). ENSO influences the interannual climate variations in the subtropical parts of South America, and weakens toward the southern tip of South America (Aceituno, 1988; Schneider and Gies, 2004; Gillett et al., 2006; Aravena and Luckman, 2009; Garreaud et al., 2009). Intensified positive AAO phases lead to a strong temperature and precipitation response (Gillett et al., 2006; Aravena and Luckman, 2009; Garreaud et al., 2009).

Climate variability in Southern Patagonia is the key driver of local changes in the cryosphere (e.g., Möller et al., 2007; Davies and Glasser, 2012). A variety of environmental paleorecords offer the possibility to study climate changes and short term climate variability (e.g., storm events) in Southern Patagonia from the late Holocene to the Last Glacial Maximum and beyond (e.g., Villalba et al., 2003; Lamy et al., 2010; Kilian and Lamy, 2012). However, the network of long-term meteorological observations which is needed to calibrate paleoclimate proxies for example from dendro-climatology (Aravena et al., 2002), sediment (Kilian et al., 2007) or peat cores (Kilian et al., 2003, 2007) as well as recent (Schneider et al., 2007) and Holocene (Koch and Kilian, 2005; Kilian et al., 2013) glacier fluctuations in the Southern Andes is still sparse in Southernmost Patagonia. The mass balance modeling study of Möller and Schneider (2008) indicate a pronounced mass-balance sensitivity of the GCN Ice Cap to temperature. The presented meteorological time series provide the opportunity to study the climate forcing on recent changes of the ice cap. The quality of future surface mass balance modeling studies benefits significantly from such unique long-term time series.

Here, we revise and extend former climate studies at the GCN Ice Cap (Schneider et al., 2003; Schneider and Gies, 2004) by analyzing the main climate features and their variability. Meteorological observations since 2000 provide more robust estimates of the observed annual and seasonal means, anomalies, extremes and trends. The characteristics are related to mesoscale weather patterns, classified by a hierarchical correlation-based leader algorithm. Annual and seasonal trends in air temperature are investigated by applying the non-parametric Mann-Kendall and Sen slope estimator trend test (Mann, 1945; Kendall, 1975; Yue et al., 2002). Furthermore, we focus on how ENSO and AAO impact the regional climate.

2. DATA

2.1. Observations

We analyze meteorological time series of four AWS located close to the GCN Ice Cap and one conventional weather station (WS) at Punta Arenas in Chile (**Figure 1**). An overview of the pertinent data is given in **Table 1**. Detailed information about the geographical setting of AWS Paso Galería (PG), AWS Puerto Bahamondes (BH) and AWS Estancia Skyring (SR) is given in Schneider et al. (2003). In addition, a fourth AWS named Arévalo (AR) has operated since September 2007 and is located at the northwestern side of the ice cap at about 58 m a.s.l..

The AWS are manufactured by Campbell Scientific Ltd. (United Kingdom). The similarly designed stations are equipped

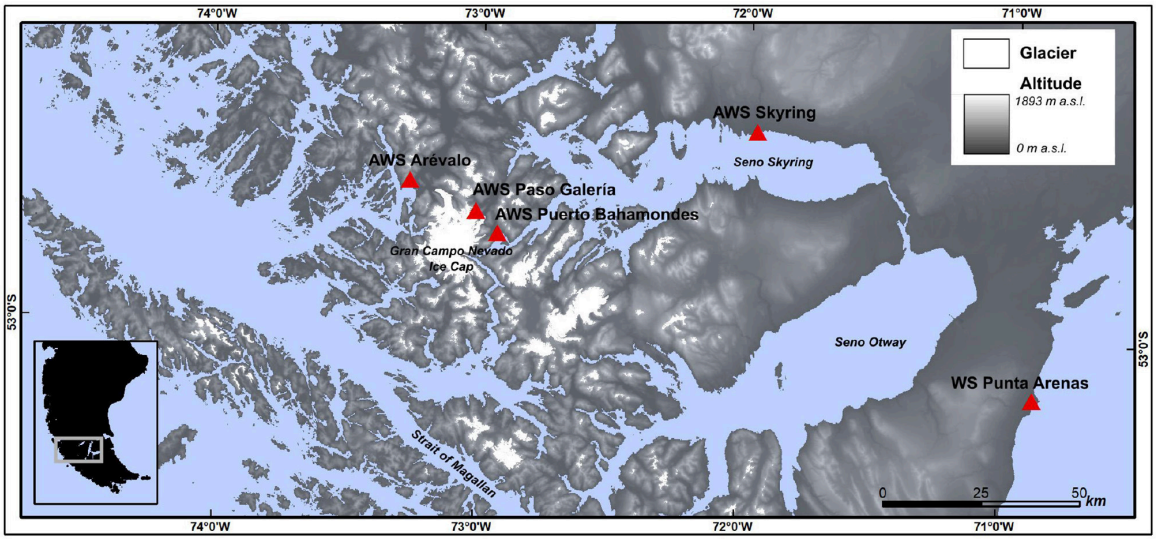

FIGURE 1 | Location of automatic weather stations (AWS) at the Gran Campo Nevado Ice Cap and the weather station (WS) at Punta Arenas. Glacier outlines are based on the Randolph Glacier Inventory 6.0.

TABLE 1 | Pertinent data to the weather station and automatic weather stations used in this study.

Name	Acronym	Latitude/Longitude	Altitude	Operating since	Variable
Arévalo	AR	52°41'S/73°16'W	58 m	September 2007	T, rH, P, SW, v, dir
Paso Galería	PG	52°45'S/73°01'W	383 m	October 1999	T, rH, P, SW, v, dir
Puerto Bahamondes	BH	52°48'S/72°56'W	26 m	October 1999	T, rH, P, SW, v, dir, sp
Skyring	SR	52°33'S/71°58'W	8 m	March 2001	T, rH, P, SW, v, dir
Punta Arenas (J.S.)	PA	53°08'S/70°53'W	6 m	Approx. 1970	T, rH, P, v, dir

Meteorological variables are air temperature (T), relative humidity (rH), precipitation (P), incoming shortwave radiation (SW), wind speed (v), wind direction (dir) and surface pressure (sp).

with sensors of air temperature, air humidity, precipitation, solar radiation, wind speed and wind direction (**Table 2**, Figure S1). All meteorological variables but precipitation are measured at 2 m above the surface. Precipitation is measured at 1 m above the ground using unshielded tipping-bucket rain gauges. This type of measurement underestimates precipitation by up to 30% at wind speeds of 1.5 m s^{-1} and even up to 50% at wind speeds of 3.0 m s^{-1} (Rasmussen et al., 2012; Buisán et al., 2017). Wind-speed induced deviations increase during snowfall due to an intensified drifting of snow (Rasmussen et al., 2012; Buisán et al., 2017). Substantial deviations are further suspected during high precipitation events, since strong precipitation events are often accompanied with strong wind gusts. During periods with very strong winds, the tipping bucket tends to shake which leads to an overestimation of precipitation. Correction factors for this kind of inaccuracy are not available. According to Schneider et al. (2003), the precision of the precipitation measurement at AWS BH and AWS PG is estimated to be about ±20%. We used this number as estimate of uncertainty for all AWS in this study. Wind-speed induced deviations have been minimized due to an additional fixation of the rain gauges in 2010 at AWS PG and in 2016 at AWS BH to avoid the shaking of the tipping bucket. Overall, precipitation data must be interpreted with care bearing in mind that these data are subject to considerable uncertainty in the order of potentially several tens of percent. Meteorological observations at the conventional WS Punta Arenas (PA) hold the longest and most complete time series. These observations (2000-2016) are measured according to the World Meteorological Organization standards. Data are provided by the Laboratory of Climatology, Instituto de la Patagonia, Universidad de Magallanes. Yearly records are published in Anales del Instituto de la Patagonia, Chile (e.g., Butorovic, 2016).

The quality of the time series is assured by performing some basic quality integrity and outlier checks (Durre et al., 2010). In case of unrealistic values, such as relative humidity larger than 100%, identical values for maximum and minimum air temperature, or a repetition of data records within a month, data are excluded. Furthermore, records are checked for daily outliers (Durre et al., 2010) and missing values within a month. Months with missing values of daily observations are not further considered. In case of precipitation, this leads to an exclusion of daily precipitation observations at AWS BH in 2000/01 and

TABLE 2 | Instrumentation at AWS Paso Galería, AWS Puerto Bahamondes, AWS Arévalo, and AWS Skyring as used in this study.

Variable	Sensor	Type	Nominal accuracy
Air temperature	Thermistor	Campbell HMP-35-AC, Campbell CS215	< 0.1 K, ±0.9°C (−40° to 70°C)
Relative humidity	Capacitor	Campbell HMP-35-AC, Campbell CS215	±3%, ±4% (0 to 100%)
Precipitation	Unheated tipping bucket rain gauges	Campbell AGR100, Young RM52203	±20% (assumption)
Wind direction	Wind vane, combined wind monitor	Campbell W200P, Young 05103	±2°, ±3°
Wind speed	Anemometer	Campbell A100R, Young 05103	1% ±0.1 m s^{-1}, 1% ±0.3 m s^{-1}
Incoming shortwave radiation	Silicon pyranometer	Campbell SP1110, Campbell CS300	±3%,±5% (daily totals)

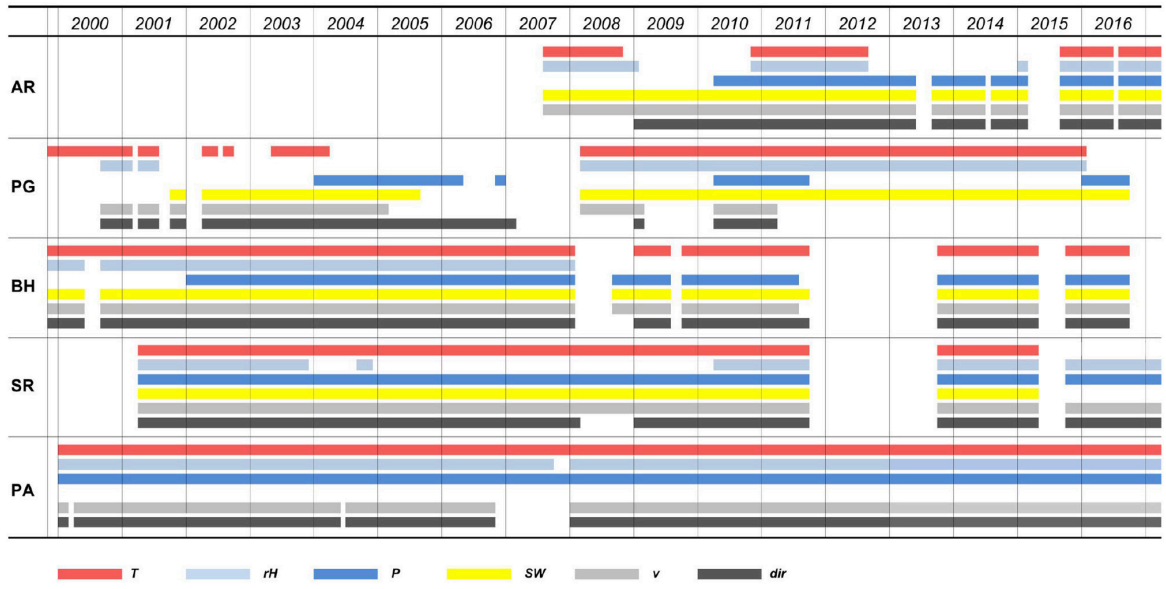

FIGURE 2 | Available observation periods at AWS Arévalo (AR), AWS Paso Galería (PG), AWS Puerto Bahamondes (BH), AWS Skyring (SR), and WS Punta Arenas (PA). Shown are measurement periods of air temperature (T), relative humidity (rH), precipitation (P), incoming shortwave radiation (SW), wind speed (v), and direction (dir).

at AWS PG in 2008/09. In addition, failures of power supply or sensors due to harsh weather conditions cause substantial data gaps in addition. **Figure 2** shows the available observation periods for each station on a monthly basis as used in this study.

2.2. Reanalysis Data

For mesoscale weather type classification, daily mean sea level pressure (MSLP) reanalysis data are obtained from the ERA-Interim dataset provided by the European Centre for Medium-Range Weather Forecasts (ECMWF) (Dee et al., 2011). The data sets are downloaded with a spatial resolution of 0.75° × 0.75° grids and 12-hourly temporal resolution (0 a.m., 12 p.m. UTC) between 1979 and 2016 for the area 10°S −80°S and 40°W −110°W covering most of South America and the Antarctic Peninsula. The selected area as well as the choice of MSLP as weather classification variable followed the weather type classification as used by Frank (2002) and Schneider et al. (2003).

2.3. Indices of Large-Scale Modes of Climate Variability

To reveal the impact of ENSO and the AAO on climate variability in Southernmost Patagonia, we compare the monthly anomalies of observations with the Oceanic Niño Index (ONI) and the Antarctic Oscillation Index (AAOI). Both indices are provided by the U.S. National Oceanic and Atmospheric Administration (NOAA) - Climate Prediction Center.

ONI identifies El Niño and La Niña events in the tropical Pacific by using a 3-month running mean of ERSST.v5 sea surface temperature anomalies in the Niño 3.4 region (5°N-5°S, 120°-170°W) (Barnston et al., 1997; Huang et al., 2017). Events are defined as five consecutive overlapping 3-month periods with anomalies ≥+0.5°C for El Niño and ≤-0.5°C for La Niña events. Data is available from http://www.cpc.ncep.noaa.gov/data/indices/oni.ascii.txt.

The monthly AAOI is constructed by projecting the monthly mean 700 hPa height anomalies poleward of 20°S onto the first

empirical orthogonal function mode of monthly mean height anomalies at 700 hPa (Thompson and Solomon, 2002). Positive phases are characterized by a strengthening and poleward shift of the westerlies with decreased surface pressure and geopotential height over the fringe of Antarctica. During negative phases, opposite conditions prevail. Monthly data of AAOI can be obtained from http://www.cpc.ncep.noaa.gov/products/precip/CWlink/daily_ao_index/aao/aao_index.html.

3. METHODS

3.1. Indices of Climate Extremes

Climate extremes of air temperature and precipitation (**Table 3**) are described using selected indices of extremes (Tank et al., 2009). In case of air temperatures extremes, time series of maximum (TX) and minimum (TN) air temperature are analyzed regarding the number of days with ice ($TX \leq 0°C$) (ID) and frost ($TN \leq 0°C$) (FD). Percentiles are calculated based on the available observations period (**Figure 2**) to define the number of days with TX < 10th percentile (P1TX), TN < 10th percentile (P1TN), TX > 90th percentile (P9TX) and TN > 90th percentile (P9TN). Furthermore, we are interested in the maximum length of a cold spell (CS) with consecutive days of TN < 10th percentile, and the maximum length of a warm spell (TWS) with consecutive days of TX > 90th percentile per year.

Precipitation extremes are described by the absolute maximum of 1-Day (PDX) and 5-Day (P5DX) precipitation (mm) as well as the annual amount of daily precipitation larger than the 95th percentile (P95P) and the 99th percentile (P99P). The maximum number of days with daily precipitation higher than 20 mm (HP) and below 1 mm (DD), and the maximum length of wet spells (PWS) and dry spells (DS) per year are also examined.

3.2. Weather Type Classification

Weather types are classified by applying the automated classification map-pattern scheme by Lund (1963) based on MSLP. The LUND-algorithm is based on so-called leader patterns. It constitutes a low computational cost predecessor of other cluster algorithms (Hartigan, 1975; Murtagh, 1985). Within the LUND-algorithm, in a first run a leader is defined as the one observation showing most similar cases (observations) of correlations higher than a given threshold with all other observations (Lund, 1963; Philipp et al., 2014a). After removal of the leader and its matching cases, e.g., all observations that correlate with the identified leader above the set threshold Pearson correlation coefficient, the remaining class leaders are called in similar iterative processes (Lund, 1963; Philipp et al., 2014a). After the determination of all leaders, single days are assigned to a specific weather type by returning all observations to the data pool and assigning each one to the nearest leader based on linear correlation (Lund, 1963; Philipp et al., 2014a). The threshold Pearson correlation coefficient for finding leader weather types in this study is set to 0.85. The Lund classification scheme accentuates the dominance of few weather types with westerly air flow. Subsequently, it finds further weather types that occur only rarely but are important and significantly different patterns. In contrast, k-mean leader algorithms tend to locate centroids in such that all classes become equally large (Philipp et al., 2014b). The latter would have resulted in many undesirably similar weather types of principally westerly airflow.

Weather type classifications are calculated from the ERA-Interim MSLP reanalysis data for the period 1979–2016.

TABLE 3 | Indices of air temperature extremes based on daily maximum (TX) and minimum (TN) air temperatures.

	AR		PG		BH		SR		PA	
	Value	**Year**	**Value**	**Year**	**Value**	**Year**	**Value**	**Year**	**Value**	**Year**
Max TX	23.6	2008	20.4	2004	24.5	2008	25.8	2004	29	2013
Max TN	−5.4	2011	−8.9	2002	−8.1	2005	−11.3	2001	−5.1	2002
Max range	15.1	2008	15.3	2002	16.1	2005	21.0	2006	19.2	2004
Max ID	8	2012	39	2012	6	2005	7	2014	4	2002
Max FD	49	2011	130	2009	66	2001/02	112	2005	100	2002
Max P1TX	69	2012	58	2012	63	2014	64	2014	58	2002
Max P1TN	61	2011	50	2003	60	2002	61	2002	68	2002
Max P9TX	56	2008	54	2001	58	2004	61	2008	53	2008
Max P9TN	51	2016	83	2013	75	2015	70	2014	50	2004
Max CS	16	2012	11	2012	19	2005	16	2001/14	13	2001
Max TWS	9	2008	14	2004	13	2005/08	13	2005	12	2008
Mean TX	7.4	07–16	5.1	00-16	8.9	00–16	9.7	01-16	10.2	00-16
Mean TN	4.5	07–16	2.3	00-16	4.0	00–16	3.2	01–16	2.6	00–16
Mean range	2.8	07–16	2.8	00-16	4.9	00-16	6.5	01–16	7.6	00–16

*Listed are the absolute maximum of daily TX and TN, of daily air temperature range, of days with ice (TX<0°C) (ID) and with frost (TN<0°C) (FD), maximum of days with TX< 10th percentile (P1TX), TN < 10th percentile (P1TN), TX> 90th percentile (P9TX) and TN> 90th percentile (P9TN), maximum length of a cold spell (CS) with consecutive days of TN < 10th percentile, and the maximum length of a warm spell (TWS) with consecutive days of TX > 90th percentile. Percentiles are calculated based on the observations period of each station (**Figure 2**).*

We apply the cost733class-1.2 software (http://cost733.geo.uni-augsburg.de/cost733class-1.2) originally designed for circulation type classifications in Europe (Philipp et al., 2014b). We checked for the optimal number of classes using a k-means leader algorithm by evaluating the increase of explained cluster variance with increasing numbers of cluster. The number of 10 weather types was found to be optimal which is in accordance with the weather type classification of Frank (2002), used by Schneider et al. (2003). Earlier weather type classifications document only six weather types (Endlicher, 1991; Compagnucci and Salles, 1997). **Figure 7** shows the resulting 10 MSLP centroids obtained from the classification procedure after Lund (1963) as used in this study.

3.3. Trend Detection

Annual and seasonal trends in air temperature based on the 17-year record of AWS PG, AWS BH, AWS SR, and WS PA are analyzed. Air temperature changes over the given time period can further be related to observed recent changes of the GCN Ice Cap outlet glaciers.

Trends are detected using the non-parametric Mann-Kendall (MK) and Sen slope estimator (SSE) trend test. The combined MK and SSE test has been frequently used to quantify the significance and magnitude of trends in climatological and hydrological time series (e.g., Hamed, 2008; Gocic and Trajkovic, 2013; Kisi and Ay, 2014; Onyutha et al., 2016). The MK test is a non-parametric test to identify linear and non-linear trends in time series (Mann, 1945; Kendall, 1975). The test does not require normally-distributed input data and has a low sensitivity to abrupt breaks due to inhomogeneous time series. The magnitude of the trend in terms of slope is the robust estimate of the median following the approach by Sen (1968) and Theil (1950).

The elimination of autocorrelation in time series analysis is essential because otherwise autocorrelation increases the chances of detecting a significant trend even in case trends are absent. Therefore, Yue et al. (2002) proposed the Trend-Free Pre-Whitening (TP) method in case both trend and lag-1 autocorrelation exist in the data record.

To detect trends in the time series we followed the described steps below:

- testing the significance of the lag-1 autocorrelation (AC) in each time series (step 1)
- in case of significant AC, TP is applied (step 2) and the MK and SSE tests are applied subsequently
- in case of insignificant AC, the MK and SSE tests are performed directly on the original time series (step 3)

The Trend-Free Pre-Whitening procedure (step 2) includes the following steps. First, the apparent linear trend of the time series X_i is removed. Afterward, the lag-1 correlation coefficient r_{ac} of the detrended time series $X_{DE,i}$ is determined. The lag-1 AC is then eliminated from $X_{DE,i}$ by:

$$X_{DE,A,i} = X_{DE,i} - r_{ac} \cdot X_{DE,i-1}. \quad (1)$$

The removed linear trend is then added to $X_{DE,A,i}$ to obtain the final blended time series to which the MK and SSE trend detection test is applied.

4. RESULTS AND DISCUSSION

4.1. Time Series and Extremes

Time series of air temperature, relative humidity, precipitation, wind speed and wind direction are analyzed regarding their daily, monthly and annual means, and anomalies. Mean annual and monthly values of the meteorological variables for each station are listed in Table S1 in the supplement. Annual means are averaged based on monthly mean values. The study period of each time series relates to the available observation period shown in **Figure 2**.

4.1.1. Air Temperature

Mean annual air temperatures for the individual measurement period of each station (**Figure 2**) along the west-east transect are 5.8°C at AWS AR, 3.8°C at AWS PG, 6.0°C at AWS BH, 6.6°C at AWS SR, and 6.6°C at WS PA.

The air temperature distribution in mountain areas with strong orographic effects can also be detected in the spatial distribution of mean daily maximum and minimum air temperature and air temperature range (**Table 3**). The absolute extremes of daily air temperatures range from −8.9°C and +20.4°C at AWS PG, from −8.1°C and +24.5°C at AWS BH, and −11.3°C and +25.8°C at AWS SR during the observation period 2000 to 2016.

The coldest temperature regime with the lowest mean of daily maximum temperature of +5.1°C and minimum temperature of 2.3°C is found at AWS PG. The numbers of frost and ice days are larger than at the other stations due to the altitude and contiguity to the ice cap (**Table 3**). In 2009, minimum temperature dropped below 0°C in 36% of the days. The lower amplitudes of the annual temperature cycle of AWS AR and AWS BH are a result of more maritime conditions compared to

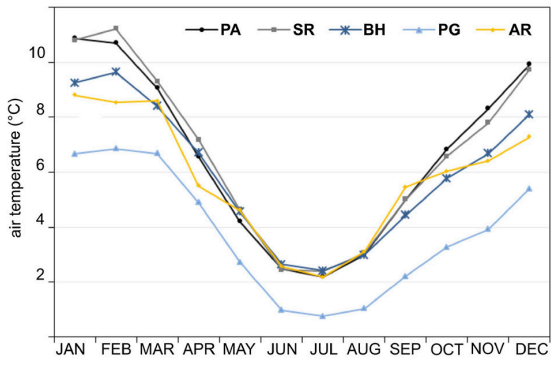

FIGURE 3 | Mean monthly air temperature at AWS Arévalo (AR), AWS Paso Galería (PG), AWS Puerto Bahamondes (BH), AWS Skyring (SR), and WS Punta Arenas (PA) averaged over the individual observation period (**Figure 2**).

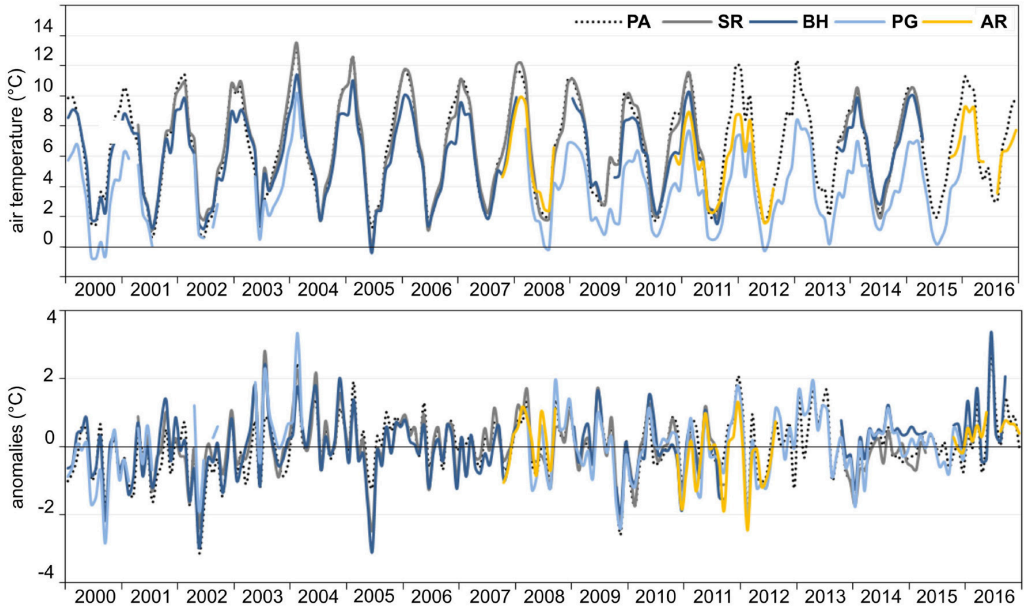

FIGURE 4 | Monthly air temperature and monthly anomalies at AWS Arévalo (AR), AWS Paso Galería (PG), AWS Puerto Bahamondes (BH), AWS Skyring (SR), and WS Punta Arenas (PA) from 2000 to 2016.

AWS SR and WS PA (**Figure 3**, Table S1). The influence of the Pacific Ocean also leads to less days with frost and ice. Toward the east the mean annual temperatures and the number of days with daily maximum air temperature exceeding the 90th percentile and daily minimum air temperature dropping below the 10th percentile increase.

Figure 4 illustrates the monthly means of air temperature and anomalies since 2000, showing a high correlation of $r = 0.94–0.99$ in temperature variability between all stations. Above average cold months were observed in spring 2000, winter 2002 and 2005, spring 2009 and summer 2011/12 at all stations. The longest cold spell and the largest numbers of days where the maximum temperature drops below the 10th percentile for AWS AR and AWS PG are found in 2012 (**Table 3**). Positive anomalies occurred during winter 2003, the summer months 2003/04 and during winter 2016.

The annual anomalies of mean, maximum and minimum temperatures suggest in general milder climate conditions with less extremes since 2012 at GCN (Tables S2, S3). This observation is supported by lower annual means of daily temperature ranges and a decreasing number of days with frost per year at all stations. Furthermore, the percentage of days per year with extreme warm (P9X) or cold conditions (P1N) are decreasing as well (Table S3). Annual changes in the duration of cold or warm spells, however, are not significant. We hypothesize that the warmer conditions are caused by the strengthening of the westerlies during the enhanced positive AAO in recent years (Marshall, 2003).

4.1.2. Wind Speed and Direction

The prevailing westerlies dominate the wind patterns year-around at GCN with mean annual wind speeds ranging from 3.1 m s^{-1} (AWS BH) to 5.1 m s^{-1} (AWS PG) (**Figure 5**). The highest mean of daily mean and maximum wind speeds of 5.1 m s^{-1} and 13.4 m s^{-1} are observed at AWS PG along with prevailing north-west winds. Mean wind speeds of 3.1 m s^{-1} at AWS BH are lower than at AWS SR and WS PA with values of 3.7 m s^{-1} and 4.5 m s^{-1}, respectively. The mean maximum wind speed of 9.7 m s^{-1} at AWS BH, however, is higher than at AWS SR (8.0 m s^{-1}). Schneider et al. (2003) pointed out that this underscores the occurrence of strong gusty winds in morphologically structured landscapes. In general, mean and maximum wind speeds decrease during the winter months at all stations but AWS AR. The characteristic southerly winds at AWS AR are caused by the topographic situation channeling the airflow.

4.1.3. Precipitation

A sharp gradient of precipitation can be found across the GCN Ice Cap within only tens of kilometers. Mean annual precipitation (2008–2016) increases from ~3,800 mm at the west side of GCN at AWS AR to ~6,100 mm at AWS PG while it decreases again on the lee-side to ~4,000 mm at AWS BH. Within a distance of about 80 km, precipitation sharply drops to ~790 mm at AWS SR. Mean annual amounts of 570 mm are observed at WS PA for the same study period. Considering the observations at AWS PG since 2002, the annual mean accounts for ~7,500 mm with the highest annual

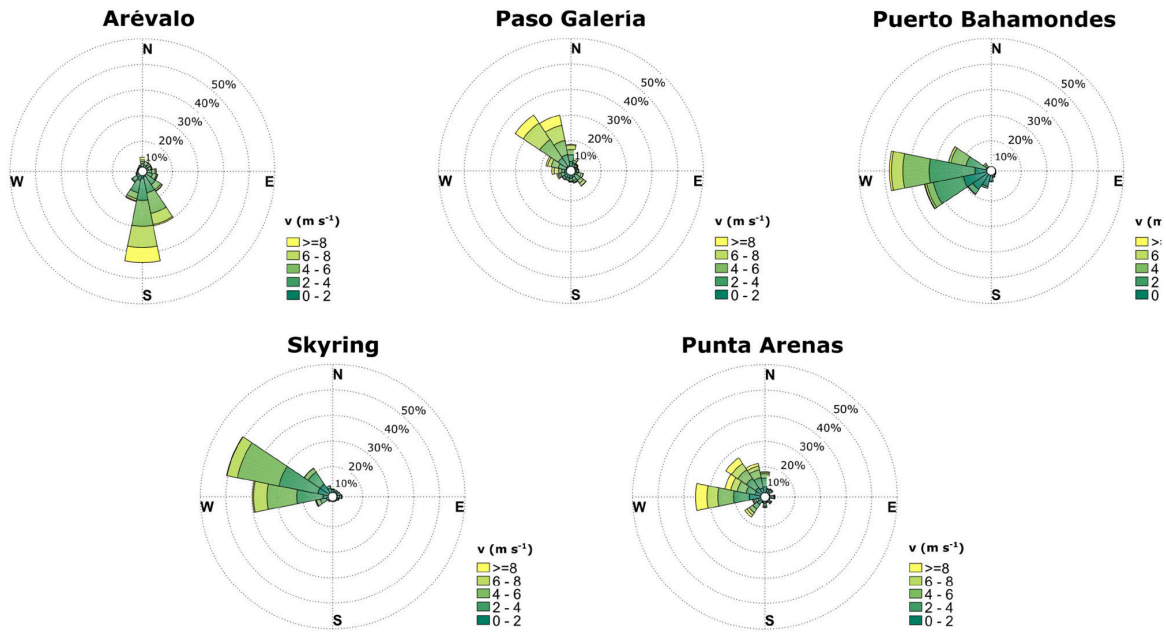

FIGURE 5 | Frequency of wind direction and wind speed (v) at AWS Arévalo, AWS Paso Galería, AWS Puerto Bahamondes, AWS Skyring, and WS Punta Arenas. The available observation period for each station can be found in **Figure 2**.

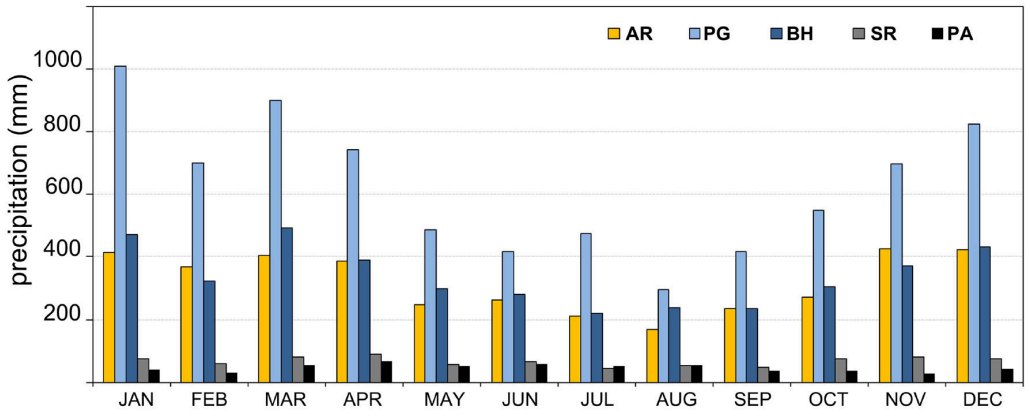

FIGURE 6 | Mean monthly precipitation AWS Arévalo (AR) (2008-2016), AWS Paso Galería (PG), AWS Puerto Bahamondes (BH), AWS Skyring (SR), and WS Punta Arenas (PA). Values were averaged from 2000 to 2016.

amount of ~9,500 mm measured in 2003. Higher measurement inaccuracies in the first years of precipitation observations must be assumed due to the less firm installation of the rain gauge. Therefore, the estimated mean annual values of AWS PG (10,900 mm ±20%) and AWS BH (6,600 mm ±20%) as provided by Schneider et al. (2003) are resulting from measurement errors during episodes of strong winds, leading to an overestimation of annual precipitation sums between 2000 and 2003.

The intra-annual variability of precipitation at AWS AR, AWS PG, and AWS BH correlates well with the highest amounts occuring during the austral summer. The drop in monthly precipitation in February is revealed at all three stations (**Figure 6**). The annual course at AWS SR is more similar to the ones at GCN, but with much lower precipitation, while the intra-annual variability at WS PA is opposite. Precipitation during the winter is slightly higher than during the austral summer. Inter-annual variations of precipitation between AWS SR and AWS

PA show opposite patterns. In years with positive precipitation anomalies at AWS SR, precipitation mostly decreases at AWS PA (Table S2). In principal, the same holds true for AWS BH and AWS PA for the few full years of available precipitation data.

The occurrence of high precipitation events of up to 620 mm in 5-days in 2004 and wet spells of up to 61 days in 2006 underscore the year-around wet conditions at GCN (**Table 4**). Individual events of extreme precipitation (P5DX, P95P, P99P) are most frequent at AWS PG. Between 2002 and 2006, 26% of the annual amount of precipitation fell during days where the daily precipitation exceeds the 95th percentile (Table S4). This ratio changes to a mean of 8% in 2010, 2011, 2016. The amounts of precipitation during extreme precipitation events and days with daily precipitation larger than 20 mm (HP) are similar between the western (AWS AR) and eastern side (AWS BH) of GCN with a high year-to-year variability between 2011 and 2016. The percentage of HP is negligible for AWS SR and WS PA. Nevertheless, daily extreme events of up to 124 mm can occur at AWS SR as observed in 2010. The lengths of wet spells are subsequently smaller while the lengths of dry spells are much larger compared to the three stations at GCN (**Table 4**).

4.2. Trends

Annual and seasonal trends in mean (T), minimum (TN) and maximum (TX) air temperature are analyzed for AWS PG, AWS BH, AWS SR, and WS PA as described in section 3.3. Significant lag-1 autocorrelation was only detected for TN of AWS BH which was corrected following the TP procedure before trend detection. An overview of the trend analysis results is given in **Table 5**.

Trends in annual mean air temperature for AWS PG and AWS PA are significant at the 90% level with a trend magnitude (Sen Slope) of $+0.05^{\circ}$C a^{-1} and $+0.02^{\circ}$C a^{-1}. An increasing

TABLE 4 | Indices of precipitation extremes.

	AR		PG		BH		SR		PA	
	Value	**Year**	**Value**	**Year**	**Value**	**Year**	**Value**	**Year**	**Value**	**Year**
Max 1-Day	125	2011	284	2004	213	2006	124	2010	51	2012
Max 5-Day	256	2011	620	2004	341	2004	201	2001	94	2012
Max P95P	1258	2014	2693	2003	1517	2007	524	2001	254	2015
Max P99P	441	2012	979	2006	620	2007	370	2001	85	2012
Max HP	79	2012	159	2003	80	2007	9	2001	7	2015
Max DD	90	2016	83	2005	128	2002	259	2006	284	2016
Max PWS	47	2016	61	2006	45	2010	15	2001	12	2006
Max DS	9	2012	14	2005	21	2006/16	50	2006	33	2005

*Listed are the absolute maximum of 1-Day and 5-Day precipitation (mm), of the total annual amount of daily precipitation larger than the 95th percentile (P95P), of the total annual amount of daily precipitation larger than the 99th percentile (P99P), the maximum number of days with daily precipitation higher than 20 mm (HP), the maximum number of days with daily precipitation below 1 mm (DD), and the maximum length of wet spells (PWS) and dry spells (DS). Percentiles are calculated based on the observations period of each station (**Figure 2**).*

TABLE 5 | Statistical results of the trend analysis for annual and seasonal mean (T), maximum (TX), and minimum (TN) air temperature in $^{\circ}$C a^{-1} for AWS Paso Galería (PG), AWS Puerto Bahamondes (BH), AWS Skyring (SR), and WS Punta Arenas (PA).

		PG			BH			SR			PA		
		T	**TX**	**TN**	**T**	**TX**	**TN**	**T**	**TX**	**TN**	**T**	**TX**	**TN**
Annual	Sen Slope	0.05	−0.15	0.31	0.03	−0.08	0.09	−0.02	−0.05	0.11	0.03	0.03	0.03
	p-value	**0.04**	0.48	**<0.01**	0.46	**0.06**	0.31	0.74	0.55	0.25	**0.04**	0.23	0.30
DJF	Sen slope	0.01	-0.24	0.16	0.01	−0.15	0.11	-0.11	-0.22	0.14	-0.01	−0.01	−0.02
	p-value	1.00	**0.02**	0.11	1.00	**0.02***	**0.04***	**0.06**	**0.03**	0.38	0.65	0.90	0.65
MAM	Sen slope	0.04	-0.03	0.22	0.04	-0.07	0.14	0.09	0.01	0.24	0.02	0.03	0.02
	p-value	0.51	0.84	**0.01**	0.45	0.44	**0.03**	0.25	0.95	**<0.01**	0.13	0.30	0.65
JJA	Sen slope	0.04	−0.12	0.15	0.09	-0.03	0.14	0.02	−0.05	0.10	0.05	0.04	0.03
	p-value	0.46	**0.04**	**0.01***	**0.08**	0.64	0.09	0.84	0.64	0.20	**0.08**	0.11	0.23
SON	Sen slope	0.02	-0.08	0.19	0.05	-0.11	0.18	0.00	−0.17	0.10	0.04	0.03	0.06
	p-value	0.65	**0.01**	**0.01**	0.14	0.08	**0.02**	0.95	0.16	0.25	0.17	0.48	0.11

*Significant values at the 90% level are shown in bold. Trends significant at the 95% level are bold and underlined. P-values denoted with * are obtained after TP procedure from time series with significant lag-1 autocorrelation. In case of annual trend calculation, years with less than 250 days per year with data were not considered.*

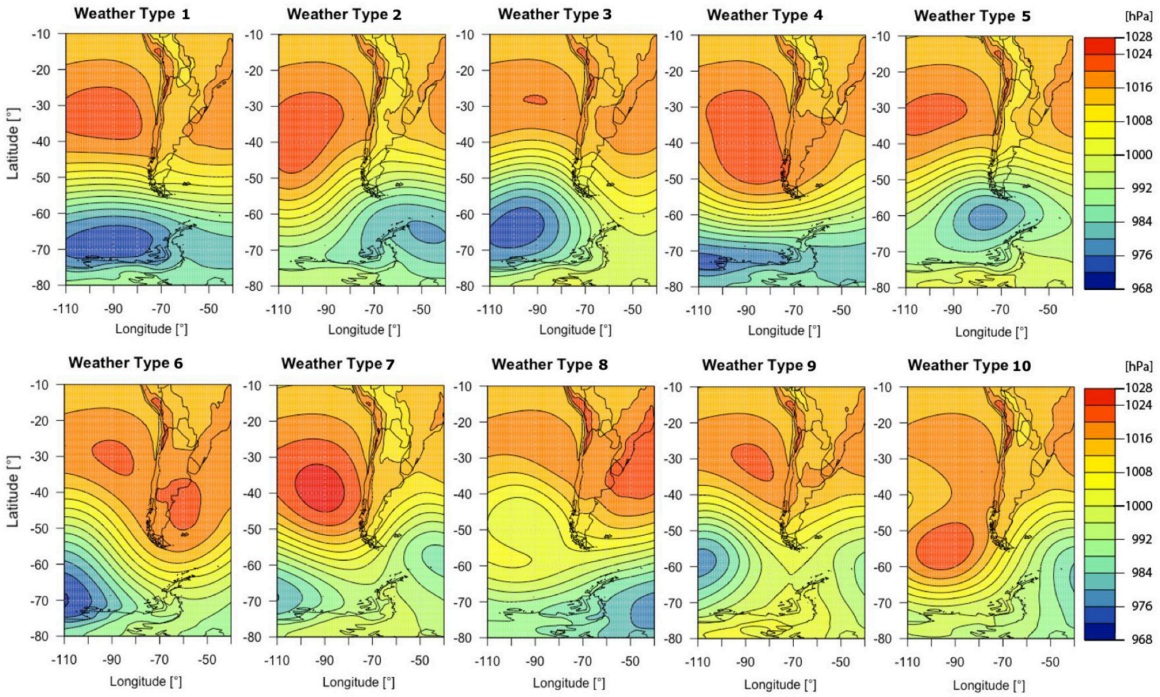

FIGURE 7 | Ten major weather types classified by means of ERA-Interim MSLP reanalysis data for the period 1979 to 2016.

trend of seasonal mean air temperature is only apparent during winter (JJA) at AWS BH and WS PA. A significant upward trend is detected in the annual TN at AWS PG of +0.31°C a^{-1} between 2000 and 2016. This upward trend is also reflected in different seasons as well. TN increases significantly during spring (SON), winter and fall (MAM) at AWS PG, and during summer (DJF), spring and fall at AWS BH. Three of four stations show upwards trends of TN during spring and fall. In contrast, significant downward trends of TX during the summer season are determined for AWS PG, AWS BH and AWS SR. The largest trend of −0.24°C a^{-1} (2000 and 2016) was found at AWS PG. No significant trend has been detected in annual and seasonal TX time series for WS PA.

4.3. Types of Synoptic Weather Patterns

Ten major types of synoptic weather patterns have been classified for Southernmost Patagonia (**Figure 7**). Weather type 1 is characterized by a strong north-south pressure gradient resulting from a distinct high-pressure cell over the Pacific and low-pressure trough over the Bellingshausen Sea, which leads to intensified westerlies. During weather type 2, the high-pressure cell is weaker and shifted toward the south, while the low-pressure cell is located south of Tierra del Fuego in the Weddell Sea. Cold and humid air masses from the south-west are advected to Southernmost Patagonia (Frank, 2002). A similar circulation pattern to type 2, but with a distinct low-pressure cell located south of Tierra del Fuego in the Drake Passage occurs during weather type 5. A north-westerly advection of humid and warm air occurs when both, the Pacific anticyclone and the low-pressure cell, are shifted toward the north-west of southern South America compared to type 1. Pressure gradients become weaker during weather type 9 while the principal synoptic configuration is mostly the same.

The atmospheric circulation of weather type 4 is dominated by an intensified high-pressure cell in the southern Pacific reaching far toward the eastern side of the Southern Andes. The persistence of this situation leads to warmer and dryer conditions. A southward shift of the Pacific anticyclone with the advection of colder air masses from south-west, is present during weather type 7. A strong high-pressure cell in the southern Atlantic accompanied with low pressure in the southern Pacific is present during weather type 6. The Atlantic anticyclone is stronger and shifted toward the north in case of type 8. Both weather patterns imply a northerly or westerly airflow with increased air temperatures. The circulation pattern of weather type 10 is dominated by a strong high-pressure cell located far toward the south in the Pacific leading to a cold and humid airflow from the south over Southernmost Patagonia.

Major synoptic weather types with distinct low-pressure cells in the Weddell Sea (types 2 and 5) or Bellingshausen Sea (types 1, 3, and 9), causing a prevailing southwesterly, northwesterly or westerly airflow, account for 68% of all days in Southernmost Patagonia. In 32% of all situations, high pressure cells over the southern Pacific (types 4, 7, and 10) and southern Atlantic (types

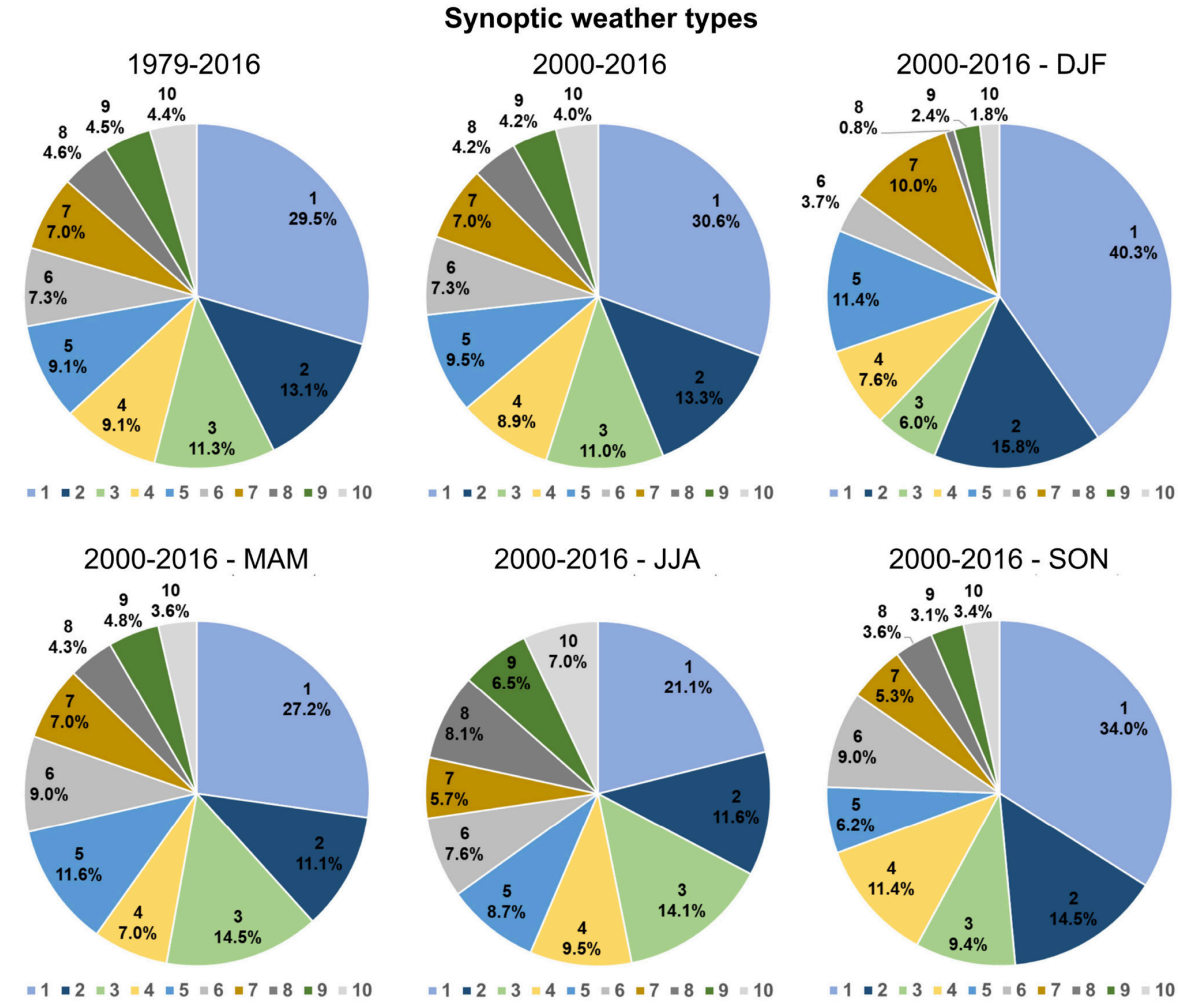

FIGURE 8 | Frequencies of synoptic weather types averaged between 1979 and 2016, 2000 and 2016 and for summer (DJF), fall (MAM), winter (JJA) and spring (SON) between 2000 and 2016.

6 and 8) determine the weather of Southernmost Patagonia. Circulation pattern type 1 with a strong zonal westerly air flow is the most common type of all weather patterns, occurring 30% of the year (**Figure 8**, **Table 6**). During the austral summer the frequency of weather patterns with westerly air flow increases to 76% compared to high-pressure influenced weather types (24%). During the austral winter anticyclonic circulation patterns account for 40% of all situations, while low-pressure weather types occur less. This is in accordance with the generally lower wind speeds found in winter at all weather stations in this study.

Anomalies of observed air temperature, precipitation, wind speed, solar radiation, and relative humidity are analyzed according to the major synoptic types of weather patterns for all five stations (**Figure 9**). Similar types of weather patterns are grouped into classes as listed in **Table 6**. Large positive air temperature anomalies are accompanied with strong westerlies (class 1) at all five stations. Air temperature anomalies at AWS BH, AWS AR, and AWS PG however are smaller compared to AWS SR and WS PA due to the influence of the nearby GCN Ice Cap and proximity to the Pacific Ocean. The impact of strong westerlies on air temperature anomalies is largest in the austral fall. On days with southwesterly airflow (class 2 and 5), air temperatures slightly drop at the stations located close to GCN Ice Cap, while air temperatures tend to rise during northwesterly airflow (class 3 and 9). The advection of colder air masses from the southwest (class 2 and 5) largely determines the air temperature variability during the summer and fall season.

The impact of circulation patterns with intensified high-pressure cells in southern Pacific and Atlantic (classes 4 and 7, 6 and 8 and 10) on air temperature variability is in general low, but

TABLE 6 | Frequency of synoptic weather types and classes (%) between 1979 and 2016 and 2000 and 2016.

	Frequency of synoptic types (%)										Frequency of synoptic classes (%)					
1979-2016	**1**	**2**	**3**	**4**	**5**	**6**	**7**	**8**	**9**	**10**	**1**	**2 and 5**	**3 and 9**	**4 and 7**	**6 and 8**	**10**
Mean	30	13	11	9	9	7	7	5	4	4	30	22	16	16	12	4
DJF	38	15	8	7	11	3	10	1	4	2	38	26	12	17	4	2
MAM	26	12	14	7	10	9	7	5	6	5	26	22	19	14	14	5
JJA	20	12	13	10	9	8	5	9	5	8	20	21	19	15	17	8
SON	34	14	10	12	6	9	6	4	3	3	34	20	13	18	12	3
2000-2016	**1**	**2**	**3**	**4**	**5**	**6**	**7**	**8**	**9**	**10**	**1**	**2 and 5**	**3 and 9**	**4 and 7**	**6 and 8**	**10**
Mean	31	13	11	9	9	7	7	4	4	4	31	23	15	16	12	4
DJF	40	16	6	8	11	4	10	1	2	2	40	27	8	18	5	2
MAM	27	11	15	7	12	9	7	4	5	4	27	23	19	14	13	4
JJA	21	12	14	10	9	8	6	8	6	7	21	20	21	15	16	7
SON	34	15	9	11	6	9	5	4	3	3	34	21	12	17	13	3

Frequencies are given as annual means and seasonal means for summer (DJF), fall (MAM), winter (JJA) and spring (SON).

highest for AWS SR and WS PA. The advection of air masses from the north and northwest under high-pressure influence (class 6 and 8) cause warmer conditions at all stations in SON and DJF, while temperatures decrease during the austral winter except for AWS AR which is the only station located clearly west of the Cordillera. The advection of cold air masses from the south (class 10) causes a significant decrease of daily air temperature at all stations with the largest negative anomalies for WS PA and AWS SR. During fall and spring, air temperatures drop significantly below the specific means (class 10).

Circulation patterns highly impact the precipitation variability at the GCN Ice Cap during all seasons. The orographic induced uplift of the humid air masses from west and southwest (classes 1 and 2 and 5) comes along with year-around positive precipitation anomalies at the GCN Ice Cap. Precipitation amounts decrease significantly during high-pressure influences, in case of classes 6 and 8 and 10. The stations located at GCN (AWS AR, AWS BH, AWS PG) obtain more than 80% of daily precipitation during westerly airflow. East of the GCN Ice Cap at AWS SR and WS PA, mean daily precipitation amounts are similar during all weather types. Precipitation increases slightly on days with southwesterly air flow at AWS SR, while at WS PA daily precipitation increases on days with north to northwesterly wind directions (classes 3 and 9 and 6 and 8). The annual precipitation amounts at AWS SR and WS PA are still mainly determined by the airflow from west (class 1) and south west (class 2 and 5) despite the fact that these stations are clearly located on the leeward of the Cordillera during westerly air flow but extreme precipitation rates are rare. Of all daily precipitation extremes (higher than the 90th percentile) 80% can be associated with classes 1 and 2 and 5 at the GCN stations, while the percentage decreases to 70% at AWS SR and 51% at WS PA. High precipitation events at WS PA are also present during the class 3 and 8 with 20 and 13% of the days, respectively. This finding indicates that precipitable water in the air column is carried across the Cordillera by strong upper air westerly winds. During classes 1 and 2 and 5, both stations experience often foehn-type weather conditions with cloud dispersal due to the subsidence of air masses on the lee-side of the Cordillera. High incoming solar radiation can therefore be observed at AWS SR during these types of weather patterns. Since the westerly air flow is also accompanied by higher air temperatures, relative humidity decreases at all stations, but strongest at AWS SR and WS PA.

Wind speed is highest during westerly (class 1) and southwesterly (class 2 and 5) airflow for all stations. AWS AR shows negative wind speed anomalies on days with strong westerlies which are caused by the location of the AWS and local effects due to the surrounding topography as described in section 4.1.2. Wind from north-northwest (classes 3 and 9 and 6 and 8) is in general weaker on days with high-pressure influence (class 6 and 8).

4.4. Teleconnection to El Nino-Southern Oscillation and Antarctic Oscillation

4.4.1. Time Series

Most of the monthly anomaly records show significant lag-1 autocorrelations at the 95% level which were eliminated before removing the trend as described in section 3.3. Time series are then correlated to ONI and AAOI also considering time lags of up to +3 months. Correlations between monthly anomalies of mean (T), maximum (TX), and minimum (TN) air temperature, rel. humidity (rH), precipitation (P) and wind speed (v), and monthly ONI and AAOI are listed in **Table 7**.

Correlations between monthly anomalies and ONI are weak (**Table 7**, **Figure 10**), which is consistent with previous studies (Schneider and Gies, 2004; Garreaud et al., 2009). Since 2000 seven cold (ONI≤-0.5) and five warm (ONI≥ +0.5) periods have been observed. A significant negative correlation of −0.26 can be identified for precipitation anomalies at AWS BH. Monthly precipitation decreases by −9% (−32 mm) during El Niño events (ONI≥ +0.5) at AWS BH compared to the monthly mean (2000-2016) while it increases by +9% during La Nina events

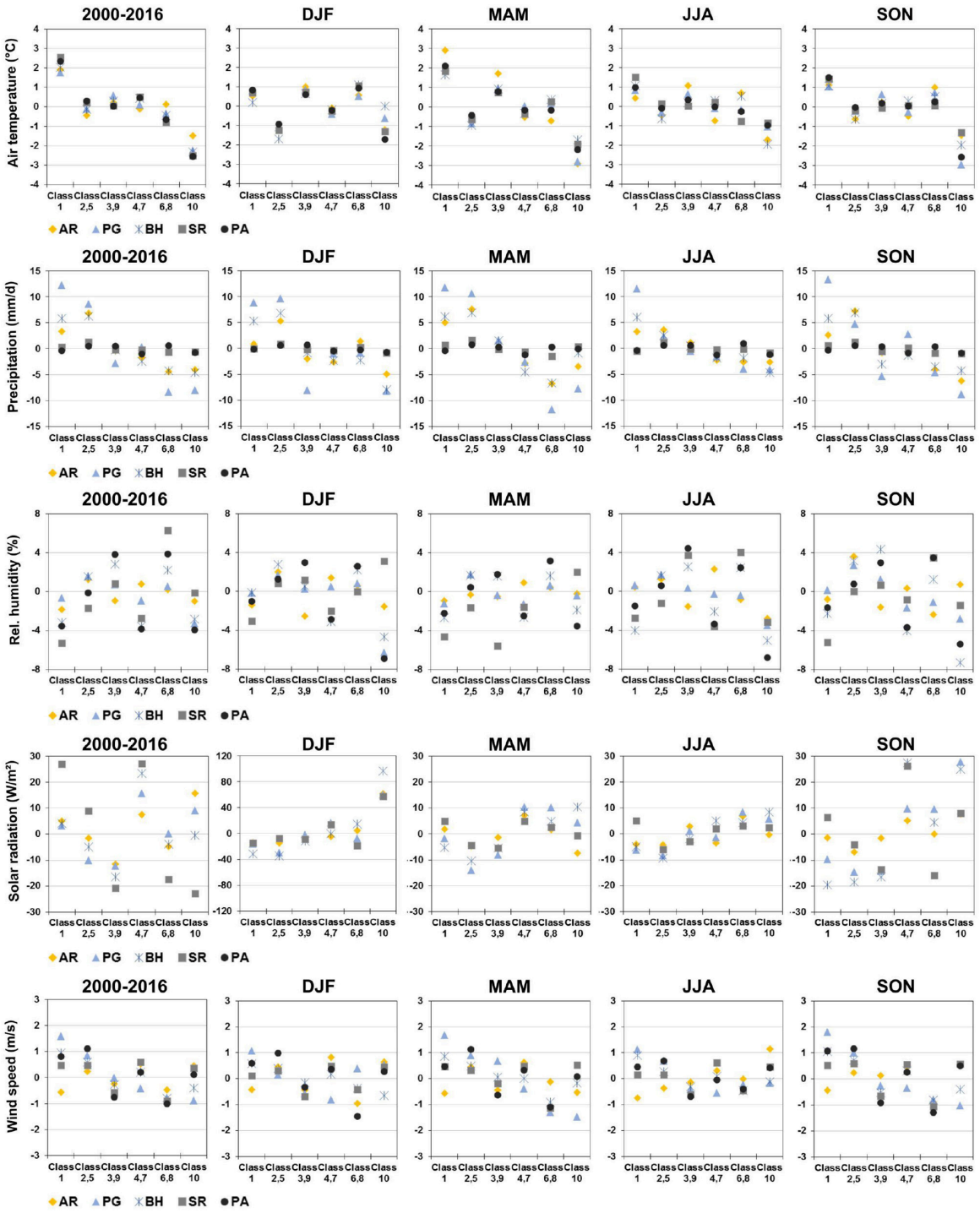

FIGURE 9 | Daily anomalies of air temperature, precipitation, relative humidity, solar radiation, and wind speed for each class of synoptic weather patterns between 2000 and 2016 and for summer (DJF), fall (MAM), winter (JJA), and spring (SON) between 2000 and 2016.

TABLE 7 | Correlation between ONI and AAOI and monthly anomalies of mean (T), maximum (TX), and minimum (TN) air temperature, relative humidity (rH), precipitation (P) and wind speed (v) at AWS Paso Galería (PG), AWS Puerto Bahamondes (BH), AWS Skyring (SR), and WS Punta Arenas (PA) for different time lags (T0 to T+3 months).

		ONI				AAOI			
		PG	**BH**	**SR**	**PA**	**PG**	**BH**	**SR**	**PA**
T	*T0*	−0.01	0.03	−0.13	**−0.12**	**0.34**	**0.49**	**0.36**	**0.42**
	T+1	0.05	0.03	−0.13	−0.10	−0.12	0.04	−0.07	−0.03
	T+2	0.05	0.05	−0.10	−0.08	−0.10	0.02	−0.04	−0.03
	T+3	0.11	0.09	−0.06	−0.04	0.05	0.07	−0.04	**0.12**
TX	*T0*	−0.02	−0.12	**−0.14**	−0.08	**0.38**	**0.39**	**0.38**	**0.43**
	T+1	0.03	−0.10	−0.11	−0.05	−0.08	−0.11	**−0.15**	−0.01
	T+2	0.03	−0.06	−0.08	−0.02	−0.04	−0.01	−0.03	−0.06
	T+3	0.09	−0.02	−0.04	0.02	**0.23**	0.12	0.13	0.11
TN	*T0*	−0.05	0.12	0.05	−0.11	**0.27**	**0.39**	**0.22**	**0.32**
	T+1	−0.01	0.10	0.01	−0.11	**−0.21**	**-0.14**	**−0.18**	−0.06
	T+2	−0.02	0.12	0.03	**−0.12**	−0.13	−0.02	−0.02	−0.03
	T+3	0.02	**0.17**	0.05	−0.10	0.01	−0.02	−0.07	0.09
rH	*T0*	**−0.29**	0.05	**0.21**	0.05	−0.06	**−0.21**	**−0.18**	−0.02
	T+1	**−0.29**	0.01	0.17	0.08	−0.06	−0.12	**0.25**	−0.07
	T+2	**−0.32**	−0.04	**0.18**	0.08	−0.10	−0.14	0.10	−0.11
	T+3	**−0.33**	−0.06	**0.19**	0.05	−0.01	0.02	0.09	0.06
P	*T0*	−0.03	**−0.26**	−0.11	0.02	**0.22**	**0.19**	0.11	−0.05
	T+1	0.01	**−0.23**	−0.10	0.00	−0.10	−0.07	0.07	−0.06
	T+2	−0.05	**−0.22**	−0.09	−0.03	0.10	0.10	0.09	0.00
	T+3	−0.08	**−0.19**	−0.10	−0.05	−0.11	0.03	0.02	−0.08
v	*T0*	0.08	**−0.17**	**−0.14**	0.01	**0.20**	**0.31**	0.05	0.12
	T+1	0.08	**−0.14**	**−0.19**	−0.02	−0.13	−0.02	−0.06	0.12
	T+2	0.00	**−0.14**	**−0.20**	−0.07	0.05	0.12	0.07	**0.17**
	T+3	0.01	**−0.15**	**−0.21**	−0.06	−0.11	−0.09	**−0.18**	−0.09

Significant values at the 90% level are shown in bold, correlations significant at 95% are bold and underlined. Times series were tested for lag-1 autocorrelation and apparent linear trends were removed before correlation analysis.

(ONI≤-0.5) (**Table 8**). The influence of ENSO on precipitation variability diminishes further to the east of the Southernmost Andes (**Table 7**). These findings are similar to Schneider and Gies (2004). However, only for AWS BH there is an indication that ENSO events may influence precipitation at GCN in the way as it is argued by Schneider and Gies (2004). Significant correlations between precipitation and ONI for any other AWS at GCN are not evident.

The link between AAO and the climate conditions at GCN and Punta Arenas is evident (**Table 7**, **Figure 10**). Positive correlations are significant for T, TX, TN at time-lag T0 for all four stations. Correlations range from +0.34 to +0.49 for T, +0.38 to +0.43 for TX and +0.22 to +0.39 for TN. Highest correlation values are found at AWS BH and WS PA. Anomalies of relative humidity ($r = -0.21$), wind speed ($r = +0.31$) and precipitation ($r = +0.19$) of AWS BH are also linked to AAO.

It is known that positive phases of AAO are associated with dryer and warmer conditions in southern South America (Gillett et al., 2006) which becomes evident in this study as well. The strengthening of the westerlies during positive AAO phases come along with an increase of mean monthly air temperatures by +20% (+0.6°C) at AWS PG, +16% (+1.1°C) at AWS BH, +14% (+1.0°C) at AWS SR and 13% (+0.9°C) at WS PA compared to the monthly average (2000-2016) (**Table 8**). Colder conditions with up to 23% (−1.0°C) below the average (AWS PG) occur during negative phases of AAO in Southernmost Patagonia. Deviations of TN between the monthly mean during negative and positive AAO phases compared to the overall mean varies between −45% (−1.2°C) to +33% (+0.6°C) at AWS PG, −26% (−1.0°C) to +22% (+0.9°C) at AWS BH, -26% (−0.8°C) to +26% (+0.8°C) at AWS SR, and −20% (−0.6°C) to +21% (+0.6°C) at WS PA. Air temperature increase during positive AAO phases is accompanied by positive precipitation and wind speed anomalies at the GCN stations. Deviations in monthly precipitation between negative and positive AAOI and the overall mean range from −16% (−96 mm) to 8% (+48 mm) at AWS PG, −9% (−32 mm) to +10% (+34 mm) at AWS BH and −6% (−4 mm) to +10% (+7 mm) at AWS SR (**Table 8**).

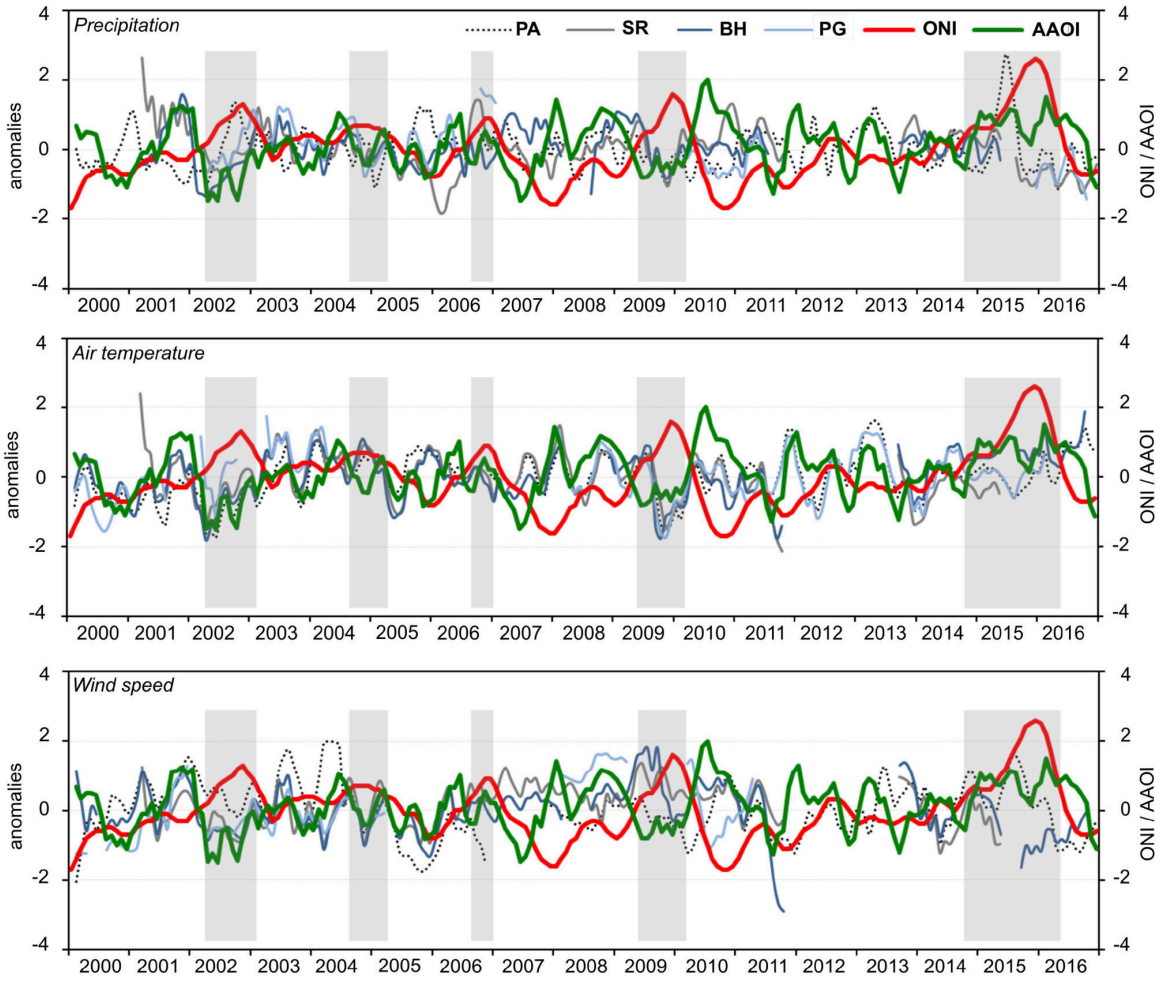

FIGURE 10 | Standardized monthly anomalies of precipitation, mean air temperature and wind speed at AWS Paso Galería (PG), AWS Puerto Bahamondes (BH), AWS Skyring (SR), and WS Punta Arenas (PA) and monthly ONI and AAOI values. El Niño events based on a threshold of +0.5°C for ONI are highlighted by the gray shading. Standardized monthly anomalies of climate variables are illustrated as a 3-month running mean.

4.4.2. Types of Synoptic Weather Patterns

We further analyze how the frequency of the major types of synoptic weather patterns changes during positive and negative phases of AAO and ENSO between 2000 and 2016 (**Table 9**). The impact of AAO on the synoptic situation in Southernmost Patagonia is largest for the synoptic classes 1, 2 and 5 and 10 since the AAO implies a weakening or strengthening of the westerly air flow. In case of negative AAO phases, days with strong westerly airflow (class 1) decrease by about one third compared to the average, while southwesterly air flow (class 2 and 5) increases by about 41% compared to average (2000–2016). On contrary, during positive AAO phases the westerly airflow dominates the climate at GCN. The high-pressure influence accompanied by cold winds from the south (class 10) is intensified during negative AAO and weakened during positive AAO. This is in good agreement with the observation of air temperature increase in Southernmost Patagonia during positive AAO phases.

During La Niña events, north-westerly advection of humid air masses (class 3 and 9) is more frequent, while the frequency for circulation patterns with high-pressure influence decreases (classes 6 and 8 and 10). During El Niño events, the frequency of north-westerly airflow decreases while weather classes with high-pressure influence are more present (classes 4 and 7 and 10). Strong La Niña events (ONI$\leq -1.0°$C) can be associated with enhanced westerlies (+27%) (**Table 9**), which is consistent with higher precipitation sums at AWS BH (Schneider and Gies, 2004). An intensified low-pressure cell over the Weddell Sea causing southwesterly air flow (class 2 and 5) is enhanced during stronger El Niño events (ONI$\geq +1.0°$C), while northwesterly

TABLE 8 | Deviations (%) of monthly mean (T), maximum (TX), and minimum (TN) air temperature, relative humidity (rH), precipitation (P) and wind speed (v) from the monthly means (2000-2016) during positive and negative ENSO and AAO phases.

		PG		BH		SR		PA		PG		BH		SR		PA	
		O+	O-	O+	O-	O+	O-	O+	O-	A+	A-	A+	A-	A+	A-	A+	A-
T	*T0*	−4	8	12	2	10	11	7	13	20	−23	16	−17	14	−13	13	−10
	T+1	4	6	20	5	21	12	14	13	6	10	7	−2	9	−1	5	2
	T+2	5	1	22	5	26	9	15	9	3	15	4	1	7	1	1	9
	T+3	4	−6	18	−1	24	1	11	3	−1	13	3	3	3	2	−2	10
TX	*T0*	−5	20	6	8	7	12	6	9	11	−11	8	−9	11	−10	9	−7
	T+1	1	19	12	11	16	12	11	9	2	12	3	0	7	−1	4	2
	T+2	3	14	13	11	20	9	12	6	0	14	2	3	5	0	1	6
	T+3	1	9	10	6	19	3	9	1	0	11	1	3	3	1	−2	7
TN	*T0*	7	1	21	0	20	12	9	22	33	−45	22	−26	26	−26	21	−20
	T+1	18	2	33	7	37	16	21	24	11	3	12	−5	16	−3	8	3
	T+2	18	−4	34	6	46	11	24	19	6	16	8	0	13	−1	3	15
	T+3	12	−12	29	−2	40	−3	17	9	1	17	7	2	4	2	−3	17
rH	*T0*	−1	−2	0	0	5	0	−2	−1	−1	0	−4	2	−2	3	−1	0
	T+1	−1	−1	−1	0	6	−2	−2	−1	0	−1	−3	2	0	0	−1	−1
	T+2	−2	−1	−2	0	8	−3	−2	0	0	0	−3	3	2	−2	−1	−1
	T+3	−2	−1	−1	2	9	−4	−1	1	0	0	−1	2	2	−3	1	−2
P	*T0*	7	−13	−9	9	−6	−10	−4	−9	8	−16	10	−9	10	−6	−8	1
	T+1	11	−5	−5	15	−4	−11	−4	−9	−7	18	−1	8	0	0	−2	−7
	T+2	14	0	1	21	−2	4	−2	2	−6	3	9	0	9	−4	5	−11
	T+3	8	−1	1	14	0	6	8	1	−22	14	−4	−5	−1	−3	−2	−8
v	*T0*	−3	0	2	3	4	4	7	−5	11	−13	11	−10	3	−1	3	−1
	T+1	0	0	3	4	4	6	5	−3	6	−1	4	−3	1	2	5	2
	T+2	3	1	3	5	4	6	3	−2	9	−7	3	−1	2	−1	5	5
	T+3	2	0	1	4	1	4	1	−4	3	−2	−2	3	−2	3	2	7

Results are listed for ONI ≥-0.5 (O+), ONI ≤-0.5 (O-), AAOI ≥0.5 (A+), and AAOI ≤-0.5 (A-) at different time lags (T0 to T+3 months) for AWS Paso Galería (PG), AWS Puerto Bahamondes (BH), AWS Skyring (SR), and WS Punta Arenas (PA).

TABLE 9 | Relative changes (%) of synoptic types and classes during positive and negative AAO and ENSO events between 2000 and 2016.

	Relative changes of synoptic types (%)										Relative changes of synoptic classes (%)					
	1	2	3	4	5	6	7	8	9	10	1	2 and 5	3 and 9	4 and 7	6 and 8	10
AAOI −0.5	−37	30	−19	−39	74	−36	51	1	96	64	−37	41	11	0	−29	64
AAOI +0.5	36	−27	−2	20	−40	21	−16	−21	−63	−43	36	−35	−19	4	−3	−43
ONI −0.5	4	−9	17	−6	3	8	8	−39	11	−18	4	−9	16	0	−16	−18
ONI +0.5	1	23	−23	12	−6	−13	2	35	−34	12	1	7	−26	8	−4	12
ONI −1.0	27	−22	18	4	−13	23	−10	−73	−33	−61	27	−22	4	−2	−19	−61
ONI +1.0	−5	49	−32	20	10	−51	5	60	−37	−18	−5	27	−33	13	−18	−18

airflow (class 3 and 9) occurs less frequently. The frequencies of high-pressure weather classes (classes 6 and 8 and 10) are below the average during both strong El Niño and La Niña events. The impact of ENSO on the variability of synoptic weather patterns generally is rather weak as already identified with respect to the meteorological observations other than precipitation at AWS BH.

5. CONCLUSION

We analyzed the main features of climate and climate variability in Southernmost Patagonia using a unique 17-year meteorological record (2000–2016) of four AWS in the vicinity of the GCN Ice Cap (53°S). Special attention was given to the link between observed mean, extremes and trends of the AWS records

as well as the impact of synoptic weather types and leading modes of global atmospheric variability (ENSO and AAO).

Annual and seasonal trends in air temperature were investigated by applying the non-parametric Mann-Kendall and Sen slope estimator trend test. A weather type classification based on the hierarchical correlations-based leader LUND-algorithm was computed using a 37-year record of ERA Interim Reanalysis data. Major synoptic weather types with distinct low-pressure cells in the Weddell Sea or Bellingshausen Sea causing a prevailing southwesterly, northwesterly or westerly airflow, determine the weather conditions in Southernmost Patagonia during 68% of the time. Circulation patterns with high-pressure cells over the Southern Pacific and Atlantic are present on 32% of all days between 2000 and 2016. The predominance of weather types with humid westerly airflow leads to significant west-east gradients of precipitation and relative humidity across the GCN Ice Cap. Mean annual precipitation (2008 to 2016) increases from ~3,800 mm at the west side of GCN at AWS AR to ~6,100 mm at AWS PG while it decreases again on the lee-side to ~4,000 mm at AWS BH. Within a distance of tens of kilometers precipitation sharply drops to below 800 mm further to the east. More than 80% of extreme precipitation events (>90th percentile) at GCN appears during synoptic types with strong westerly air flow. The occurrence of high precipitation events of up to 620 mm in 5 days and wet spells of up to 61 consecutive days underscore the year-around wet conditions at GCN. High precipitation events and long wet spells become less frequent toward the east of GCN.

We further identify extremes of daily maximum and minimum air temperatures of up to +25.8°C and -11.3°C along with the largest daily temperature range being located on the east side of GCN. Days with daily maximum temperatures exceeding the 90th percentile and days with daily minimum temperature falling below 0°C are less frequent since 2012 indicating a stronger maritime influence in the study region in recent years which might be attributable to increased positive AAO in recent years (Marshall, 2003). Mean annual air temperature increases by +0.05°C a^{-1} at GCN and +0.02°C a^{-1} at AWS Punta Arenas during the study period (2000–2016).

The influence of ENSO on intra-annual precipitation and temperature variations is not evident for all investigated stations. At AWS BH precipitation decreases by -9% compared to the monthly mean (2000-2016) during El Niño events while it increases by +9% during La Niña events. The evolution of the AAO determines the synoptic weather types along with air temperature and precipitation variations. Positive AAO phases on average are linked to an intensified westerly airflow (type 1) and warmer conditions in Southernmost Patagonia. Circulation patterns with high-pressure influence leading to colder and dryer conditions in Southernmost Patagonia are more frequent during negative AAO phases.

AUTHOR CONTRIBUTIONS

SW processed and analyzed the data and drafted the manuscript. DS prepared the synoptic weather type classification. TS, RK, CS designed, installed and maintain the measurement network at GCN. All authors discussed the results and jointly worked on the manuscript.

FUNDING

This study was funded by the CONYCET-BMBF project GABY-VASA, grant No. 01DN15007, by the German Research Foundation project Gran Campo Nevado, grant No. SCHN 680/1-1 and by the German Research Foundation project MANAU, grant No. SA 2339/3-1.

ACKNOWLEDGMENTS

We thank Marcelo Arévalo, Marco Möller, Paul Bumeder, Michael Glaser, Johannes Koch, Michael Moritz, Markus Stickling and many others for their help in the field at Gran Campo Nevado Ice Cap during the past 17 years. We are grateful for technical support and advice regarding the weather type classification by Andreas Philipp, University of Augsburg. We thank all reviewers and the editor for their input which helped improving the manuscript considerably.

SUPPLEMENTARY MATERIAL

The Supplementary Material for this article can be found online at: https://www.frontiersin.org/articles/10.3389/feart.2018.00053/full#supplementary-material

REFERENCES

Aceituno, P. (1988). On the functioning of the southern oscillation in the south american sector. part I: surface climate. *Monthly Weather Rev.* 116, 505–524.

Aravena, J., Lara, A., Wolodarsky-Franke, A., Villalba, R., and Cuq, E. (2002). Tree-ring growth patterns and temperature reconstruction from nothofagus pumilio (fagaceae) forests at the upper tree line of southern chilean patagonia. *Rev. Chil. Hist. Nat.* 75, 361–376. doi: 10.4067/S0716-078X2002000200008

Aravena, J.-C., and Luckman, B. H. (2009). Spatio-temporal rainfall patterns in southern south america. *Int. J. Climatol.* 29, 2106–2120. doi: 10.1002/joc.1761

Barnston, A., Chelliah, M., and Goldenberg, S. (1997). Documentation of a highly enso-related sst region in the equatorial pacific. *Atmosphere-Ocean* 35, 367–383. doi: 10.1080/07055900.1997.9649597

Buisán, S., Earle, M., Collado, J., Kochendorfer, J., Alastrué, J., Wolff, M., et al. (2017). Assessment of snowfall accumulation underestimation by tipping bucket gauges in the spanish operational network. *Atmos. Meas. Tech.* 10:1079. doi: 10.5194/amt-10-1079-2017

Butorovic, N. (2016). Resumen meteorológico año 2015. estación jorge schythe. *Anal. Inst. Patag.* 44, 102–110. doi: 10.4067/S0718-686X2016000100009

Carrasco, J., Casassa, G., and Rivera, A. (2002). "Meteorological and climatological aspect of the southern patagonia icefield," in *The Patagonia Icefields*, eds G. Casassa, F. Sepulveda, and R. Sinclair (New York, NY: Kluwer-Plenum), 29–41.

Compagnucci, R. H., and Salles, M. A. (1997). Surface pressure patterns during the year over southern south america. *Int. J. Climatol.* 17, 635–653.

Davies, B., and Glasser, N. (2012). Accelerating shrinkage of patagonian glaciers from the little ice age (ad 1870) to 2011. *J. Glaciol.* 58, 1063–1084. doi: 10.3189/2012JoG12J026

Dee, D., Uppala, S., Simmons, A., Berrisford, P., Poli, P., Kobayashi, S., et al. (2011). The era-interim reanalysis: configuration and performance of the

data assimilation system. *Q. J. R. Meteorol. Soc.* 137, 553–597. doi: 10.1002/qj.828

Durre, I., Menne, M. J., Gleason, B. E., Houston, T. G., and Vose, R. S. (2010). Comprehensive automated quality assurance of daily surface observations. *J. Appli. Meteorol. Climatol.* 49, 1615–1633. doi: 10.1175/2010JAMC2375.1

Endlicher, W. (1991). Zur klimageographie und klimaökologie von südpatagonien. 100 jahre klimatologische messungen in punta arenas. *Freiburger Geographische Hefte* 32, 181–211.

Fogt, R. L., and Bromwich, D. H. (2006). Decadal variability of the enso teleconnection to the high-latitude south pacific governed by coupling with the southern annular mode. *J. Clim.* 19, 979–997. doi: 10.1175/JCLI3671.1

Frank, A. (2002). *Semi-objektive klassifikation und statistische auswertung von wetterlagen südpatagoniens [semi-Objective Classification and Statistical Analysis of Weather Types of South Patagonia]*. Master thesis, Univ. Freiburg, Germany .

Garreaud, R., Lopez, P., Minvielle, M., and Rojas, M. (2013). Large-scale control on the patagonian climate. *J. Clim.* 26, 215–230. doi: 10.1175/JCLI-D-12-00001.1

Garreaud, R. D., Vuille, M., Compagnucci, R., and Marengo, J. (2009). Present-day south american climate. *Palaeogeogr. Palaeoclimatol. Palaeoecol.* 281, 180–195. doi: 10.1016/j.palaeo.2007.10.032

Gillett, N. P., Kell, T. D., and Jones, P. D. (2006). Regional climate impacts of the southern annular mode. *Geophys. Res. Lett* 33:L23704. doi: 10.1029/2006GL027721

Gocic, M., and Trajkovic, S. (2013). Analysis of changes in meteorological variables using mann-kendall and sen's slope estimator statistical tests in serbia. *Global Planet. Change* 100(Suppl. C), 172–182. doi: 10.1016/j.gloplacha.2012.10.014

Hamed, K. H. (2008). Trend detection in hydrologic data: the mann–kendall trend test under the scaling hypothesis. *J. Hydrol.* 349, 350–363. doi: 10.1016/j.jhydrol.2007.11.009

Hartigan, J. (1975). *Clustering Algorithms*. Wiley Series in Probability and Mathematical Statistics. New York, NY: John Wiley & Sons.

Huang, B., Thorne, P. W., Banzon, V. F., Boyer, T., Chepurin, G., Lawrimore, J. H., et al. (2017). Extended reconstructed sea surface temperature, version 5 (ersstv5): Upgrades, validations, and intercomparisons. *J. Clim.* 30, 8179–8205. doi: 10.1175/JCLI-D-16-0836.1

Kendall, M. (1975). *Rank Correlation Methods*. London: Griffin.

Kilian, R., Baeza, O., Breuer, S., Ríos, F., Arz, H., Lamy, L., et al. (2013). Late glacial and holocene paleogeopgraphical and paleoecological evolution of the seno skyring and otway fjord systems in the magellanes region. *Anal. Inst. Patag.* 41, 7–21. doi: 10.4067/S0718-686X2013000200001

Kilian, R., Hohner, H., Biester, H., Wallrabe-Adams, C., and Stern, C. (2003). Holocene peat and lake sediment tephra record from the southernmost andes (53-55°s). *Rev. Geol. Chile* 30. 47–64. doi: 10.4067/S0716-02082003000100002

Kilian, R., and Lamy, F. (2012). A review of glacial and holocene paleoclimate records from southernmost patagonia (49–55°s). *Q. Sci. Rev.* 53, 1–23. doi: 10.1016/j.quascirev.2012.07.017

Kilian, R., Schneider, C., Koch, J., Fesq-Martin, M., Biester, H., Casassa, C., et al. (2007). Palaeoecological constraints on late glacial and holocene ice retreat in the southern andes (53°s). *Global Planet. Change* 59, 49–66. doi: 10.1016/j.gloplacha.2006.11.034

Kisi, O., and Ay, M. (2014). Comparison of mann–kendall and innovative trend method for water quality parameters of the kizilirmak river, turkey. *J. Hydrol.* 513(Suppl. C), 362–375. doi: 10.1016/j.jhydrol.2014.03.005

Koch, J., and Kilian, R. (2005). 'little ice age' glacier fluctuations, gran campo nevado, southernmost chile. *Holocene* 15, 20–28. doi: 10.1191/0959683605hl780rp

Lamy, F., Kilian, R., Arz, H., Francois, J.-P., Kaiser, J., Prange, M., et al. (2010). Holocene changes in the position and intensity of the southern westerly wind belt. *Nat. Geosci.* 3, 695–699. doi: 10.1038/ngeo959

Lund, I. (1963). Map-pattern classification by statistical methods. *J. Appl. Meteorol.* 2, 56–65.

Mann, H. (1945). Nonparametric tests against trend. *Econometrica* 13, 245–259. doi: 10.2307/1907187

Marshall, G. J. (2003). Trends in the southern annular mode from observations and reanalyses. *J. Clim.* 16, 4134–4143. doi: 10.1175/1520-0442(2003)016<4134:TITSAM>2.0.CO;2

Möller, M., and Schneider, C. (2008). Climate sensitivity and mass-balance evolution of gran campo nevado ice cap, southwest patagonia. *Ann. Glaciol.* 48, 32–42. doi: 10.3189/172756408784700626

Möller, M., Schneider, C., and Kilian, R. (2007). Glacier change and climate forcing in recent decades at gran campo nevado, southernmost patagonia. *Ann. Glaciol.* 46, 136–144. doi: 10.3189/172756407782871530

Murtagh, F. (1985). "Multidimensional clustering algorithms," in *COMPSTAT Lectures 4*, eds J. M. Chambers, J. Gordesch, A. Klas, L. Lebart, and P. P. Sint (Wien-Würzburg: Physica Verlag), 1–131.

Onyutha, C., Tabari, H., Taye, M. T., Nyandwaro, G. N., and Willems, P. (2016). Analyses of rainfall trends in the nile river basin. *J. Hydroenviron. Res.* 13(Suppl. C), 36–51. doi: 10.1016/j.jher.2015.09.002

Paruelo, J., Beltran, A., Jobbagy, E., Sala, O., and Golluscio, R. (1998). The climate of patagonia: general patterns and controls on biotic processes. *Ecol. Aust.* 8, 85–101.

Philipp, A., Beck, C., Esteban, P., Kreienkamp, F., Krennert, T., Lochbihler, K., et al. (2014a). *cost733class-1.2 - User Guide*. Available online at: http://cost733.geo.uni-augsburg.de/cost733class-1.2.

Philipp, A., Beck, C., Huth, R., and Jacobeit, J. (2014b). Development and comparison of circulation type classifications using the cost 733 dataset and software. *Int. J. Climatol.* 36, 2673–2691. doi: 10.1002/joc.3920

Rasmussen, R., Baker, B., Kochendorfer, J., Meyers, T., Landolt, S., Fischer, A. P., et al. (2012). How well are we measuring snow: the noaa/faa/ncar winter precipitation test bed. *Bull. Am. Meteorol. Soc.* 93, 811–829. doi: 10.1175/BAMS-D-11-00052.1

Schneider, C., and Gies, D. (2004). Effects of el niño–southern oscillation on southernmost south america precipitation at 53°s revealed from ncep–ncar reanalyses and weather station data. *Int. J. Climatol.* 24, 1057–1076. doi: 10.1002/joc.1057

Schneider, C., Glaser, M., Kilian, R., Santana, A., Butorovic, N., and Casassa, G. (2003). Weather observations across the southern andes at 53°s. *Phys. Geogr.* 24, 97–119. doi: 10.2747/0272-3646.24.2.97

Schneider, C., Schnirch, M., Acuña, C., Casassa, G., and Kilian, R. (2007). Glacier inventory of the gran campo nevado ice cap in the southern andes and glacier changes observed during recent decades. *Glob. Plan. Change* 59, 87–100. doi: 10.1016/j.gloplacha.2006.11.023

Sen, P. (1968). Estimates of the regression coefficient based on kendall's tau.. *J. Am. Stat. Assoc.* 63, 1379–1389.

Tank, A. K., Zwiers, F., and Zhang, X. (2009). Guidelines on analysis of extremes in a changing climate in support of informed decisions for adaption. *Clim. Data Monit.* 72, 1–55.

Theil, H. (1950). A rank-invariant method of linear and polynomial regression analysis. *Proc. K. Ned. Akad. Wet.*, A53, 386–392.

Thompson, D. W. J., and Solomon, S. (2002). Interpretation of recent southern hemisphere climate change. *Science* 296, 895–899. doi: 10.1126/science.1069270

Villalba, R., Lara, A., Boninsegna, J. A., Masiokas, M., Delgado, S., Aravena, J. C., et al. (2003). "Large-scale temperature changes across the southern andes: 20th-century variations in the context of the past 400 years," in *Climate Variability and Change in High Elevation Regions: Past, Present & Future*, ed H. F. Diaz (Dordrecht: Springer), 177–232.

Weidemann, S., Sauter, T., Schneider, L., and Schneider, C. (2013). Impact of two conceptual precipitation downscaling schemes on mass-balance modeling of gran campo nevado ice cap, patagonia. *J. Glaciol.* 59, 1106–1116. doi: 10.3189/2013JoG13J046

Yue, S., Pilon, P., Phinney, B., and Cavadias, G. (2002). The influence of autocorrelation on the ability to detect trend in hydrological series. *Hydrol. Process.* 16, 245–259. doi: 10.1002/hyp.1095

Conflict of Interest Statement: The authors declare that the research was conducted in the absence of any commercial or financial relationships that could be construed as a potential conflict of interest.

frontiers

Supplementary Material:
A 17-year record of meteorological observations across the Gran Campo Nevado Ice Cap in Southern Patagonia, Chile, related to synoptic weather types and climate modes

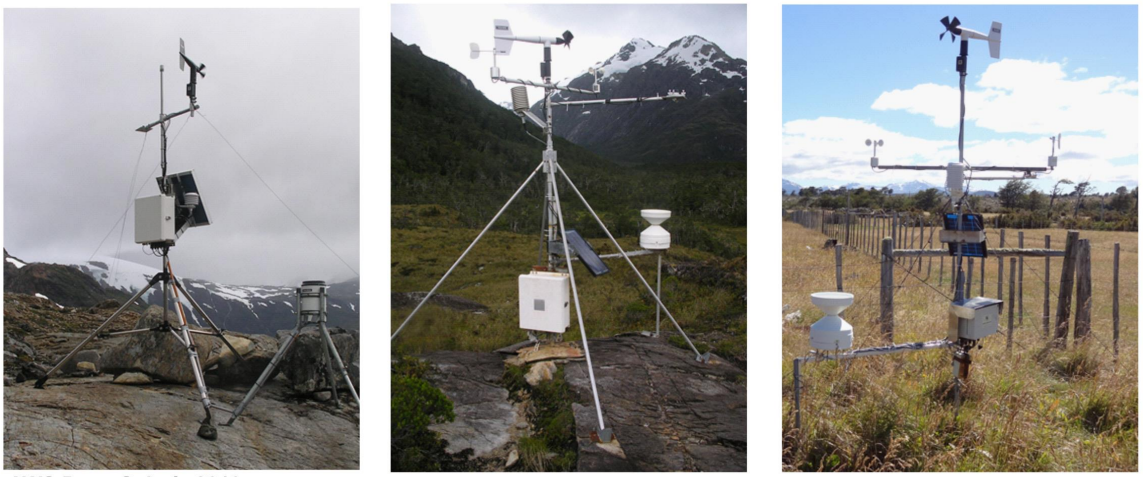

Figure S1: Pictures of the automatic weather stations Paso Galería, Puerto Bahamondes and Skyring at the Gran Campo Nevado Ice Cap provided by Christoph Schneider.

Table S1. Monthly mean of daily mean (T), maximum (TX) and minimum (TN) air temperature, relative humidity (rH), incoming shortwave radiation (SW), wind speed (v), maximum wind speed (vx), wind direction (dir), and monthly precipitation sums at AWS Arévalo (AR), AWS Paso Galería (PG), AWS Puerto Bahamondes (BH), AWS Skyring (SR), and WS Punta Arenas (PA). Averaged values for each month were calculated based on the available observation period and before averaging the annual means.

	AR									PG								
	T	*TX*	*TN*	*rH*	*P*	*SW*	*v*		*dir*	*T*	*TX*	*TN*	*rH*	*P*	*SW*	*v*	*vx*	*dir*
JAN	8.8	10.5	7.2	80	414	103	4.7		165	6.7	8.1	5.4	79	1009	107	6.2	16.0	255
FEB	8.5	10.4	6.9	78	367	91	4.6		172	6.9	8.4	5.4	82	700	100	5.5	15.0	266
MAR	8.6	10.1	7.1	82	404	60	4.7		158	6.7	8.1	5.1	82	901	66	5.2	12.3	232
APR	5.5	6.9	4.2	84	387	35	4.8		161	4.9	6.4	3.4	83	741	47	5.4	13.0	257
MAY	4.6	6.0	3.3	82	249	21	5.0		146	2.7	4.0	1.2	85	487	28	4.9	11.3	264
JUN	2.6	4.0	1.1	85	261	14	5.1		151	1.0	2.4	-0.4	86	416	20	4.2	12.3	223
JUL	2.2	3.5	0.9	84	211	19	4.7		173	0.7	2.1	-0.5	85	474	26	4.5	12.6	229
AUG	3.1	4.3	2.0	82	169	43	4.5		153	1.0	2.4	-0.2	85	296	48	4.7	12.4	233
SEP	5.5	7.3	3.8	77	236	70	4.1		145	2.2	3.7	0.7	82	417	81	4.5	13.0	213
OCT	6.0	6.8	5.3	78	270	91	4.8		153	3.3	4.6	1.8	81	550	104	5.3	14.0	247
NOV	6.4	7.5	5.3	80	425	102	5.1		159	3.9	5.3	2.5	80	697	110	5.3	14.6	247
DEC	7.3	8.3	6.2	80	421	113	4.9		165	5.4	6.7	3.9	81	824	121	5.6	14.8	268
Mean	**5.8**	**7.1**	**4.4**	**81**	**3813**	**64**	**4.7**		**158**	**3.8**	**5.2**	**2.4**	**83**	**7513**	**71**	**5.1**	**13.4**	**245**

	BH									SR								
	T	*TX*	*TN*	*rH*	*P*	*SW*	*v*	*vx*	*dir*	*T*	*TX*	*TN*	*rH*	*P*	*SW*	*v*	*vx*	*dir*
JAN	9.2	12.1	7.2	76	470	132	3.9	11.6	264	10.8	13.9	7.0	61	74	203	4.3	8.9	273
FEB	9.6	12.7	7.4	75	324	115	3.5	10.8	256	11.2	14.4	7.2	71	60	163	4.0	8.5	269
MAR	8.4	11.2	6.2	76	493	76	3.4	10.9	256	9.3	12.5	5.8	75	80	110	3.9	8.4	270
APR	6.7	9.4	4.7	78	390	44	3.1	10.0	256	7.2	9.9	4.0	75	90	65	3.6	8.1	274
MAY	4.6	7.1	2.6	84	297	24	2.6	8.5	253	4.7	7.5	1.4	80	57	36	3.1	7.4	274
JUN	2.7	5.2	0.8	86	281	17	2.4	8.1	251	2.5	4.9	-0.6	80	66	24	3.1	7.2	276
JUL	2.4	5.0	0.6	83	220	23	2.4	7.9	249	2.4	5.0	-0.7	81	44	31	3.0	7.1	263
AUG	3.0	5.7	1.1	82	238	39	2.5	8.0	245	3.1	5.9	-0.2	80	54	55	3.1	7.3	255
SEP	4.4	7.6	2.4	79	235	79	2.5	8.0	244	5.0	8.3	1.4	77	48	98	3.3	7.6	256
OCT	5.8	8.7	3.4	75	305	113	3.4	10.4	259	6.6	10.0	2.8	72	76	161	3.9	8.3	266
NOV	6.7	9.7	4.4	75	372	135	3.6	11.1	264	7.8	11.1	4.2	71	80	205	4.4	8.9	272
DEC	8.1	11.1	6.1	75	433	149	3.6	11.3	266	9.7	13.2	6.0	73	74	217	4.3	8.8	272
Mean	**6.0**	**8.8**	**3.9**	**79**	**4057**	**79**	**3.1**	**9.7**	**255**	**6.6**	**9.7**	**3.2**	**75**	**803**	**114**	**3.7**	**8.0**	**268**

	PA								
	T	*TX*	*TN*	*rH*	*P*		*v*	*vx*	*dir*
JAN	11.0	15.4	6.4	68	40		5.1	12.3	277
FEB	10.8	15.2	6.2	70	31		4.8	11.6	270
MAR	9.1	13.4	5.0	74	54		4.7	11.9	276
APR	6.6	10.6	3.1	77	66		4.2	11.5	283
MAY	4.2	7.6	1.1	81	52		3.8	10.2	273
JUN	2.5	5.4	-0.2	82	60		3.5	10.0	263
JUL	2.1	5.3	-0.6	80	55		3.5	9.8	266
AUG	2.9	6.4	0.0	78	58		3.9	10.0	259
SEP	5.0	8.9	1.4	75	38		4.1	10.3	264
OCT	6.9	11.1	2.7	70	38		5.2	12.0	270
NOV	8.4	12.6	4.0	68	30		5.9	13.2	269
DEC	10.0	14.4	5.4	68	43		5.6	12.7	267
Mean	**6.6**	**10.5**	**2.9**	**74**	**565**		**4.5**	**11.3**	**270**

Table S2. Annual means of daily mean (T), maximum (TX) and minimum (TN) air temperature and the absolute annual anomalies (AT, ATX, ATN) in $^{\circ}C$ as well as the annual sums (P) and anomalies (AP) of precipitation in mm at AWS Arévalo (AR), AWS Paso Galería (PG), AWS Puerto Bahamondes (BH), AWS Skyring (SR), and WS Punta Arenas (PA). Days per year of available data are listed in Tab.S3 and Tab.S4

	AR								PG							
	T	*AT*	*TX*	*ATX*	*TN*	*ATN*	*P*	*AP*	*T*	*AT*	*TX*	*ATX*	*TN*	*ATN*	*P*	*AP*
2000	-	-	-	-	-	-	-	-	3.0	-0.8	5.1	-0.1	0.5	-1.8	-	-
2001	-	-	-	-	-	-	-	-	3.5	-0.2	5.2	0.1	1.2	-1.1	-	-
2002	-	-	-	-	-	-	-	-	2.3	-1.5	4.5	-0.7	0.5	-1.9	4490	-3023
2003	-	-	-	-	-	-	-	-	3.3	-0.5	4.5	-0.7	0.4	-2.0	9472	1959
2004	-	-	-	-	-	-	-	-	8.2	4.5	10.1	4.9	5.3	2.9	8449	937
2005	-	-	-	-	-	-	-	-	-	-	-	-	-	-	7229	-284
2006	-	-	-	-	-	-	-	-	-	-	-	-	-	-	5762	-1751
2007	6.0	0.2	8.4	1.2	3.5	-0.9	-	-	-	-	-	-	-	-	-	-
2008	5.9	0.1	8.3	1.1	3.6	-0.8	-	-	3.4	-0.4	5.4	0.2	1.3	-1.0	-	-
2009	-	-	-	-	-	-	-	-	3.4	-0.4	5.6	0.4	1.3	-1.0	-	-
2010	5.8	0.0	8.5	1.4	3.0	-1.4	2248	-1565	3.6	-0.2	5.9	0.7	1.4	-1.0	4243	-3270
2011	5.6	-0.2	7.5	0.4	3.7	-0.8	3673	-141	3.8	0.0	5.7	0.5	2.1	-0.3	4470	-3043
2012	5.0	-0.8	5.5	-1.7	4.5	0.1	4474	661	3.5	-0.3	3.9	-1.2	3.1	0.7	-	-
2013	-	-	-	-	-	-	3561	-253	4.3	0.5	4.7	-0.4	3.9	1.5	-	-
2014	-	-	-	-	-	-	4285	472	3.8	0.0	4.2	-1.0	3.4	1.0	-	-
2015	6.4	0.7	6.9	-0.2	6.0	1.5	1456	-2358	3.7	-0.1	4.2	-1.0	3.3	0.9	-	-
2016	7.0	1.2	7.4	0.3	6.5	2.1	2741	-1072	7.3	3.5	8.0	2.8	6.7	4.4	3986	-3527

	BH								SR							
	T	*AT*	*TX*	*ATX*	*TN*	*ATN*	*P*	*AP*	*T*	*AT*	*TX*	*ATX*	*TN*	*ATN*	*P*	*AP*
2000	5.7	-0.3	8.9	0.1	2.9	-1.0	-	-	-	-	-	-	-	-	-	-
2001	5.8	-0.2	8.6	-0.2	3.1	-0.8	3293	-764	5.4	-0.9	8.6	-1.1	1.4	-1.8	1034	231
2002	5.2	-0.7	8.5	-0.3	3.0	-0.9	2633	-1425	6.2	-0.2	9.2	-0.5	2.0	-1.2	608	-195
2003	6.2	0.2	9.4	0.6	3.7	-0.2	4514	456	6.9	0.5	10.1	0.4	3.0	-0.1	937	134
2004	6.5	0.5	9.8	1.0	4.1	0.2	4174	117	7.4	1.0	10.9	1.2	3.4	0.2	855	52
2005	5.6	-0.3	9.2	0.5	3.4	-0.5	3702	-355	6.5	0.2	10.1	0.4	2.5	-0.7	736	-67
2006	5.9	-0.1	9.3	0.5	3.8	-0.1	3813	-244	6.8	0.5	10.2	0.5	3.0	-0.2	600	-203
2007	5.7	-0.2	9.1	0.3	3.6	-0.3	4913	856	6.7	0.3	9.9	0.2	3.2	0.0	741	-62
2008	9.9	3.9	11.1	2.4	5.3	1.4	1969	-2089	6.9	0.6	10.3	0.5	3.2	0.0	771	-32
2009	6.4	0.4	9.2	0.4	3.7	-0.2	3950	-107	6.6	0.2	9.8	0.1	2.9	-0.3	697	-106
2010	5.7	-0.3	9.1	0.3	3.4	-0.5	4269	212	6.5	0.2	10.1	0.4	2.7	-0.4	1050	247
2011	5.4	-0.6	8.5	-0.3	3.0	-0.9	2336	-1721	6.1	-0.3	9.3	-0.4	2.5	-0.7	674	-129
2012	-	-	-	-	-	-	-	-	-	-	-	-	-	-	-	-
2013	6.9	1.0	7.9	-0.9	6.0	2.1	1282	-2776	7.6	1.3	8.8	-0.9	6.6	3.4	326	-477
2014	6.2	0.2	7.2	-1.6	5.2	1.3	4320	263	6.3	0.0	7.4	-2.3	5.3	2.1	881	78
2015	8.2	2.2	9.3	0.5	7.2	3.2	2123	-1934	9.3	2.6	10.5	0.8	8.1	4.9	478	-325
2016	6.6	0.6	7.6	-1.2	5.6	1.7	2044	-2014	-	-	-	-	-	-	421	-382

	PA							
	T	*AT*	*TX*	*ATX*	*TN*	*ATN*	*P*	*AP*
2000	6.2	-0.4	10.0	-0.6	2.5	-0.4	496	-71
2001	6.1	-0.5	10.1	-0.5	2.4	-0.5	490	-76
2002	5.9	-0.8	9.8	-0.7	2.1	-0.8	539	-27
2003	6.3	-0.3	10.5	0.0	2.5	-0.4	590	24
2004	7.2	0.6	11.2	0.7	3.6	0.7	564	-2
2005	6.8	0.2	10.8	0.3	2.9	0.1	572	6
2006	6.9	0.2	10.8	0.3	3.3	0.4	673	107
2007	6.6	0.0	10.4	-0.1	3.1	0.3	589	23
2008	6.9	0.3	10.8	0.2	3.2	0.3	536	-30
2009	6.4	-0.2	10.3	-0.3	2.7	-0.2	498	-68
2010	6.4	-0.2	10.3	-0.2	2.5	-0.4	429	-137
2011	6.9	0.3	10.6	0.0	3.1	0.2	642	76
2012	6.4	-0.2	10.1	-0.4	2.9	0.0	638	72
2013	7.1	0.5	10.9	0.4	3.4	0.5	709	143
2014	6.5	-0.1	10.3	-0.2	2.8	0.0	497	-69
2015	6.6	-0.1	10.4	-0.2	2.6	-0.3	753	187
2016	7.2	0.6	11.4	0.9	3.0	0.1	429	-137

Table S3. Indices of air temperature extremes based on daily maximum (TX) and minimum (TN) air temperatures per year. Listed are the mean air temperature (T), the absolute maximum of daily TX, TN and air temperature range (R), the maximum of days with ice (TX$<0°C$) (ID) and with frost (TN$<0°C$) (FD), the maximum of days with TX $<$ 10th percentile (P1TX), TN $<$ 10th percentile (P1TN), TX$>$ 90th percentile (P9TX) and TN $>$ 90th percentile (P9TN), the maximum length of a cold spell (CS) with consecutive days of TN $<$ 10th percentile, and the maximum length of a warm spell (TWS) with consecutive days of TX $>$ 90th percentile per year. Percentiles are calculated based on the individual observation period. D: Days per year with available data.

	AR													PG										
	T	*TX*	*TN*	*R*	*FD*	*ID*	*P1X*	*P1N*	*P9X*	*P9N*	*CS*	*TWS*	*D*	*T*	*TX*	*TN*	*R*	*FD*	*ID*	*P1X*	*P1N*	*P9X*	*P9N*	*CS*	*TWS*	*D*
2000	-	-	-	-	-	-	-	-	-	-	-	-	0	3.0	15.8	-7.2	11.9	47	9	16	28	8	1	5	2	117
2001	-	-	-	-	-	-	-	-	-	-	-	-	0	3.5	12.2	-7.9	9.8	61	12	25	31	21	6	5	4	181
2002	-	-	-	-	-	-	-	-	-	-	-	-	0	2.3	15.8	-8.9	15.3	63	10	16	32	10	3	4	4	150
2003	-	-	-	-	-	-	-	-	-	-	-	-	0	3.3	11.6	-7.4	11.3	107	9	21	50	5	1	4	1	235
2004	-	-	-	-	-	-	-	-	-	-	-	-	0	8.2	20.4	-0.6	11.1	1	0	0	0	44	20	0	14	91
2005	-	-	-	-	-	-	-	-	-	-	-	-	0	-	-	-	-	-	-	-	-	-	-	-	-	0
2006	-	-	-	-	-	-	-	-	-	-	-	-	0	-	-	-	-	-	-	-	-	-	-	-	-	0
2007	6.0	16.4	-0.5	9.1	6	0	0	7	9	0	0	3	92	-	-	-	-	-	-	-	-	-	-	-	-	0
2008	5.9	23.6	-3.6	15.1	36	1	30	47	56	14	5	9	274	3.4	15.7	-7.1	11.5	119	14	30	49	43	22	5	7	306
2009	-	-	-	-	-	-	-	-	-	-	-	-	0	3.4	16.7	-4.8	13.1	130	6	16	45	53	15	3	6	365
2010	5.8	15.4	-0.2	10.7	3	0	0	5	8	0	0	2	61	3.6	16.3	-6.9	11.2	111	7	13	36	45	14	4	6	365
2011	5.6	19.2	-5.4	13.8	49	0	31	61	45	20	7	8	365	3.8	17.5	-6.0	11.4	101	8	19	42	54	31	7	8	365
2012	5.0	12.6	-1.7	2.1	19	8	69	27	4	30	16	1	240	3.5	11.6	-3.7	1.6	63	39	58	17	13	46	11	3	366
2013	-	-	-	-	-	-	-	-	-	-	-	-	0	4.3	16.3	-5.0	1.8	43	22	42	14	26	83	8	5	365
2014	-	-	-	-	-	-	-	-	-	-	-	-	0	3.8	13.6	-4.1	1.6	34	17	36	8	15	48	7	4	365
2015	6.4	13.8	1.6	1.9	0	0	2	0	4	7	1	1	92	3.7	14.0	-3.6	2.1	56	33	57	14	21	60	7	4	365
2016	7.0	16.3	-0.2	1.9	1	0	17	2	16	51	8	4	305	7.3	13.3	1.6	1.9	0	0	0	0	6	16	0	2	29

	BH													SR										
	T	*TX*	*TN*	*R*	*FD*	*ID*	*P1X*	*P1N*	*P9X*	*P9N*	*CS*	*TWS*	*D*	*T*	*TX*	*TN*	*R*	*FD*	*ID*	*P1X*	*P1N*	*P9X*	*P9N*	*CS*	*TWS*	*D*
2000	5.7	15.6	-4.4	15.2	20	0	8	18	8	3	3	2	122	-	-	-	-	-	-	-	-	-	-	-	-	0
2001	5.8	16.8	-6.5	13.4	66	3	41	48	28	15	11	6	365	5.4	18.3	-11.3	15.8	99	2	41	51	16	6	16	4	275
2002	5.2	21.8	-7.5	15.5	66	0	45	60	35	21	7	5	365	6.2	23.7	-9.4	18.1	103	2	55	61	38	15	7	8	362
2003	6.2	19.2	-5.5	12.2	39	1	22	30	30	13	6	4	361	6.9	21.9	-7.6	14.4	71	2	20	30	23	18	6	3	361
2004	6.5	24.2	-6.5	15.2	39	1	27	33	58	35	3	7	359	7.4	25.8	-9.0	18.5	74	1	20	28	59	37	8	8	366
2005	5.6	21.3	-8.1	16.1	63	6	50	49	49	33	19	13	365	6.5	24.2	-11.0	20.2	112	6	43	48	52	34	11	13	365
2006	5.9	22.0	-5.2	14.8	52	1	32	44	46	27	5	5	364	6.8	22.9	-9.3	21.0	81	4	33	39	48	26	5	5	365
2007	5.7	22.7	-4.7	14.5	52	0	33	42	44	28	7	4	365	6.7	19.5	-5.9	16.4	85	3	31	36	38	30	5	5	365
2008	9.9	24.5	-0.6	14.7	3	0	1	1	34	26	1	13	153	6.9	24.7	-10.3	17.5	86	2	48	38	61	52	5	12	366
2009	6.4	19.9	-3.3	12.9	45	0	28	31	36	23	5	4	302	6.6	25.2	-6.4	17.0	76	1	25	24	33	22	5	4	365
2010	5.7	20.0	-6.4	15.5	42	3	25	33	30	17	6	6	365	6.5	20.2	-9.2	16.7	71	3	28	33	26	18	4	7	365
2011	5.4	21.0	-6.0	15.9	51	0	38	44	34	19	7	6	273	6.1	21.8	-8.6	17.3	76	0	30	26	25	20	7	7	273
2012		-	-	-	-	-	-	-	-	-	-	-	0	-	-	-	-	-	-	-	-	-	-	-	-	0
2013	6.9	12.2	0.7	2.9	0	0	1	0	0	13	1	0	92	7.6	13.6	1.8	4.0	0	0	1	0	0	24	1	0	92
2014	6.2	16.5	-2.6	4.2	16	4	63	13	8	55	12	2	362	6.3	18.5	-4.3	4.3	24	7	64	10	4	70	16	1	365
2015	8.2	17.4	1.6	4.2	0	0	2	0	12	75	1	4	212	9.3	16.5	1.5	5.8	0	0	1	0	6	60	1	3	120
2016	6.6	16.6	-3.3	4.4	21	2	54	17	20	67	13	4	274	-	-	-	-	-	-	-	-	-	-	-	-	0

	PA												
	T	*TX*	*TN*	*R*	*FD*	*ID*	*P1X*	*P1N*	*P9X*	*P9N*	*CS*	*TWS*	*D*
2000	6.2	22.0	-8.2	16.2	77	1	42	41	30	28	11	4	366
2001	6.1	19.2	-8.4	16.2	87	0	37	40	26	17	13	5	365
2002	5.9	23.6	-11.4	17.6	100	4	58	68	37	28	10	8	365
2003	6.3	20.2	-6.7	17.2	73	0	33	39	22	18	5	3	365
2004	7.2	26.0	-5.4	19.2	56	0	25	26	47	50	3	7	366
2005	6.8	25.2	-7.5	19.0	83	0	33	47	48	41	6	11	365
2006	6.9	20.0	-6.0	15.6	67	0	30	36	39	43	3	5	365
2007	6.6	25.0	-6.4	15.4	71	1	32	35	29	41	5	4	365
2008	6.9	23.2	-6.0	16.3	68	0	46	41	53	49	7	12	366
2009	6.4	25.0	-7.1	15.8	70	0	28	39	34	27	3	4	365
2010	6.4	19.4	-9.8	17.1	76	2	36	40	21	14	8	3	365
2011	6.9	24.8	-10.1	19.1	78	0	33	39	38	45	8	6	365
2012	6.4	21.3	-7.0	18.3	83	0	43	44	30	42	6	4	366
2013	7.1	29.0	-9.8	16.5	60	0	26	28	37	47	6	5	365
2014	6.5	22.5	-6.3	18.0	60	0	29	28	28	31	7	5	365
2015	6.6	24.5	-9.2	18.5	83	0	45	36	34	24	5	6	365
2016	7.2	23.8	-6.9	18.8	82	0	17	36	48	46	2	4	366

Table S4. Indices of precipitation extremes per year. Listed are the annual precipitation (P) (mm), the absolute maximum of 1-Day (PDX) and 5-Day (P5DX) precipitation (mm), of the total annual amount of daily precipitation larger than the 95th percentile (P95P), of the total annual amount of daily precipitation larger than the 99th percentile (P99P), the maximum number of days with daily precipitation higher than 20 mm (HP), the maximum number of days with daily precipitation below 1 mm (DD), and the maximum length of wet spells (PWS) and dry spells (DS) per year. D: Days per year with available data.

	AR										PG									
	P	*PDX*	*P5DX*	*P95P*	*P99P*	*HP*	*DD*	*PWS*	*DS*	*D*	*P*	*PDX*	*P5DX*	*P95P*	*P99P*	*HP*	*DD*	*PWS*	*DS*	*D*
2000	-	-	-	-	-	-	-	-	-	0	-	-	-	-	-	-	-	-	-	0
2001	-	-	-	-	-	-	-	-	-	0	-	-	-	-	-	-	-	-	-	0
2002	-	-	-	-	-	-	-	-	-	0	4490	157	313	583	301	76	72	53	5	275
2003	-	-	-	-	-	-	-	-	-	0	9472	224	504	2693	759	159	57	43	6	365
2004	-	-	-	-	-	-	-	-	-	0	8449	284	620	2231	582	156	69	38	10	366
2005	-	-	-	-	-	-	-	-	-	0	7229	268	420	2041	775	119	83	47	14	365
2006	-	-	-	-	-	-	-	-	-	0	5762	193	541	2082	979	95	16	61	8	181
2007	-	-	-	-	-	-	-	-	-	0	-	-	-	-	-	-	-	-	-	0
2008	-	-	-	-	-	-	-	-	-	0	-	-	-	-	-	-	-	-	-	0
2009	-	-	-	-	-	-	-	-	-	0	-	-	-	-	-	-	-	-	-	0
2010	2248	55	117	105	0	33	56	42	7	275	4243	86	334	326	0	80	59	51	9	275
2011	3673	125	256	671	440	55	75	47	8	365	4470	125	328	392	0	85	68	47	7	273
2012	4474	108	248	1186	441	79	75	38	9	366	-	-	-	-	-	-	-	-	-	0
2013	3561	72	202	745	212	60	47	41	4	274	-	-	-	-	-	-	-	-	-	0
2014	4285	99	202	1258	195	70	64	29	5	332	-	-	-	-	-	-	-	-	-	0
2015	1456	98	154	238	98	17	36	23	7	151	-	-	-	-	-	-	-	-	-	0
2016	2741	97	192	279	97	45	90	47	8	305	3986	109	259	291	0	77	79	44	8	274

	BH										SR									
	P	*PDX*	*P5DX*	*P95P*	*P99P*	*HP*	*DD*	*PWS*	*DS*	*D*	*P*	*PDX*	*P5DX*	*P95P*	*P99P*	*HP*	*DD*	*PWS*	*DS*	*D*
2000	-	-	-	-	-	-	-	-	-	0	-	-	-	-	-	-	-	-	-	0
2001	3293	125	306	1305	444	47	68	37	7	245	1034	122	201	524	370	9	155	15	18	275
2002	2633	105	155	239	105	35	128	21	6	365	608	51	60	113	51	2	233	8	15	362
2003	4514	120	269	1264	222	74	83	37	7	361	937	51	81	203	51	5	196	12	14	361
2004	4174	127	341	879	244	70	83	33	7	359	855	62	110	183	143	4	213	9	13	366
2005	3702	153	324	983	562	50	107	26	7	365	736	24	63	208	0	6	235	5	13	365
2006	3813	213	305	871	517	54	113	36	21	364	600	45	87	181	45	5	259	11	50	365
2007	4913	174	286	1517	620	80	82	32	9	365	741	29	48	108	0	2	229	6	15	365
2008	1969	91	264	595	91	31	28	22	5	153	771	40	55	79	40	2	221	9	20	366
2009	3950	114	282	937	114	71	60	34	4	302	697	30	54	64	0	1	211	10	16	365
2010	4269	107	242	505	107	76	69	45	6	365	1050	124	154	421	226	5	209	11	13	365
2011	2389	99	202	436	194	40	28	37	5	181	674	42	62	243	42	5	166	7	18	273
2012	-	-	-	-	-	-	-	-	-	0	-	-	-	-	-	-	-	-	-	0
2013	1282	65	193	233	0	22	9	28	4	92	326	56	79	135	56	2	40	7	5	92
2014	4320	125	285	1031	406	71	99	41	7	365	881	36	68	201	69	5	223	12	14	365
2015	2123	122	233	371	122	35	64	30	7	212	478	32	64	32	0	1	157	10	18	242
2016	2044	82	201	312	0	29	118	30	21	274	421	18	41	18	0	0	259	8	30	366

	PA									
	P	*PDX*	*P5DX*	*P95P*	*P99P*	*HP*	*DD*	*PWS*	*DS*	*D*
2000	496	31	42	96	31	1	262	5	12	366
2001	490	22	38	87	0	1	267	5	23	365
2002	539	39	70	127	39	4	268	6	20	365
2003	590	23	49	123	0	4	236	5	21	365
2004	564	38	49	111	38	2	246	8	14	366
2005	572	27	51	153	0	4	263	6	33	365
2006	673	30	40	137	30	5	233	12	16	365
2007	589	40	73	107	70	3	252	9	17	365
2008	536	30	50	82	60	3	268	5	31	366
2009	498	32	64	89	32	3	267	5	14	365
2010	429	21	48	92	0	2	268	7	19	365
2011	642	36	58	156	70	4	256	5	21	365
2012	638	51	94	153	85	4	248	6	22	366
2013	709	48	67	184	48	3	249	8	21	365
2014	497	27	45	87	0	2	272	7	20	365
2015	753	43	86	254	77	7	253	8	15	365
2016	429	37	53	106	68	3	284	7	27	366

A.2 Publication 2

Glacier Mass Changes of Lake-Terminating Grey and Tyndall Glaciers at the Southern Patagonia Icefield Derived From Geodetic Observations and Energy and Mass Balance Modeling.

Weidemann S.S., Sauter T., Malz P., Jaña R., Arigony-Neto J., Casassa G. and Schneider C. (2018): Glacier Mass Changes of Lake-Terminating Grey and Tyndall Glaciers at the Southern Patagonia Icefield Derived From Geodetic Observations and Energy and Mass Balance Modeling. Front. Earth Sci. 6:81. doi:10.3389/feart.2018.00081

Status: Published.

Own contribution:

- design of the study (with co-authors)
- collection of meteorological and glaciological data (field work) (with co-authors)
- statistical downscaling of Reanalysis data
- processing of MODIS cloud cover data
- simulation climatic mass balance using COSIMA including uncertainty assessment
- calculation of frontal ablation amounts
- analysis and interpretation of the results (with co-authors)
- creating figures and tables
- writing the first draft of the manuscript
- incorporating the corrections by co-authors and reviewers

frontiers in Earth Science

ORIGINAL RESEARCH
published: 19 June 2018
doi: 10.3389/feart.2018.00081

Glacier Mass Changes of Lake-Terminating Grey and Tyndall Glaciers at the Southern Patagonia Icefield Derived From Geodetic Observations and Energy and Mass Balance Modeling

Stephanie S. Weidemann[1,2], Tobias Sauter[3], Philipp Malz[3], Ricardo Jaña[4], Jorge Arigony-Neto[5], Gino Casassa[6,7] and Christoph Schneider[1]*

[1] Geography Department, Humboldt University, Berlin, Germany, [2] Department of Geography, RWTH Aachen University, Aachen, Germany, [3] Department of Geography, Friedrich-Alexander University, Erlangen, Germany, [4] Instituto Antártico Chileno, Punta Arenas, Chile, [5] Instituto de Oceanografia, Universidade Federal do Rio Grande, Rio Grande, Brazil, [6] Geoestudios Ltda, San José de Maipo, Chile, [7] Dirección de Programas Antárticos y Subantárticos, Universidad de Magallanes, Punta Arenas, Chile

OPEN ACCESS

Edited by:
Thomas Vikhamar Schuler, University of Oslo, Norway

Reviewed by:
Qiao Liu, Institute of Mountain Hazards and Environment (CAS), China
Daniel Farinotti, ETH Zürich, Switzerland
Alexander H. Jarosch, University of Iceland, Iceland

***Correspondence:**
Stephanie S. Weidemann
s.weidemann@geo.rwth-aachen.de

Specialty section:
This article was submitted to Cryospheric Sciences, a section of the journal Frontiers in Earth Science

Received: *26 November 2017*
Accepted: *29 May 2018*
Published: *19 June 2018*

Citation:
Weidemann SS, Sauter T, Malz P, Jaña R, Arigony-Neto J, Casassa G and Schneider C (2018) Glacier Mass Changes of Lake-Terminating Grey and Tyndall Glaciers at the Southern Patagonia Icefield Derived From Geodetic Observations and Energy and Mass Balance Modeling. Front. Earth Sci. 6:81. doi: 10.3389/feart.2018.00081

In this study we demonstrate how energy and mass fluxes vary in space and time for Grey and Tyndall glaciers at the Southern Patagonia Icefield (SPI). Despite the overall glacier retreat of most Patagonian glaciers, a recent increase in mass loss has been observed, but individual glaciers respond differently in terms of spatial and temporal changes. In this context, the detailed investigation of the effect of mass balance processes on recent glacier response to climate forcing still needs refinement. We therefore quantify surface energy-fluxes and climatic mass balance of the two neighboring glaciers, Grey and Tyndall. The COupled Snow and Ice energy and MAss balance model COSIMA is applied to assess recent surface energy and climatic mass balance variability with a high temporal and spatial resolution for a 16-year period between April 2000 and March 2016. The model is driven by downscaled 6-hourly atmospheric data derived from ERA-Interim reanalysis and MODIS/Terra Snow Cover and validated against ablation measurements made in single years. High resolution precipitation fields are determined by using an analytical orographic precipitation model. Frontal ablation is estimated as residual of climatic mass balance and geodetic mass balance derived from TanDEM-X/SRTM between 2000 and 2014. We simulate a positive glacier-wide mean annual climatic mass balance of $+1.02 \pm 0.52$ m w.e. a^{-1} for Grey Glacier and of $+0.68 \pm 0.54$ m w.e. a^{-1} for Tyndall Glacier between 2000 and 2014. Climatic mass balance results show a high year to year variability. Comparing climatic mass balance results with previous studies underlines the high uncertainty in climatic mass balance modeling with respect to accumulation on the SPI. Due to the lack of observations accumulation estimates differ from previous studies based on the methodological approaches. Mean annual ice loss by frontal ablation is estimated to be 2.07 ± 0.70 m w.e. a^{-1} for Grey Glacier

and 3.26 ± 0.82 m w.e. a^{-1} for Tyndall Glacier between 2000 and 2014. Ice loss by surface ablation exceeds ice loss by frontal ablation for both glaciers. The overall mass balance of Grey and Tyndall glaciers are clearly negative with −1.05 ± 0.18 m w.e. a^{-1} and −2.58 ± 0.28 m w.e. a^{-1} respectively.

Keywords: Patagonia, glacier climatic mass balance, frontal ablation, energy and mass balance model, orographic precipitation model, TanDEM-X

1. INTRODUCTION

1.1. Rationale

Most Patagonian glaciers have been thinning and retreating at high rates during the past decades. Mass loss of the Northern Patagonia Icefield (NPI) and the Southern Patagonia Icefield (SPI) contributed to sea-level rise by 0.042 ± 0.002 mm a^{-1} between 1964/1975 and 2000 (Rignot et al., 2003), increasing to 0.067 ± 0.004 mm a^{-1} between 2000 and 2012 (Willis et al., 2012b). The main driver of the long-term demise of the ice-fields is most likely to be the warming climate (e.g., Rignot et al., 2003; Sakakibara and Sugiyama, 2014). Observed annual air temperatures at surface stations have increased by + 0.04°C to + 1.4°C south of 46°S during the past century (Rosenblüth et al., 1995). No significant trend of precipitation has been observed since 1950, but large inter-annual and decadal variations have been found (Carrasco et al., 2008; Aravena and Luckman, 2009; Lenaerts et al., 2014). Reanalysis data from 1960 to 2000 however show a slight decrease in solid precipitation over the ice-fields as a result of increasing air temperatures (Rasmussen et al., 2007).

Despite the general retreat of the outlet glaciers of the NPI and SPI, the individual responses show spatial and temporal non-uniform patterns (e.g., Aniya et al., 1996; Rivera and Casassa, 1999; Rivera et al., 2007; Lopez et al., 2010; Davies and Glasser, 2012; Sakakibara and Sugiyama, 2014; Minowa et al., 2015; Malz et al., 2018). Recent retreats of calving glaciers, such as Upsala and Jorge Montt glaciers are associated with ice flow acceleration and ice dynamical thinning near the calving front (Naruse and Skvarca, 2000; Rivera et al., 2012; Jaber et al., 2013; Muto and Furuya, 2013; Sakakibara and Sugiyama, 2014; Mouginot and Rignot, 2015). However, only a small number of NPI and SPI outlet glaciers show an extraordinary retreat including a recent ice speed acceleration between 2000 and 2011. The mean ice speed of the NPI and SPI even decreased between 2000 and 2011 compared to the time period of 1984 to 2000 (Sakakibara and Sugiyama, 2014). The recent increase in mass loss of the NPI and SPI therefore still seems to be mainly caused by long-term warming, while fjord geometry and ice dynamic processes are responsible for the rapid frontal retreat of individual calving glaciers, which enhances the mass loss (Casassa et al., 1997; Koppes et al., 2011; Rivera et al., 2012; Willis et al., 2012a,b; Sakakibara and Sugiyama, 2014). Recent surface mass balance modeling studies, however, estimate positive surface mass balance for the NPI and SPI, suggesting a slight increase in precipitation and cooling of the upper-atmospheric temperatures during the last decade as being the main driver (Lenaerts et al., 2014; Schaefer et al., 2015; Mernild et al., 2016). The contrasting pattern of observed glacier retreat and positive surface mass balance are assumed to be a result of increasing ice flow velocities associated with ice loss due to calving. However, ice loss due to increasing ice flow velocities has been observed only for those few tide-water glaciers undergoing a recent rapid glacier change.

In this study we demonstrate how energy and mass fluxes vary in space and time for Grey and Tyndall glaciers at the SPI. We aim to compute high resolution 6-hourly fields of surface energy fluxes and climatic mass balance for two neighboring glacier catchments by applying the COupled Snowpack and Ice surface energy and MAss balance model (COSIMA) (Huintjes et al., 2015) between 2000 and 2016. Different statistical downscaling methods are used to derive atmospheric input datasets. Precipitation fields are generated by applying an orographic precipitation model (OPM hereafter) based on the linear theory of orographic precipitation by Smith and Barstad (2004). The model has also been implemented successfully in several previous glaciological studies (Schuler et al., 2008; Jarosch et al., 2012; Weidemann et al., 2013). Cloudiness patterns are obtained from MODIS satellite data product MOD10A1 to correct for spatial variations of solar radiation. Geodetic mass balance changes are obtained by subtracting high-resolution TanDEM-X and SRTM data between 2000 and 2014 (Malz et al., 2018). We derive frontal ablation from modeled climatic mass balance and geodetic mass balance for each glacier for the same study period. The paper focuses on the validation of the downscaling results of atmospheric input data, and the comparison of modeled surface energy-fluxes, modeled climatic mass balance, and derived frontal ablation between both study sites.

1.2. Study Area

The study sites Grey and Tyndall glaciers are located at the southeastern part of the SPI (50.7°S–51.30°S, 73.5°W–73.1°W) (**Figure 1**). In 2016, glacier areas were 239.0 and 301.4 km^2, respectively (Meier et al., 2018). The Equilibrium Line Altitude (ELA) is estimated to be 970 ± 50 m above sea level (a.s.l.) for Grey Glacier (De Angelis, 2014; Schaefer et al., 2015) and 925 ± 25 m a.s.l. for Tyndall Glacier (Nishida et al., 1995; De Angelis, 2014).

Grey Glacier calves into a proglacial lake divided into three glacier termini which have shown different retreat and thinning rates over the last decades. The highest flow velocities of up to 2.8 m d^{-1} are observed at the central front of the glacier (Schwalbe et al., 2017). The glacier front has remained rather stable over the past two decades. According to Davies and Glasser (2012), both glaciers showed similar annual shrinkage of about −0.1 to −0.15% (1970–2011), with the fastest period of area loss occurring from 1986 to 2001.

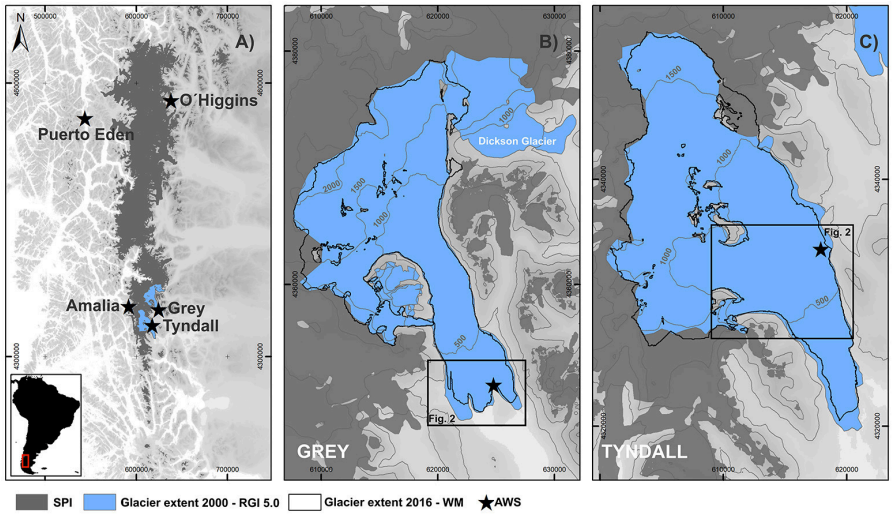

FIGURE 1 | (A) The location of Grey and Tyndall glaciers at the SPI and the location of the weather stations Puerto Eden, O'Higgins, Amalia, Tyndall and Grey, **(B)** Grey Glacier including the location of AWS Grey, **(C)** Tyndall Glacier including the location of AWS Tyndall. Glacier outlines are visualized for 2000 based on the RGI 5.0 and for 2016 based on a new glacier inventory by Meier et al. (2018). The coordinates are in UTM zone 18S in meters.

Information on accumulation amounts on the central part of the SPI are rare and mostly rely on a few firn cores retrieved of shallow to medium depth. The harsh weather conditions and the strong influence of meltwater percolation in the main plateaus are the prime reasons for sparse datasets (Godoi et al., 2002; Casassa et al., 2006). Three drilling sites located on the SPI allow estimation of a mean accumulation of 1.2 m water equivalent (w.e.) a^{-1} at Perito Moreno at 2,000 m a.s.l. in 1980/81-1985/86 (Aristarain and Delmas, 1993), 12.9–14.7 m w.e. a^{-1} at 1,756 m a.s.l. at Tyndall Glacier in 1998/99 with a firn-ice transition at 42.5 m depth (Godoi et al., 2002; Shiraiwa et al., 2002; Kohshima et al., 2007), and 3.4–7.1 m w.e. a^{-1} at 2,600 m a.s.l. at Pio XI Glacier for the period 2000–2006 with a firn-ice transition at 50.6 m depth (Schwikowski et al., 2013). These observations suggest high spatial differences of accumulation in the upper part of the SPI, indicating also that these findings might be strongly influenced by local conditions at the drilling sites.

2. DATA

2.1. Observations

Two automatic weather stations (AWS) are situated at Grey Glacier. AWS Grey has been running since March 2015 and measures hourly incoming solar radiation, wind speed and direction, air temperature, relative humidity at 2 m above the surface, and precipitation. Precipitation is measured at a height of 1 m using an unshielded tipping-bucket rain gauge. AWS Grey is located on rock close to the glacier margin between the eastern and middle front of Grey Glacier (**Figure 1**) at 50.98°S, 73.22°W at 229 m a.s.l. For modeling purpose, we installed an additional basic AWS in the ablation area at 50.97°S, 73.22°W for a period of 6 months from March 2015 to September 2015, measuring solar radiation, air temperature, and relative humidity. High coefficients of determination of 0.95–0.98 have been detected between the hourly datasets of both stations. To account for the cooling effect of the glacier surface we applied a bias-correction of air temperature as described in section 3.1.1.

The Chilean Water Directorate (DGA) provides additional AWS datasets within the study area. The AWS Tyndall is installed at 51.14°S, 73.35°W on the ablation area of Tyndall Glacier at 627 m a.s.l. and has been running since December 2013. This dataset contains hourly data of incoming and outgoing shortwave and longwave radiation, air temperature and humidity, surface pressure, wind speed and wind direction. Precipitation data of the weather stations Puerto Eden, O'Higgins, and Amalia are used for OPM validation. The weather stations Amalia and Puerto Eden are located west of the SPI at 50.95°S, 73.69°W at 60 m a.s.l. and 49.1°S, 74.4°W at 10 m a.s.l., while the weather station O'Higgins is situated at 48.91°S, 73.11°W at 265 m a.s.l. on the eastern margin of the SPI (**Figure 1**). Precipitation at Puerto Eden was measured from 1998 to 2010 although there are several data gaps. Data from the weather station O'Higgins covers the period from 2010 to 2014 while precipitation data from the weather station Amalia is limited to the period from June 2015 to April 2016.

Additionally, ablation stake measurements are available for Grey Glacier and Tyndall Glacier. Observations at Grey Glacier are limited to three time periods from January to March 2015, March to September 2015, and September 2015 to January 2016. Surface elevation changes of up to −8 m during the austral summer 2015/16 caused a complete melt-out of most stakes. Stake measurements were taken along a transect between 550 and 576 m a.s.l. on Tyndall Glacier from November 2012 to May 2013 (Geoestudios, 2013).

2.2. Reanalysis Data

Atmospheric model input datasets for COSIMA and OPM are derived from the latest large-scale ERA-Interim reanalysis product supplied by the European Centre for Medium-Range Weather Forecasts (ECMWF) (Dee et al., 2011).

COSIMA is forced by downscaled 6-hourly surface incoming solar radiation SW_{in} (W m^{-2}) and air temperature T_{2m} (°C), as well as relative humidity rH_{2m} (%), surface pressure p_s (hPa), and wind speed at 2 m u_{2m} (m s^{-1}), derived from the grid point located closest to the study sites (51.0°S, 73.5°W) for the time period from April 1st, 2000 to March 31st, 2016.

Running the OPM to compute liquid P_{liq} and solid precipitation P_{solid} (m) requires the following 6-hourly ERA-Interim atmospheric datasets: horizontal and vertical wind components, temperature, relative humidity, geopotential heights, and large-scale precipitation. The environmental and moist adiabatic lapse rates are calculated using datasets of air temperatures from the 850 and 500 hPa levels. The wind components of the 850 hPa level are used as large-scale prevailing wind conditions. The data of precipitation and relative humidity (850 hPa) are needed to calculate the background precipitation and filter constraints within the OPM routine as described in section 3.1.3. Since the atmospheric input of the OPM should represent upstream conditions, data is averaged over six grid points located west along the SPI (50.0°S–53.0°S, 75°W–73.5°W).

2.3. Cloud Cover

Cloud cover information is required to correct the spatial distribution of incoming solar radiation. Binary cloud cover information is included by default in the daily MODIS (Moderate Resolution Imaging Spectroradiometer) snow cover product MOD10A1 Version 6 (Hall and Riggs, 2016) with a spatial resolution of 500 m. MOD10A1 has also been used successfully in previous studies over snow and ice-covered grounds (e.g., Möller et al., 2011; Spiess et al., 2016).

Daily fractional cloud cover is further derived by averaging the binary cloud cover information of a fixed 5 × 5 grid point window for each central grid point within the COSIMA modeling domain. This method is used to calculate fractional cloud cover in the MODIS product MOD06L2 and has also been customized for the MOD10A1 product by Möller et al. (2011). Fractional cloud cover information serves as COSIMA input for parametrization of the incoming and outgoing longwave radiation.

2.4. Elevation Data And Glacier Outline

The digital elevation model (DEM) generated from the Shuttle Radar Topography Mission (SRTM) (Hoffmann and Walter, 2006; Jarvis et al., 2008) is used as the reference surface elevation in 2000 for COSIMA and OPM runs. COSIMA and OPM runs are carried out with a spatial resolution of 500 and 1,000 m, respectively. Glacier outlines for model runs have been used from the Randolph Glacier Inventory RGI 5.0 for 2000 (Consortium, 2015) to compare COSIMA results with previous surface mass balance studies (Schaefer et al., 2015; Mernild et al., 2016). In the RGI 5.0 the catchment of Grey Glacier also includes the neighboring Dickson Glacier (**Figure 1**).

Mean annual surface height changes between 2000 and 2014 are derived from SRTM and TanDEM-X data (Malz et al., 2018). This data is further needed for geodetic mass balance and frontal ablation estimations. Furthermore, annual surface height changes are considered in the altitude dependent calculation of atmospheric variables, e.g., air temperature in COSIMA.

3. METHODOLOGY

3.1. Surface Energy And Mass Balance

Climatic mass balance changes are estimated using the open source COupled Snowpack and Ice surface energy and MAss balance model (COSIMA) that was designed and validated in detail by Huintjes et al. (2015). COSIMA combines a surface energy balance model with a multi-layer sub-surface snow and ice model to fully resolve energy fluxes and mass balance processes.

The energy balance model combines all energy fluxes F that contribute to the surface energy budget and calculates the energy available for surface melting Q_{melt} (Oerlemans, 2001):

$$F = SW_{in} \cdot (1-\alpha) + LW_{in} + LW_{out} + Q_{sens} + Q_{lat} + Q_g + Q_{liq}. \quad (1)$$

It takes into consideration: the shortwave incoming radiation SW_{in}, the albedo α, the incoming LW_{in} and outgoing longwave radiation LW_{out}, the sensible Q_{sens} and the latent heat flux Q_{lat}, the ground heat flux Q_g, and the heat flux of liquid precipitation Q_{liq}. The latter is normally neglected (Cuffey and Paterson, 2010) but has been included here due to the significant amount of liquid precipitation in the ablation area of Patagonian glaciers.

Ablation occurs due to sublimation, subsurface melt, and surface melt. Q_{melt} requires the surface temperature T_s to be at the melting point (0°C) and a positive energy flux F toward the surface to prevail. In this case, Q_{melt} equals F. If T_s is below the melting point, no melt occurs. The subsurface snow module is structured in layers of 0.2 m thickness with a domain depth of 100 m (**Table 1**). Each layer is characterized by a temperature, density and liquid water content. The densification of the dry-snow pack is calculated using an empirical relation according to Herron and Langway (1980). The initial density profile of the snow pack is calculated by a linear interpolation between 250 and 550 kg m^{-3}. Different values of albedo for snow, firn and ice are considered (**Table 1**). A key variable to link the surface and subsurface modules is T_s since it controls the conductive heat flux between the surface and the two upper subsurface layers as well as defining LW_{out} and providing the lower temperature for calculating sensible and latent heat flux according to the bulk approach. Energy balance and subsurface heat conduction each provide T_s. Both modules are solved iteratively until the convergence of T_s. The initial subsurface temperature T_{sub} profile is linearly scaled from depth to the glacier surface between -1°C and 0°C (**Table 1**). In case modeled T_{sub} or T_s exceeds the melting point, it is set to 0°C and the remaining energy is used for subsurface or surface melt, respectively.

The parametrization of α is calculated as a function of snowfall frequency and snow depth following the scheme of Oerlemans and Knap (1998). The amount of incoming longwave radiation

TABLE 1 | Best-fit COSIMA and OPM parameter settings.

	Parameter	*Value*/ Range	Unit	Fixed/ Calculated	Source
COSIMA	Total domain depth	100	m	F	–
	Model layer thickness	0.1	m	F	–
	Ice albedo	0.3	–	F	Schaefer et al., 2015
	Fresh snow albedo	0.9	–	F	Huintjes et al., 2015
	Firn albedo	0.45	–	F	Schaefer et al., 2015
	Temperature lapse rate	−0.73	°C 100 m^{-1}	F	ERA-Interim
	Surface pressure gradient	−0.105	hPa m^{-1}	F	ERA-Interim
	Snow density for P_{solid}	250	kg m^{-3}	F	Huintjes et al., 2015
	Threshold for P_{solid} to P_{liq}	0–2.0	°C	F	Möller et al., 2007
	Snow pack density profile	250 to 550	kg m–3	C	Huintjes et al., 2015
OPM	Uplift sensitivity factor	0.006*	–	C	Smith and Barstad, 2004
	Water vapor scale height	2466*	m	C	Smith and Barstad, 2004
	Conversion/fallout time scale	1453*	m s^{-1}	C	Jiang and Smith, 2003
	Brunt-Väisälä frequency	0.008*	s^{-1}	C	Smith and Barstad, 2004
	Averaged falling speed	1.3	m s^{-1}	F	Weidemann et al., 2013
	Froude number	0.87*	–	C	Kunz and Kottmeier, 2006
	Threshold Froude number	≥1	–	F	–
	Thresholds relative humidity	90	%	F	Smith and Barstad, 2004

*Values denoted with * are mean values.*

is parametrized from air temperature, water vapor pressure and cloud cover fraction while outgoing longwave radiation is calculated from the surface temperature using the Stefan-Boltzmann law, assuming an emissivity of one.

Turbulent heat fluxes Q_{sens} and Q_{lat}, are calculated through the bulk aerodynamic method according to Oerlemans (2001) between the surface and two meters above ground by means of T_{2m}, rH_{2m} and u_{2m}. Q_g describes the sum of conductive heat flux and the energy flux from penetrating shortwave radiation. Heat flux through liquid precipitation depends on the temperature differences between the surface and a height of 2 m and the amount of liquid precipitation (Maniak, 2010).

Melt water production at the glacier surface serves as input for the snow model to simulate percolation, retention and refreezing of melt water within the snow pack. COSIMA is described in more detail by Huintjes et al. (2015).

3.1.1. Air Temperature

Air temperature is statistically downscaled from ERA-Interim data to AWS Grey and AWS Tyndall by using Quantile Mapping (e.g., Panofsky and Brier, 1968; Gudmundsson et al., 2012). Quantile Mapping is a common technique for statistical bias correction of climate-model outputs by mapping the modeled cumulative distribution function of the variable of interest onto the observed cumulative distribution function that has been derived from empirical percentiles (Gudmundsson et al., 2012).

Bias-corrected air temperature is spatially interpolated using a fixed lapse rate from the AWS locations. The lapse rate is calculated from nine ERA-Interim grid points over the study area using monthly T_{2m}. Furthermore, the surface elevation is updated each mass balance year based on the mean annual surface elevation changes from 2000 to 2014 observed by Malz et al. (2018). Surface elevation changes since 2014 are then kept constant.

3.1.2. Solar Radiation

Incoming shortwave radiation SW_{in} is taken from ERA-Interim and downscaled to AWS data using Quantile Mapping. The spatial distribution of SW_{in} is derived from a modified radiation model according to Kumar et al. (1997) that computes clear-sky direct and diffuse shortwave radiation depending on the geographical position, elevation, albedo and shading by the surrounding terrain, and the slope and aspect of each grid cell. The potential clear-sky radiation $SW_{in,pot,glacier}$ is corrected for cloud cover by downscaled ERA-Interim $SW_{in,AWS}$ at the AWS grid point.

At each time step the ratio $r_{SW,pot,glacier}$ of $SW_{in,pot,AWS}$ at the AWS location and any other pixel $SW_{in,pot,glacier}$ in the glacier domain is calculated. The spatial distribution of $SW_{in,glacier}$ including the effects of cloud cover and terrain shading at each grid point is calculated by:

$$SW_{in,glacier} = r_{SW,pot,glacier} \cdot SW_{in,AWS}. \quad (2)$$

Equation (2) assumes a homogenous cloud cover over the glacier area. Since in reality the cloud cover varies between the AWS location and the upper parts of the glacier, an additional cloud cover correction factor is included. In cases when the cloud cover differs between the AWS location and any other location on the glacier, $SW_{in,glacier}$ is calculated as follows:

$$SW_{in,glacier,cloudy} = r_{SW,pot,glacier} \cdot SW_{in,AWS} \cdot \acute{\eta} \quad (3)$$

$$SW_{in,glacier,clear} = r_{SW,pot,glacier} \cdot \frac{SW_{in,AWS}}{\acute{\eta}} \quad (4)$$

Equation (3) corrects the distribution of incoming solar radiation glacier-wide in case of clear sky conditions at the AWS and cloudy conditions over the glacier, while Equation (4) is used in case of inverse conditions between AWS and the remaining parts of the glacier. $\acute{\eta}$ describes an empirical coefficient being 0.4 at 51°S (Budyko, 1974). The coefficient implies that during fully overcast conditions the clear-sky incoming shortwave radiation is reduced by 60%.

3.1.3. Precipitation

Precipitation distribution is modeled using an analytical orographic precipitation model (OPM) based on the linear steady-state theory of airflow dynamics (Smith and Barstad, 2004; Barstad and Smith, 2005). A more detailed description and validation of the model itself is given by Smith and Barstad (2004) and Barstad and Smith (2005) while the methodical application as used in this study is described in more detail in Weidemann et al. (2013).

The OPM estimates precipitation resulting from forced orographic uplift of air masses over a mountain assuming stable and saturated atmospheric conditions. The model estimates the condensation rate by the terrain-induced vertical air velocity, the horizontal wind speed and advection of water vapor, and includes effects of airflow dynamics and downslope evaporation as well. The main term of the linear model describing the orographic precipitation generation is solved in Fourier space for each Fourier component (k,l) as follows:

$$\hat{P}(k,l) = \frac{C_w \cdot i \cdot \sigma \cdot \hat{h}(k,l)}{(1 - i \cdot m \cdot H_w)(1 + i \cdot \sigma \cdot \tau_c)(1 + i \cdot \sigma \cdot \tau_f)}. \quad (5)$$

Equation (5) includes an uplift sensitivity factor C_w, the water vapor scale height H_w, the complex number i, the intrinsic frequency σ, the Fourier transform of the orography $\hat{h}$, and the vertical wavenumber m and the delay time scales for conversion τ_c and fallout τ_f of hydrometeors. The thermodynamic sensitivity C_w accounts for the effects of saturation water vapor density, the moist adiabatic and environmental lapse rates. H_w mainly depends on the environmental air temperature and lapse rate. Airflow dynamics are represented by the intrinsic frequency, including the vertical and horizontal winds. One of the airflow features included is the decay of vertical velocity with altitude which is described by m. The calculation of m contains the buoyancy frequency in saturated atmosphere and the moist Brunt-Väisälä frequency N_m to consider the effect of moist air masses on the static stability. Additionally, the precipitation generation is shifted downstream from the water source region depending on the wind speed and the cloud time parameter τ_c and τ_f.

The final term of orographic precipitation distribution is obtained by an inverse Fourier Transformation

$$P_{oro}(x,y) = \int\int \hat{P}(k,l) \cdot e^{i\cdot(kx+ly)} \cdot dk \cdot dl. \quad (6)$$

Final total precipitation fields are then generated by considering large-scale precipitation which we hereafter refer to as background precipitation P_{back}. The procedure of final precipitation and P_{back} calculations is described in the following.

The application of the OPM is limited to stable and saturated air masses, not capturing flow blocking effects or being applicable during unstable atmospheric conditions. Time intervals which do not fulfill the model constraints have to be filtered out. To ensure saturated and stable atmospheric conditions, relative humidity rH, N_{m}, and the moist Froude number are suitable as model constraints (e.g., Smith and Barstad, 2004; Schuler et al., 2008; Jarosch et al., 2012; Weidemann et al., 2013). The moist Froude number describes the airflow regime as a dimensionless number and can be associated to specific orographic precipitation patterns (Kunz and Kottmeier, 2006). In this study, it is used as an index to ensure linear airflow without flow blocking.

We need to run the OPM twice to replace the orographic fraction of ERA-Interim precipitation by high resolution orographic precipitation fields (e.g., Schuler et al., 2008; Weidemann et al., 2013). In the first step, the OPM is forced by ERA-Interim atmospheric and elevation data to determine P_{back} under consideration of the model constraints by subtracting the modeled orographic fraction from ERA-Interim precipitation. The second step implies the application of the OPM to the SRTM elevation model at a high spatial resolution of 1 km using the same input parameters to achieve high resolution P_{oro} fields. A threshold is applied to ensure positive values of P_{oro}. Finally, high-resolution total precipitation fields (P) are calculated by means of P_{oro} and P_{back} under consideration of the model constraints. In case model constraints are complied with, P_{oro} is added to P_{back}. Otherwise, only P_{back} is assumed.

The amount of solid precipitation P_{solid} is calculated by:

$$P_{solid} = P \cdot f, \quad (7)$$

$$f = 0.5 \cdot (-tanh((T_{2m} - 1) \cdot 3) + 1). \quad (8)$$

Applying Equation (7), the proportion of solid precipitation to total precipitation f is smoothly scaled between 100% and 0% within a T_{2m} range of 0°C and 2°C (Möller et al., 2007; Weidemann et al., 2013).

3.2. COSIMA-Calibration

As calibration for climatic mass balance results we use ablation stake measurements made at Grey Glacier from 2015/2016. We run COSIMA with varying parameter settings of model domain depth, layer depth, initial temperature profile, and albedo values for ice and snow based on values used in Huintjes et al. (2015) and Schaefer et al. (2015) to achieve the best model fit at the location of stakes for the measurement period. The RMSE between the

best model fit and observed values is ±0.53 m w.e. COSIMA reproduces well the measured ablation amounts in winter and summer, as shown in **Figure 2**. In case of Grey Glacier, COSIMA tends to underestimate ablation. Best fit model parameters are listed in **Table 1**.

Surface mass balance observations based on stake measurements at Tyndall Glacier from November 2012 to May 2013 are in good agreement with modeled climatic mass balance as well, with a RMSE of ±0.64 m w.e. COSIMA overestimates ablation in average by 6.5%.

3.3. COSIMA-Uncertainties

The uncertainties of modeled climatic mass balance are estimated by accounting for uncertainties in the spatial distribution of input datasets of air temperature and solid precipitation due to the lack of observations in the accumulation area. The spatial distribution of air temperature is determined by the chosen lapse rate, while the amount of modeled precipitation is mainly controlled by the OPM filter constraint *rH*. We therefore include varying values of these for the assessment of climatic mass balance uncertainties as described in the following section.

The best fit parameter setting based on our findings is listed in **Table 1** including a calculated air temperature lapse rate of 0.73°C 100 m^{-1} and a threshold for the OPM filter constraint *rH* of 90%. In addition, a second air temperature lapse rate of 0.67°C 100 m^{-1}—as used in earlier mass balance studies (e.g., Fernández and Mark, 2016)—and two *rH* thresholds of 85 and 95% are considered. In total, six runs are carried out for the mass balance year 2015/16 to assess the uncertainty of glacier-wide climatic mass balance and surface height change related to this climatic mass balance. This results in standard deviations of ±0.52 m w.e. and ±0.65 m w.e. for Grey Glacier and ±0.54 and ±0.67 m for Tyndall Glacier.

3.4. Geodetic Mass Balance Derived From TanDEM-X/SRTM

For DEM production, a differential SAR interferometric approach was used to generate a DEM out of bi-static TanDEM-X and TanSAR-X image pairs. Afterwards, the resulting DEM needed refined horizontal and vertical adjustments on the reference DEM (SRTM). Details about the interferometric processing and postprocessing can be found in detail in Malz et al. (2018).

After DEM generation, annual surface elevation changes were computed by differencing the TanDEM-X from the reference SRTM DEM for the time period between both acquisitions with

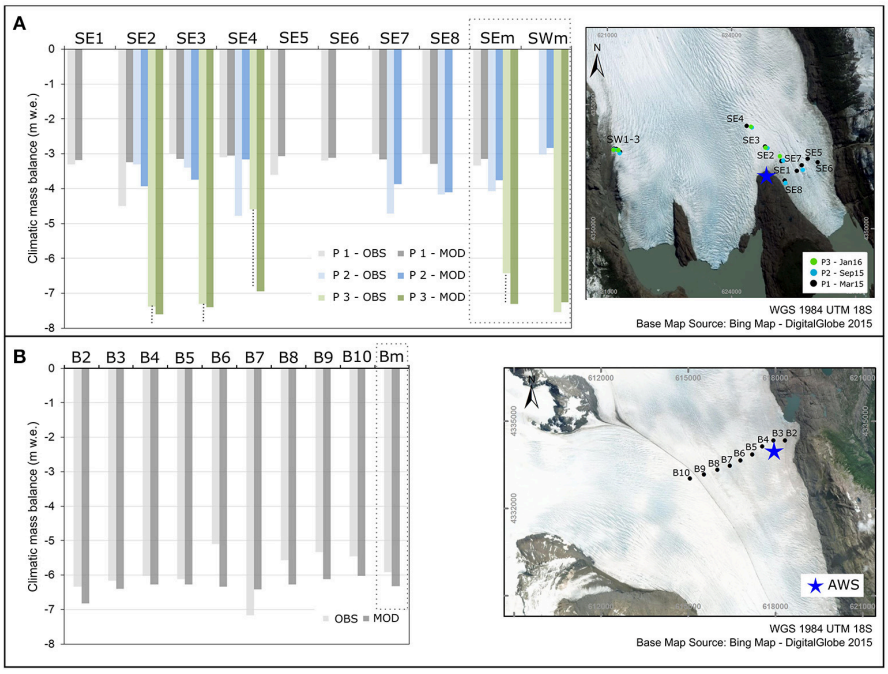

FIGURE 2 | Comparison of modeled and observed climatic mass balance at Grey Glacier and Tyndall Glacier by means of ablation stake data. **(A)** Measurements at Grey Glacier were carried out three times: from January 2015 to March 2015 (P1), March 2015 to September 2015 (P2), and September 2015 to January 2016 (P3). *SWm* is the mean of measured ablation at the western glacier tongue and *SEm* mean values of the ablation at the eastern glacier tongue. The black dashed lines indicate that the observed surface mass balance values represent only minimum values since these stakes melted completely out over the austral summer 2015/16, **(B)** surface mass balance observations at Tyndall Glacier are available along a transect (B2-B10) from November 2012 to May 2013 (Geoestudios, 2013). *Bm* is the mean of measured ablation. The coordinates of the subset maps are in UTM zone 18S in meters.

a spatial resolution of 30 × 30 m. In this study, we further interpolated the final product to a spatial resolution of 500 m × 500 m as used in COSIMA to later derive the amount of frontal ablation. For both glaciers, surface height changes based on TanDEM-X/SRTM are converted to mass balance changes using a constant density of 850 kg m^{-3} (Huss, 2013) and to volume changes by multiplying with the pixel area (500 × 500 m).

We assess the uncertainties of elevation change rate dh/dt and mass balance M using a simplified error propagation of Malz et al. (2018). Mass balance uncertainty (ϵ_M) is estimated using:

$$\epsilon_M = |M| \cdot \sqrt{\left(\frac{\delta_{dh/dt}}{dh/dt}\right) \cdot \left(\frac{\delta_\rho}{\rho}\right)} \quad (9)$$

considering the uncertainty δ of elevation change rate dh/dt and of density ρ for mass conversion. The uncertainty of elevation change rate includes the error of the relative vertical accuracy of SRTM and TanDEM-X DEM, the radar penetration into snow and ice and an inaccuracy resulting from the extrapolation during gap filling Malz et al. (2018). For Grey and Tyndall glaciers, this results in $\delta_{dh/dt}$ of 0.19 and 0.24 m a^{-1} for the study period of 2000–2014. A density uncertainty δ_ρ of 60 kg m^{-3} is taken into account while converting elevation changes to mass balance changes.

4. RESULTS AND DISCUSSION

4.1. Atmospheric Data

The evaluation of COSIMA input based on ERA-Interim, downscaled ERA-Interim and MODIS is summarized in Table S1 for Grey and Tyndall glaciers for each mass balance year (April 1st to March 31). Results of downscaled air temperature, solar radiation and precipitation will be discussed in more detail in the following section. Annual glacier-wide means and standard deviations are given below for the study period of 2000 to 2016.

4.1.1. Air Temperature

Downscaling results of daily ERA-Interim T_{2m} by means of station data are visualized in **Figure 3** for both AWS Grey and AWS Tyndall, respectively. Data from AWS Tyndall is split into a validation [April to October 2015 (yellow)] and calibration period. For the validation period, low temperatures are underestimated while high temperatures are overestimated.

The glacier-wide mean T_{2m} averaged over the whole study period is −2.4 ± 0.6°C for Grey Glacier and −0.7 ± 0.5°C for Tyndall Glacier. Glacier-wide air temperatures are higher than the mean value for the complete study period from 2003/04 to 2008/09 and 2011/12 to 2015/16. Air temperatures are lower than the average by 1.0°C to 1.3°C in 2001/02 and 2002/03. For the mass balance years 2004/05 to 2008/09, Mernild et al. (2016) simulates lower glacier-wide air temperatures of −2.7 ± 0.2°C and −1.0 ± 0.2°C compared to our results of −2.1 ± 0.2°C and −0.4 ± 0.2°C for Grey and Tyndall glaciers, respectively. For the time period of 2009/10 to 2013/14 both studies show slightly colder conditions.

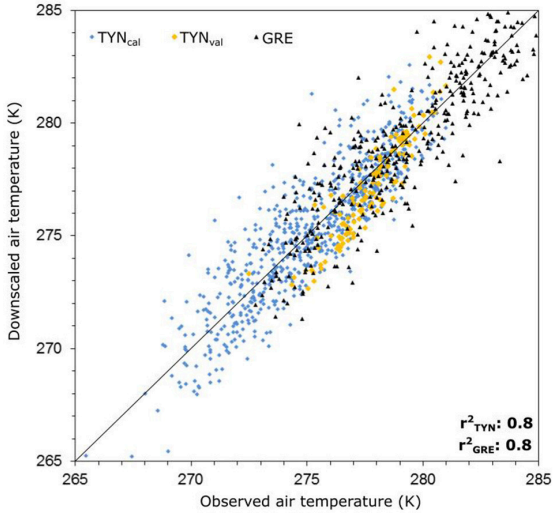

FIGURE 3 | Downscaled ERA-Interim T_{2m} vs. observed data of AWS Grey (GRE) and AWS Tyndall (TYN). Data of AWS Tyndall from April to October 2015 (yellow) is used as validation.

4.1.2. Solar Radiation and Cloud Cover

SW_{in} of ERA-Interim and AWS Tyndall and AWS Grey are in good agreement with each other and achieve high correlation. The bias-correction based on Quantile Mapping as described earlier led to better results regarding the overall sums and maximal values. As shown in **Figure 4** downscaled ERA-Interim data and observed data are in good agreement. The coefficient of determination is 0.8 for both AWS. Spatial fields of SW_{in} corrected by AWS data and MODIS cloud cover show an altitude-dependent pattern. The glacier-wide means of SW_{in} averaged over the study period are 109 ± 4 and 127 ± 5 W m^{-2} for Grey and Tyndall glaciers respectively (Table S1).

Cloud cover patterns by MODIS10A1 show overcast conditions during 90% of the time at the upper parts of both glaciers. Mean cloud cover is less in the lower parts with values ranging from 55 to 80%. The glacier-wide mean is 85 ± 0.1% for Grey Glacier, while overcast conditions at Tyndall Glacier occur 79 ± 0.1 % of the time.

4.1.3. Precipitation

OPM runs have been carried out with varying thresholds of the model constraint rH according to the values used in previous studies (e.g., Crochet et al., 2007; Schuler et al., 2008; Jarosch et al., 2012) to find the best model fit compared to observed data. We chose the measurement period from AWS Grey from April 2015 to March 2016 to be the calibration period and, the available data from AWS Grey and the weather station Amalia to be the calibration data. Best fits have been achieved using the constraint $rH \geq 90$ which has also been applied successfully at the Gran Campo Nevado Ice Cap by Weidemann et al. (2013). For the given constraints, the OPM performs 55% of the time.

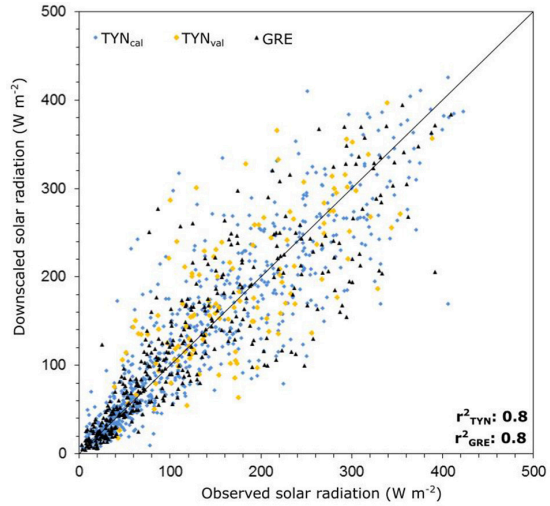

FIGURE 4 | Downscaled ERA-Interim SW_{in} vs. observed data of AWS Grey (GRE) and AWS Tyndall (TYN). Data of AWS Tyndall from April to October 2015 (yellow) is used as validation.

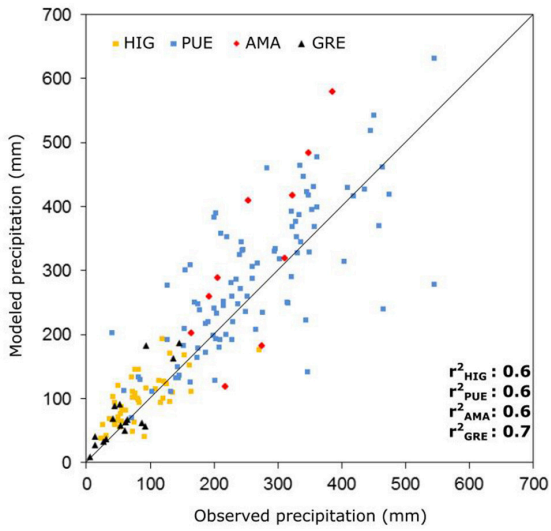

FIGURE 5 | Monthly modeled precipitation (mm) by OPM simulations and observed precipitation of the weather stations Puerto Eden (PUE), O'Higgins (HIG), Amalia (AMA), Tyndall (TYN), and Grey (GRE).

Best-fit OPM results are compared to observed precipitation data from four weather stations as illustrated in **Figure 5**. The explained variance between modeled and observed monthly precipitation data are 64% for the stations Puerto Eden, Amalia, and O'Higgins, and 73% for AWS Grey. The amount of modeled orographic precipitation accounts for 79.7 and 41.2% of the total modeled precipitation amount for the weather station Amalia and the AWS Grey, respectively. The weather stations Puerto Eden and O'Higgins are less influenced by orographic effects (orographic fraction less than 15%) due to the larger distance to the mountain range leading to a small fraction of modeled orographic precipitation. At these locations, modeled precipitation is mainly determined by the modeled background precipitation, which is based on ERA-Interim precipitation. The annual amounts of ERA-Interim precipitation are reduced by up to 15% in the central parts of the mountain range after subtracting the modeled orographic fraction from ERA-Interim precipitation as part of the background precipitation calculation.

Varying the filter constraint rH determines the amount of modeled orographic precipitation which is either reduced or enhanced. Therefore, this affects in particular the modeled precipitation at the locations of the weather station Amalia and the AWS Grey, which are highly influenced by orographic effects. Mean annual modeled precipitation amounts increase by 3–6% using $rH \geq 85$ at the four weather stations, while they decrease by 2–14% using $rH \geq 95$. Maximal annual precipitation amounts are in general shifted slightly to the windward side of the SPI mountain range. Depending on the filter constraints, the maximal annual precipitation amounts differ by around ±15% compared to $rH \geq 90$.

In general, the OPM tends to overestimate precipitation amounts at the weather stations. Despite possible measurement inaccuracies, the results are still in good agreement with observed data. Precipitation measuring equipment, such as installed at Grey Glacier, tends to underestimate precipitation in cases of snowfall or high wind speeds.

The glacier-wide mean annual precipitation amounts are 5.9 ± 1.0 m w.e. a^{-1} at Grey Glacier and 7.1 ± 1.1 m w.e. a^{-1} at Tyndall Glacier, averaged over the study period of 2000–2016. Mernild et al. (2016) simulate glacier-wide annual precipitation amounts of 10.26 ± 0.54 m w.e. a^{-1} for Grey Glacier and 9.19 ± 0.46 m w.e. a^{-1} for Tyndall Glacier between 2004/05 and 2013/14. These values are significantly higher than our findings. For the same period, we simulate glacier-wide mean annual precipitation of 6.27 ± 1.0 m w.e. a^{-1} for Grey Glacier and 7.45 ± 1.1 m w.e. a^{-1} for Tyndall Glacier.

The modeled ratio of solid to overall precipitation accounts for about 84.5 and 69.5% for Grey and Tyndall glaciers, respectively. Mean values for the SPI are estimated between 55% (Mernild et al., 2016) and 59% (Schaefer et al., 2015). Higher ratios of solid to overall precipitation for Grey and Tyndall glaciers compared to the mean value for the SPI seem reasonable since more than about 80% of the total falls in higher elevations as solid precipitation. This is at least partly due to the southern and lee-side location of these glaciers within the SPI.

4.2. Modeled Surface Energy Balance

The glacier-wide mean monthly surface energy balance components for both glaciers averaged between 2000 and 2016 are shown in **Figure 6**. The glacier-wide energy input is dominated year-around by LW_{in} (+ 279 W m^{-2}) and SW_{in} (+ 109 W m^{-2}), followed by Q_{sens} (+ 11 W m^{-2}), Q_g (+ 4 W m^{-2}) and Q_{liq} (+ 1 W m^{-2}). Available energy at the glacier surface is

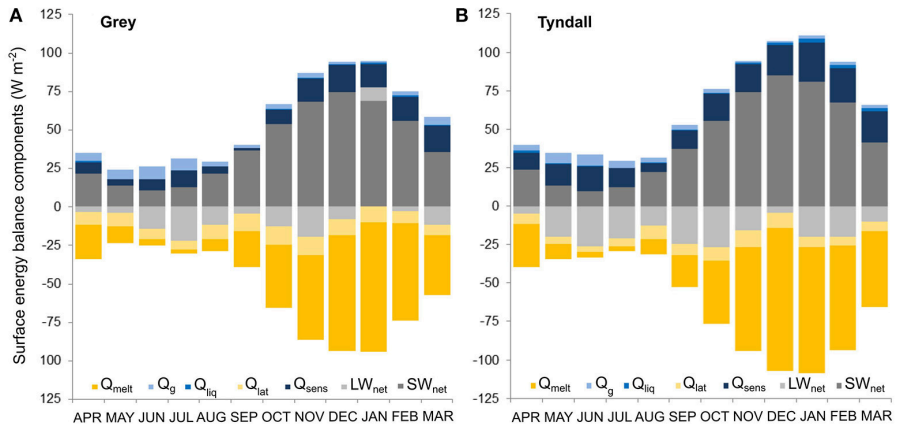

FIGURE 6 | Monthly surface energy balance components averaged between April 2000 and March 2016 for **(A)** Grey Glacier and **(B)** Tyndall Glacier. Abbreviations are explained in Equation 1.

consumed by LW_{out} (-288 W m^{-2}), SW$_{out}$ (−70 W m^{-2}), Q_{lat} (−9 W m^{-2}), and Q_{melt} (−36 W m^{-2}). The main source of melt energy is SW_{net} (+ 39 W m^{-2}).

The highest SW_{net} values are reached during the summer months (October to March) due to higher incoming solar radiation. Albedo values are similar throughout the year with a glacier wide-mean of 0.6. The highest values of Q_{sens} are reached during the austral summer months while Q_g is slightly higher during the winter. LW_{in} exceeds the amount of LW_{out} in January over extensive areas of the glacier and air temperatures are above the melting point and relative humidity is high in January. This atmospheric situation results in a large down-welling long-wave radiation from the atmosphere toward the glacier surface. The glacier and snow emission, however, are restricted to emission at 0°C. Therefore, LW_{out} is limited to 311 W m^{-2}. In consequence, the model calculates positive LW_{net} for the core melt phase in the austral summer.

Q_{liq} is negligible regarding the glacier-wide mean. However, it plays a more prominent role as a source of melt energy in the ablation area. Positive Q_g may result due to the assumption of the ice temperature at the bottom of the model domain section (3.1), which may lead to unrealistic high positive Q_g values especially at higher elevation where the annual air temperature is lower.

The energy budget of a snowpack is also affected by snow drift. Since COSIMA does not integrate snow drift parametrization, sublimation at the glacier surface may be overestimated (Barral et al., 2014; Huintjes et al., 2015). Furthermore, katabatic flow over large glaciers generates turbulences and enhances the turbulent exchange (Q_{lat}, Q_{sens}) (Oerlemans and Grisogono, 2002). Surface melt may therefore be underestimated by neglecting katabatic winds when applying COSIMA.

The surface energy balance components of Tyndall Glacier do not show any significant differences compared to Grey Glacier between 2000 and 2016. The glacier-wide energy input is also dominated by LW_{in} (+ 273 W m^{-2}) and SW_{in} (+ 127 W m^{-2}), followed by Q_{sens} (+ 16 W m^{-2}), Q_g (+ 3 W m^{-2}) and Q_{liq} (+ 1 W m^{-2}). Energy sinks are LW_{out} (-291 W m^{-2}), SW$_{out}$ (-82 W m^{-2}), Q_{lat} (−7 W m^{-2}), and Q_{melt} (-40 W m^{-2}). The modeled radiation terms at the AWS Tyndall pixel are in good agreement with observed data. The overall mean of SW_{in}, SW$_{out}$, LW_{in}, and LW_{out} differ by 5–7% for the mass balance year of 2015/16.

4.3. Modeled Climatic Mass Balance

Modeled glacier-wide mean annual climatic mass balance are positive for Grey Glacier with +0.86 ± 0.52 m w.e. a^{-1} and for Tyndall Glacier with +0.41 ± 0.54 m w.e. a^{-1} for the study period from April 2000 to March 2016 (Table S2).

Negative climatic mass balance years of Grey Glacier are simulated for 2001/02, 2004/05, 2011/12, and 2015/16, while the most negative climatic mass balance is reached in 2015/16 (Table S2). In mass balance years where the climatic mass balance is negative, either less P_{solid}, higher T_{2m}, or higher SW_{in} amounts occurred compared to the average (**Figure 7**). High positive climatic mass balance years are modeled for 2007/08 and 2013/14 caused by above-average P_{solid} amounts and lower SW_{in} values. Very low mean T_{2m} compensate low amounts of P_{solid} and SW_{in} in 2000/01. The glacier-wide mean climatic mass balance for the period 2000–2016 ranges from −11.9 ± 2.1 m w.e. a^{-1} in the lowest areas of the ablation area to + 10.3 ± 1.8 m w.e. a^{-1} in the top parts of the accumulation area (**Figures 8**, **9**).

Modeled mean annual ELA accounts for 960 ± 70 m a.s.l. ranging from 900 to 1,140 m a.s.l. These values are in good agreement with estimated mean ELA of De Angelis (2014) and Schaefer et al. (2015). The highest values for ELA of up to 1,140 m a.s.l. are simulated for the climatic mass balance years 2004/05 and 2015/2016. According to Malz et al. (2018), larger surface lowering have been observed at both outer glacier tongues of Grey Glacier. This pattern can also be distinguished in the modeled climatic mass balance results mainly because of the elevation feedback in air temperature as a consequence of the fact that the lateral glacier tongues have a lower surface elevation than Grey Glacier's middle branch (**Figure 8**).

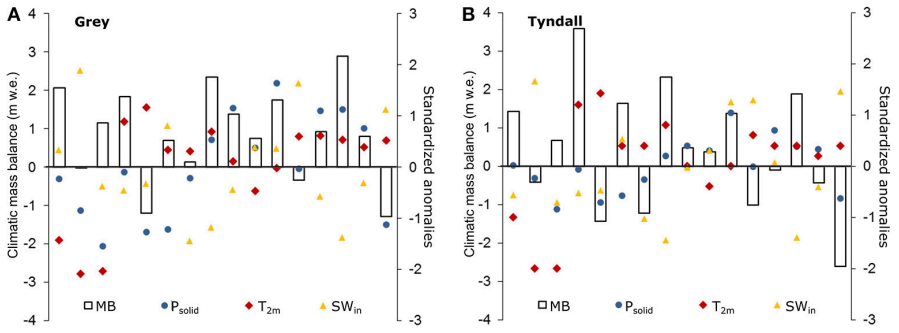

FIGURE 7 | Modeled annual climatic mass balance (MB) based on COSIMA simulations and standardized anomalies of P_{solid}, T_{2m}, SW_{in} from the mean between April 2000 and March 2016 for **(A)** Grey Glacier and **(B)** Tyndall Glacier.

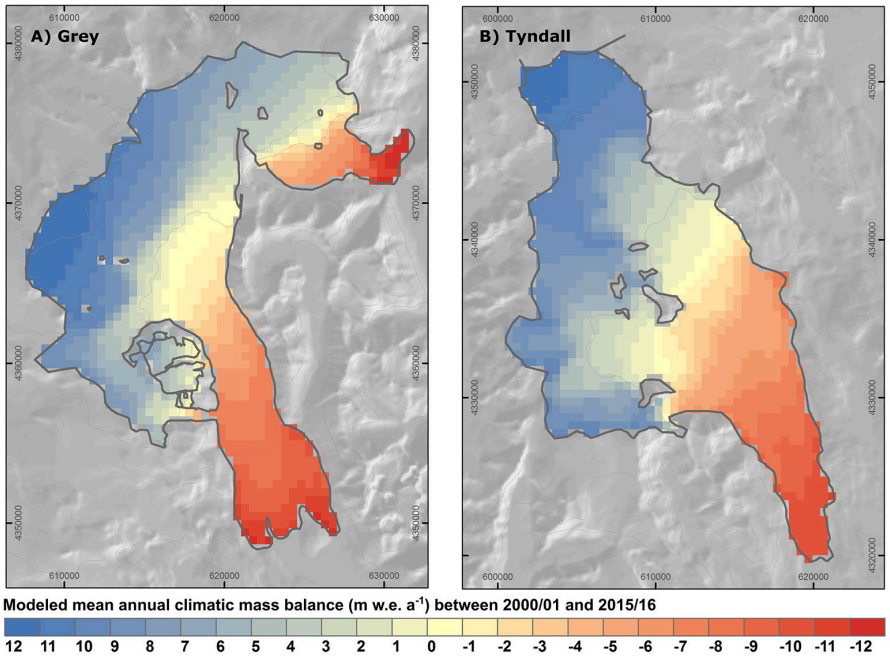

FIGURE 8 | Modeled mean annual climatic mass balance in m w.e. a^{-1} based on COSIMA simulations for the study period April 2000 to March 2016 for **(A)** Grey Glacier and **(B)** Tyndall Glacier. The coordinates are in UTM zone 18S in meters.

For Tyndall Glacier, negative climatic mass balance is simulated in 2001/02, 2004/05, 2006/07, 2011/12, 2012/13, 2014/5, and 2015/16 (Table S2). The inter-annual variations of climatic mass balance are high, ranging from -2.60 ± 0.54 to $+3.60 \pm 0.54$ m w.e. a^{-1}. In positive climatic mass balance years higher P_{solid}, lower T_{2m}, or lower SW_{in} amounts occurred compared to the average of each variable (**Figure 7**). Very high positive climatic mass balance in 2003/2004 is caused by high solid precipitation amounts in the lower altitudes. The combination of high air temperatures, high incoming solar radiation, and low solid precipitation amounts caused the strongly negative mass balance year in 2015/16.

The glacier-wide mean climatic mass balance for the period 2000–2016 ranges from -10.9 ± 3.2 m w.e. a^{-1} in the lowest areas of the ablation area to $+11.4 \pm 1.9$ m w.e. a^{-1} in the top parts of the accumulation area. In some years modeled annual ablation is as negative as -13.5 m w.e. a^{-1} and maximum accumulation reaches up to $+ 14.7$ m w.e. a^{-1} (**Figure 10**). The amount of accumulation in the highest altitudes seems reasonable compared to the study of Kohshima et al. (2007) who estimated

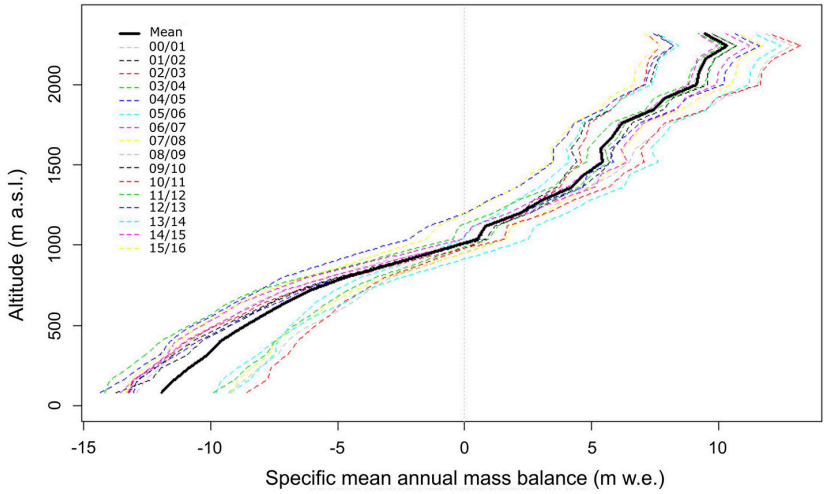

FIGURE 9 | Modeled climatic mass balance profiles for Grey Glacier for each mass balance year from 2000/2001 (00/01) to 2015/2016 (15/16). Climatic mass balance is averaged over 80 m altitude bins.

an annual net accumulation in the period of the austral winter 1998 to the austral winter 1999 of + 12.9 m w.e. at 1,756 m a.s.l. The mean modeled ELA is 920 ± 60 m a.s.l. ranging from 760 m a.s.l. to 1,000 m a.s.l. ELA values are within the range of previous estimates by Nishida et al. (1995), Casassa et al. (2014), and De Angelis (2014).

Comparing modeled climatic mass balance results with previous studies, especially Mernild et al. (2016), we simulate less positive climatic mass balance including high year to year variations. According to Mernild et al. (2016), mean annual surface mass balance was estimated to be about +2.86 ± 0.28 and +0 .71 ± 0.35 m w.e. a^{-1} between 2004/05 to 2008/2009 for Grey and Tyndall glaciers, respectively, with a slight increase in positive surface mass balance for the following period between 2009/10 and 2013/2014. COSIMA climatic mass balance results for the period 2004/05 to 2008/09 are less positive with +0.67 ± 0.52 m w.e. for Grey Glacier and +0.35 ± 0.54 m w.e. a^{-1} for Tyndall Glacier. The increase in positive climatic mass balance for the following period to 2013/14 is also reproduced by COSIMA. The contributions of subsurface melt, sublimation, refreezing, and evaporation are comparatively small (Table S2). The amounts of sublimation and evaporation are similar to values of Mernild et al. (2016).

The main reason for the differences in climatic mass balance is the amount of modeled annual precipitation. Current estimates from Schaefer et al. (2013); Lenaerts et al. (2014); Mernild et al. (2016) based on numerical simulations suggest average accumulation rates of 8-9 m w.e. a^{-1} for the SPI. At isolated locations, extreme precipitation rates of up to 30 m w.e. a^{-1} are suspected. These rather unrealistic amounts may result from an overestimation of modeled water vapor over the SPI. However, the lack of observed accumulation data of the SPI as described in section 1.2 and especially at Grey and Tyndall glaciers does not allow a detailed validation of modeled precipitation amounts.

4.4. Observed Geodetic Balance and Derived Frontal Ablation

Glacier-wide mean annual surface height changes between 2000 and 2014 simulated by COSIMA show an overall increase of +2.34 ± 0.65 m a^{-1} for Grey Glacier and +1.93 ± 0.67 m a^{-1} Tyndall Glacier due to high accumulation amounts. Observed mean annual surface height changes based on TanDEM-X/SRTM data indicate glacier average ice thinning of -1.23 ± 0.19 m a^{-1} and −3.04 ± 0.24 m a^{-1} for Grey and Tyndall glaciers, respectively. **Figure 11** illustrates the spatial differences of surface height changes between COSIMA and TanDEM-X/SRTM, interpolated to 500 m, for both glaciers. TanDEM-X/SRTM observes glacier thinning even in the accumulation areas, while COSIMA estimates a gain of mass in the accumulation area and a loss of mass in the ablation area (**Figure 12**).

The spatial distribution of surface height at the glacier fronts of Grey are non-uniform. Differences between both datasets at the outer tongues are small, especially at the western part, while high differences occur at the middle part of Grey Glacier. The latter is caused by a constant ice flow into this branch over time. Surface height changes and the front position of this middle branch remain constant over the entire study period. The western and eastern branches of the glacier tongue, however, seem to be partially decoupled from the main ice flow causing surface lowering which is mainly driven by climatic mass balance processes. The different ice dynamical effects at the glacier fronts are underlined by observed ice velocities based on LandSat-8 by Schwalbe et al. (2017). The highest velocities are observed at the middle part of the glacier terminus while the ice flow within the outer fronts is smaller. At Tyndall Glacier, we observe a more uniform pattern at the front but also a retreat of the glacier front (**Figure 11**). As expected, the smallest differences of surface height changes between COSIMA and TanDEM-X/SRTM are close to the mean ELA of both glaciers (**Figure 12**).

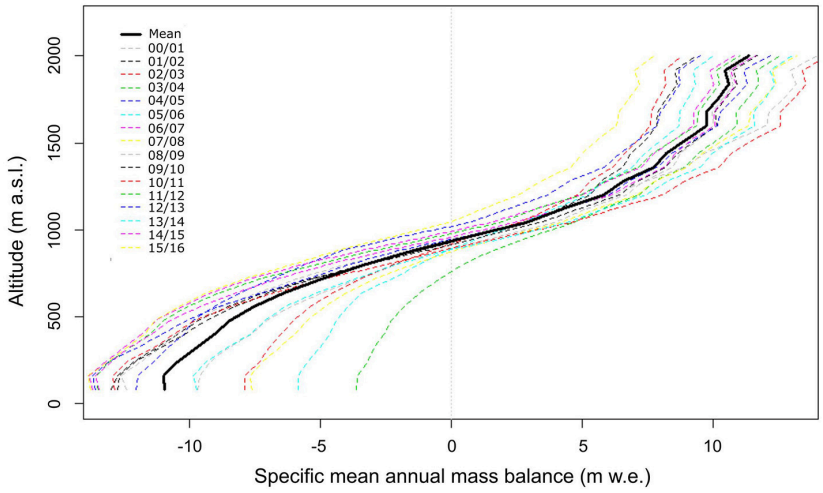

FIGURE 10 | Modeled climatic mass balance profiles for Tyndall Glacier for each mass balance year from 2000/2001 (00/01) to 2015/2016 (15/16). Climatic mass balance is averaged over 80 m altitude bins.

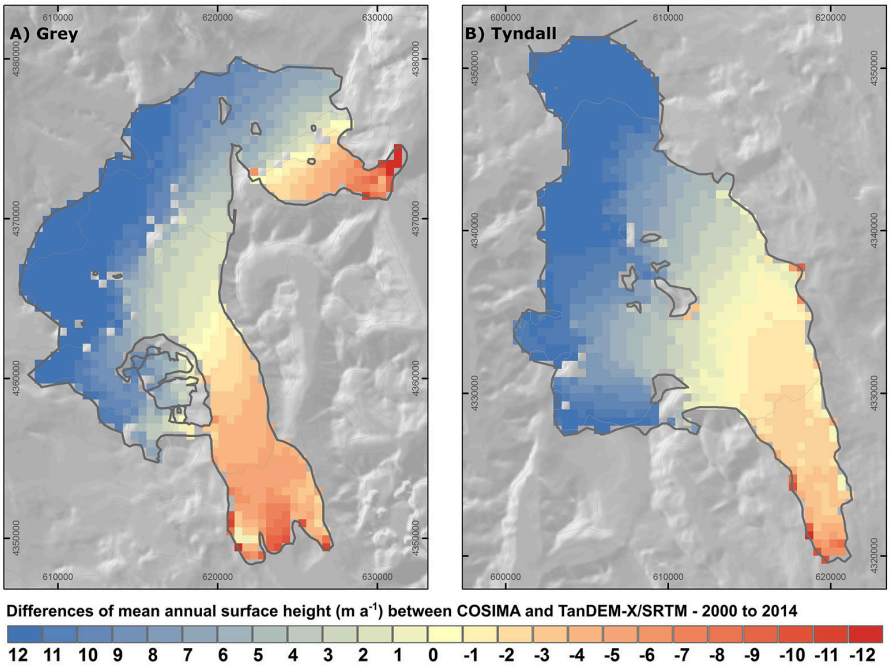

FIGURE 11 | Differences between mean annual surface height changes (m) based on COSIMA as the result of climatic mass balance and mean annual surface height changes (m) based on TanDEM-X/SRTM, interpolated to a spatial resolution of 500 m, between 2000 and 2014 for **(A)** Grey Glacier and **(B)** Tyndall Glacier. The coordinates are in UTM zone 18S in meters.

The glacier-wide mean annual climatic mass balance by COSIMA for the period of 2000–2014 is $+1.02 \pm 0.52$ m w.e.a^{-1} and $+0.68 \pm 0.54$ m w.e.a^{-1} for Grey and Tyndall glaciers, respectively. The positive climatic mass balance is mainly influenced by high accumulation amounts in the upper parts of the glaciers. A significant increase of glacier mass in the

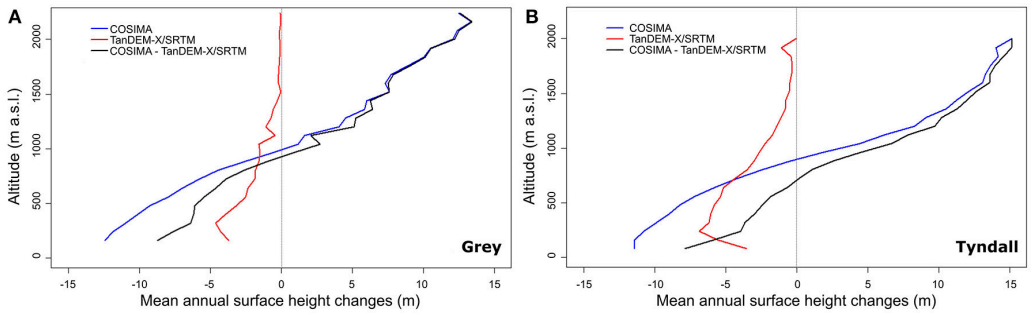

FIGURE 12 | Profiles of differences between mean surface height changes (m) based on COSIMA as the result of climatic mass balance and mean annual surface height changes (m) based on TanDEM-X/SRTM for **(A)** Grey Glacier and **(B)** Tyndall Glacier. Differences are averaged over 80 m altitude bins.

accumulation area has not been observed by TanDEM-X/SRTM (**Figure 12**).

Converting surface height changes by TanDEM-X/SRTM into mass balance changes yields in a mean geodetic mass balance of -1.05 ± 0.18 m w.e.a^{-1} for Grey Glacier and -2.58 ± 0.28 m w.e.a^{-1} for Tyndall Glacier. Since different densities for snow, firn, and ice are used within COSIMA, the mean density for converting surface height changes into climatic mass balance changes is lower within the COSIMA model than the density of 850 kg m^{-3} assumed for converting observed surface height changes by TanDEM-X/SRTM.

The differences between the modeled climatic mass balance and the geodetic mass balance are assumed to equal the amount of ice loss by frontal ablation which accounts for 2.07 ± 0.70 m w.e. a^{-1} for Grey Glacier and 3.26 ± 0.82 m w.e. a^{-1} for Tyndall Glacier. Ice loss by surface melt is larger than by frontal ablation with mean annual amounts of 3.48 m w.e.a^{-1} and 3.71 m w.e.a^{-1}, respectively.

Schaefer et al. (2015) inferred a frontal ablation, that they denoted as calving flux, of 1.51–1.55 ± 0.10 and 1.58-1.69 ± 0.11 km^3 a^{-1} from 2000 to 2011 for Grey and Tyndall glaciers. Integrating the differences of surface height changes between COSIMA and TanDEM-X/SRTM into volume changes results in frontal ablation of 1.09 ± 0.26 and 1.49 ± 0.28 km^3 a^{-1} for Grey and Tyndall glaciers from 2000 to 2014. Our findings underline a significant difference in recent volume loss between both glaciers due to differences in ice dynamical processes.

5. CONCLUSION

Recent climatic mass balance is calculated for 16 years between April 2000 and March 2016 using the surface energy and mass balance model COSIMA. COSIMA is driven by downscaled ERA-Interim data and MODIS cloud cover data. We successfully applied a linear orographic precipitation model to simulate precipitation fields with high spatial and temporal resolution.

We simulate a positive glacier-wide mean annual climatic mass balance of $+1.02 \pm 0.52$ m w.e. a^{-1} for Grey Glacier and of $+0.68 \pm 0.54$ m w.e. a^{-1} for Tyndall Glacier between 2000 and 2014. Climatic mass balance results show a high year to year variability. Main sources of melt energy are incoming solar radiation and the sensible heat flux. Modeled climatic mass balance for both glaciers is mainly controlled by the amount of solid precipitation and surface melt. The contributions of subsurface melt, sublimation, refreezing, and of evaporation are comparatively small. The lack of observed accumulation data causes high uncertainties in climatic mass balance simulations regarding the glacier-wide amount of solid precipitation. Therefore, climatic mass balance results of this study and previous ones differ considerably because of the use of different precipitation modeling scheme and atmospheric input data.

The comparison of surface height changes between COSIMA and TanDEM-X/SRTM data between 2000 and 2014 underlines the strong ice dynamical effects on glacier mass balance at Grey and Tyndall glaciers. Ice losses by frontal ablation are estimated to be 2.07 ± 0.70 m w.e. a^{-1} for Grey Glacier and 3.26 ± 0.82 m w.e. a^{-1} for Tyndall Glacier between 2000 and 2014. However, ice loss by surface ablation still exceeds the ice loss by frontal ablation. Surface height changes and changes of the frontal position differ significantly between the three fronts of Grey Glacier. Ice loss at the lateral branches seem to result mainly from negative climatic mass balance while the calving front of the central branch remains stable over the entire study period due to a sustained influx of ice in this part of the glacier.

Using geodetic and climatic mass balance to derive frontal ablation has been successfully applied in other studies (Nuth et al., 2012; Schaefer et al., 2015). The lack of observation and, in particular, information about the bedrock topography or ice thickness limit the applicability of high resolution ice dynamical models up to now. Nevertheless, the use of ice dynamical models will be a crucial advancement to fully quantify the ice dynamical processes and impact on the overall mass change, in future studies.

The outcomes of this study further confirm that the chosen methodological approaches to assess surface energy-fluxes and climatic mass balance are promising and suitable to be applied to the entire SPI in future investigations.

AUTHOR CONTRIBUTIONS

SW carried out COSIMA simulations, processed and analyzed the data. SW, TS, CS jointly designed the study and prepared the manuscript. PM processed surface height changes based on TanDEM-X/SRTM. RJ, JA-N, GC organized all logistics for the field campaigns. SW, TS, CS, RJ, JA-N, GC contributed to the field work. All authors discussed the results and reviewed the manuscript.

FUNDING

This research was funded by the CONICYT-BMBF project GABY-VASA: 01DN15007, 01DN15020, and BMBF20140052.

ACKNOWLEDGMENTS

We thank the Chilean Weather Service (DMC) and Chilean Water Directorate (DGA) for providing weather station data, and Marius Schaefer for providing stake measurements from Grey Glacier. We thank all participants, and especially Marcelo Arévalo, Guisella Gacitúa, Inti Gonzalez, Roberto Garrido, Matthias Braun, and Wolfgang Meier for their support during the field work at Grey Glacier. CONAF granted access to Torres del Paine National Park and provided support. Bigfoot and Hotel Lago Grey provided navigation support at Grey Lake. We thank all reviewers, the editor Thomas Schuler and the chief editor Regine Hock for their input which markedly helped to improve the manuscript.

SUPPLEMENTARY MATERIAL

The Supplementary Material for this article can be found online at: https://www.frontiersin.org/articles/10.3389/feart.2018.00081/full#supplementary-material

REFERENCES

Aniya, M., Sato, H., Naruse, R., Skvarca, P., and Casassa, G. (1996). The use of satellite and airborne imagery to inventory outlet glaciers of the southern patagonia icefield, south america. *Photogramm. Eng. Remote Sens.* 62, 1361–1369.

Aravena, J.-C., and Luckman, B. H. (2009). Spatio-temporal rainfall patterns in southern south america. *Int. J. Climatol.* 29, 2106–2120. doi: 10.1002/joc.1761

Aristarain, A. J., and Delmas, R. J. (1993). Firn-core study from the southern patagonia ice cap, south. *J. Glaciol.* 39, 249–254. doi: 10.1017/S0022143000015914

Barral, H., Genthon, C., Trouvilliez, A., Brun, C., and Amory, C. (2014). Blowing snow in coastal adelie land, antatrctica: three atmopsheric-moisture issues. *Cryosphere* 8, 1905–1919. doi: 10.5194/tc-8-1905-2014

Barstad, I., and Smith, R. B. (2005). Evaluation of an orographic precipitation model. *J. Hydrometeorol.* 6, 85–99. doi: 10.1175/JHM-404.1

Budyko, M. (1974). *Climate and Life*. New York, NY: Academic Press Inc.

Carrasco, J., Osorio, R., and Casassa, G. (2008). Secular trend of the equilibrium-line altitude on the western side of the southern andes, derived from radiosonde and surface observations. *J. Glaciol.* 54, 538–550. doi: 10.3189/002214308785837002

Casassa, G., Brecher, H., Rivera, A., and Aniya, M. (1997). A century-long recession record of glacier o'higgins, chilean patagonia. *Ann. Glaciol.* 24, 106–110.

Casassa, G., Luis, A. R., and Schwikowski, M. (2006). "Glacier mass balance data for southern south america (30°s-56°s)," in *Glacier Science and Environmental Change*, ed P. Knight (Oxford: Blackwell), 239–241.

Casassa, G., Rodríguez, J. L., and Loriaux, T. (2014). "A new glacier inventory for the southern patagonia icefield and areal changes 1986–2000," in *Global Land Ice Measurements from Space*, eds J. S. Kargel, G. J. Leonard, M. P. Bishop , A. Kääb, and B. H. Raup (Berlin; Heidelberg: Springer), 639–660.

Consortium, R. (2015). "Randolph glacier inventory – a dataset of global glacier outlines: Version 5.0.: Technical report" in *Global Land Ice Measurements from Space* (Colorado, CO Digital Media.)

Crochet, P., Jóhannesson, T., Jónsson, T., Sigurðsson, O., Björnsson, H., Pálsson, F., et al. (2007). Estimating the spatial distribution of precipitation in iceland using a linear model of orographic precipitation. *J. Hydrometeorol.* 8, 1285–1306. doi: 10.1175/2007JHM795.1

Cuffey, K., and Paterson, W. (2010). *The pyhsics of Glaciers, 4th Edn*. Burlington VT; Oxford: Butterworth-Heinemann; Elsevier Inc.

Davies, B., and Glasser, N. (2012). Accelerating shrinkage of patagonian glaciers from the little ice age (ad 1870) to 2011. *J. Glaciol.* 58, 1063–1084. doi: 10.3189/2012JoG12J026

De Angelis, H. (2014). Hypsometry and sensitivity of the mass balance to changes in equilibrium-line altitude: the case of the southern patagonia icefield. *J. Glaciol.* 60, 14–28. doi: 10.3189/2014JoG13J127

Dee, D., Uppala, S., Simmons, A., Berrisford, P., Poli, P., Kobayashi, S., et al. (2011). The era-interim reanalysis: configuration and performance of the data assimilation system. *Q. J. R. Meteorol. Soci.* 137, 553–597. doi: 10.1002/qj.828

Fernández, A., and Mark, B. (2016). Modeling modern glacier response to climate changes along the andes cordillera: a multiscale review. *J. Adv. Model. Earth Syst.* 8, 467–495. doi: 10.1002/2015MS000482

Geoestudios (2013). Implementación nivel 2 estrategia nacional de glaciares: Mediciones glaciológicas terrestres en chile central, zona sur y patagonia. *Report Dirección General de Aguas, Santiago, Chile*, SIT 327, 1–475.

Godoi, M. A., Shiraiwa, T., Kohshima, S., and Kubota, K. (2002). "Firn-core drilling operation at tyndall glacier, southern patagonia icefield," in *The Patagonian Icefields: A Unique Natural Laboratory for Environmental and Climate Change Studies*, eds G. Casassa, F. V. Sepúlveda, and R. M. Sinclair (Boston, MA: Springer US), 149–156.

Gudmundsson, L., Bremnes, J. B., Haugen, J. E., and Engen-Skaugen, T. (2012). Technical note: downscaling rcm precipitation to the station scale using statistical transformations - a comparison of methods. *Hydrol. Earth Syst. Sci.* 16, 3383–3390. doi: 10.5194/hess-16-3383-2012

Hall, D. K., and Riggs, G. A. (2016). *Modis/Terra Snow Cover Daily l3 Global 500m grid v005, 2000 to 2016*. Boulder, CO:. NASA National Snow and Ice Data Center Distributed Active Archive Center.

Herron, M., and Langway, C. (1980). Firn densification: an empirical model. *J. Glaciol.* 25, 373–385. doi: 10.1017/S0022143000015239

Hoffmann, J., and Walter, D. (2006). How complementary are srtm-x and-c band digital elevation models? *Photogramm. Eng. Remote Sens.* 72, 261–268. doi: 10.14358/PERS.72.3.261

Huintjes, E., Sauter, T., Schröter, B., Maussion, F., Yang, W., Kropáček, J., et al. (2015). Evaluation of a coupled snow and energy balance model for zhadang glacier, tibetan plateau, using glaciological measurements and time-lapse photography. *Arctic Antarctic Alpine Res.* 47, 573–590. doi: 10.1657/AAAR0014-073

Huss, M. (2013). Density assumptions for converting geodetic glacier volume change to mass change. *Cryosphere* 7, 877–887. doi: 10.5194/tc-7-877-2013

Jaber, W. A., Floricioiu, D., Rott, H., and Eineder, M. (2013). "Surface elevation changes of glaciers derived from srtm and tandem-x dem differences," in *IGARSS 2013* (IEEE Xplore), 1893–1896.

Jarosch, A. H., Anslow, F. S., and Clarke, G. K. C. (2012). High-resolution precipitation and temperature downscaling for glacier models. *Clim. Dyn.* 38, 391–409. doi: 10.1007/s00382-010-0949-1

Jarvis, A., Reuter, H., Nelson, A., and Guevara, E. (2008). Hole-filled SRTM for the globe Version 4, available from the CGIAR-CSI SRTM 90m Database. Available online at: http://srtm.csi.cgiar.org

Jiang, Q., and Smith, R. B. (2003). Cloud timescales and orographic precipitation. *J. Atmos. Sci.* 60, 1543–1559. doi: 10.1175/2995.1

Kohshima, S., Takeuchi, N., Uetake, J., Shiraiwa, T., Uemura, R., Yoshida, N., et al. (2007). Estimation of net accumulation rate at a patagonian glacier by ice core analyses using snow algae. *Glob. Planet. Change* 59, 236–244. doi: 10.1016/j.gloplacha.2006.11.014

Koppes, M., Conway, H., Rasmussen, L. A., and Chernos, M. (2011). Deriving mass balance and calving variations from reanalysis data and sparse observations, glaciar san rafael, northern patagonia, 1950–2005. *Cryosphere* 5, 791–808. doi: 10.5194/tc-5-791-2011

Kumar, L., Skidmore, A. K., and Knowles, E. (1997). Modelling topographic variation in solar radiation in a gis environment. *Int. J. Geogr. Infor. Sci.* 11, 475–497. doi: 10.1080/136588197242266

Kunz, M., and Kottmeier, C. (2006). Orographic enhancement of precipitation over low mountain ranges. part i: model formulation and idealized simulations. *J. Appl. Meteorol. Clim.* 45, 1025–1040. doi: 10.1175/JAM2389.1

Lenaerts, J. T. M., van den Broeke, M. R., van Wessem, J. M., van de Berg, W. J., van Meijgaard, E., van Ulft, L. H., et al. (2014). Extreme precipitation and climate gradients in patagonia revealed by high-resolution regional atmospheric climate modeling. *J. Clim.* 27, 4607–4621. doi: 10.1175/JCLI-D-13-00579.1

Lopez, P., Chevallier, P., Favier, V., Pouyaud, B., Ordenes, F., and Oerlemans, J. (2010). A regional view of fluctuations in glacier length in southern south america. *Glob. Planet. Change* 71, 85–108. doi: 10.1016/j.gloplacha.2009.12.009

Malz, P., Meier, W., Casassa, G., Jaña, R., Skvarca, P., and Braun, M. H. (2018). Elevation and mass changes of the southern patagonia icefield derived from tandem-x and srtm data. *Rem. Sens.* 10:188. doi: 10.3390/rs10020188

Maniak, U. (2010). *Hydrologie und Wasserwirtschaft: Eine Einführung für Ingenieure*. Verlag; Heidelberg: Springer.

Meier, W., Hochreuther, P., Grießinger, J., and Braun, M. (2018). An updated multi-temporal glacier inventory for the patagonian andes with changes between the little ice age and 2016. *Front. Earth Sci.* 6:62. doi: 10.3389/feart.2018.00062

Mernild, S. H., Liston, G. E., Hiemstra, C., and Wilson, R. (2016). The andes cordillera. Part III: glacier surface mass balance and contribution to sea level rise (1979–2014). *Int. J. Climatol.*. 37, 3154–3174. doi: 10.1002/joc.4907

Minowa, M., Sugiyama, S., Sakakibara, D., and Sawagaki, T. (2015). Contrasting glacier variations of glaciar perito moreno and glaciar ameghino, southern patagonia icefield. *Ann. Glaciol.* 56, 26–32. doi: 10.3189/2015AoG70A020

Möller, M., Finkelnburg, R., Braun, M., Hock, R., Jonsell, U., Pohjola, V. A., et al. (2011). Climatic mass balance of the ice cap vestfonna, svalbard: a spatially distributed assessment using era-interim and modis data. *J. Geophys. Res. Earth Surf.* 116, 1–14. doi: 10.1029/2010JF001905

Möller, M., Schneider, C., and Kilian, R. (2007). Glacier change and climate forcing in recent decades at gran campo nevado, southernmost patagonia. *Ann. Glaciol.y* 46, 136–144. doi: 10.3189/172756407782871530

Mouginot, J., and Rignot, E. (2015). Ice motion of the patagonian icefields of south america: 1984–2014. *Geophys. Res. Lett.* 42, 1441–1449. doi: 10.1002/2014GL062661

Muto, M., and Furuya, M. (2013). Surface velocities and ice-front positions of eight major glaciers in the southern patagonian ice field, south america, from 2002 to 2011. *Rem. Sens. Environ.* 139, 50–59. doi: 10.1016/j.rse.2013.07.034

Naruse, R., and Skvarca, P. (2000). Dynamic features of thinning and retreating glaciar upsala, a lacustrine calving glacier in southern patagonia. *Arctic Antarctic Alpine Res.* 32, 485–491. doi: 10.2307/1552398

Nishida, K., Satow, K., Aniya, M., Casassa, G., and Kadota, T. (1995). Thickness change and flow of glaciar tyndall, patagonia. *Bull. Glacier Res.* 13, 29–34.

Nuth, C., Schuler, T. V., Kohler, J., Altena, B., and Hagen, J. O. (2012). Estimating the long-term calving flux of kronebreen, svalbard, from geodetic elevation changes and mass-balance modeling. *J. Glaciol.* 58, 119–133. doi: 10.3189/2012JoG11J036

Oerlemans, J. (2001). *Glaciers and Climate Change*. Lisse: Swets and Zeitlinger.

Oerlemans, J., and Grisogono, B. (2002). Glacier winds and parametrisations of the related surface heat fluxes. *Tellus* 54, 440–452. doi: 10.3402/tellusa.v54i5.12164

Oerlemans, J., and Knap, W. (1998). A 1 year record of global radiation and albedo in the ablation zone of morteratschgletscher, switzerland. *J. Glaciol.* 44, 239–247.

Panofsky, H., and Brier, G. (1968). *Some Applications of Statistics to Meteorology*. Earth and Mineral Sciences Continuing Education, College of Earth and Mineral Sciences.

Rasmussen, L., Conway, H., and Raymond, C. (2007). Influence of upper air conditions on the patagonia icefields. *Global Planet. Change* 59, 203–216. doi: 10.1016/j.gloplacha.2006.11.025

Rignot, E., Rivera, A., and Casassa, G. (2003). Contribution of the patagonia icefields of south america to sea level rise. *Science* 302, 434–437. doi: 10.1126/science.1087393

Rivera, A., Benham, T., Casassa, G., Bamber, J., and Dowdeswell, J. A. (2007). Ice elevation and areal changes of glaciers from the northern patagonia icefield, chile. *Glob. Planet. Change* 59, 126–137. doi: 10.1016/j.gloplacha.2006.11.037

Rivera, A., and Casassa, G. (1999). Volume changes on pío xi glacier, patagonia: 1975–1995. *Glob. Planet. Change* 22, 233–244. doi: 10.1016/S0921-8181(99)00040-5

Rivera, A., Koppes, M., Bravo, C., and Aravena, J. C. (2012). Little ice age advance and retreat of glaciar jorge montt, chilean patagonia. *Clim. Past* 8, 403–414. doi: 10.5194/cp-8-403-2012

Rosenblüth, B., Casassa, G., and Fuenzalida, H. A. (1995). Recent climatic changes in western patagonia. *Bull. Glacier Res.* 13 127–132.

Sakakibara, D., and Sugiyama, S. (2014). Ice-front variations and speed changes of calving glaciers in the southern patagonia icefield from 1984 to 2011. *J. Geophys. Res. Earth Surf.* 119, 2541–2554. doi: 10.1002/2014JF003148

Schaefer, M., Machguth, H., Falvey, M., and Casassa, G. (2013). Modeling past and future surface mass balance of the northern patagonia icefield. *J. Geophys. Res. Earth Surf.* 118, 571–588. doi: 10.1002/jgrf.20038

Schaefer, M., Machguth, H., Falvey, M., Casassa, G., and Rignot, E. (2015). Quantifying mass balance processes on the southern patagonia icefield. *Cryosphere* 9, 25–35. doi: 10.5194/tc-9-25-2015

Schuler, T. V., Crochet, P., Hock, R., Jackson, M., Barstad, I., and Jóhannesson, T. (2008). Distribution of snow accumulation on the svartisen ice cap, norway, assessed by a model of orographic precipitation. *Hydrol. Process.* 22, 3998–4008. doi: 10.1002/hyp.7073

Schwalbe, E., Gröhnert, M., Koschitzki, R., Cárdenas, C., and Maas, H. (2017). "Determination of spatio-temporal velocity fields at grey glacier using terrestrial image sequences and optical satellite imagery," in *LFirst IEEE International Symposium of Geoscience and Remote Sensing (GRSS-CHILE)* (Valdivia).

Schwikowski, M., Schläppi, M., Santibañez, P., Rivera, A., and Casassa, G. (2013). Net accumulation rates derived from ice core stable isotope records of pío xi glacier, southern patagonia icefield. *Cryosphere* 7, 1635–1644. doi: 10.5194/tc-7-1635-2013

Shiraiwa, T., Kohshima, S., Uemura, R., Yoshida, N., Matoba, S., Uetake, J., et al. (2002). High net accumulation rates at the campo de hielo patagonico sur, south america, revealed by analyses of a 45.97m long ice core. *Ann. Glaciol* 35, 84–90. doi: 10.3189/172756402781816942

Smith, R. B., and Barstad, I. (2004). A linear theory of orographic precipitation. *J. Atmos. Sci.* 61, 1377–1391. doi: 10.1175/1520-0469(2004)061<1377:ALTOOP>2.0.CO;2

Spiess, M., Schneider, C., and Maussion, F. (2016). Modis-derived interannual variability of the equilibrium-line altitude across the tibetan plateau. *Ann. Glaciol.* 57, 140–154. doi: 10.3189/2016AoG71A014

Weidemann, S., Sauter, T., Schneider, L., and Schneider, C. (2013). Impact of two conceptual precipitation downscaling schemes on mass-balance modeling of gran campo nevado ice cap, patagonia. *J. Glaciol.* 59, 1106–1116. doi: 10.3189/2013JoG13J046

Willis, M. J., Melkonian, A. K., Pritchard, M. E., and Ramage, J. M. (2012a). Ice loss rates at the northern patagonian icefield derived using a decade of satellite remote sensing. *Rem. Sens. Environ.* 117, 184–198. doi: 10.1016/j.rse.2011.09.017

Willis, M. J., Melkonian, A. K., Pritchard, M. E., and Rivera, A. (2012b). Ice loss from the southern patagonian ice field, south america, between 2000 and 2012. *Geophys. Res. Lett.* 39, 1–6. doi: 10.1029/2012GL053136

Conflict of Interest Statement: The authors declare that the research was conducted in the absence of any commercial or financial relationships that could be construed as a potential conflict of interest.

frontiers

Supplementary Material: Glacier mass changes of lake-terminating Grey and Tyndall glaciers at the Southern Patagonia Icefield derived from geodetic observations and energy and mass balance modeling

1 SUPPLEMENTARY DATA

Table S1. Glacier-wide mean of air temperature T_{2m} $(^{\circ}C)$, total precipitation P *(m w.e.)*, cloud cover fraction f_{cc} $(\%)$, surface pressure p_s *(hPa)*, shortwave radiation SW_{in} $(W\,m^{-2})$, relative humidity rH_{2m} $(\%)$ and wind speed u_{2m} $(m\,s^{-1})$ as COSIMA atmospheric input data for Grey and Tyndall glaciers per mass balance year. Values of rH_{2m} and u_{2m} are used from one ERA-Interim grid point without any further downscaling or spatial interpolation.

	GREY					TYNDALL					ERA	
year	T_{2m}	P	f_{cc}	p_s	SW_{in}	T_{2m}	P	f_{cc}	p_s	SW_{in}	rH_{2m}	u_{2m}
2000/01	-3.2	5.4	0.75	874	110	-1.2	6.6	0.69	900	125	88	2.9
2001/02	-3.6	4.7	0.86	875	116	-1.7	5.8	0.74	902	135	87	2.9
2002/03	-3.6	4.4	0.89	874	108	-1.7	5.3	0.78	901	124	88	2.7
2003/04	-1.8	5.9	0.83	874	108	-0.1	7.2	0.73	902	125	86	3.0
2004/05	-1.7	4.6	0.87	875	108	0.0	5.7	0.74	902	125	86	3.0
2005/06	-2.2	4.7	0.86	874	112	-0.5	5.9	0.77	902	130	85	2.8
2006/07	-2.2	5.8	0.86	874	104	-0.5	6.8	0.76	902	122	87	3.1
2007/08	-1.9	6.6	0.85	875	105	-0.3	7.8	0.74	904	121	86	3.1
2008/09	-2.3	7.4	0.87	874	108	-0.7	8.6	0.78	903	127	86	3.1
2009/10	-2.6	6.2	0.87	872	111	-0.9	7.3	0.78	901	129	86	3.3
2010/11	-2.4	7.4	0.86	874	111	-0.7	9.0	0.78	903	133	85	3.1
2011/12	-2.0	6.0	0.86	875	115	-0.4	7.2	0.76	904	133	85	3.0
2012/13	-2.0	6.8	0.85	875	107	-0.5	8.0	0.77	904	127	86	3.1
2013/14	-2.0	7.2	0.85	874	104	-0.5	8.2	0.77	904	121	86	3.3
2014/15	-2.1	6.6	0.86	875	108	-0.6	7.7	0.77	904	125	85	2.9
2015/16	-2.1	4.8	0.85	875	113	-0.5	5.6	0.75	905	134	84	2.9
2000/16	**-2.4**	**5.9**	**0.85**	**874**	**109**	**-0.7**	**7.1**	**0.76**	**903**	**127**	**86**	**3.0**

Table S2. Glacier-wide annual rates of climatic mass balance MB, solid precipitation P_{solid}, surface melt M_{sur}, subsurface melt M_{sub} and sublimation S in m w.e.. Sums of refreezing and evaporation are not listed.

	GREY					TYNDALL				
year	MB	P_{solid}	M_{sur}	M_{sub}	S	MB	P_{solid}	M_{sur}	M_{sub}	S
2000/01	2.06	4.81	2.36	0.35	0.07	1.44	4.88	3.03	0.39	0.08
2001/02	-0.02	4.28	3.73	0.49	0.14	-0.42	4.51	4.35	0.53	0.12
2002/03	1.14	3.70	2.10	0.34	0.07	0.68	3.60	2.53	0.38	0.06
2003/04	1.83	4.92	2.64	0.42	0.07	3.60	4.76	0.90	0.28	0.02
2004/05	-1.20	3.93	4.50	0.56	0.12	-1.44	3.80	4.64	0.58	0.10
2005/06	0.69	3.97	2.79	0.47	0.07	1.64	3.99	1.98	0.42	0.04
2006/07	0.13	4.82	4.11	0.47	0.13	-1.23	4.47	5.09	0.54	0.12
2007/08	2.34	5.45	2.66	0.41	0.07	2.32	5.15	2.46	0.40	0.06
2008/09	1.38	5.97	4.03	0.47	0.12	0.48	5.46	4.43	0.51	0.13
2009/10	0.75	5.31	4.00	0.47	0.14	0.37	5.31	4.39	0.50	0.12
2010/11	1.74	6.38	4.05	0.47	0.14	1.37	6.43	4.47	0.51	0.12
2011/12	-0.35	4.97	4.64	0.59	0.13	-1.01	4.84	5.18	0.61	0.12
2012/13	0.92	5.92	4.41	0.53	0.13	-0.10	5.91	5.38	0.99	0.11
2013/14	2.89	5.95	2.64	0.36	0.12	1.88	5.43	3.12	0.40	0.86
2014/15	0.79	5.64	4.23	0.51	0.09	-0.44	5.35	5.14	0.57	0.11
2015/16	-1.30	4.05	4.65	0.60	0.13	-2.60	3.91	5.76	0.69	0.12
2000/14	**1.02**	**5.03**	**3.48**	**0.46**	**0.11**	**0.68**	**4.90**	**3.71**	**0.50**	**0.15**
2000/16	**0.86**	**5.00**	**3.60**	**0.47**	**0.11**	**0.41**	**4.86**	**3.93**	**0.52**	**0.14**

A.3 Publication 3

Recent Climatic Mass Balance of the Schiaparelli Glacier at the Monte Sarmiento Massif and Reconstruction of Little Ice Age Climate by Simulating Steady-State Glacier Conditions.

Weidemann S.S., Arigony-Neto J., Jaña R., Netto G., Gonzalez I., Casassa G., Schneider C. (2020): Recent Climatic Mass Balance of the Schiaparelli Glacier at the Monte Sarmiento Massif and Reconstruction of Little Ice Age Climate by Simulating Steady-State Glacier Conditions. Geosciences, 10 (7), 272. https://doi.org/10.3390/geosciences10070272

Status: Published.

Own contribution:

- design of the study (with co-authors)
- collection of meteorological and glaciological data (field work) (with co-authors)
- statistical downscaling of Reanalysis data
- simulation of climatic mass balance using COSIPY including uncertainty assessment
- link climatic mass balance results to measured lake level data
- calculation of Little Ice Age glacier heights
- simulation of Little Ice Age climate conditions
- analysis and interpretation of the results (with co-authors)
- creating figures and tables
- writing the first draft of the manuscript
- incorporating the corrections by co-authors and reviewers

geosciences

MDPI

Article

Recent Climatic Mass Balance of the Schiaparelli Glacier at the Monte Sarmiento Massif and Reconstruction of Little Ice Age Climate by Simulating Steady-State Glacier Conditions

Stephanie Suzanne Weidemann [1,2,*], Jorge Arigony-Neto [3], Ricardo Jaña [4], Guilherme Netto [5], Inti Gonzalez [6,7], Gino Casassa [8,9] and Christoph Schneider [1]

1 Geography Department, Humboldt-Universität zu Berlin, 10099 Berlin, Germany; christoph.schneider@geo.hu-berlin.de
2 Department of Geography, RWTH Aachen University, 52056 Aachen, Germany
3 Instituto de Oceanografia, Universidade Federal do Rio Grande, 96203-900 Rio Grande, Brazil; jorgearigony@furg.br
4 Instituto Antártico Chileno, 6200000 Punta Arenas, Chile; rjana@inach.cl
5 Centro de Desenvolvimento Tecnológico, Universidade Federal de Pelotas, 96010-610 Pelotas, Brazil; guilherme.netto@gmail.com
6 Programa Doctorado Ciencias Antárticas y Subantárticas, Universidad de Magallanes, 6200000 Punta Arenas, Chile; inti.gonzalez@cequa.cl
7 Centro de Estudios del Cuaternario de Fuego-Patagonia y Antartica, 6200000 Punta Arenas, Chile
8 Centro de Investigación Gaia Antártica, Universidad de Magallanes, 6200000 Punta Arenas, Chile; gino.casassa@gmail.com
9 General Water Directorate (DGA), 8320000 Santiago de Chile, Chile
* Correspondence: weidemann_stephanie@web.de

Received: 14 June 2020; Accepted: 11 July 2020; Published: 15 July 2020

Abstract: The Cordillera Darwin Icefield loses mass at a similar rate as the Northern and Southern Patagonian Icefields, showing contrasting individual glacier responses, particularly between the north-facing and south-facing glaciers, which are subject to changing climate conditions. Detailed investigations of climatic mass balance processes on recent glacier behavior are not available for glaciers of the Cordillera Darwin Icefield and surrounding icefields. We therefore applied the coupled snow and ice energy and mass balance model in Python (COSIPY) to assess recent surface energy and mass balance variability for the Schiaparelli Glacier at the Monte Sarmiento Massif. We further used COSIPY to simulate steady-state glacier conditions during the Little Ice Age using information of moraine systems and glacier areal extent. The model is driven by downscaled 6-hourly atmospheric data and high resolution precipitation fields, obtained by using an analytical orographic precipitation model. Precipitation and air temperature offsets to present-day climate were considered to reconstruct climatic conditions during the Little Ice Age. A glacier-wide mean annual climatic mass balance of -1.8 ± 0.36 m w.e. a^{-1} was simulated between between April 2000 and March 2017. An air temperature decrease between -0.9 °C and -1.7 °C in combination with a precipitation offset of up to +60% to recent climate conditions is necessary to simulate steady-state conditions for Schiaparelli Glacier in 1870.

Keywords: Monte Sarmiento Massif; Schiaparelli Glacier; glacier climatic mass balance; glacier surface energy and mass balance model; Little Ice Age

1. Introduction

1.1. Rationale

Along with the Northern (NPI) and Southern Patagonian Icefield (SPI), the Cordillera Darwin Icefield (CDI) and surrounding icefields have experienced extraordinary losses of ice during the last few decades. The CDI is located in the southernmost Andes in Tierra del Fuego (54°20′ S to 55°00′ S, 68°15′ W to 71°20′ W) [1] (Figure 1). It is composed of a main continuous ice body along the mountain range with an area of 1760 km^2 [2] and a few smaller ice bodies farther west which are separated by fjords. In total the CDI and neighboring ice bodies cover an area of 2605 km^2 (derived from satellite imagery acquired in the period 2001 to 2004) [3]. The highest peak of the main icefield is Monte Darwin (2488 m a.s.l.) [1], while the most prominent peak of the western ice bodies is Monte Sarmiento (2300 m a.s.l.) [4], which lies at the center of a 138 km^2 icefield [2], which we refer to as Monte Sarmiento Massif (MSM) [4]. Many glaciers in the Cordillera Darwin advanced during the Little Ice Age (LIA) [4–7], as did glaciers elsewhere in the Southern Patagonian Andes (e.g., [8–11]). Most glaciers reached their maximum extent during a series of late advances between 1700 to 1900 [4,5,7]. Despite a high regional variability in climate anomalies during the LIA, a well-defined cold-interval has been reconstructed between ~1640 and ~1850. During this period, the mean air temperature was 0.86°C lower than the 1900–1990 mean for the southern parts of the Southern Andes [12]. Glacier recession has been documented between the late LIA maximum and 1920, while the following period until the 1960s was dominated by standstills and minor readvances [4,8]. After changes in the Pacific Decadal Oscillation in 1976 [12], summer air temperatures increased [13] and most glaciers in Patagonia and Tierra del Fuego started to retreat, some at extraordinary rates [2,14,15]. Mass loss of the CDI occurred at an average thinning rate of -1.5 ± 0.6 m w.e. a^{-1}, which contributed to sea-level rise by 0.001 ± 0.004 mm a^{-1} between 2000 and 2011 [3]. Similarly to observations at the NPI and SPI [1,14,16–23], individual glacier responses come along with the long-term demise of the icefield mainly caused by a warming climate and changing precipitation patterns [15].

The predominantly south and southwesterly airflow during winter in particular leads to enhanced precipitation at the southern and western side of the east–west running Cordillera Darwin and drier conditions along the north-eastern part [1,4,15]. Changes in wind pattern have enhanced the precipitation gradient between south-facing and north-facing glaciers since the beginning of the 20th century [15,24]. Thinning rates are almost twice as large for glaciers located on the north-eastern part of the CDI compared to those on the south-western side [3]; in particular, land and lake-terminating glaciers in the Cordillera Darwin have been subject to a remarkable retreat within recent decades [2,14].

The increasing number of remote sensing studies of the Southernmost Andes are particularly useful for updating the glacier inventories of the Southern Andes and for assessing glacier volume and area changes for different periods (e.g., [2,14,22,25]). However, to improve our understanding of glacier processes and to estimate future changes, the applications of dynamical ice models and surface mass balance models need to be further extended. In this respect, accurate estimates of downscaled atmospheric variables and in-situ observations are crucial to achieve reliable model results [26].

In this study we present a detailed estimate of the climatic mass balance (CMB) for recent and past glacier extents of the Schiaparelli Glacier, the largest glacier of the Monte Sarmiento Massif in Tierra del Fuego (Figure 1). We follow the methodological approach of [27] to simulate the CMB by applying the coupled snowpack and ice surface energy and mass balance model in Python COSIPY (updated version of COSIMA) [28,29]. We force the model with downscaled 6-hourly ERA-interim data. Model results are calibrated and validated by means of meteorological observation and ablation measurements. The study focuses on the detailed validation of the downscaling results of atmospheric input data, modeled surface energy-fluxes and modeled climatic mass balance for the study period 2000 and 2017. In addition, precipitation and air temperature offsets are applied to the downscaled ERA-interim data to derive both the recent and LIA glacier steady-state conditions. This procedure

allows one to reconstruct LIA climate by simulating CMB in equilibrium using the glacier extent in 1870.

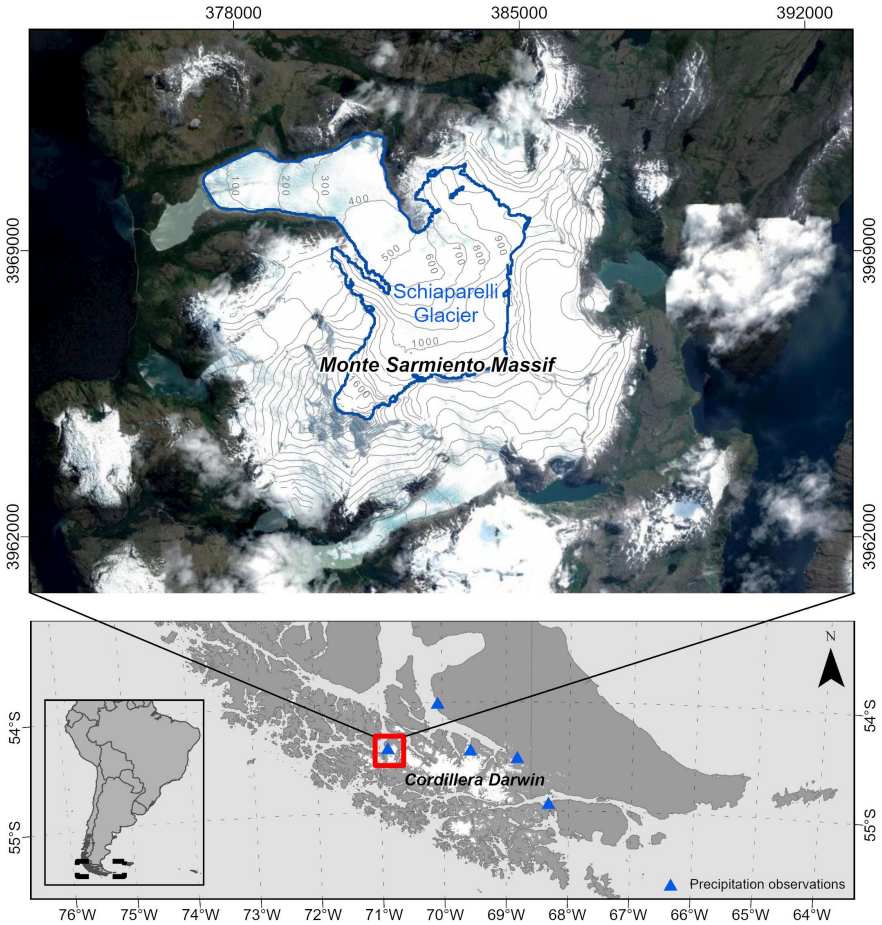

Figure 1. Location of the Monte Sarmiento Massif and location of the weather stations used in this study; glacier outlines are visualized for 2016 based on the glacier inventory by [2]. Sources of the satellite imagery: ESRI, Digital Globe, GeoEye, Earthstar Geographics, CNES/Airbus DS, USDA, USGS, AeroGRID, IGN, and the GIS User Community. Elevation contour lines of 100 m are illustrated. The coordinates are in UTM zone 19S in meters.

1.2. Study Site

Schiaparelli Glacier descends north-west from Monte Sarmiento (54.39° S to 54.45° S, 70.90° W to 70.77° W), at the southwestern tip of Isla Grande de Tierra del Fuego (Figure 1). The glacier calves into a moraine-dammed proglacial lake which formed after glacier recession in the 1940s [7]. Schiaparelli Glacier underwent late Little Ice Age advances [7]. The existence of three terminal moraine ridges at Schiaparelli Glacier implies a glacial recession without distinct readvances since 1749 ± 5 CE [7]. This year reflects the maximum date of the first moraine stabilization. The oldest deposition of the middle moraine and the one closest to the recent glacier front were dated to 1789 ± 5 CE and 1867 ± 5 CE [7]. The glaciated parts of the Monte Sarmiento Massif have shrunk from 199.3 km^2 in 1870 to 183.1 km^2 in 2011 [14], in particular, due to the shrinkage of the land-terminating glaciers. Area loss was accelerated between 1986 and 2001 [14] while it slowed down after 2001. At Schiaparelli Glacier, an area loss of about 7.5 km^2 from 31.8 km^2 in ∼1870 to 24.3 km^2 2016 was determined [2].

2. Materials and Methods

2.1. Meteorological and Glaciological Observations

Two automatic weather stations (AWS) are situated within the study area of the Schiaparelli Glacier (Figure 2). $AWS_{GLACIER}$ is located on the lower part of the glacier at 54.4° S, 70.87° W at about 140 m a.s.l. (location measured in September 2015). The AWS was installed in March 2013 but had to be reinstalled in June 2015 due to the glacier's movement and the formation of crevasses close to the station. A second AWS (AWS_{ROCK}) has been installed additionally on rock to minimize measurement inaccuracies and failures. The AWS is located on the southern side of the glacier close to the glacier margin (Figure 2) at 54.4° S, 70.87° W, 92 m a.s.l. Both AWS measure hourly air temperature, relative humidity, incoming solar radiation, wind speed, and wind direction. Surface pressure is measured at $AWS_{GLACIER}$, while precipitation is measured using an unshielded and unheated tipping-bucket rain gauge at AWS_{ROCK}. For modeling purposes, we use hourly data of air temperature, relative humidity, surface pressure, and wind speed of $AWS_{GLACIER}$ and incoming solar radiation and precipitation of AWS_{ROCK}.

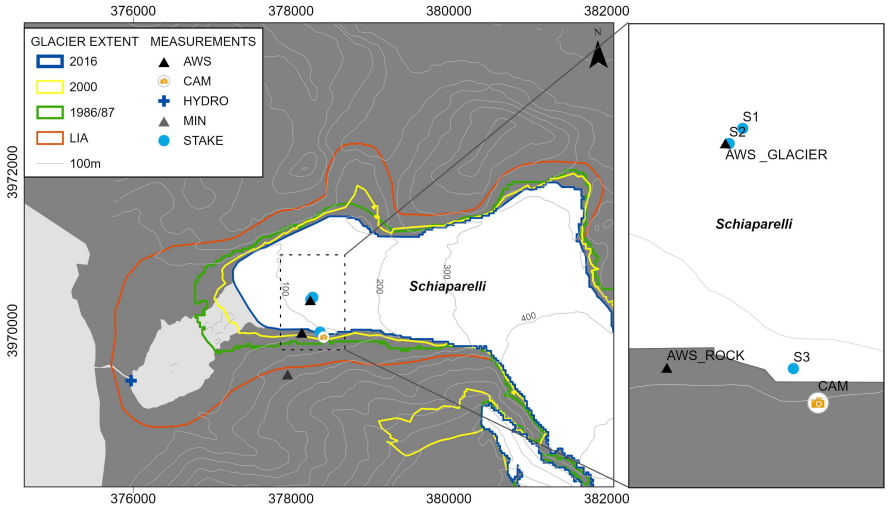

Figure 2. Location of installed measuring devices at Schiaparelli Glacier; locations of ablation stakes (S1–S3) are illustrated as in April 2016. "HYDRO" denotes the location of a lake level measurement device at the outflow of the proglacial lake Lago Azul. Glacier outlines are visualized for LIA (1870), 1986/87, and 2016/17 based on the glacier inventory by [2] and for 2000 based on the RGI 6.0 inventory [30]. The coordinates are in UTM zone 19S in meters.

Precipitation datasets of three weather stations, provided by the Chilean Water Directorate (DGA), and one weather station of Charlie Porter ([24], provided by Eñaut Izagirre Estibaritz via personal communication) are used to validate the spatial distribution of modeled precipitation. The data of the following four weather stations (geographical location, data period) have been chosen: Marinelli Glacier (Charlie Porter) (54.43° S, 69.57° W, 08/2011 to 07/2014), Río Azopardo (DGA) (54.50° S, 68.82° W, 08/2011 to 08/2016), Puerto Navarino (DGA) (54.93° S, 68.32° W, Aug 08/2011 to 02/2017 with short data gaps), Río Cóndor (DGA) (54.00° S, 70.08° W, 01/2012 to 02/2017) (Figure 1).

Ablation on the glacier was measured between September 2015 and April 2017. The reading of the ablation stakes (S1 to S3) has been performed twice a year. A higher temporal resolution of individual ablation measurement (S3) was achieved by means of time-lapse imagery (CAM, Figure 2) between September 2015 and April 2016 at the glacier margin. Therefore, we installed a self-constructed time lapse camera south of the glacier margin which took pictures of the glacier area with one installed ablation stake every two hours. The stake is marked every 1.5 m. From this image time series we can

determine the periods in which 1.5 m of melt had occurred, providing higher temporal resolution compared to the manual semi-annual readings of ablation stakes.

Lake water level and temperature have been recorded hourly using a HOBO water level pressure sensor (HYDRO, Figure 2). It was installed close to the glacier outflow at the southwest margin of Lago Azul between April 2016 and March 2017. Data gaps occurred during the first austral winter because the measurement site fell dry due to a unexpectedly low lake level.

2.2. Reanalysis Data

Atmospheric model input datasets for COSIPY and the orographic precipitation model (OPM) [27,31] were derived from the latest large-scale ERA-interim reanalysis product supplied by the European Centre for Medium-Range Weather Forecasts (ECMWF) [32]. COSIPY is forced by downscaled 6-hourly surface incoming solar radiation SW_{in} (W m^{-2}) and air temperature T_{2m} (°C), surface pressure p_s (hPa) as well as relative humidity rH_{2m} (%), cloud cover fraction N, and wind speed u_{2m} (m s^{-1}) at 2 m. Data are derived as the means from four grid points covering the study site (−54.5° S and −54.75° S, 71.25° W, and 70.5° W) for the time period from 1 April 2000 to 31 March 2017. Running the OPM to compute total precipitation requires 6-hourly ERA-interim datasets of horizontal and vertical wind components, air temperature at the 850 and 500 hPa level, relative humidity, geopotential heights, and large-scale precipitation. Time series of wind, precipitation, and relative humidity are taken from the 850 hPa level to describe the large-scale prevailing wind conditions and to calculate the background precipitation and filter constraints within the OPM routine [27]. Atmospheric input data were averaged over four grid points located west along the Cordillera Darwin (54.0° S to 54.75° S, 75° W to 74.25° W) to represent upstream conditions.

2.3. Elevation and Glacier Outline

The digital elevation model (DEM) generated from the Shuttle Radar Topography Mission (SRTM) [33,34] is used as the reference surface elevation in 2000 for COSIPY and OPM runs. COSIPY and OPM runs are carried out with spatial resolutions of 200 m and 1000 m, respectively. Glacier outlines for COSIPY model runs have been obtained from the glacier inventory of [2] for 1870 and for 2016 (Figure 2). According to [2], glacier extent during the LIA was digitized manually using the 1986 glacial extent as the starting point and clearly visible morphological evidence, such as vegetation trimlines or moraine systems. The latter represents the maximum extent of the LIA which does not necessarily represent the end of the LIA (∼1870 AD).

2.4. Surface Energy and Climatic Mass Balance Model

Surface energy fluxes and climatic mass balance are estimated using the open-source surface and energy mass balance model COSIPY [29] which is the updated version of the former coupled snowpack and ice surface energy and mass balance model (COSIMA) [28], with updated physics and optimized computational performance. COSIMA is described in detail in [28] and has been successfully applied for selected glaciers at the Southern Patagonia Icefield [27]. Only a short description of the model physics is therefore provided in the following. COSIPY combines a surface energy balance model with a multi-layer sub-surface snow and ice model to resolve estimated energy fluxes and surface mass balance processes [29]. All energy fluxes F that contribute to the surface energy budget and the energy available for surface melting Q_{melt} [35] are considered in the energy balance model:

$$F = SW_{in} \cdot (1 - \alpha) + LW_{in} + LW_{out} + Q_{sens} + Q_{lat} + Q_g. \quad (1)$$

The model takes into consideration: the incoming shortwave radiation SW_{in}, the albedo α, the incoming LW_{in} and outgoing longwave radiation LW_{out}, the sensible Q_{sens} and latent heat fluxes Q_{lat}, and the ground heat flux Q_g. Ablation occurs due to sublimation, evaporation, subsurface melt, and surface melt. Q_{melt} requires the surface temperature T_s to be at the melting point (0 °C) and a positive energy

flux F towards the surface to prevail. In this case, Q_{melt} equals F. Each layer is characterized by a temperature, density, and liquid water content. Turbulent heat fluxes Q_{sens} and Q_{lat}, are calculated based on the the bulk aerodynamic method [35] between the surface and two meters above ground by means of T_{2m}, rH_{2m}, and u_{2m}. Q_g consists of fluxes of heat conduction and penetrating shortwave radiation [28]. Detailed information about the parameter settings in COSIPY, e.g., model domain, layer depth, and albedo values, can be found in Table 1.

Table 1. COSIPY and OPM parameter settings based on findings from [27]. Values denoted with * are mean values.

	Parameter	Value/Range	Unit	Fixed/Calculated	Source
COSIPY	Total domain depth	100	m	F	-
	Model layer thickness	0.1	m	F	-
	Ice albedo	0.3	-	F	[36]
	Fresh snow albedo	0.9	-	F	[28]
	Firn albedo	0.45	-	F	[36]
	Initial subsurface temperature	273.15	°C	F	[27]
	Air temperature lapse rates	−0.67, −0.73	°C 100 m^{-1}	F	[27]
	Surface pressure gradient	−0.105	hPa m^{-1}	F	[27]
	Snow density for P_{solid}	250	kg m^{-3}	F	[28]
	Threshold for P_{solid} to P_{liq}	0–2.0	°C	F	[37]
	Snow pack density profile	250 to 550	kg m^{-3}	C	[28]
OPM	Uplift sensitivity factor	0.006 *	-	C	[38]
	Water vapor scale height	2382 *	m	C	[38]
	Conversion/fallout time scale	1824 *	m s^{-1}	C	[39]
	Brunt-Väisälä frequency	0.009 *	s^{-1}	C	[38]
	Averaged falling speed	1.3	m s^{-1}	F	[27]
	Thresholds relative humidity	80, 85, 90	%	F	[38]

2.4.1. Climate Forcing of COSIPY

COSIPY is driven by surface incoming solar radiation SW_{in} (W m^{-2}), air temperature T_{2m} (°C), relative humidity rH_{2m} (%), surface pressure p_s (hPa), wind speed at 2 m u_{2m} (m s^{-1}), cloud cover fraction N, and total precipitation RRR. We use different approaches to downscale ERA-interim data of T_{2m}, rH_{2m}, p_s, SW_{in}, and total precipitation RRR by means of observed data which are described in more detail in [27].

Precipitation fields are modeled using an analytical OPM based on the linear steady-state theory of airflow dynamics [38,40]. A more detailed description and validation of the model itself is given by [38] and [40] while the methodical application as used in this study is described in more detail in [27,31]. The OPM estimates RRR resulting from the forced orographic uplift of air masses over a mountain assuming stable and saturated atmospheric conditions. The model estimates the condensation rate by the terrain-induced vertical air velocity, and the horizontal wind speed and advection of water vapor, and includes effects of airflow dynamics and downslope evaporation as well. The main term of the linear model describing the orographic precipitation (P_{oro}) generation is solved in Fourier space for each Fourier component (k,l) as follows.

$$\hat{P}_{oro}(k,l) = \frac{C_w \cdot i \cdot \sigma \cdot \hat{h}(k,l)}{(1 - i \cdot m \cdot H_w)(1 + i \cdot \sigma \cdot \tau_c)(1 + i \cdot \sigma \cdot \tau_f)}. \quad (2)$$

Equation (2) includes an uplift sensitivity factor C_w, the water vapor scale height H_w, the complex number i, the intrinsic frequency σ, the Fourier transform of the orography $\hat{h}$, the vertical wavenumber m, and the delay time scales for conversion τ_c and fallout τ_f of hydrometeors. The thermodynamic sensitivity C_w accounts for the effects of saturation water vapor density, and the moist adiabatic and environmental lapse rates. H_w mainly depends on the environmental air temperature and lapse rate.

Airflow dynamics are represented by the intrinsic frequency, including the vertical and horizontal winds. One of the airflow features included is the decay of vertical velocity with altitude which is described by m. The calculation of m contains the buoyancy frequency in a saturated atmosphere and the moist Brunt-Väisälä frequency N_{m} to consider the effect of moist air masses on the static stability. Additionally, the precipitation generation is shifted downstream from the water source region depending on the wind speed and the cloud time parameters τ_c and τ_f. The total amount of precipitation RRR is assessed by considering the large-scale precipitation which in this study is derived from ERA-interim precipitation data. For detailed information about the procedure and the parameter settings, the reader is referred to [27] and Table 1. The amount of solid precipitation is determined in COSIPY by applying a hyperbolic tangent function [27,37] to the modeled OPM precipitation fields. The proportion of solid precipitation to total precipitation is smoothly scaled between 100% and 0% within a T_{2m} range of 0 °C and 2 °C [27,37]. The temperature range of the transition from liquid to solid is similar to the assumptions used by [36,41] to determine the solid precipitation fraction.

OPM runs have been carried out with varying thresholds of the model constraint rH according to the values used in previous studies (e.g., [27,42–44]) to find the best model fit compared to observed data. OPM runs were calibrated with observed data from AWS_{ROCK} between October 2015 to September 2016. Best-fits have been achieved using the constraint $rH \geq 85$. Best-fit OPM results were compared to observed precipitation data of five weather stations (Figure 3A). The explained variance between modeled and observed monthly precipitation data was 93% for ROCK, 74% for AZO, 71% for MAR, 43% for NAV, and 44% for CON. The amount of modeled orographic precipitation of the total modeled precipitation amount is highest for AWS_{ROCK} with 43%. The AWS is located at the western side of the Monte Sarmiento Massif and therefore strongly influenced by orographic effects. OPM results for the other weather stations were mainly determined by the downscaling results of ERA-interim precipitation, because their locations are less influenced by orographic effects. The glacier-wide mean of RRR averaged over the study period 2000 to 2017 is 4.0 m w.e. a^{-1} with a maximal amount of 5.6 ± 0.5 m w.e. a^{-1} in the upper part of the glacier. The glacier-wide amount of solid precipitation to total precipitation is about 38 %.

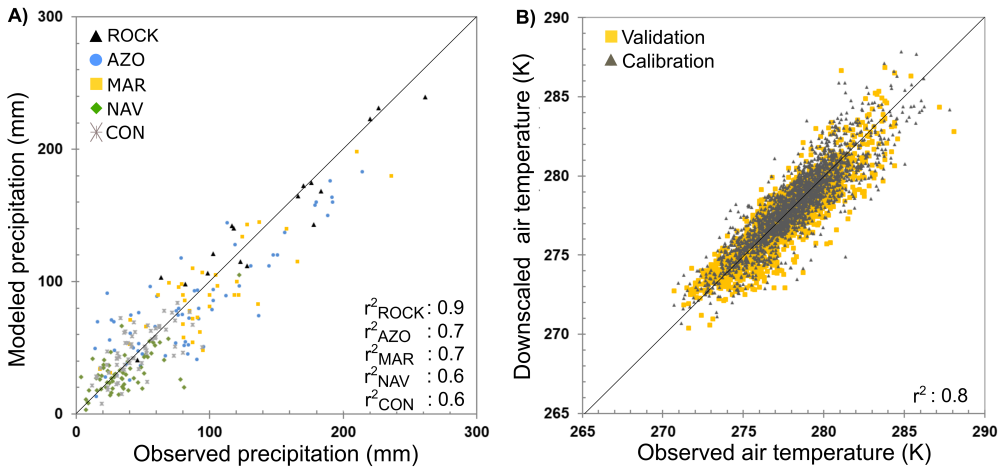

Figure 3. Downscaled ERA-interim vs. observed data for (**A**) precipitation and (**B**) air temperature. In (**A**) monthly modeled precipitation (mm) by OPM simulations and observed precipitation of the weather stations at Schiaparelli Glacier (ROCK), Rio Azopardo en Desembocadura (AZO), Marinelli Glacier (MAR), Puerto Navarino (NAV), and at Rio Condor (CON) are shown. (**B**) Observations from April 2013 to February 2015 at $\mathrm{AWS}_{GLACIER}$ were used as a validation dataset and the calibration was based on observations between October 2015 and April 2017.

T_{2m}, rH_{2m}, and p_s were statistically downscaled from ERA-interim data to AWS$_{GLACIER}$ by using quantile mapping (e.g., [45,46]). Bias-corrected air temperature and surface pressure were spatially interpolated using a fixed lapse rates from the AWS location (Table 1). Downscaling results of daily ERA-interim T_{2m} by means of station data are visualized in Figure 3B. For the validation period, the chosen downscaling method tends to overestimate low temperatures while high temperatures are slightly underestimated. The glacier-wide mean T_{2m} averaged between 2000 and 2017 is 0.6 ± 0.3 °C.

Incoming shortwave radiation SW_{in} was also downscaled from ERA-interim data to the measured solar radiation at AWS$_{ROCK}$ using quantile mapping. The spatial distribution of SW_{in} was then derived from a modified radiation model according to [47] that computes clear-sky direct and diffuse shortwave radiation depending on the geographical position, elevation, albedo, and shading by the surrounding terrain, and the slope and aspect over the glacier domain. At each time step and grid cell, the potential clear-sky radiation is corrected for cloud cover by means of downscaled SW_{in}. Therefore, we calculate the ratio between potential clear-sky radiation at AWS$_{ROCK}$ and any other pixel within the glacier domain. SW_{in} at each pixel is then derived by multiplying the calculated ratio and the downscaled SW_{in} at AWS$_{ROCK}$. The glacier-wide mean SW_{in} averaged between 2000 and 2017 is +91 W m^{-2}.

2.4.2. Uncertainty Assessment of COSIPY and OPM

Ablation stake measurements carried out at Schiaparelli Glacier between 2015 and 2017 were used to validate the modeled climatic mass balance. We forced COSIPY once with observed timeseries. In this case only N was taken from ERA-interim and used to calculate longwave incoming radiation. Secondly, we ran COSIPY with downscaled ERA-interim data. The RMSE between model ran and observed values were ± 0.67 m w.e. for the AWS run and ± 0.71 m w.e. for the ERA-interim run between October 2015 and March 2017. COSIPY driven by both observed and downscaled input data reproduces measured ablation well (Figure 4). The uncertainties of modeled climatic mass balance were estimated by accounting for uncertainties in the spatial distributions of input datasets of air temperature and solid precipitation due to the lack of observations in the accumulation area. The spatial distribution of air temperature is determined by the chosen lapse rate, while the amount of modeled precipitation is mainly controlled by the OPM filter constraint rH which regulates the amount of orographic induced precipitation to large-scale precipitation within the OPM [27]. We therefore include varying values of air temperature lapse rate and the OPM filter constraint rH for the assessment of climatic mass balance uncertainties. In total, six runs were carried out for the mass balance years 2015/16 and 2016/17 to assess the uncertainty of glacier-wide climatic mass balance. As lower and upper air temperature lapse rates, we assumed 0.67 °C and 0.73 °C 100 m^{-1} as used in earlier mass balance studies (e.g., [27]). Thresholds of 80%, 85%, and 90% for rH were considered. The standard deviation between those six different model runs was ± 0.36 m w.e. Best-fit simulation results were achieved using 0.67 °C and running the OPM with a rH threshold of 85%.

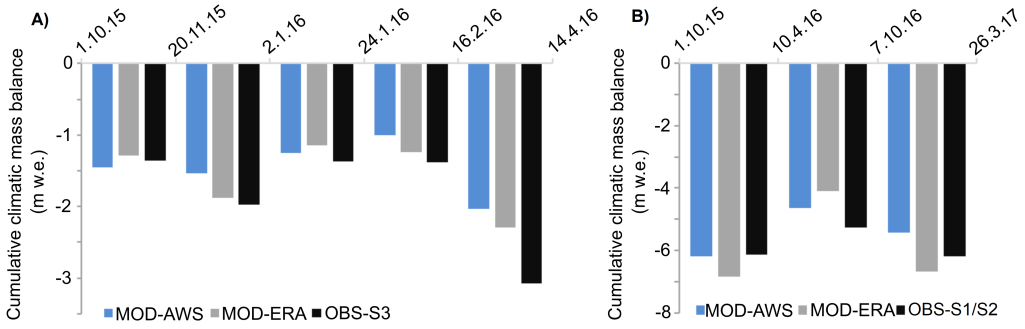

Figure 4. Comparison of modeled (automatic weather stations (AWS) and ERA) and observed climatic mass balance at Schiaparelli Glacier by means of (**A**) ablation stake S3 and (**B**) ablation stakes S1 and S2 as mean values (Figure 2).

2.5. Little Ice Age Estimations

We followed the approach of [48] to reconstruct LIA climate by assuming that the glacier was in equilibrium over a short period of time during the formation of the associated terminal moraines when climate started to shift from LIA to present-day climate conditions. First, we simulated the climatic conditions which were needed to derive steady-state conditions for the recent extent of Schiaparelli Glacier. Therefore, precipitation and air temperature offsets to the present-day climate were used as COSIPY forcing to derive an average CMB in equilibrium. We chose the time period 2000 to 2010 as the simulation period. LIA climate was then reconstructed, using precipitation and air temperature offsets along with the LIA glacier extent [49] and adapted glacier height by means of SRTM data and moraine system information. All other input parameters of COSIPY as well as the altitudinal gradients remained unchanged. Glacier height during the LIA was reconstructed by using glacier outline information from 2000 and LIA as well as SRTM data with a resolution of 200 m (Figure 5). First, we compared vegetation trimline and moraine information [7] with SRTM heights extracted at the LIA outline of the glacier. We then calculated height differences (h_{dif}) for each pixel between the glacier outline of 2000 and LIA (Figure 5A). We then manually digitized the glacier flowline based on the center of elevation contours (contour lines of 50 m). The maximum height difference along the LIA outlines ($h_{dif,max}$) perpendicular to any position along the flowline was added to the height (h) of the pixel at this position of the flowline (Figure 5A). Finally, we linearly interpolated between the heights at the glacier's LIA outlines and the height adjusted flowline (Figure 5A). This procedure was limited to the part of the glacier where the LIA glacier outline extends further than the glacier outline in 2000 (Figure 5A, inset). The resulting height changes are visualized in Figure 5B. For Schiaparelli Glacier, this area approximately coincides with the area below the ELA. The heights of the upper parts were left unchanged. For LIA climate reconstruction, COSIPY was driven using the DEM adapted to LIA conditions. We further used COSIPY runs based on the initial SRTM heights for comparison and uncertainty assessment. The standard deviation between all runs is $\pm$ 0.12 m w.e.

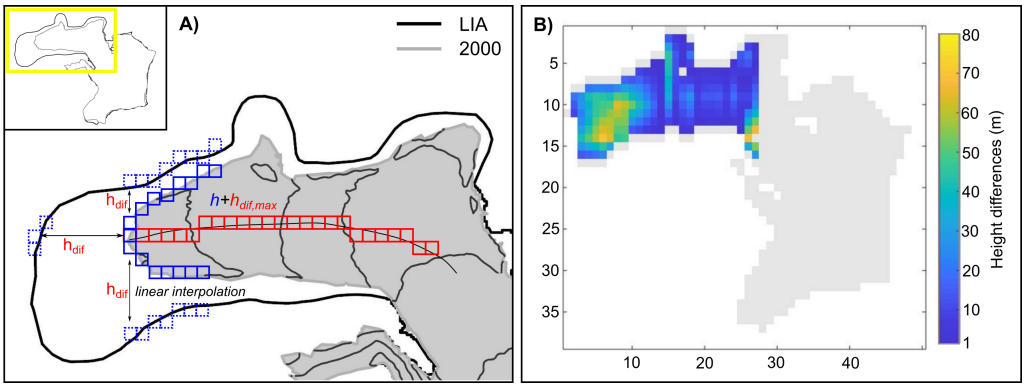

Figure 5. Schematic illustration of Little Ice Age (LIA) height calculations using SRTM data and glacier outlines from 1870 (LIA) [2] and 2000 [30] (**A**), and calculated height differences between the digital elevation model (DEM) adapted to LIA conditions and the initial SRTM-dervied DEM (**B**).

3. Results and Discussion

The evaluations of COSIPY-modeled surface energy fluxes and climatic mass balance are discussed in the following.

The glacier-wide mean annual surface energy balance and climatic mass balance components are shown in Figure 6A,B. The glacier-wide energy input is dominated year-around by LW_{in} (+292 W m^{-2}) and SW_{in} (+91 W m^{-2}), followed by Q_{sens} (+32 W m^{-2}). Available energy at the glacier surface is consumed by LW_{out} (-296 W m^{-2}), SW_{out} ($-$65 W m^{-2}), Q_{lat} ($-$9 W m^{-2}), Q_g ($-$1 W m^{-2}), and Q_{melt} ($-$44 W m^{-2}). The modeled glacier-wide mean annual CMB for Schiaparelli Glacier is estimated

to -1.8 ± 0.36 m w.e. a^{-1} averaged between April 2000 and March 2017. The CMB is negative for each year during the complete study period (Figure 6B). Glacier melt was highest during the mass balance year 2016/17, followed by the mass balance years between 2003/04 and 2006/07. The highest CMB of -0.7 ± 0.36 m w.e. a^{-1} is modeled for the mass balance year 2009/10 which coincides with above-average P_{solid} amounts and lower T_{2m} values (Figure 7A). Mean annual T_{2m} values which are above the average as in the mass balance years 2007/08 and 2008/09 cause high negative CMB values and cannot be fully compensated by positive P_{solid} amounts or low SW_{in} values. In general, the climatic mass balance is dominated by surface melt (60%) and solid precipitation (37%). Sublimation, deposition, refreezing, and evaporation play only minor roles. Strong correlations between CMB and T_{2m} (r = −0.77) and CMB and P_{solid} (r = 0.80) reflect this finding (Figure 7B). However, we cannot find any meaningful correlation between CMB and SW_{in}. Modeled annual ELA ranges from 650 ± 50 m a.s.l. to 800 ± 50 m a.s.l. with a mean of 730 ± 50 m a.s.l. These ranges are similar to values in [4].

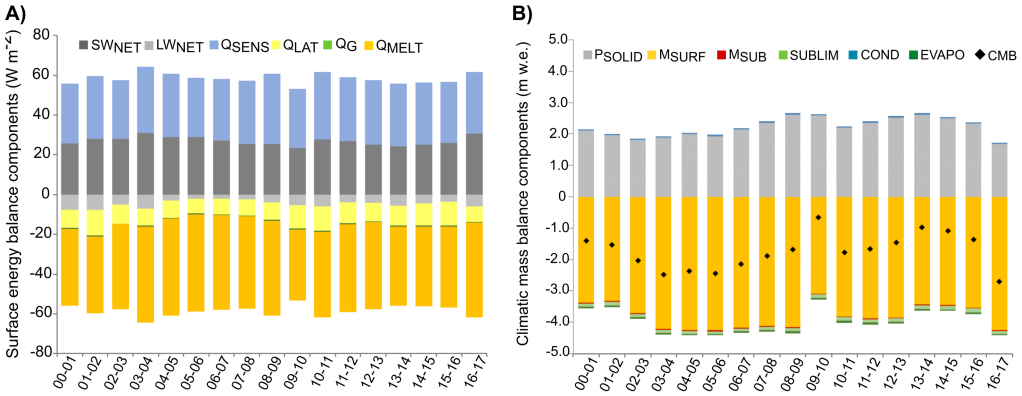

Figure 6. Annual surface energy balance components (**A**) and climatic mass balance (**B**) averaged between April 2000 and March 2017. Abbreviations are explained in Equation (1).

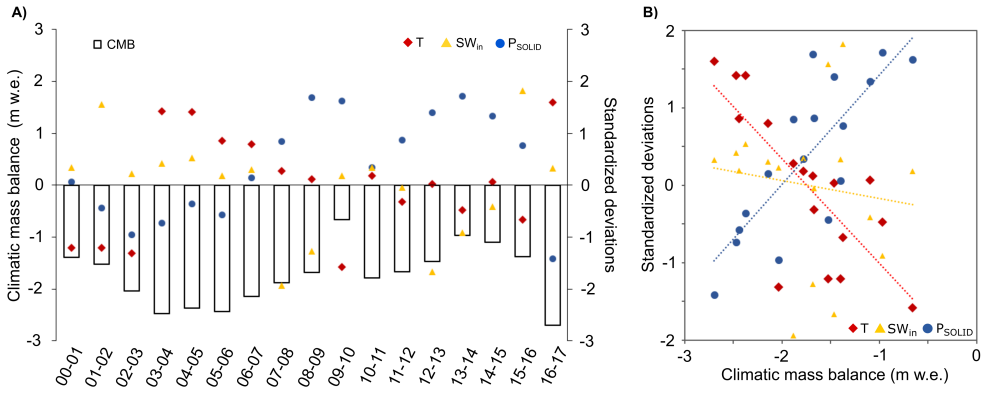

Figure 7. Modeled annual climatic mass balance (CMB) based on COSIPY simulations and standardized anomalies of P_{solid}, T_{2m}, and SW_{in} from the mean between April 2000 to March 2017 for each mass balance year (**A**) and correlations between modeled annual CMB and standardized anomalies of P_{solid}, T_{2m}, and SW_{in} from the mean between April 2000 to March 2017 (**B**).

In a previous study of [27], CMB simulations using the former version of COSIPY were carried out at the two lake-terminating glaciers Grey and Tyndall located at the eastern side of the SPI (Table 2). Climate conditions at Grey Glacier and Tyndall Glacier are wetter and colder compared to Schiaparelli Glacier as a result of higher altitudes in general and the stronger influence of orographic effects on precipitation distribution (e.g., [27,50]). Comparing the energy balance components, it is striking that

the shortwave net radiation is much lower at the MSM than at the SPI while the sensible heat flux is more important as a source of energy input at the glacial surface. All three glaciers underwent a massive retreat in the past decade. However, climatic mass balance simulations are positive with a glacier-wide mean annual of +0.86 ± 0.52 m w.e. a^{-1} for Grey Glacier and +0.41 ± 0.54 m w.e. a^{-1} for Tyndall Glacier between 2000 and 2016, while the CMB of Schiaparelli Glacier is clearly negative with −1.69 ± 0.36 m w.e. a^{-1}. The positive CMB of Grey Glacier and Tyndall Glacier cannot fully compensate the mass loss which is caused by dynamical ice processes, especially calving into the lakes and frontal ablation. Remote sensing studies of [3,23] do not show extensive glacier thinning at Schiaparelli Glacier. Therefore, we conclude that mass loss due to surface mass balance processes seems to be the main reason for the recent areal changes of Schiaparelli Glacier. This is in accordance with several other studies [24,51] that suggest that the recent mass loss of most glaciers at the CDI and surrounding icefields is rather driven by atmospheric warming than by dynamical ice processes such as calving, except for a few calving glaciers, such as Marinelli, which has experienced a remarkable retreat of more than 10 km between 1945 and 2000 [52].

Table 2. Comparison of glacier characteristics and COSIPY/COSIMA results between the glaciers Grey (SPI), Tyndall (SPI), and Schiaparelli (MSM), averaged over the period 2000–2016. Listed are glacier size (km^2) and modeled annual glacier-wide mean CMB, ELA, P_{solid}, T_{2m}, SW_{net}, LW_{net}, Q_{sens}, and Q_{lat}.

Glacier	Size km^2	CMB m w.e.	ELA m a.s.l	P_{solid} m w.e.	T_{2m} °C	SW_{net} W m^{-2}	LW_{net} W m^{-2}	Q_{sens} W m^{-2}	Q_{lat} W m^{-2}
Grey	239	+0.86 ± 0.52	960 ± 70	5.9 ± 1.0	−2.4 ± 0.6	39	−9	11	−9
Tyndall	301	+0.41 ± 0.54	920 ± 60	7.1 ± 1.1	−0.7 ± 0.5	45	−18	16	−7
Schiaparelli	24	−1.69 ± 0.36	730 ± 50	2.3 ± 0.3	0.6 ± 0.3	26	−5	32	−10

3.1. Link between Climatic Mass Balance and Lake Level Changes

We compare meteorological data and modeled climatic glacier mass balance with lake level height changes at Lago Azul on a daily basis for a short measurement period during the austral summer 2016/2017 (Figure 8). Relating daily air temperature to the height of the lake level showed the highest correlation r=0.6 using a time lag of +1 day (d + 1) (Figure 8A). Lower correlations were calculated for larger time lags. There was no pronounced link between the other meteorological observations and lake level changes; in particular, we could not obtain any meaningful correlation between precipitation and lake level (Figure 8B) .

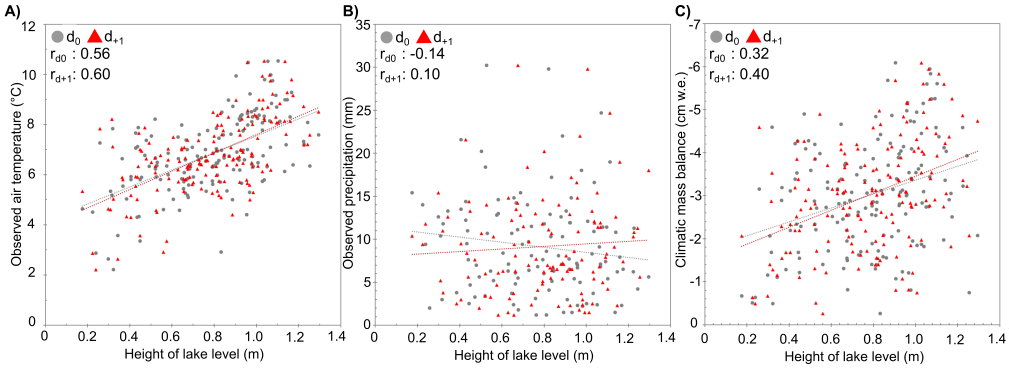

Figure 8. Correlations between (**A**) daily observed air temperature and change of lake level, (**B**) daily observed total precipitation and change of lake level, and (**C**) climatic mass balance averaged over the ablation area and changes of lake level height for the period October 2015 and April 2016. A time lag of +1 day (d + 1) is also considered.

The correlation between CMB, averaged over the area beneath the mean modeled ELA, and lake level height changes is r = 0.40 at d + 1 (Figure 8C). Information on frontal ablation and lake bathymetry

will allow a more extensive analysis of the link between glacier runoff and changes in lake level height and outflow in the future.

3.2. Reconstruction of LIA Climate

The reconstruction of steady state climate conditions during LIA requires as starting point a glacier in equilibrium under present-day climate conditions. We therefore, first simulate the climatic conditions which are needed to derive steady-state conditions for the recent extent of Schiaparelli Glacier. Several temperature (TO) and precipitation offset (PO) combinations lead to a zero CMB of Schiaparelli Glacier based on the recent extent (Table 3). An air temperature decrease between −0.5 °C and −0.9 °C in combination with a precipitation increase of up to 30% seems to be realistic. A zero CMB under actual climate conditions between 2000 and 2010 would imply a glacier length reduction of about 3.8 km back from the glacier front in 2016. Precipitation and air temperature offsets to the present-day climate are used as COSIPY forcing to derive an average CMB in equilibrium. We choose the combination TO = −0.6 °C and PO = 20% for representing the recent steady-state climate conditions. LIA climate is then reconstructed, using precipitation and air temperature offsets along with the LIA glacier extent [2] and the adapted glacier height. Forcing COSIPY with the recent steady-state climate conditions, the CMB of Schiaparelli Glacier in 1870 is negative with -1.64 ± 0.48 m w.e. a^{-1}. A nearly zero CMB is simulated by forcing the model with air temperature offsets between −0.4 and −0.8 °C in combination with an increase in precipitation of up to 30% to the artificial steady-state of 2000–2010 (Table 4). The higher the air temperature offset, the smaller the precipitation offset. Previous studies about Holocene climate reconstruction in Southern Patagonia [53–55] indicate colder and wetter conditions during the LIA. According to [4] temperature anomalies differed regionally; the mean air temperature was below the 1900–1990 means by 0.86 °C in the southern parts of Southern Andes. For Schiaparelli Glacier, we obtained with respect to the actual climate in 2000–2010, a combined lowering of air temperature between −0.9 °C and −1.7 °C, a precipitation increase of up to +60% by summing up the offsets for steady state conditions in 2000–2010, and the further adjustment of climate to allow LIA steady-state conditions of CMB.

Table 3. Precipitation (PO) and air temperature offsets (TO) are combined to simulate steady-state conditions (m w.e. a^{-1}) for the recent extent of Schiaparelli Glacier.

TO/PO	−10%	−5%	0%	5%	10%	15%	20%	25%	30%
0.0 °C			−1.81						
−0.4 °C								−0.29	−0.17
−0.5 °C							−0.22	−0.08	0.05
−0.6 °C						−0.14	−0.01	0.13	
−0.7 °C					−0.07	0.06	0.20		
−0.8 °C			−0.16	−0.02	0.12				
−0.9 °C		−0.13	0.02						
−1.0 °C	−0.10	0.05	0.19						

Table 4. Precipitation (PO) and air temperature offsets (TO) are combined to simulate steady-state conditions (m w.e. a^{-1}) for the LIA extent of Schiaparelli Glacier based on the adapted SRTM heights.

TO/PO	−10%	−5%	0%	5%	10%	15%	20%	25%	30%
0.0 °C			−1.64						
−0.4 °C							−0.23	−0.09	0.05
−0.5 °C						−0.17	−0.02	0.12	
−0.6 °C					−0.13	0.03			
−0.7 °C				−0.08	0.07				
−0.8 °C			−0.03	0.12					
−0.9 °C	−0.13	0.01	0.17						
−1.0 °C	0.05	0.19	0.34						

4. Conclusions

The surface energy and mass balance model COSIPY was applied to simulate the climatic mass balance of Schiaparelli Glacier between 2000 and 2017 and during the LIA (1870). A glacier-wide mean annual climatic mass balance of -1.8 ± 0.36 m w.e. a^{-1} was simulated between between April 2000 and March 2017. A lowest negative CMB of -0.7 ± 0.36 m w.e. a^{-1} was modeled for the mass balance year 2009/10 as the result from the above-average P_{solid} amounts and lower T_{2m} values compared to the mean between 2000 and 2017. Incoming solar radiation and the sensible heat flux are the main sources of energy input at the glacial surface. The contributions of subsurface melt, sublimation, refreezing, and evaporation are comparatively small. Observed air temperature and modeled climatic mass balance can be linked to changes in lake level heights at Lago Azul. Frontal ablation and calving seem to play a minor role in the mass balance of Schiaparelli Glacier when compared to other larger glaciers in CDI and SPI. An extended record of lake level from on-going measurements combined with runoff measurements at the outlet from the lake to the sea will allow a more detailed assessment of the glacial hydrology at Schiaparelli glacier in future studies. We assumed a zero CMB at the turning point of Schiaparelli Glacier from being in equilibrium in 1870 to retreating until now. Assuming recent steady-state climate conditions, the CMB of Schiaparelli Glacier in 1870 would have been significantly negative with -1.64 ± 0.48 m w.e. a^{-1}. A nearly zero CMB was simulated by forcing COSIPY with air temperature offsets between -0.4 to -0.8 °C in combination with an increase in precipitation of up to +30% to the present-day steady state climate conditions. The upper limit of air temperature decrease is similar to previous studies about Holocene climate reconstruction in Southern Patagonian [53–55] which also indicate colder and wetter conditions during the LIA. The lack of observed accumulation data causes high uncertainties in surface mass balance simulations regarding the glacier-wide amount of solid precipitation. Missing information about the bedrock topography or ice thickness limited the applicability of dynamical ice models up to now. Future studies incorporating ice-dynamical modeling will allow one to quantify ice's dynamical processes and their impact on the overall mass loss compared to the climatic mass balance forcing.

Author Contributions: S.S.W. and C.S. jointly designed the study and discussed the steps of the analysis. S.S.W. carried out COSIPY simulations, and processed and analyzed the data. S.S.W. and C.S. prepared the manuscript. R.J. and I.G. organized all logistics for the field campaigns. S.S.W., J.A.-N., G.N., R.J., and I.G. contributed to the fieldwork. All authors discussed the results and reviewed the manuscript. Conceptualization, S.S.W. and C.S.; data curation, S.S.W., J.A.-N., R.J., G.N., I.G., and C.S.; formal analysis, S.S.W.; funding acquisition, R.J. and C.S.; methodology, S.S.W. and C.S.; project administration, C.S.; resources, R.J. and C.S.; validation, S.S.W.; visualization, S.S.W.; writing—original draft, S.S.W. and C.S.; writing—review and editing, J.A.-N., R.J., G.N., I.G. and G.C. All authors have read and agreed to the published version of the manuscript.

Funding: This research was funded by the CONICYT-BMBF project GABY-VASA: 01DN15007 and BMBF20140052 and the FAPERGS project INCT da Criosfera (17/2551-0000518-0).

Acknowledgments: We thank the Chilean Water Directorate (DGA) and Charlie Porter and Eñaut Izagirre Estibaritz for providing weather station data. We thank all participants, especially Marcelo Arévalo, Guisella Gacitúa, Roberto Garrido, and Wolfgang Meier, for their support during the field work at Schiaparelli Glacier, and Anselm Arndt for his technical support implementing COSIPY. We acknowledge support by the German Research Foundation (DFG) and the Open Access Publication Fund of Humboldt-Universität zu Berlin. We thank all reviewers for their input which helped to improve the manuscript considerably.

Conflicts of Interest: The authors declare no conflict of interest. The funders agency had no role in the design of the study; in the collection, analyses, or interpretation of data; in the writing of the manuscript, or in the decision to publish the results.

Abbreviations

The following abbreviations are used in this manuscript:

AWS	Automatic Weather Station
CDI	Cordillera Darwin Icefield
CMB	Climatic Mass Balance
COSIPY	Coupled Snowpack and Ice Surface Energy and Mass Balance Model in Python

COSIMA	COupled Snowpack and Ice Surface Energy and Mass Balance Model
ELA	Equilibrium Line Altitude
LIA	Little Ice Age
MSM	Monte Sarmiento Massif
NPI	Northern Patagonia Icefield
OPM	Orographic Precipitation Model
PO	Precipitation Offset
SPI	Southern Patagonia Icefield
TO	Temperature Offset

References

1. Lopez, P.; Chevallier, P.; Favier, V.; Pouyaud, B.; Ordenes, F.; Oerlemans, J. A regional view of fluctuations in glacier length in southern South America. *Glob. Planet. Chang.* **2010**, *71*, 85–108. [CrossRef]
2. Meier, W.J.H.; Grießinger, J.; Hochreuther, P.; Braun, M.H. An Updated Multi-Temporal Glacier Inventory for the Patagonian Andes With Changes Between the Little Ice Age and 2016. *Front. Earth Sci.* **2018**, *6*, 62. [CrossRef]
3. Melkonian, A.K.; Willis, M.J.; Pritchard, M.E.; Rivera, A.; Bown, F.; Bernstein, S.A. Satellite-derived volume loss rates and glacier speeds for the Cordillera Darwin Icefield, Chile. *Cryosphere* **2013**, *7*, 823–839. [CrossRef]
4. Strelin, J.; Casassa, G.; Rosqvist, G.; Holmlund, P. Holocene glaciations in the Ema Glacier Valley, Monte Sarmiento Massif, Tierra del Fuego. *Palaeogeogr. Palaeoclimatol. Palaeoecol.* **2008**, *260*, 299–314. [CrossRef]
5. Masiokas, M.H.; Rivera, A.; Espizua, L.E.; Villalba, R.; Delgado, S.; Aravena, J.C. Glacier fluctuations in extratropical South America during the past 1000 years. *Palaeogeogr. Palaeoclimatol. Palaeoecol.* **2009**, *281*, 242–268. [CrossRef]
6. Koch, J. Little Ice Age and recent glacier advances in the Cordillera Darwin, Tierra del Fuego, Chile. *Anales Instituto Patagonia (Chile)* **2015**, *43*, 127–136. [CrossRef]
7. Meier, W.J.H.; Aravena, J.C.; Grießinger, J.; Hochreuther, P.; Soto-Rogel, P.; Zhu, H.; Pol-Holz, R.D.; Schneider, C.; Braun, M.H. Late Holocene Glacial Fluctuations of Schiaparelli Glacier at Monte Sarmiento Massif, Tierra del Fuego (54°24'S). *Geosciences* **2019**, *9*. [CrossRef]
8. Koch, J.; Kilian, R. 'Little Ice Age' glacier fluctuations, Gran Campo Nevado, southernmost Chile. *Holocene* **2005**, *15*, 20–28. [CrossRef]
9. Aniya, M. Holocene glaciations of Hielo Patagacico (Patagonia Icefield), South America: A brief review. *Geochem. J.* **2013**, *47*, 97–105. [CrossRef]
10. Glasser, N.F.; Harrison, S.; Winchester, V.; Aniya, M. Late Pleistocene and Holocene palaeoclimate and glacier fluctuations in Patagonia. *Glob. Planet. Chang.* **2004**, *43*, 79–101. [CrossRef]
11. Kilian, R.; Lamy, F. A review of Glacial and Holocene paleoclimate records from southernmost Patagonia (49–55°S). *Quat. Sci. Rev.* **2012**, *53*, 1–23. [CrossRef]
12. Villalba, R.; Lara, A.; Boninsegna, J.A.; Masiokas, M.; Delgado, S.; Aravena, J.C.; Roig, F.A.; Schmelter, A.; Wolodarsky, A.; Ripalta, A. Large-Scale Temperature Changes Across the Southern Andes: 20th-Century Variations in the Context of the Past 400 Years. In *Climate Variability and Change in High Elevation Regions: Past, Present & Future*; Diaz, H.F., Ed.; Springer: Dordrecht, The Netherlands, 2003; pp. 177–232. [CrossRef]
13. Rosenblüth, B.; Fuenzalida, H.A.; Aceituno, P. Recent temperature variations in southern South America. *Int. J. Climatol.* **1997**, *17*, 67–85. [CrossRef]
14. Davies, B.; Glasser, N. Accelerating shrinkage of Patagonian glaciers from the Little Ice Age (AD 1870) to 2011. *J. Glaciol.* **2012**, *58*, 1063–1084. [CrossRef]
15. Holmlund, P.; Fuenzalida, H. Anomalous glacier responses to 20th century climatic changes in Darwin Cordillera, southern Chile. *J. Glaciol.* **1995**, *41*, 465–473. [CrossRef]
16. Aniya, M.; Sato, H.; Naruse, R.; Skvarca, P.; Casassa, G. The use of satellite and airborne imagery to inventory outlet glaciers of the southern Patagonia Icefield, South America. *Photogramm. Eng. Remote Sens.* **1996**, *62*, 1361–1369.
17. Rivera, A.; Casassa, G. Volume changes on Pío XI glacier, Patagonia: 1975–1995. *Glob. Planet. Chang.* **1999**, *22*, 233–244. [CrossRef]

18. Rivera, A.; Benham, T.; Casassa, G.; Bamber, J.; Dowdeswell, J.A. Ice elevation and areal changes of glaciers from the Northern Patagonia Icefield, Chile. *Glob. Planet. Chang.* **2007**, *59*, 126–137. [CrossRef]
19. Willis, M.J.; Melkonian, A.K.; Pritchard, M.E.; Ramage, J.M. Ice loss rates at the Northern Patagonian Icefield derived using a decade of satellite remote sensing. *Remote Sens. Environ.* **2012**, *117*, 184–198. [CrossRef]
20. Sakakibara, D.; Sugiyama, S. Ice-front variations and speed changes of calving glaciers in the Southern Patagonia Icefield from 1984 to 2011. *J. Geophys. Res. Earth Surf.* **2014**, *119*, 2541–2554. [CrossRef]
21. Minowa, M.; Sugiyama, S.; Sakakibara, D.; Sawagaki, T. Contrasting glacier variations of Glaciar Perito Moreno and Glaciar Ameghino, Southern Patagonia Icefield. *Ann. Glaciol.* **2015**, *56*, 26–32. [CrossRef]
22. Malz, P.; Meier, W.; Casassa, G.; Jaña, R.; Skvarca, P.; Braun, M.H. Elevation and Mass Changes of the Southern Patagonia Icefield Derived from TanDEM-X and SRTM Data. *Remote Sens.* **2018**, *10*. [CrossRef]
23. Braun, M.H.; Malz, P.; Sommer, C.; Farías-Barahona, D.; Sauter, T.; Casassa, G.; Soruco, A.; Skvarca, P.; Seehaus, T.C. Constraining glacier elevation and mass changes in South America. *Nat. Clim. Chang.* **2019**, *9*, 130–136. [CrossRef]
24. Koppes, M.; Hallet, B.; Anderson, J. Synchronous acceleration of ice loss and glacial erosion, Glaciar Marinelli, Chilean Tierra del Fuego. *J. Glaciol.* **2009**, *55*, 207–220. [CrossRef]
25. Dussaillant, I.; Berthier, E.; Brun, F.; Masiokas, M.; Hugonnet, R.; Favier, V.; Rabatel, A.; Pitte, P.; Ruiz, L. Two decades of glacier mass loss along the Andes. *Nat. Geosci.* **2019**, *12*, 802–808. [CrossRef]
26. Masiokas, M.H.; Rabatel, A.; Rivera, A.; Ruiz, L.; Pitte, P.; Ceballos, J.L.; Barcaza, G.; Soruco, A.; Bown, F.; Berthier, E.; et al. A Review of the Current State and Recent Changes of the Andean Cryosphere. *Front. Earth Sci.* **2020**, *8*, 99. [CrossRef]
27. Weidemann, S.S.; Sauter, T.; Malz, P.; Jaña, R.; Arigony-Neto, J.; Casassa, G.; Schneider, C. Glacier Mass Changes of Lake-Terminating Grey and Tyndall Glaciers at the Southern Patagonia Icefield Derived From Geodetic Observations and Energy and Mass Balance Modeling. *Front. Earth Sci.* **2018**, *6*, 81. [CrossRef]
28. Huintjes, E.; Sauter, T.; Schröter, B.; Maussion, F.; Yang, W.; Kropáček, J.; Buchroithner, M.; Scherer, D.; Kang, S.; Schneider, C. Evaluation of a Coupled Snow and Energy Balance Model for Zhadang Glacier, Tibetan Plateau, Using Glaciological Measurements and Time-Lapse Photography. *Arctic Antarctic Alpine Res.* **2015**, *47*, 573–590. [CrossRef]
29. Sauter, T.; Arndt, A.; Schneider, C. COSIPY v1.2–An open-source coupled snowpack and ice surface energy and mass balance model. *Geosci. Model Dev. Discuss.* **2020**, *2020*, 1–25. [CrossRef]
30. Consortium, R. Randolph Glacier Inventory—A Dataset of Global Glacier Outlines: Version 5.0.: Technical Report; In *Global Land Ice Measurements from Space*. Digital Media: Boulder CO, USA, 2015. [CrossRef]
31. Weidemann, S.; Sauter, T.; Schneider, L.; Schneider, C. Impact of two conceptual precipitation downscaling schemes on mass-balance modeling of Gran Campo Nevado ice cap, Patagonia. *J. Glaciol.* **2013**, *59*, 1106–1116. [CrossRef]
32. Dee, D.; Uppala, S.; Simmons, A.; Berrisford, P.; Poli, P.; Kobayashi, S.; Andrae, U.; Balmaseda, M.; Balsamo, G.; Bauer, P.; et al. The ERA-Interim reanalysis: configuration and performance of the data assimilation system. *Q. J. R. Meteorol. Soc.* **2011**, *137*, 553–597. [CrossRef]
33. Hoffmann, J.; Walter, D. How Complementary are SRTM-X and-C Band Digital Elevation Models? *Photogramm. Eng. Remote Sens.* **2006**, *72*, 261–268. [CrossRef]
34. Jarvis, A.; Reuter, H.; Nelson, A.; Guevara, E. *Hole-Filled Seamless SRTM data V4*; International Centre for Tropical Agriculture (CIAT): Cali, Colombia, 2008.
35. Oerlemans, J. *Glaciers and Climate Change*; Swets and Zeitlinger: Lisse, The Netherland, 2001.
36. Schaefer, M.; Machguth, H.; Falvey, M.; Casassa, G.; Rignot, E. Quantifying mass balance processes on the Southern Patagonia Icefield. *Cryosphere* **2015**, *9*, 25–35. [CrossRef]
37. Möller, M.; Schneider, C.; Kilian, R. Glacier change and climate forcing in recent decades at Gran Campo Nevado, southernmost Patagonia. *Ann. Glaciol.* **2007**, *46*, 136–144. [CrossRef]
38. Smith, R.B.; Barstad, I. A Linear Theory of Orographic Precipitation. *J. Atmos. Sci.* **2004**, *61*, 1377–1391. [CrossRef]
39. Jiang, Q.; Smith, R.B. Cloud Timescales and Orographic Precipitation. *J. Atmos. Sci.* **2003**, *60*, 1543–1559. [CrossRef]
40. Barstad, I.; Smith, R.B. Evaluation of an Orographic Precipitation Model. *J. Hydrometeorol.* **2005**, *6*, 85–99. [CrossRef]

41. Aguirre, F.; Carrasco, J.; Sauter, T.; Schneider, C.; Gaete, K.; Garín, E.; Adaros, R.; Butorovic, N.; Jaña, R.; Casassa, G. Snow Cover Change as a Climate Indicator in Brunswick Peninsula, Patagonia. *Front. Earth Sci.* **2018**, *6*, 130. [CrossRef]
42. Crochet, P.; Jóhannesson, T.; Jónsson, T.; Sigurðsson, O.; Björnsson, H.; Pálsson, F.; Barstad, I. Estimating the Spatial Distribution of Precipitation in Iceland Using a Linear Model of Orographic Precipitation. *J. Hydrometeorol.* **2007**, *8*, 1285–1306. [CrossRef]
43. Schuler, T.V.; Crochet, P.; Hock, R.; Jackson, M.; Barstad, I.; Jóhannesson, T. Distribution of snow accumulation on the Svartisen ice cap, Norway, assessed by a model of orographic precipitation. *Hydrol. Process.* **2008**, *22*, 3998–4008. [CrossRef]
44. Jarosch, A.H.; Anslow, F.S.; Clarke, G.K.C. High-resolution precipitation and temperature downscaling for glacier models. *Clim. Dyn.* **2012**, *38*, 391–409. [CrossRef]
45. Panofsky, H.; Brier, G. *Some Applications of Statistics to Meteorology*; Earth and Mineral Sciences Continuing Education, College of Earth and Mineral Sciences: University Park, PA, USA, 1968.
46. Gudmundsson, L.; Bremnes, J.B.; Haugen, J.E.; Engen-Skaugen, T. Technical Note: Downscaling RCM precipitation to the station scale using statistical transformations—A comparison of methods. *Hydrol. Earth Syst. Sci.* **2012**, *16*, 3383–3390. [CrossRef]
47. Kumar, L.; Skidmore, A.K.; Knowles, E. Modelling topographic variation in solar radiation in a GIS environment. *Int. J. Geogr. Inf. Sci.* **1997**, *11*, 475–497. [CrossRef]
48. Huintjes, E.; Loibl, D.; Lehmkuhl, F.; Schneider, C. A modelling approach to reconstruct Little Ice Age climate from remote-sensing glacier observations in southeastern Tibet. *Ann. Glaciol.* **2016**, *57*, 359–370. [CrossRef]
49. Meier, W.J.H. Glacier inventory for the Patagonian Andes, link to shape files, 2018. Supplement to: Meier, Wolfgang Jens-Henrik; Grießinger, Jussi; Hochreuther, Philipp; Braun, Matthias Holger: An Updated Multi-Temporal Glacier Inventory for the Patagonian Andes With Changes Between the Little Ice Age and 2016. *Front. Earth Sci.* **2018**, *6*, 62. [CrossRef]
50. Sauter, T. Revisiting extreme precipitation amounts over southern South America and implications for the Patagonian Icefields. *Hydrol. Earth Syst. Sci.* **2020**, *24*, 2003–2016. [CrossRef]
51. Bown, F.; Rivera, A.; Zenteno, P.; Bravo, C.; Cawkwell, F. First Glacier Inventory and Recent Glacier Variation on Isla Grande de Tierra Del Fuego and Adjacent Islands in Southern Chile. In *Global Land Ice Measurements from Space*; Kargel, J.S., Leonard, G.J., Bishop, M.P., Kääb, A., Raup, B.H., Eds.; Springer: Berlin/Heidelberg, Germany, 2014; pp. 661–674. [CrossRef]
52. Porter, C.; Santana, A. Rapid 20th century retreat of Ventisquero Marinelli in the Cordillera Darwin Icefield. *An. Inst. Patagonia* **2003**, *31*, 17–26.
53. Kilian, R.; Schneider, C.; Koch, J.; Fesq-Martin, M.; Biester, H.; Casassa, G.; Arévalo, M.; Wendt, G.; Baeza, O.; Behrmann, J. Paleoecological constraints on Late Glacial and Holocene ice retreat in the Southern Andes (53°S). *Glob. Planet. Chang.* **2007**, *59*, 49–66. [CrossRef]
54. Villalba, R. Climatic fluctuations in northern Patagonia during the last 1000 years as inferred from tree-ring records. *Quat. Res.* **1990**, *34*, 346–360. [CrossRef]
55. Haberzettl, T.; Corbella, H.; Fey, M.; Janssen, S.; Lücke, A.; Mayr, C.; Ohlendorf, C.; Schäbitz, F.; Schleser, G.H.; Wille, M.; et al. Lateglacial and Holocene wet-dry cycles in southern Patagonia: chronology, sedimentology and geochemistry of a lacustrine record from Laguna Potrok Aike, Argentina. *Holocene* **2007**, *17*, 297–310. [CrossRef]

Acknowledgments

I would like to thank a number of people who have supported me in various ways during my PhD and who made this time very enjoyable and full of experiences.

My greatest thanks go to Christoph Schneider, who supported my interest in the scientific research of glaciers by giving me the opportunity to work within the GABY-VASA project. I am very grateful to him for sharing his expertise in many fields and being reachable at any time in particular during the review processes and despite the long distance between Aachen and Berlin. His endless enthusiasm and motivation helped me a lot to bridge the somewhat difficult times during my PhD.

I would also like to thank my former colleagues from the Department of Geography at the RWTH Aachen University, who accompanied and supported me in various ways before and during my PhD. I would like to thank Tobias Sauter, Eva Huntjes, Marinka Spiess, Marco Möller, and Rebecca Möller for the constantly open doors and for sharing their knowledge with me about programming, energy and mass balance modeling, project administration and for giving me a lot of valuable advices. My roommate at the time, Lars Schneider, for his help in preparing the field campaigns and for the good talks.

A very special thanks to all Chilean partners of the GABY-VASA project, who welcomed me with open arms and who shared their extensive knowledge and experience in working on Patagonian glaciers with me. I would also like to thank Ricardo Jaña and Inti Gonzalez for their tremendous efforts to make the field work as smooth and successful as possible. Marcelo Arévalo, Guisella Gacitúa, Diego Espinoza, Roberto Garrido Cortés, Leonardo Bergami, Christian Goebel, Jorge Arigony-Neto, Guillherme Netto, Jussi Grießinger, and Wolfgang Meier for their help during the field work at Grey Glacier and Schiaparelli Glacier and for the very enjoyable time during our trips. My stays in Patagonia became the most unforgettable moments during my PhD.

I would also like to thank all my co-authors, other project partners and all the people I met along the way during workshops, summer schools, and conferences and who gave me further ideas for my work through many interesting conversations.

Finally, I am forever grateful to my family and friends, for their love and support during this time. Most of all I want to thank Christian for supporting me unconditionally to pursue my dreams and goals and for not stopping encouraging me during the past years.

Declaration

Ich erkläre, dass ich die Dissertation selbständig und nur unter Verwendung der von mir gemäß § 7 Abs. 3 der Promotionsordnung der Mathematisch-Naturwissenschaftlichen Fakultät, veröffentlicht im Amtlichen Mitteilungsblatt der Humboldt-Universität zu Berlin Nr. 42/2018 am 11.07.2018 angegebenen Hilfsmittel angefertigt habe.

Aachen, Mai 2021 Stephanie Suzanne Weidemann